Particle Attrition in Circulating Fluidised Bed Systems

by

Fabio Fulchini

Submitted in accordance with the requirements for the degree of

Doctor of Philosophy

The University of Leeds

School of Chemical and Process Engineering

March 2020

The candidate confirms that the work submitted is his own, except where work which has formed part of jointly authored publications has been included. The contribution of the candidate and the other authors to this work has been explicitly indicated below. The candidate confirms that appropriate credit has been given within the thesis where reference has been made to the work of others.

The methodology presented in **Chapter 4** of this thesis about the prediction of particle attrition in a cyclone by CFD-DEM is currently published in a pre-proof version in *Powder Technology Journal*. The co-authors have had a supervisory role.

The simulations and part of the experimental work of **Chapter 4** are the result of a collaboration with Mr. Antonino Alessi, of Università degli Studi della Calabria, who spent six months at the University of Leeds to produce his Master thesis.

The numerical analysis of particle attrition in a jet in a fluidised bed, presented in the Appendix, has been published in *EPJ Web of Conferences* of *Powders and Grains 2017*. The co-authors have had a supervisory role.

Alla mia famiglia

ACKNOWLEDGEMENTS

I hereby would like to express my appreciation and gratefulness to all the people who have helped, directly and indirectly, to achieve the ambitious objectives of this PhD project.

I am grateful to have been under the wise guidance of Professor Mojtaba Ghadiri, I am thankful for his constant dedication and keen enthusiasm in supervising my work. This thesis would not have been possible without his timely advice and guidance and I thank you for having made a researcher out of me! To my co-supervisor, Antonia Borissova Dimitrova, I want to express all my gratitude for having been such an excellent adviser and for having constantly supported me. Special thanks go to Benjamin Amblard, a wonderful supervisor, a friend and a fantastic football player. Thank you for having provided me with daily valuable technical and moral support. I want to thank Ann Cloupet for her sincere support and encouragement as well as excellent guidance when everything seemed to not work. I would like to express my appreciation to Stephan Bertholin and Mahdi Yazdanpanah for having believed in me since the beginning, motivated me and given me the freedom to express my creativity and research attitude in this challenging project. I hope to have proven myself worthy of your trust.

I would like to thank all the fantastic technicians for their help in setting up the experimental rigs and having dedicated me their time to solve the uncountable technical problems encountered. In particular, I wish to thank Robert Harris (Bob) of University of Leeds, Robert Beaumont, William Pelletant and Florian Montjovet of IFP Energies Nouvelles.

I would like to take this opportunity to acknowledge and thank all the members in Ghadiri Research Group for making me feel welcomed. I really value for all the help and encouragement that they give during these years. Special thanks go to my dear friends Selasi Dogbe, Wei Pin Goh, Wenguang Nan, Mehrdad Pasha and Alejandro Lopez.

My gratitude also goes to all the friends that I made during these four-years life journey: my bossy flatmate Alessio Dragonetti, the crazy horse Marco Scala, Vittorio Petrazzuoli and the VP car, the French man Federico Bussolati, the warrior Davide Lorito and the most Neapolitan person I know Sina Tebianian. I thank you for the fantastic time spent together. I

also would like to thank Francois Gael for having kept me in good shape during my time in Lyon.

I am eternally grateful to Tina Bonakdar for her unconditional support and for always believing in me. I could not have achieved this without you.

My thoughts go to my family, my dear mother and father, my sister Emanuela, my beautiful nephew Giovanni Paolo and my brother Simone to whom I wish a successful career as a chemical engineer. I am sorry to have been far from you. I thank you for everything you did. Without you I could have never gotten this far.

ABSTRACT

Particle attrition plays an important role throughout the cycles of a circulating fluidised bed (CFB) and a fluidised bed (FB) process, gradually depriving the bed inventory of valuable mass and changing the bed particle size distribution. The mass loss has to be compensated by a make-up stream. For economic and design purposes, attrition cannot be neglected. Although the particles may be efficient catalysts (or reactants), if the compensation for the lost material amounts to very high expenses, the whole process may become uneconomical. It is then clear that the choice of the solids material should take into account its attrition propensity. The main sources of attrition in fluidised bed systems are the jet region, the bubbling bed and the cyclone. It is common practice to predict particle attrition in industrial scale fluidised bed systems by the population balance method, but is it possible to link that prediction with the breakage propensity of a single particle?

This work aims at developing a predictive tool for particle attrition in fluidised and circulating fluidised beds, by attempting to build a path line from the single particle breakage propensity to the attrition occurring in the process. Here, the reference industrial process is the Chemical Looping Combustion (CLC). The CLC is a circulating fluidised bed process under development and as such, the choice of a solids material is critical. A powder of crushed manganese oxide is a candidate material for the CLC process and is used here as test material, as well as its equilibrium equivalent. For simplicity, the two materials are referred to as F-CLC (fresh CLC particles) and E-CLC (equilibrium CLC particles), respectively.

The single particle breakability of F-CLC and E-CLC is assessed by impact tests. The experimental results are then used to correlate the extent of breakage upon impact with the particle size and impact velocity, according to the theoretical model of chipping of Zhang and Ghadiri (2002). Further tests are carried out to unveil the effect of impact angle and number of impacts. The results suggest that E-CLC is highly more inclined to attrition than F-CLC. Moreover, the single particle breakage is found to correlate with the magnitude of the impact velocity and the sin of the angle of impact for both materials.

Recalling the modelling approach of Ghadiri and co-workers, the single particle breakage model, as derived, and the model of surface wear of Archard and Charj (1953) are coupled

with CFD-DEM (Computational Fluid Dynamic-Discrete Element Method) simulations to compute the attrition of F-CLC particles in a Stairmand cyclone. Moreover, the same cyclone is used to characterise attrition of F-CLC particles experimentally as a function of particle size, gas inlet velocity and solids loading. Remarkably, the outcomes of the two approaches are found to agree well. A correlation is eventually derived which expresses the extent of attrition in a cyclone as a function of the variables mentioned above. The analysis revealed that the main source of attrition in the cyclone is given by the particle-wall collisions at the opposite section of cyclone inlet, at any operating conditions. Particle-particle collisions and particle sliding against the wall become significant contributors of attrition at high and low solids loading, respectively.

Attrition in the jet region is evaluated at room temperature as the steady state loss rate, using a semi-pilot scale fluidised bed equipped with a porous distributor and a central orifice of variable size. The results of the tests show that jet attrition of F-CLC and E-CLC can be described by two different correlations. The steady state attrition propensity of E-CLC is found to be higher than F-CLC, confirming the outcomes of the impact tests. The analysis on the fines collected on the filter reveals that they are mainly composed by very small particles of about 1 μm.

The correlations of cyclone and jet attrition are implemented in a non-dimensional population balance model (PBM) that simulates attrition in a fluidised bed and a circulating fluidised bed. The latter is composed of a fluidised bed where the recycle of solids is provided by a cyclone. The PBM is validated for the fluidised bed configuration against the experimental PSD (Particle Size Distribution) of F-CLC particles after jet attrition in the fluidised bed. The PBM is eventually used to simulate hypothetical cases of a FB and CFB with low and high single particle breakability as well as low and high superficial velocities to assess the dynamic response of the system in terms of material loss, solids circulation rate, requirements for a make-up and PSD in different regions of the system. The simulations allowed to identify the presence of two subsequent regimes where the loss is firstly dictated by the pre-existing fines of the bed inventory and then by attrition. During the two regimes the mean particle size of the bed inventory increases and decreases, respectively. The PBM reveals that the circulation rate is strongly affected by attrition because of the accumulation of entrained particles which are large enough to be captured by the cyclone and recycled. The loss of material and the need for the make-

up stream are found to increase using either larger superficial velocities and/or weaker particles.

TABLE OF CONTENTS

LIST OF FIGURES

LIST OF TABLES

NOMENCLATURE

Symbol	Description	Unit measure
	Latin letters	
A	area	m^2
a	particle acceleration	$m\ s^{-2}$
a_{cyc}	height of the slotted entry of the cyclone inlet	m
A_p	subfunction of the correlation for particle velocity in the inlet pipe of the cyclone	-
Ar	Archimede's number	-
b_{cyc}	base of the slotted entry of the cyclone inlet	m
B_p	subfunction of the correlation for particle velocity in the inlet pipe of the cyclone	-
b_{sp}	single particle breakage constant term	-
C	generic attrition constant	variable
C_D	drag coefficient	-
C_{solids}	solids concentration	-
d	diameter	m
$d_{50,Ai}$	characteristic particle size of the inner feed	m
d_p	particle size	m
$d_{p,\infty}$	particle size at terminal velocity	m
e	percentage error	%
E	Young's modulus	Pa
e	percentage error	%
e_a	fitting parameter of beta function	-
e_b	fitting parameter of beta function	-
e_n	coefficient of restitution	-
E_r	reduced Young's modulus	Pa
F	force	N
f_{mat}	material properties constant (Vogel and Peukert, 2003)	-
g	gravity	$m\ s^{-2}$
G	particle shear modulus	Pa

h	height	m
H	hardness	Pa
h_c	indentation penetration depth	m
I	momentum of inertia	kg m^2
K^*	total entrainment flux of solids	kg m^{-2} s^{-1}
$K_\infty{}^*$	dispersed non-cluster entrainment flux of solids (not a function of bed height)	kg m^{-2} s^{-1}
$K_h{}^*$	cluster entrainment flux of solids (function of bed height)	kg m^{-2} s^{-1}
k_{ind}	indenter shape factor	-
L	length of the inlet pipe	m
m	mass	kg
M	torque	N m
$\dot{m}$	mass flow rate	kg s^{-1}
N	number of classes	-
N^d	normalised drag force	-
N_p	number of particles	-
N_u	number of unbroken particles (Salman et al. 1995)	-
P	pressure	Pa
Q	gas volumetric flow rate	m^3 s^{-1}
R	extent of breakage	-
$\dot{R}$	normalised attrition rate	s^{-1}
R_{Ai}	cumulative PSD of the inner feed of the cyclone	-
Re_p	particle Reynolds number	-
r	attrition rate	kg s^{-1}
r_p	particle radius	m
S	stiffness	N m^{-1}
s	distance	m
St_m	particle stokes number	-
t	time	s
T	temperature	°C
TDH	Transport Disengagement Height	m
u	fluid velocity	m s^{-1}

$u_{cyc,0}$	cyclone gas transition velocity from no/little breakage to breakage	m s^{-1}
$u_{jet,0}$	gas jet transition velocity from no/little breakage to breakage	m s^{-1}
V	volume	m^3
v_p	particle velocity	m s^{-1}
$v_{p,0}$	particle transition velocity from no/little breakage to breakage upon impact	m s^{-1}
$v_{p,\infty}$	particle terminal velocity	m s^{-1}
V_W	wear volume	m^3
w	particle relative velocity	m s^{-1}
W_k	specific impact energy	J kg^{-1}
x	mass fraction	-
$\chi_{breakability}$	multiplying factor of the breakability index	-
x_i	position of particle i	m
y	fraction of particles in contact with the wall	-

Greek letters

α	constant of (Ghadiri and Zhang, 2002)	-
α_A	Constant of the model of Archard	-
α_{wear}	Constant of the normalised model of Archard	m^{-3}
β	scaling factor used for the debris PSD in the population balance	-
μ	solid loading of the cyclone feed material	kg_{solid} kg_f^{-1}
μ_f	fluid viscosity	Pa s^{-1}
μ_{lim}	critical solid loading of the cyclone feed material	kg_{solid} kg_f^{-1}
μ_s	coefficient of static friction	-
δ_n	normal particle over-lap	-
γ	non-dimensional bubble-through factor	-
Δt	time step	s
ε	void degree	-
η_{col}	efficiency of collision	-
η_{eff}	cyclone efficiency of gas/solids separation	-

η_n	normal damping coefficient	-
η_t	tangential damping coefficient	-
θ	angle of impact	rad
ν	Poisson's ratio	-
ρ	density	kg m^{-3}
τ	average particle residence time	s
τ_f	fluid stress tensor	Pa
φ	angular position	rad
ω	particle angular velocity	rad s^{-1}
Π_m	momentum coupling number	-

<u>Abbreviation, subscript and superscript</u>

0	refers to the initial conditions
AJI	attrition jet index
att	attrition
av	average
bb	refers to the bubbling bed region
bed	refers to the bed inventory
cell	refers to the fluid cell for CFD resolution
CFB	circulating fluidised bed
chip	refers to chipping mechanism
col	collisions
crit	critical
cyc	cyclone
de	debris particle
dis	dissipated
E-CLC	equilibrium chemical looping combustion particles
el	elastic
elut	elutriation
eq	equivalent
exit	refers to the exit
EXP	experiment
f	fluid

FB	fluidised bed
F-CLC	fresh chemical looping combustion particles
filter	refers to the filter
fr	fragmentation
freeboard	refers to the freeboard
i	refers to a single particle in Chapter 4; refers to a size class in Chapter 6
IF	inner feed (cyclone)
imp	impact
in	inlet
ind	refers to the indenter
jet	refers to the jet region
make-up	refers to the make-up stream
max	maximum
mf	minimum fluidisation
min	minimum
mp	mother particle
n	normal component
NS	Navier-Stokes
or	orifice
p	refers to a single particle
pb	porous base
PSD	Particle Size Distribution
P-P (or pp)	particle-particle
P-W (or pw)	particle-wall
r	rolling
RANS	Reynolds Averaged Navier Stokes
rbnd	rebound
rec	recycle
Saut	Sauter mean diameter
so	sieve mesh opening
solids	refers to the solids
sup	superficial

t	tangential component
tot	total
VF	vortex finder (cyclone)
w	wall
wear	refers to wear mechanism

1. INTRODUCTION

CHAPTER 1

The term “attrition” refers to undesired particle breakage, (Bemrose and Bridgwater, 1987). In fluidised and circulating fluidised beds, attrition is a major issue. The bed solids are in vigorous motion and thus inevitably subjected to mechanical stresses due to interparticle and particle-wall collisions, causing a gradual degradation of the solids material. Thermal and chemical stresses are also responsible for particle attrition. Depending on the type/magnitude of the stress applied and the material properties, the particles can degrade in different ways. The main consequence of attrition is the generation of small fines that cannot be kept inside the system, creating an additional burden on the filtration system, and most importantly causing the loss of valuable material, (Werther and Reppenhagen, 2003). Along with the generation of fines, the so-called mother particles are gradually shrunk or even broken into fragments. This leads to an undesired shift from the initial PSD, strongly affecting the performance of the process. In fact, the PSD of the bed solids, in combination with the operating conditions, dictates the solids circulation rate, the heat and mass transfer (Molerus, 1992) the conversion and the selectivity of reaction (Werther, 1992).

Attrition induced by mechanical stresses in fluidised beds is usually categorised into “surface abrasion” and “fragmentation” (Blinichev and Streltsov, 1968; Pell, 1990; Pis et al. 1991). The former describes patterns of breakage such as chipping and wear which are characterised by the removal of the irregularities of the particle surfaces leading to the formation of small fines and a slight reduction of the size of the mother particle. The latter refers to the formation of fragments, making the distinction between mother and daughter particles no longer applicable, as shown in Figure 1-1.

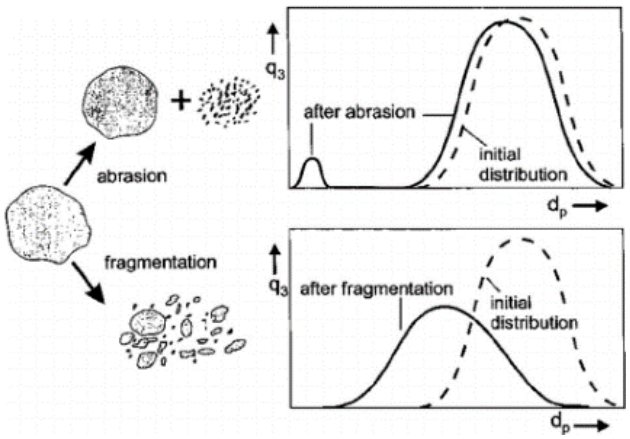

Figure 1-1. Schematic definition of attrition mechanisms given by Pis et al. (1991)

The two mechanisms do not usually take place separately, they are rather combined in different proportions, which makes the description of the process somewhat complicated.

The natural tendency would be to use a material which is strong enough to avoid extreme cases of attrition like fragmentation. The inclination of a particle to undergo attrition depends on their mechanical properties, size, shape, structure, surface roughness, history and the process conditions, mainly the gas velocity (dictating the solids velocity and residence time), temperature and chemical reaction.

In fluidised bed systems, particle attrition can occur in different regions at different extents and following different mechanisms (Zenz and Kelleher, 1980; Vaux and Keairns, 1980). These are usually the vicinity of the multi-hole distributor (or more commonly addressed to as jet region), the bubbling fluidised bed, the cyclones, the conveying lines and the solids feeding devices. The first three have been extensively studied as they are recognised to be the main sources, (Pell, 1990). Attrition in the jet region occurs as a result of inter-particle impacts and shearing because of particles being entrained in the jet core. In the bubbling bed, attrition originates from low velocity inter-particle collisions caused by the movement of the bubbles, while in the cyclone, attrition is caused by high velocity particle impacts at the entrance as well as particle sliding on the wall. As reported by Werther and Reppenhagen, (1999) for FCC catalyst, at high superficial velocities the cyclone is the main source of attrition, followed by the jet region and the bubbling bed, Figure 1-2.

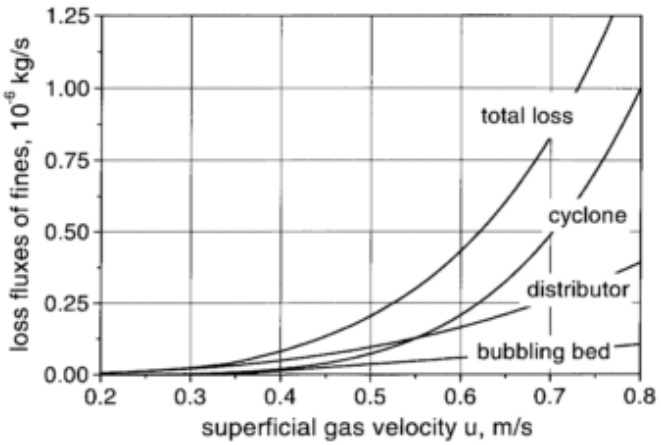

Figure 1-2. Main sources of attrition as a function of superficial velocities according to Werther and Reppenhagen, (1999)

Since attrition affects the single particle and extends to the full process, there are various criteria based on which attrition may be qualitatively and quantitatively characterised. Obviously, there is no universal procedure for the measurement of a material propensity to attrition (Werther and Reppenhagen, 2003). For instance, a single particle or a bulk sample can be subjected to a certain stress to in order to assess its tendency to undergo attrition in terms of extent of breakage as well as shift in PSD.

The Grace-Davison Jet-Cup attrition test, for instance, can qualitatively reproduce the relative attrition propensity of different materials by inducing surface abrasion of particles, which are sheared between themselves and against the wall by mean of a tangential air jet at the bottom of the conical cup (Dessalces et al. 1994; Amblard et al. 2015). The most common attrition-modelling approach requires the use of test facilities that simulate the stress of a certain region of the process. For the assessment of the jet and bubbling bed induced attrition, the most popular equipment are those of Forsythe and Hertwig (1949) and Gwyn (1969). They are lab-scale fluidised beds with one and three submerged jets, respectively. In case of cyclone attrition, Zenz and Kelleher (1980) and Reppenhagen and Werther (2000) used an isolated cyclone to respectively look at the change in PSD and the steady state mass loss, both after several passes through it. Most of the results of these tests reveal the average effect on all particles; hence it is hard to establish the dominant mechanism. Moreover, they are usually used as guidelines in design procedure as they might not be directly transferable to large-scale processes, (Boerefijn et al. 2000). For these reasons, a second attrition-modelling approach relies on

the response of the material to a well-defined stress like compression, impact, or shear coupled with the frequency and extent of the same stress occurring in a certain region of interest (Yuregir et al. 1986; Boerefijn et al. 2000; Ghadiri et al. 1994). Ghadiri and co-workers (Ghadiri et al. 1992; Ghadiri et al. 1994; Ghadiri M, Cleaver JAS, 1995; Zhang et al. 1998; Boerefijn et al. 2000) have applied this concept to the jet attrition using the single particle breakage propensity upon impact, coupled with the particle dynamics obtained from a hydrodynamic model of submerged jet. Following the same philosophy, exploiting the latest development in computational capabilities, the particle dynamics can be now achieved by CFD-DEM simulations, (Xu et al. 2014).

Whatever the method, the aim of such assessments is the development of attrition models which correlate the attrition-induced material loss rate with some known process conditions and material properties.

The attrition rates, alone, do not give insights on the change in PSD but, they can be used to represent the kinetic of particle size reduction in a population balance model, so that the full description of the fate of a solids system, undergoing to attrition, can be achieved (Levenspiel et al. 1968; Werther and Hartge, 2004; Redemann et al. 2009). The population balance model can thus provide a picture of the dynamic response of the process in terms of mass loss and adjusting PSD of the bed inventory. Though, these models are often simplified considering only surface abrasion and no formation of physical fines.

As reported above, predicting the impact of attrition on the process performances can be quite challenging. A good description of the process can be only achieved by considering the single particle attrition propensity and the particle dynamics, established in different regions of the process, as a function of the operating conditions. Many authors have tried to establish universal methodologies for the attrition assessment. In reality, there is a significant amount of literature which is often in disagreement. This leads to the necessity of carrying out a comprehensive attrition investigation of a novel material.

1.1 Background

The Chemical Looping Combustion (CLC) is a developing carbon capture technique where the combustion between the fuel and the oxidiser is not realised with the oxygen of the air, but rather with that carried by solid particles, addressed to as "oxygen carriers". This allows to have an easy separable flue gas stream composed mainly of CO_2 and water, thus allowing the former to be efficiently isolated, sequestered and/or re-utilised, (Hossain and de Lasa, 2008). The CLC is a circulating fluidised bed where the solids are first reduced in the so-called "fuel reactor" and then oxidised in the "air reactor". The two reactors are usually risers and the solids chemical loop is regulated by the continuous recirculation of the entrained particles captured by cyclones, Figure 1-3.

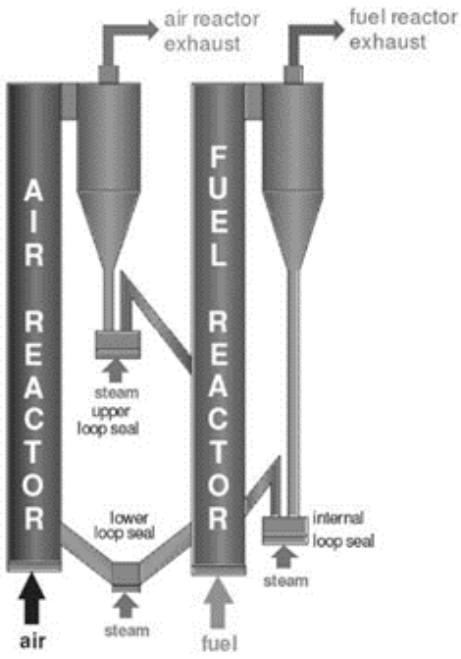

Figure 1-3. A schematic representation of the CLC process

The chances for attrition to take place are plenty, hence the oxygen carriers should be resilient enough to avoid incontrollable deviation from the desired operating conditions and, of course, loss of valuable material.

In this work, a population balance model is developed and used to simulate the effect of particle attrition on the dynamic behaviour of a fluidised bed and a circulating fluidised bed. The material attrition propensity is initially evaluated experimentally at single

particle level. Particle attrition is then assessed in the jet region of a fluidised bed and a cyclone by means of both experimental and computational approaches.

The material of interest is a crushed manganese oxide, used in two forms: fresh and used. They are respectively referred to as F-CLC (fresh-CLC) and E-CLC (equilibrium-CLC).

1.2 Objectives and Structure of the thesis

The project, sponsored by Total, is in partnership between the University of Leeds (Leeds, UK) and IFP Energies Nouvelles (Solaize, FR). The four years research work has been equally divided and carried out between the University of Leeds and IFP Energies Nouvelles's facilities.

The main aim of this PhD project is to develop a predictive tool for particle attrition in circulating fluidised beds and to gain a detailed understating of the factors affecting attrition at single particle level and in different regions like the cyclone and the proximity of the multi-hole distributor.

A schematic diagram of the project is shown in Figure 1-4.

The analysis begins at the single particle by characterising the single particle tendency to undergo breakage upon impact, for different impact velocities, particle sizes and angles of impact. Their surface, internal structure and mechanical properties are also evaluated in order to better evaluate the consequences of the chemical looping combustion on the material. The attrition study is then moved to the cyclone and the jet region, where the objectives are the understanding of the underlying mechanisms leading to attrition using fully coupled CFD-DEM simulations and the development of attrition correlations using inputs of the single particle breakage analysis. The attrition correlations, describing the rate of formation of fines and the particle shrinking rate, are eventually implemented in a population balance model to describe the dynamic behaviour of the process as a result of jet, bubbling bed and cyclone attrition.

As the thesis covers quite diverse aspects of particle attrition from the single particle to the process, for consistency, each Chapter has a dedicated literature review. The thesis is structured in a way that the knowledge gained in one chapter can be passed onto the next

one. The chapters are about the following topics: material characterisation, single particle attrition analysis, cyclone attrition analysis, jet attrition analysis and process attrition. An outline of their contents is reported below:

CHAPTER 2 The two materials are characterised in terms of chemical composition by EDX analysis, particle size distribution by sieving analysis, density by mercury porosimetry technique, surface morphology by SEM analysis, internal structure, and mechanical properties by nano-indentation technique. (University of Leeds)

CHAPTER 3 In this Chapter, the single particle breakage propensity of the fresh and equilibrium solids materials is evaluated by using a conventional and a non-conventional impact tester, by carrying out controlled particle impacts, as a function of particle size, a wide range of impact velocities, angle of impact and number of impacts. (University of Leeds)

CHAPTER 4 A Stairmand cyclone is used to set-up an attrition rig by means of which the attrition of F-CLC particles is evaluated varying the gas inlet velocity, the particle size and solids loading. The experiments are then simulated by CFD-DEM simulations using Ansys Fluent coupled with EDEM®. The outcomes, in terms of frequency and extent of stress, are coupled with single particle breakage models to compute the overall attrition extent which is then compared with the experimental results. (University of Leeds)

CHAPTER 5 The jet attrition rates of both materials are found experimentally as the steady state loss rate using a semi-pilot scale fluidised bed equipped with a porous distributor and singular central orifice. A jet induced correlation is eventually developed as a function of orifice size and jet velocity. Moreover, the particle size distribution and particles morphology of before and after fluidisation as well as the fines collected on the filter are investigated. (IFP Energies Nouvelles)

CHAPTER 6 A 0D dynamic population balance model of attrition in a fluidised bed and circulating fluidised bed with make-up is developed, using the sequential modular approach, described and used to simulate hypothetical cases of stronger/weaker particles and different operating conditions. The interest here is the evolution of the particle size

distribution of the bed inventory, the solids circulation rate and loss rate. (IFP Energies Nouvelles)

CHAPTER 7 In this Chapter, general conclusions are drawn. The limitations are discussed along with ideas that can encourage potential future work.

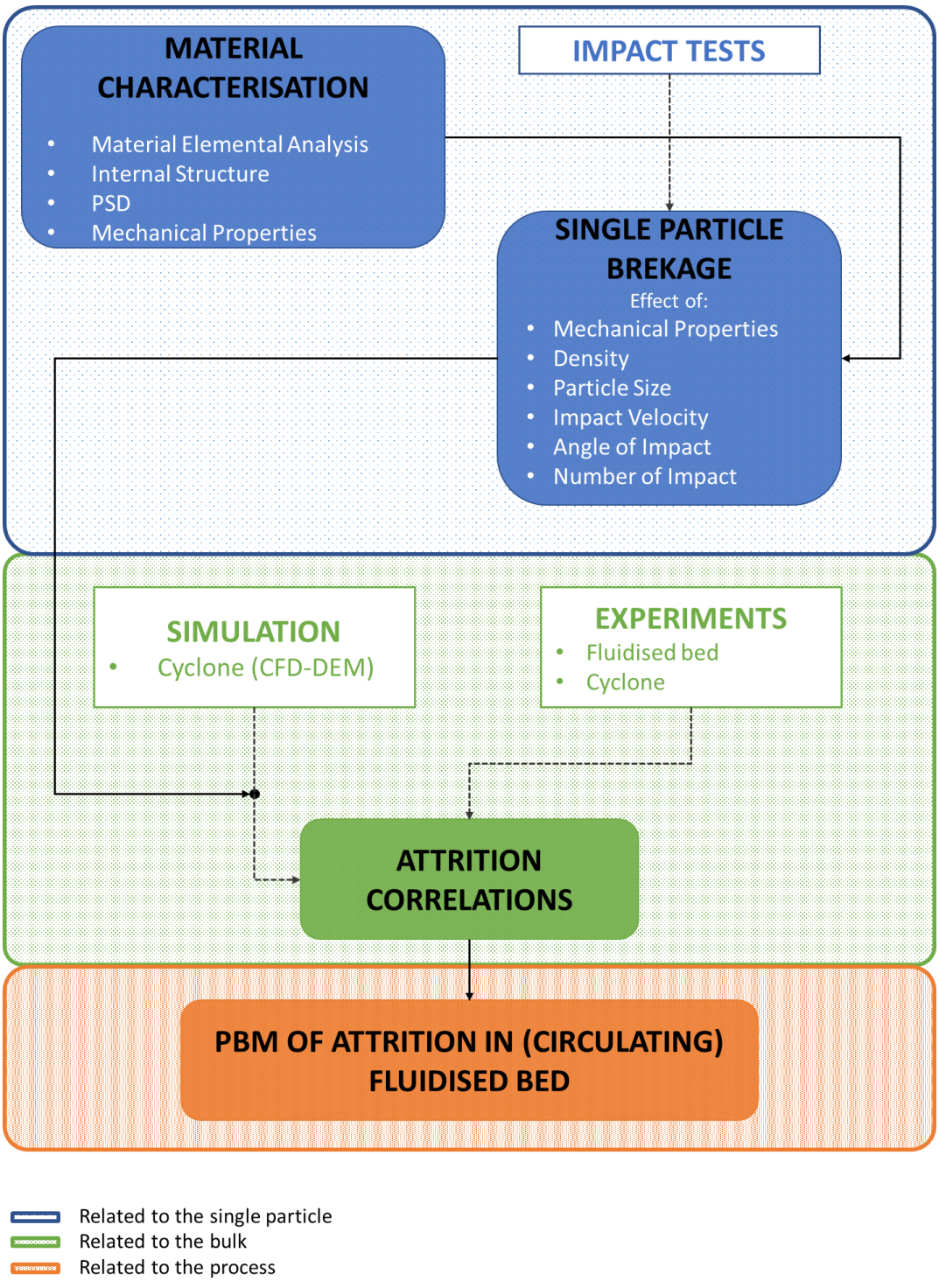

Figure 1-4. Schematic diagram of the research project

2. MATERIALS CHARACTERISATION

CHAPTER 2

The materials used in this work are characterised and prepared for the experimental tests. Essential features such as chemical composition, particle size distribution, particle density, surface morphology, internal porosity as well as mechanical properties are evaluated and discussed.

This work has been carried out at the University of Leeds across the 1st and 2nd year of this PhD project.

2.1 The Materials

The solids materials are crushed naturally occurring manganese oxide, provided by IFP Energies Nouvelles (Solaize, France), which is intended to be used in the Chemical Looping Combustion process. Two types of particles were supplied: a fresh unused sample and one actually used in the CLC process, hereinafter referred to as equilibrium CLC particles. For simplicity, in this dissertation, they are referred to as with the abbreviation F-CLC and E-CLC, respectively.

The batches of supplied powders amounted to about 50 kg of F-CLC and 5 kg of E-CLC. The E-CLC went under a cycle of oxidation and reduction with air at 850°C and CH_4 at 900°C, respectively. This material has been circulated in the system and often the loss has been replenished with fresh material, making it a mixture of particles with different ages. F-CLC is the primary test material of this project.

2.2 Material Preparation

Powder sampling is crucial, especially when it comes to large batches of material. Due to handling and transportation the batch of powder could be segregated causing potential errors in particle size distribution analysis. The splitting-blending method allows to obtain small quantities of materials that are representative of the whole batch. The operation is explained schematically in Figure 2-1, (Germaine and Germaine, n.d.). The splitting is

carried out using a static laboratory riffle splitter. Referring to the splitting-blending of the F-CLC powder, out of 50 kg of the initial batch "A", the 64th fraction called "A/64" is obtained and finally divided till a 512th fraction of the initial batch. The final samples weigh around 90 grams which is a suitable amount to be used for sieving analysis and particle size distribution characterisation.

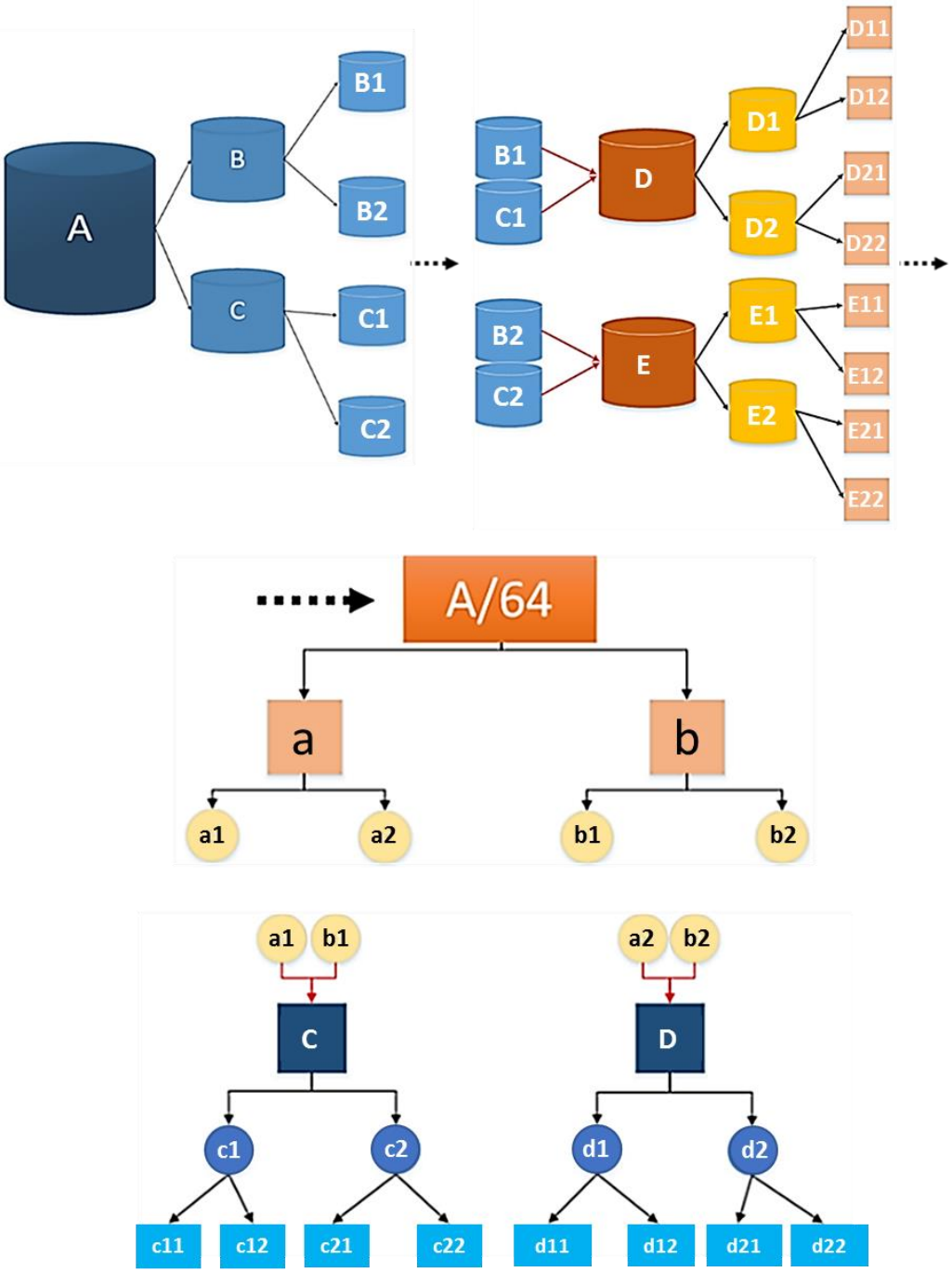

Figure 2-1. Splitting-Blending procedure

2.3 Material Characterisation

2.3.1 Chemical Analysis

The Energy-dispersive X-ray spectroscopy (EDX) technique, (Goldstein, 2003), is used for the chemical characterisation of F-CLC and E-CLC. The emission spectra obtained by EDX allows identifying which elements are present in the specimen and its relative abundancy in terms of mole or mass fraction. The proportion between manganese and the oxygen is then calculated so that the state of oxidation of manganese can be worked out. It needs to be noted that the EDX technique only provides information of the exposed surface of the material. It is therefore a reliable method for the chemical characterisation of chemically homogeneous materials.

For this purpose, 16 spectra per specimen are obtained and averaged. The elements mass fractions and the Mn/O mass ratios are reported in Table 2-1a and b, respectively. The analysis reveals that the F-CLC, that has a Mn/O mass ratio of 2.01, is attributable to a mixture composed by the 83% of MnO_2 and the rest by MnO as it is comparable to the commercially available manganese dioxide/manganese oxide powder, which has the 84.1% in weight of MnO_2 and 1.6% of Fe, (©2016 Reade International Corp, n.d.). The E-CLC has a Mn/O mass ratio of 2.43. It therefore can be attributed to Mn_3O_4 that has a Mn/O mass ratio of 2.56.

Table 2-1. a) mass fraction of the elements composing F-CLC and E-CLC. b) Mn/O mass ratio for F-CLC, E-CLC and various Manganese oxides

a)

element	Mn	O	C	Fe	Al	Si	K	Ti	P	Na
F-CLC	57.50%	29%	5%	4%	traces	traces	traces	traces	traces	traces
E-CLC	63%	26%	4%	3%	traces	traces	traces	traces	traces	traces

b)

material	**F-CLC**	**E-CLC**	MnO	MnO_2	Mn_2O_3	Mn_3O_4	MnO_3	Mn_2O_7
Mn/O	**2.01**	**2.43**	3.43	1.71	2.29	2.56	1.14	0.98

2.3.2 Particle Size Distribution

The particle size distribution (PSD) is evaluated by hand/mechanical sieving, for the two materials, using DIN 4188 sieve type of 315 mm. The sieve shaker RETSCH AS 300 is used for mechanical sieving. The samples are initially sieved mechanically at a relatively

low vibration rate to avoid any undesired breakage, then sieving is carried out manually to have a better control on the procedure. Manual sieving is carried out according to the standard procedure mentioned in (Germaine and Germaine, n.d.). The PSD are reported below in Figure 2-2 and Figure 2-3. For each material, the PSD is determined for three separate samples and the results are combined. The red bars, shown in the PSD, are the most representative size cuts chosen to carry out the experimental breakage analysis, Table 2-2. The PSD of the F-CLC clearly shows a bimodal trend. The PSD of E-CLC still presents the bimodal trend but it is less marked and shifted towards smaller sizes with respect to F-CLC, clearly as a result of attrition. Their characteristic measures of particle size distribution d_{10}, d_{50}, d_{90}, d_{Saut} and d_{av} based on the sieving analysis are reported in Table 2-3 along with the coefficient of variation.

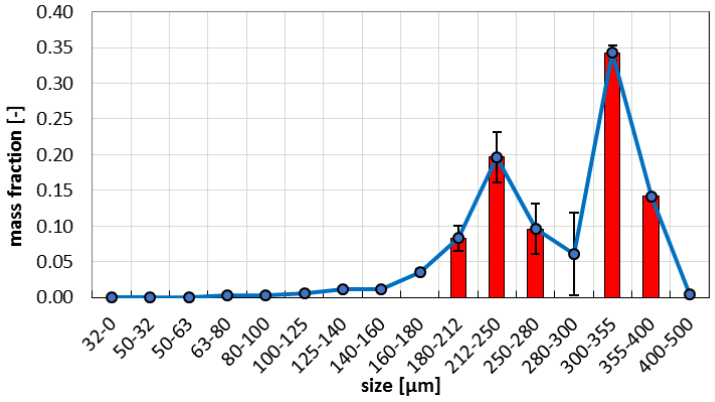

Figure 2-2. PSD of the F-CLC evaluated by manual and mechanical sieving

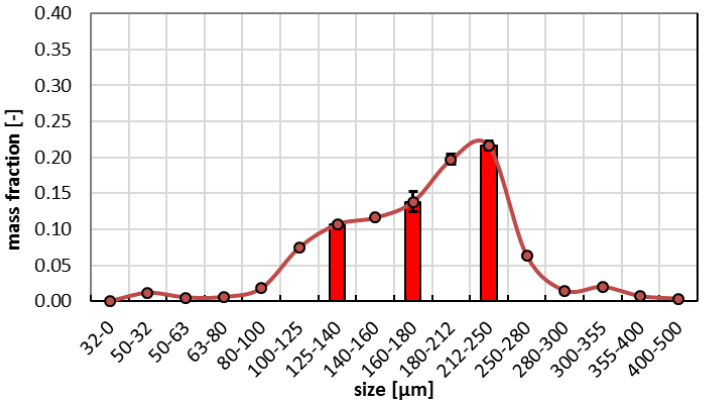

Figure 2-3. PSD of the E-CLC evaluated by manual and mechanical sieving

Table 2-2. Representative size cuts used to carry out the breakage tests

	F-CLC	E-CLC
Representative size cuts [µm]	355-400	212-250
	300-355	160-180
	250-280	125-140
	212-250	-
	180-212	-

Table 2-3. D_{10}, D_{50}, D_{90}, D_{Saut} and D_{av} of F-CLC, E-CLC and E-FCC

Characteristic particle size [µm]	F-CLC	E-CLC
d_{10}	**170** (CV=5%)	**108** (CV=0.8%)
d_{50}	**271** (CV=6%)	**173** (CV=0.9%)
d_{90}	**341** (CV=1%)	**236** (CV=0.5%)
d_{Saut}	**262** (CV=2%)	**160** (CV=0.5%)
d_{av}	**284** (CV=2%)	**186** (CV=0.4%)

2.3.3 Surface and Structural Analysis

The particles are viewed by the Scanning Electron Microscopy (SEM). The image analysis is important to characterise the particle surfaces. The micrographs are reported in Figure 2-4 for F-CLC and E-CLC. The images reveal that the F-CLC particles shape is very irregular, as expected, because they are crushed natural mineral ore. Their surfaces have very sharp edges and asperities, which make the particles very prone to breakage regardless of the strength of the material. As a result, the sample is also quite dusty. The effect of attrition is with no doubts exposed on E-CLC specimen. As the micrographs show, they have also become highly porous, with large cavities visible. The size of these cavities indicates that there is a substantial transformation of their internal structure, due to chemical/thermal stresses. The particle shape is still irregular, their surfaces are rough. They have been continuously subjected to chipping. It also appears that the E-CLC particles are of different ages, as some of them seem fresher than others. The internal structure of the two CLC samples is investigated by SEM, looking at sliced particles. For preparation, they are first embedded in liquid resin. The solidified resin is ground/polished to reveal the surfaces of the cut particles. The images are shown below

in Figure 2-5. The F-CLC particles show some internal heterogeneity and random macro-pores, while the E-CLC particles are characterised by a remarkable internal macro-porosity. Some of the E-CLC particles seem fresh, some other highly porous and surrounded by a denser shell, some hollow, but most of them look extremely porous inside. Presumably, the shell has formed by sintering at high temperature, while the formation of the internal cavities could be due to continuous compression/expansions caused by both thermal effect and cyclic reduction/oxidation. The change of oxidation state leads to enlargement and reduction of the particles producing structural defects, such as weak spots, pores and cavities with consequent release of material. Substantial work is needed to analyse these mechanisms of degradation. Using the "Mercury Intrusive Porosimetry", it is possible to map the porosity of the F-CLC and E-CLC particles. This is shown in Figure 2-6. The presence of meso and macro pores for the F-CLC and extensive larger macro pores for the E-CLC can be deduced. The particle envelope density is evaluated using the same technique and reported in Table 2-4.

According to the analysis on particle size distribution and particle density, the material is a Geldart group B, (Baeyens and Geldart, 1986).

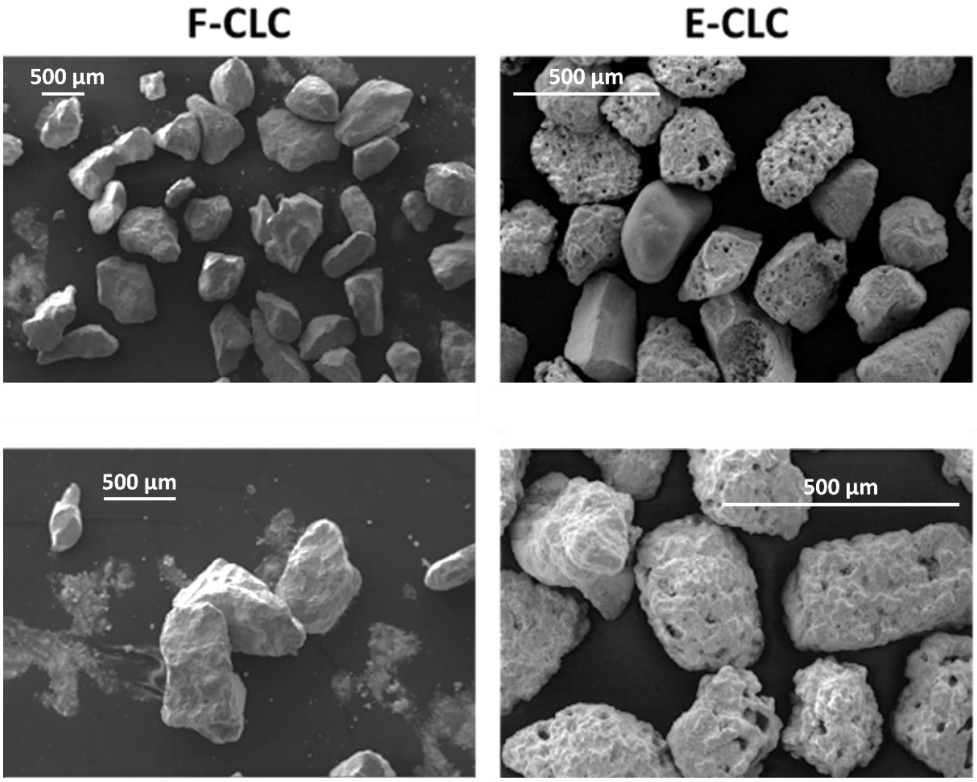

Figure 2-4. SEM micrographs of F-CLC (left), E-CLC (right)

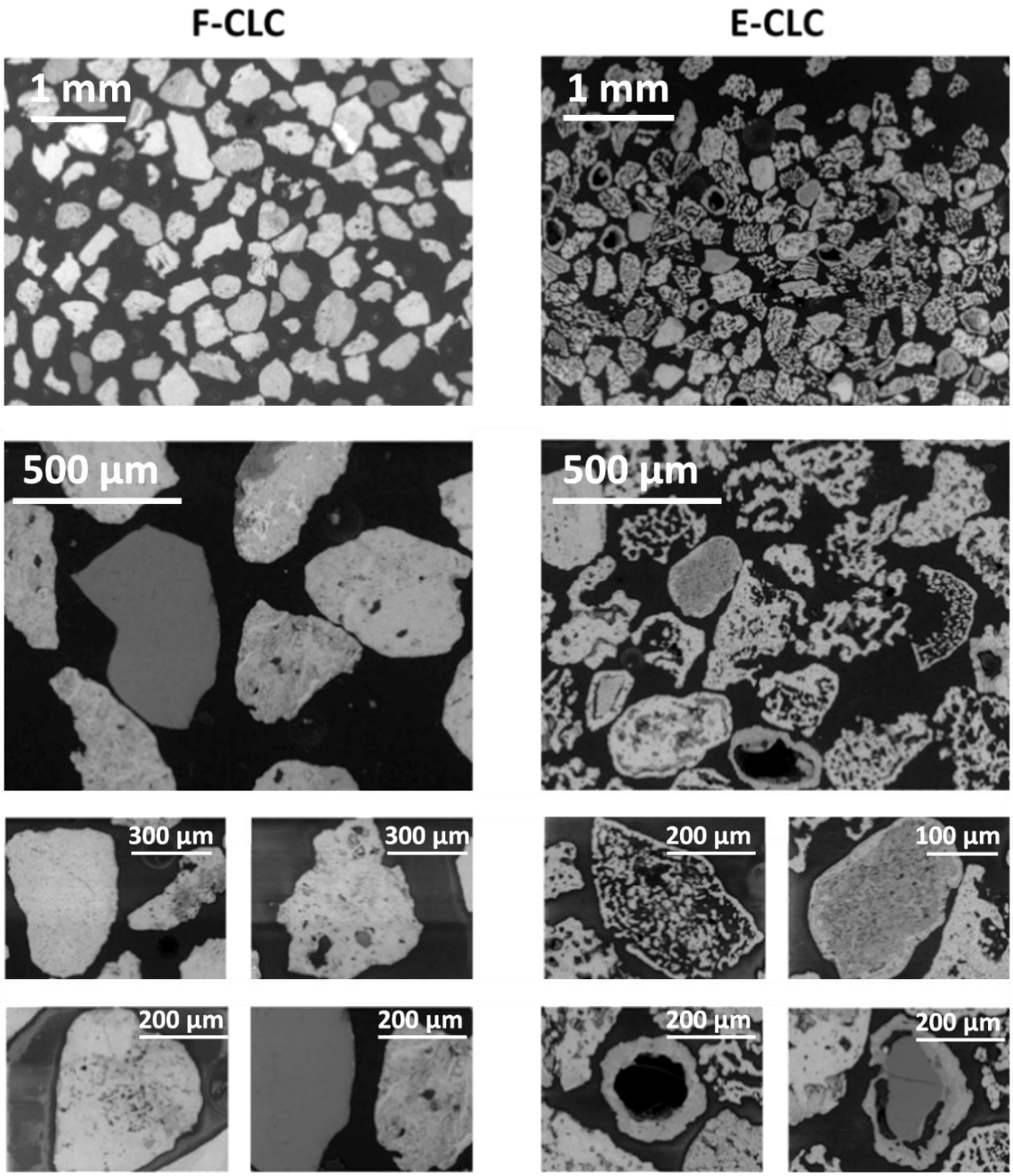

Figure 2-5. SEM micro-graphs showing the internal structure of F-CLC (left) and E-CLC (right)

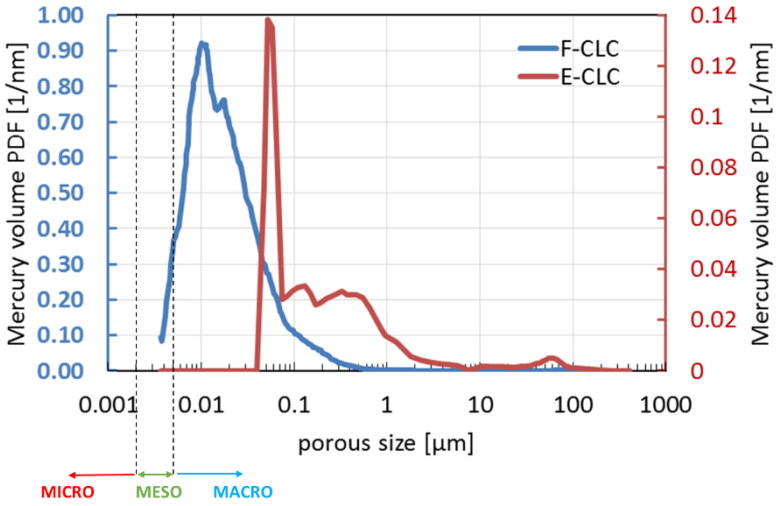

Figure 2-6. Pores size distribution for F-CLC and E-CLC particles obtained from the "Mercury Intrusion Porosimetry"

Table 2-4. Particle envelope density

F-CLC	E-CLC
3300 kg/m^3	3000 kg/m^3

2.3.4 Mechanical Properties by Nano-Indentation

The nano-indentation technique is used to determine the mechanical behaviour and properties of the two materials, such as Young's modulus of elasticity (E), Hardness (H) and critical stress intensity factor, also known as the fracture toughness (K_c), (Taylor et al. 2004; Ghadiri and Zhang, 2002; Kotsis et al. 1998). The surface of the material is loaded, at a known rate, for a certain time with a hard indenter of known geometry whilst the material response in terms of displacement during the entire loading/unloading cycle is recorded. These mechanical properties can be deduced from curve of load (F) versus displacement (h), Figure 2-7, while the fracture toughness can be determined by analysis of the cracks on the sample. The experiment could be affected by the material inhomogeneity and porosity, as experienced by Kotsis et al. (1998), by jumps in displacements at constant load.

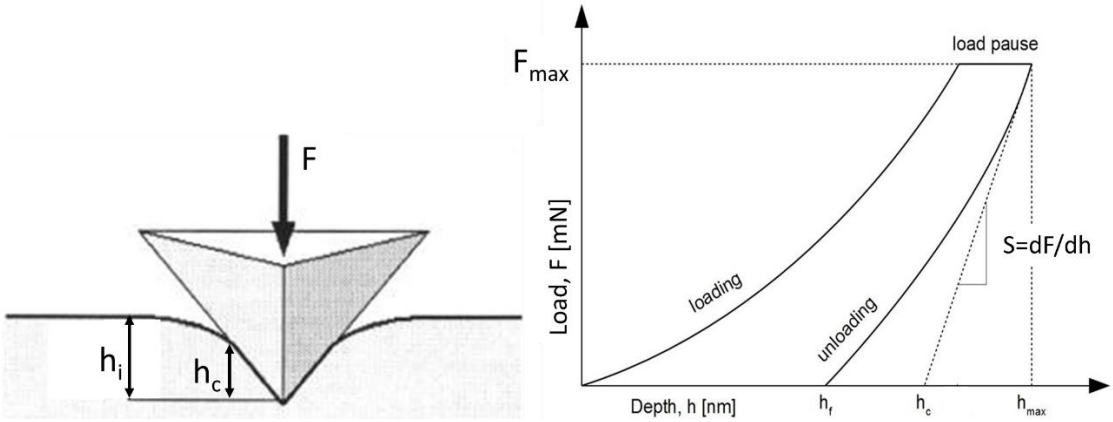

Figure 2-7. Typical curve of loading and unloading by nanoindentation

2.3.4.1 Young's Modulus

Young's modulus, E, represents the resistance of solid materials to elastic deformation. As shown in Figure 2-7, the Stiffness (S) is calculated as the slope of the tangent to the initial unloading curve, $S = \frac{dF}{dh}$. From S it is possible to calculate the reduced modulus of contact, E_r as:

$$E_r = \frac{\sqrt{\pi}}{2}\frac{S}{\sqrt{A}} \tag{2-1}$$

where A is the plastic contact area, calculated according to Equation. 2-2

$$A = k_{ind} h_c^2 \tag{2-2}$$

k_{ind} is the indenter shape factor and h_c is the penetration depth of the indenter. The Young's modulus E is then obtained from Equation. 2-3:

$$\frac{1}{E_r} = \frac{\left(1-\nu^2\right)}{E} + \frac{\left(1-\nu_{ind}^2\right)}{E_{ind}} \tag{2-3}$$

where E_{ind} is the indenter Young's modulus, ν and ν_{ind} are the Poisson's ratios of the material and the indenter, respectively.

2.3.4.2 Hardness

The hardness and yield stress represent the resistance of the material to plastic deformation. The Hardness is defined by Equation. 2-4:

$$H = \frac{F_{max}}{A} \quad (2\text{-}4)$$

where F_{max} is the maximum force applied, as displayed in Figure 2-7.

2.3.4.3 Fracture Toughness

The fracture toughness, K_c, is a measure of the resistance of crack propagation in a material. The stress must be high enough to initiate fracture and the energy release must be sufficiently high to produce new surfaces, (Mashadi and Newton, 1987). The fracture toughness based on indentation fracture is based on the length of cracks and the geometry of the indenter, (Evans and Wilshaw, 1976).

The ratio between Hardness and Fracture toughness, H/K_c, is regarded as the brittleness index of a material, as proposed by (Lawn and Marshall, 1979). It represents two competing mechanical responses, plastic deformation and fracture, (Roberts et al. 1993). This index allows to classify different materials according to their brittleness susceptibility

It should be noted that nano-indentation is carried out at a quasi-static loading regime, whereas the inertial effects are negligible and thus the strain rate is very low. The strain rate is defined as the ratio of the deformation induced in the specimen, by the applied stress, with the time during which it occurs, (Verral et al. 1977). Under dynamic conditions the strain rate is high and the effect of inertia, i.e. mass and acceleration, cannot be ignored. The dislocation mobility reduces thus increasing the yield stress and consequently hardness, (Ghadiri, 2006). The elastic-plastic contact time is reduced, and less time is allowed for the material to react plastically. As a result of this, semi-brittle materials tend to behave like brittle at high strain rates. The mechanical properties measured at low strain rates, e.g. compression or indentation, are hence not directly applicable at high strain rates, e.g. impact test.

2.3.4.4 Experimental Results

The surfaces of F-CLC and E-CLC are indented at maximum loads of 25, 50 and 75 mN with a rate of 5 mN/s, using the Berkovich type indenter by a Nano Test apparatus of Micro Materials (Whrexham, UK). The indentation curves obtained at 25 mN for F-FCLC and E-CLC are shown in Figure 2-8 and Figure 2-9, respectively. The latter presents the

characteristic displacement jumps caused by the extreme porosity of the material. The curves allow to establish the semi-brittle behaviour of the material because there is some permanent deformation accompanied by elastic recovery. The average Young's modulus and hardness of F-CLC and E-CLC are calculated using the curves obtained with a maximum load of 25 mN, according to Equation. 2-3 and Equation. 2-4. The values are reported in Table 2-5. They suggest that a drastic change in mechanical properties has occurred between the fresh and the equilibrium material. The brittleness, defined as the ratio between the Young's modulus with the Hardness, is found to be greater for F-CLC than E-CLC. This outcome suggests that the fresh material is going to experience a much greater degree of elastic deformation as compared to the equilibrium. The indentations carried out at higher maximum loads such as 75 and 150 mN are not used for the calculation of "E" and "H" because the unloading curve has a negative slope that would give a negative Young's modulus which is not physically permitted. The reason behind this behaviour are to date not fully understood and future work is needed. One explanation could be the effect of the bed of resin that supports the sliced particles or errors in measurements. The indentations on the E-CLC was found difficult to carry out because of their highly porous structure. The presence of cavities influences the loading curve as shown in Figure 2-9 and consequently hard to characterise, in fact only 3 indentations were performed satisfactorily. By looking at the indents on the surface of F-CLC particles at the maximum load, Figure 2-10, no crack is observed. This is probably because the load is not high enough to initiate fracture, therefore the fracture toughness could not be quantified. Further experimental investigation is needed.

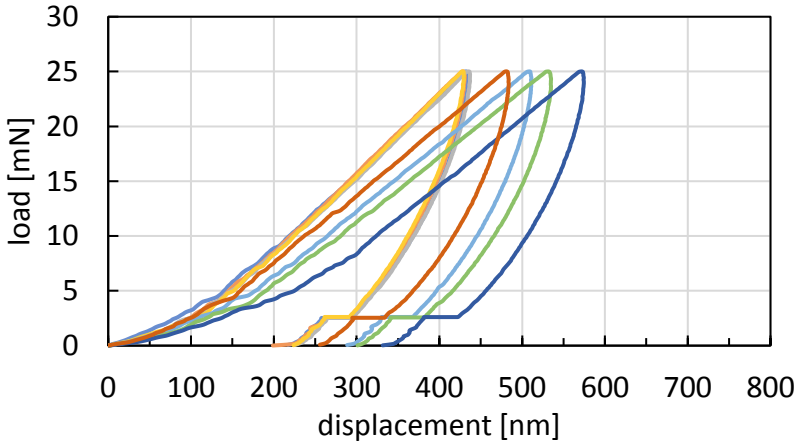

Figure 2-8. Load-displacement curves for F-CLC at 25mN of maximum load

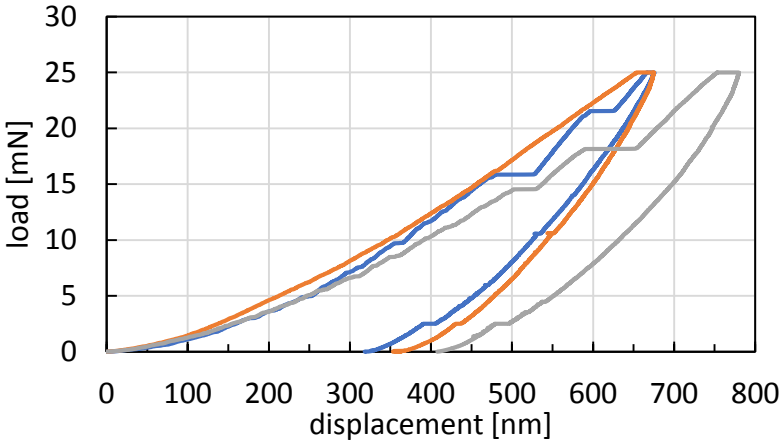

Figure 2-9. Load-displacement curves for E-CLC at 25mN of maximum load

Table 2-5. Young's modulus and Hardness of F-CLC and E-CLC by nano-indentation

	F-CLC	**E-CLC**
E [GPa]	**192.5** (CV=3%)	**41.4** (CV=11%)
H [GPa]	**5.2** (CV=9%)	**2.9** (CV=20%)

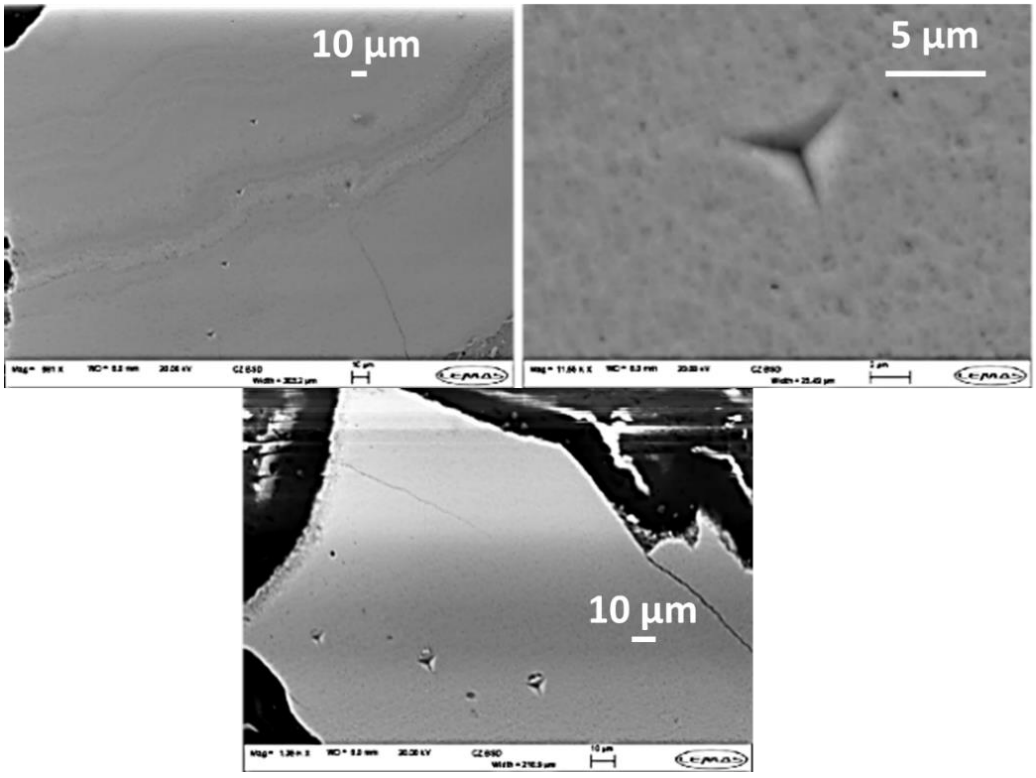

Figure 2-10. Indentations on F-CLC surface at 150 mN of maximum load

2.4 Concluding Remarks

The EDX analysis shows that the fresh manganese oxide is mainly composed of MnO_2. The equilibrium material is a mixture of fresh and used particles with a Mn/O proportion which is close to Mn_3O_4. The fresh and equilibrium particles differ in size, density, internal structure and mechanical properties. The Sauter mean diameters of F-CLC and E-CLC is 262 and 160 μm, respectively. Their PSDs are bimodal, and the particles shape very irregular. The surfaces of the equilibrium particles are rough and porous with large cavities. Image analysis and the "Mercury Intrusive Porosimetry" reveal that the fresh material presents some macro-porosity of size between 10 to 100 nm, while the equilibrium material has a much greater degree of macro-porosity of size range between 40 to 100,000 nm, due to the high thermal and chemical stresses undergone.

The stiffness and hardness of the two materials are evaluated by the nano-indentation technique. The tests show that the fresh material is stiffer and harder. The material resistance to the fracture formation, the fracture toughness, could not be evaluated because no crack was formed for the conditions tested.

3. SINGLE PARTICLE BREAKAGE

CHAPTER 3

In this Chapter, attrition at single particle level is addressed. A literature survey on the different modes of failure and patterns of breakage is reported. The single particle breakage of F-CLC and E-CLC upon impact is obtained experimentally using single particle impact testers. Two devices are used in order to investigate a wide range of impact velocities. The effects of particle size, impact angle and number of impacts on the extent of breakage is also investigated. A correlation of single particle breakage upon impact is developed for F-CLC and E-CLC particles and the breakability index of the two materials is quantified.

This work has been carried out at the University of Leeds in the 1st and 2nd year of this PhD project.

3.1 Literature Review

Understanding particle breakage is a key factor in order to predict the impact of attrition in fluidised and circulating fluidised bed systems. Single particle breakage has been studied extensively, there are many factors influencing attrition such as particle size, shape, density, internal structure, surface roughness, mechanical properties, environmental conditions and type of stress experienced, (Bemrose and Bridgwater, 1987).

Particles of irregular shape, containing numerous asperities or sharp edges, tend to break more extensively because of the high concentration of stress in the small cross section of the asperities. Boerefijn et al. (2000) and Reppenhagen and Werther, (2000) evaluated the tendency of attrition of fresh and equilibrium FCC catalyst in different set-ups finding always the fresh particles to be more prone to attrition. Pitchumani et al. (2003) used an impact tester to check the evolution of size and shape of a $NaHPO_4$ particles under low velocity repeated impacts (1.88-2.50 m s^{-1}), noticing a disappearance of the edges with increasing number of collisions, leading to a decrease in attrition rates till a stable value

is reached. Samimi, (2003) and Cleaver et al. (1993) reported a decrease in the breakage extent with the number of impacts, using detergent powder and sodium carbonate monohydrate, respectively, by carrying out controlled single particle impacts, finding the extent of breakage to reduce more drastically during the first three impacts. Using the same particle impact tester, Boerefijn et al. (2000) assessed the breakage of both fresh and equilibrium FCC catalyst, finding the fresh catalyst to be more extensively prone to breakage than equilibrium one. They also obtained a linear dependency on particle size and a quadratic dependency on impact velocity for both fresh and equilibrium FCC.

In general, particle strength increases as the particle size decreases because larger particles tend to have more micro-cracks and inhomogeneities, (Cleaver et al. 1993).

Papadopoulos, (1998) studied the effect of impact angle using porous silica particles of 1 mm, where 90° represents a normal impact, as shown in Figure 3-1.

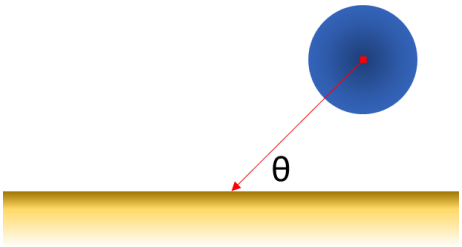

Figure 3-1. Illustration of the angle of impact

He noticed a gradual increase of the breakage extent with impact angle as opposite to Samimi, (2003) who worked on the effect of impact angle of agglomerates. Nevertheless, neither of them established a direct dependency of the breakage extent with the normal component of the kinetic energy (kinetic energy with the normal component of impact velocity), as it is claimed to be the only contributor to breakage by Vervoorn, (1986), Salman et al. (1995) and Hadavi et al. (2016). Wang et al. (2019) recently proposed a model for the equivalent particle velocity upon angled impacts, where both normal and tangential component of the velocity are present as well the sliding friction coefficient, μ_s, as shown below in Equation. 3-1:

$$v_{p,eq} = v_p \sqrt{\sin^2\theta + \alpha^2 \mu_s^2 \sin^2\theta \cos^2\theta} \qquad (3\text{-}1)$$

where v_p is the impact velocity, and α a fitting parameter.

There are different terms used to describe particle breakage, such as wear, surface abrasion, chipping, fragmentation, etc. Each of these terms corresponds to a particular case. For the sake of clarity, a detailed summary of the various modes of failure and mechanisms of particle breakage is given in the next section.

3.1.1 Modes of Failure

As stated by Thornton and Ning, (1998), when a particle is subjected to a certain stress deformation can occur. This is initially non-permanent (elastic) but it can be followed by permanent deformation (plastic) and even propagation of cracks. Particles can fail differently depending on their material properties and the loading conditions, such as type, magnitude and how quickly it is applied (in case of strain-rate sensitive materials). Based on their tendency to undergo plastic deformation, three main modes of failure are distinguished: brittle, ductile and semi-brittle.

3.1.1.1 Brittle Mode of Failure

A particle failing in the brittle mode experiences mainly elastic deformation, but limited plastic deformation before bond rupture and crack propagation occur, (Hutchings, 1993). A material with the brittle mode of failure is naturally strong, but its strength depends on the pre-existing internal and surface flaws. As shown by Antonyuk et al. (2006) and Lawn, (1993), the crack initiates from the perimeter of the loading contact area, where the stresses are tensile with the propagation of cracks. When a blunt indenter is loaded on a flat surface of a brittle material, a classical ring and Hertzian cone crack are formed due to the presence of pre-existing flaws or pores that act as stress concentrator, (Lowrison, 1974; Antonyuk et al. 2006). If the cone cracks reach the surface little chips of material are removed (Lawn, 1993; Couroyer, 2000). For a porous material, many fine particles are formed with a characteristic size distribution (within the range of 0.5-100 μm) where the lower limit is equivalent to the average distance between the pores, (Antonyuk et al. 2006).

3.1.1.2 Ductile Mode of Failure

In the case of ductile mode of failure, the material experiences extensive plastic deformation before breakage is induced by dislocation mobility of atomic or molecular planes over one another, (Hutchings, 1993). Failure occurs at the point of maximum shear stress. Metals and

some soft materials such as some polymers are mostly damaged under this mode of failure, (Hutchings, 1993).

3.1.1.3 Semi-Brittle Mode of Failure

Semi-brittle materials exhibit an intermediate behaviour where elastic-plastic deformation is followed by crack propagation. Three types of cracks are formed in semi-brittle materials: radial, median, and lateral, as shown in Figure 3-2

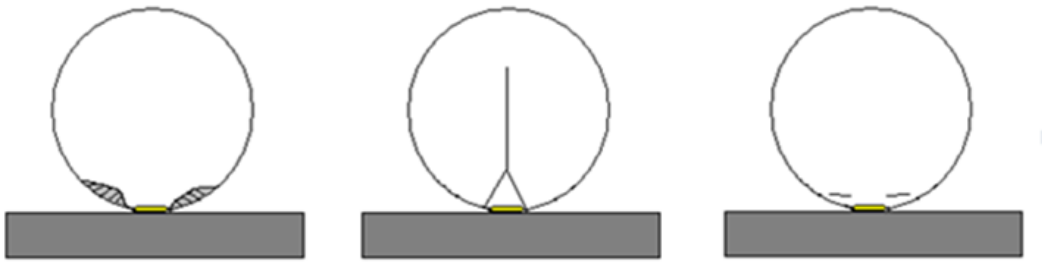

Figure 3-2. Illustration of radial, median and lateral cracks, (Salman et al. 2004)

Radial cracks are formed during loading by tensile stresses around sub-surface flaws near the elastic-plastic boundary and can propagate through the whole volume of the material, while median cracks are formed under the plastic zone, (Lawn and Evans, 1977; Lawn and Evans, 1980). Radial and median cracks are responsible for fragmentation. Lateral cracks are formed instead on unloading. Their propagation is initiated at the interface of the elastic and plastic contact zone, (Ghadiri and Zhang, 2002), which is near the surface of the material, and therefore responsible for surface wear and chipping, (Ghadiri and Zhang, 2002; Lawn and Evans, 1980).

3.1.2 Pattern of Breakage

Based on the pattern of the cracks propagation different breakage mechanisms are observed. It is important at this stage to define the various terms used to describe particle breakage as the definitions reported in literature are sometimes subjective.

According to Unland, (2007), a particle can undergo surface and/or body damage as shown in Figure 3-3.

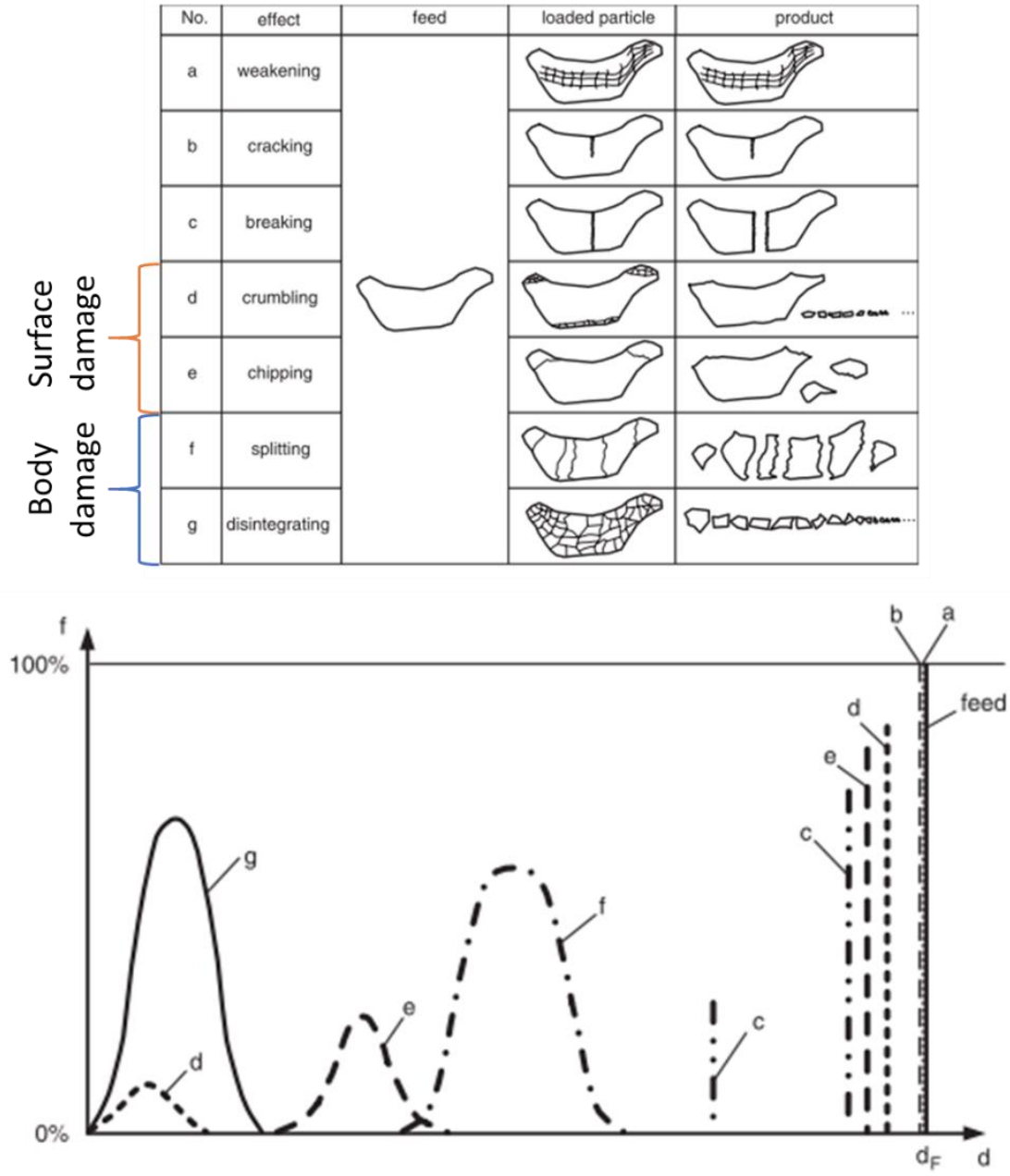

Figure 3-3. Different particle pattern of breakage (volume fraction against particle size where d_F is the feed particle size), (Unland, (2007)

3.1.2.1 Surface Damage

"Crumbling" and "chipping", as defined by Unland, (2007), Figure 3-3, are the result of surface damage and give rise to the formation of fine debris and small surface chips, respectively. The two mechanisms are often considered together and referred to as "surface abrasion" as in both cases there is still a clear distinction between the mother and daughter particles, (Pis et al. 1991). Reppenhagen and Werther, (2000), refer to

"crumbling" as "surface abrasion" when the mother particle size is barely changed and fines of less than 10 μm size are formed. They use the term "fragmentation" to describe the process that leads to the removal of relatively large portions of the surface (which is chipping according to Unland, (2007) and Ghadiri and Zhang, (2002)). According to Hutchings, (1993), any surface damage is referred to as wear. Wear mechanisms are subdivided into "surface abrasion" and "erosion" whether breakage happens as a result of sliding against a surface or impact, respectively.

3.1.2.1.1 Surface Wear

Archard and Charj, (1953) derived a contact-based model of surface wear and assumes removal of lumps at contact areas formed by plastic deformation, Equation. 3-2. The model shows that the volume of debris produced by the surface asperities is independent of the actual contact surface area and linearly dependent upon the normal load applied, F_n, between the two surfaces and inversely proportional to the material hardness, H:

$$V_{de} = \alpha_A \frac{F_n \Delta s}{H} \tag{3-2}$$

where V_{de} is the abraded volume loss, α_A is a constant that determines the efficiency of material removal (less than 1) and Δs is the sliding distance.

Ning and Ghadiri, (2006) considered the surface damage of two particles shearing against each other to be caused by the formation of lateral cracks due to elastic-plastic work. The lateral crack is formed by the residual tensile stress, after the contact force reaches the yield value, during the unloading stage.

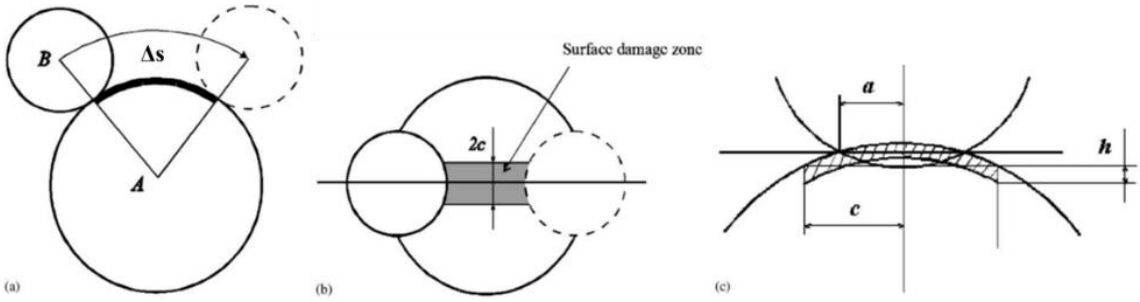

Figure 3-4. Abrasive wear by lateral crack formation: (a) sliding distance; (b) surface damage zone and (c) enlarged contact area, (Ning and Ghadiri, 2006).

They developed a model based on indentation fracture mechanics, where the volume of wear, V_w, can be calculated as the contribution of the material removal due to loading/unloading in a static point and by sliding, as shown in Equation. 3-3:

$$V_w = \frac{0.07F_n^{5/4}}{K_c\pi^{5/4}H^{1/4}}\left[2\Delta s + \frac{\pi^{1/4}H^{1/4}F_n^{3/4}}{17.1K_c}\right] \quad (3\text{-}3)$$

It is noted how similarly to Archard's law, there is dependency on the ratio between load applied and hardness although with different power indices.

3.1.2.1.2 Chipping

Vogel and Peukert, (2003) describe the impact breakage of brittle material as the probability of breakage, S, as shown in Equation. 3-4:

$$S = 1 - \exp\left[-f_{mat}d_p\left(W_k - W_{k,min}\right)\right] \quad (3\text{-}4)$$

where f_{mat} is a fitting parameters reflecting the material properties, $W_{k,min}$ the minimum kinetic energy that causes breakage and W_k denotes the particle specific impact energy.

For the semi-brittle failure mode, Ghadiri and Zhang, (2002) proposed a mechanistic model for breakage applicable for the chipping regime. The volume fraction of debris, as the ratio of volume of chips to the volume of original particles, determines the attrition extent, R, according to Equation. 3-5:

$$R \propto \frac{H}{K_c^2}\rho_p d_p v_p^2 \quad (3\text{-}5)$$

where H is the hardness, K_c the fracture toughness, ρ_p the particle density, d_p the particle size and v_p the particle impact velocity. Similarly to Vogel and Peukert, (2003), the minimum energy that causes little/no breakage is identified as the transition velocity, $v_{p,0}$. Linearisation of the model of Vogel and Peukert (2003) for small extents of breakage (such as chipping) leads to the same dependencies of the model of chipping of Ghadiri and Zhang (2002).

A common approach to assess the fraction of debris generated is to consider a cut-off sieve size above which only mother particles are expected, and below which the particles are considered debris. This cut-off size is typically taken as two sieve size cuts below the

lower size of the feed particles, (Ahmadian and Ghadiri, 2007; Kwan et al. 2004). Zhang and Ghadiri, (2002) define the extent of breakage of a single particle gravimetrically, i.e. using the mass of feed particles, m_f, the mass of mother particles, m_{mp}, and mass of debris, m_{de}. Due to uncertainty arisen from manual handling and possible loss of material, they propose three different way of closing the mass balance: R^- is used when the loss is attributed to mother particles, R^+, when the loss is attributed to debris and R^*, when the analysis is based on the collected material, so that the loss is not attributable, as shown below:

$$R^- = \frac{m_{de}}{m_f} \tag{3-6}$$

$$R^+ = \frac{m_f - m_{mp}}{m_f} \tag{3-7}$$

$$R^* = \frac{m_{de}}{m_{de} + m_{mp}} \tag{3-8}$$

3.1.2.2 Body damage

"Splitting" and "disintegration", according to Unland, (2007), as shown in Figure 3-3, are the result of body damage and are usually referred to as "fragmentation", (Werther and Reppenhagen, 2003). In both mechanisms there is no longer distinction between mother and daughter particles. Papadopoulos, (1998) refers to "splitting" simply as "fragmentation", because of the formation of large fragments.

In case of "disintegration", the particle is completely shattered into several small pieces. The latter usually occurs for granules and agglomerates, (Reynolds et al. 2005). Papadopoulos, (1998) proposed a way to identify the pattern of breakage, by means of the Schumann's plot, (Schumann, 1940), as shown in Figure 3-5, such as chipping/surface abrasion, fragmentation and disintegration depending on the shape of the cumulative percentage undersize as a function of normalised particle size.

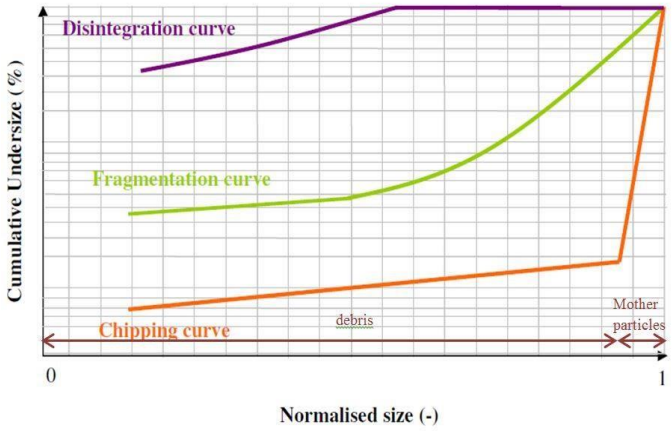

Figure 3-5. Patterns of breakage, (Papadopoulos, 1998)

3.1.2.2.1 Fragmentation

To date, there is no theory which can relate the product size distribution to the material properties and stress conditions in a predictive way. Ghadiri and Zhang, (2002) proposed a relationship to estimate the force for fracture of a sphere of diameter d_p based on indentation fracture. The fragmentation force (F_{fr}) for crack extension is given by Equation. 3-9:

$$F_{fr} \propto \left(K_c d_p\right)^{4/3} H^{-1/3} \tag{3-9}$$

Salman et al. (1995) proposed an empirical model of fragmentation to quantify the probability of breakage by counting the number of unbroken particles, N_u, after impact tests as a function of impact velocity, using a two-parameters cumulative Weibull distribution, k_1 and k_2, as shown in Equation. 3-10:

$$N_u = 100 \exp\left[-\left(\frac{v_p}{k_1}\right)^{k_2}\right] \tag{3-10}$$

On the other hand, Hadavi et al. (2016) quantify fragmentation as the ratio of number of particles after and before the impact.

3.2 Motivation and Objectives

As mentioned above, the way that the single particle experiences breakage depends on several factors, their mode of failure, mechanical properties and surface morphology. These, along with the type and magnitude of stress undergone, will dictate the extent of

breakage. The attrition tendency of the single particle needs to be fully investigated as it is the necessary requirement to understand attrition at the process level. There is some work reported on the behaviour of fresh and equilibrium catalyst upon impact, however the information is insufficient to be able to predict how these fresh and equilibrium manganese-based oxygen carriers are going to behave. The main interest here is to study the relative tendency of undergoing attrition of F-CLC and E-CLC particles as a function of particle size, impact velocity, angle of impact and number of impacts.

3.3 Methodology for Single Particle Breakage Assessment

Two main techniques are used to characterise the impact breakage propensity of the particles, the Scirocco Impact Test (SIT) and the Single Particle Impact Test (SPIT). The former allows to reach higher impact velocities as compared to the latter. Also, the two techniques are for the first time used here to assess particle breakage gravimetrically to check their consistency in the overlapping impact velocity range. In order to isolate the effect of size, the tests are carried out on narrow size cuts which are most representative of the whole PSD. The masses of debris, m_{de}, and of mother particle, $m_{mp,}$ are obtained by sieving the material after the test using a cut-off sieve size which is two sizes below the lower size of the feed particles according to DIN sieve standard, as described in section 3.1.2.1.2. This method is valid up to the point that the size of mother particle, d_{mp}, is equal to size of the sieve mesh opening, d_{so}. Beyond this limit there is no more distinction between mother and debris particles, therefore it can be seen as the theoretical threshold from chipping/surface abrasion to fragmentation. The latter, in fact, occurs when the particle breaks into several pieces of comparable sizes or at least when there is no clear distinction between mother particle and the rest. Considering spherical particles, as shown in Figure 3-6, this threshold can be calculated according to Equation. 3-11.

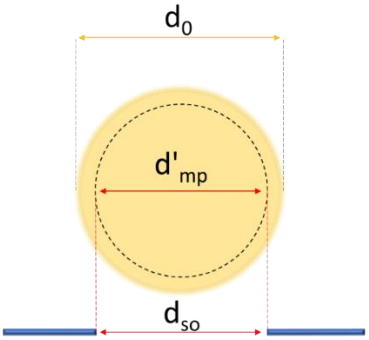

Figure 3-6. Schematically representation of a particle of diameter "d_f" at the sieve opening of diameter "d_{so}"

$$R' = \frac{m'_{de}}{m_f} = \frac{m_f - m'_{mp}}{m_f} = 1 - \frac{m'_{mp}}{m_f} = 1 - \left(\frac{d'_{mp}}{d_f}\right)^3 = 1 - \left(\frac{d_{so}}{d_f}\right)^3 \quad (3\text{-}11)$$

Using German standard DIN 4188 sieve type, d_{so}/d_f is generally around 0.85 which corresponds to a R' of 0.38, where d_f is set as the lower limit of the feed size cut. The size cuts used for impact testing, their cut-off sieve size and theoretical threshold to fragmentation are reported in Table 3-1 and Table 3-2 for F-CLC, E-CLC, respectively. This limit is certainly overestimated because it is calculated considering spheres, while real particles have shape that can affect sieving and therefore influence the breakage assessment. Nevertheless, the approach is only valid for a maximum of R'~0.4.

Table 3-1. Cut-off sieve sizes used for mother particles-debris separation for F-CLC

F-CLC feed size cuts [µm]	**355-400**	**300-355**	**250-280**	**212-250**	**180-212**
cut-off sieve size [µm]	300	250	212	180	150
R′ [-]	0.39	0.42	0.39	0.38	0.42

Table 3-2. Cut-off sieve sizes used for mother particles-debris separation for E-CLC

E-CLC feed size cuts [µm]	**212-250**	**160-180**	**125-140**
cut-off sieve size[µm]	180	140	106
R′ [-]	0.38	0.33	0.39

The material is very dusty as shown in Figure 2-4. In fact, dust readily adheres to particles surfaces and this adversely affects the breakage results contributing to the mass of debris.

Therefore, before the tests, in order to get rid of these fines, the particles are 'washed' by wet sieving using water and later on dried in an oven. Manganese oxides do not dissolve in water. Later experimental inspection showed no weakening of the particles due to washing as its breakability after few repeated impacts is equal to that of the non-washed material.

3.3.1 Single Particle Impact Test (SPIT)

The Single Particle Impact Test developed by Ghadiri and co-workers, shown in Figure 3-7, is used to assess the single particle breakage propensity.

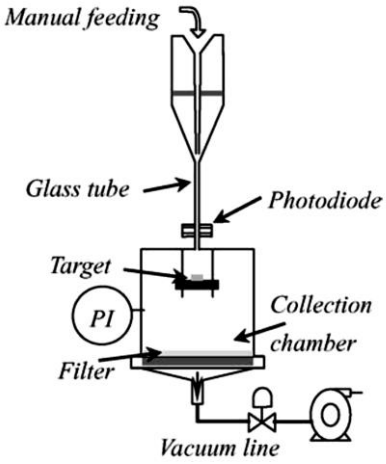

Figure 3-7. Single Particle Impact test rig (Samimi, 2003)

The particles are almost singularly fed into the system by a vibrating feeder. Acceleration of particles is induced by a vacuum line. They are impacted onto a target of sapphire at a certain velocity which is detected by photodiodes and displayed on screen. Impact velocity can be varied by adjusting the pressure of the vacuum line. The gas flow rate is calibrated to achieve the desired impact velocity. The test can cover a wide range of velocities depending on particle size. The total amount of material used for each condition is 6 g. Considering the particle size range used here, this amount would lead to few hundreds of thousands of single particle impacts. The results are therefore to be considered as representative of an average behaviour between all the impacts. After impact, the material is collected and sieved to separate the mother particles from the debris in order to calculate the extent breakage. The tests are performed at five particle impact velocities: 2, 8, 14, 20 and 26 m s^{-1}, using 5 g of material. This is carried out for both washed and non-washed material. The effect of the angle of impact is analysed at

impact velocities of 8, 14 and 20 m s^{-1} using oblique targets at 30°, 45° and 60°, as shown in Figure 3-8. The effect of fatigue is also investigated by carrying out 6 repeated impacts, again at 2, 8, 14, 20 and 26 m s^{-1} on both washed and non-washed F-CLC particles of 355-400 µm and washed E-CLC particles of 212-250 µm.

The results are presented in terms of R^*, R^-, R^+ and R. The former three are defined by Equation. 3-6, Equation. 3-7 and Equation. 3-8, the latter is the arithmetic mean of R^+ and R^-.

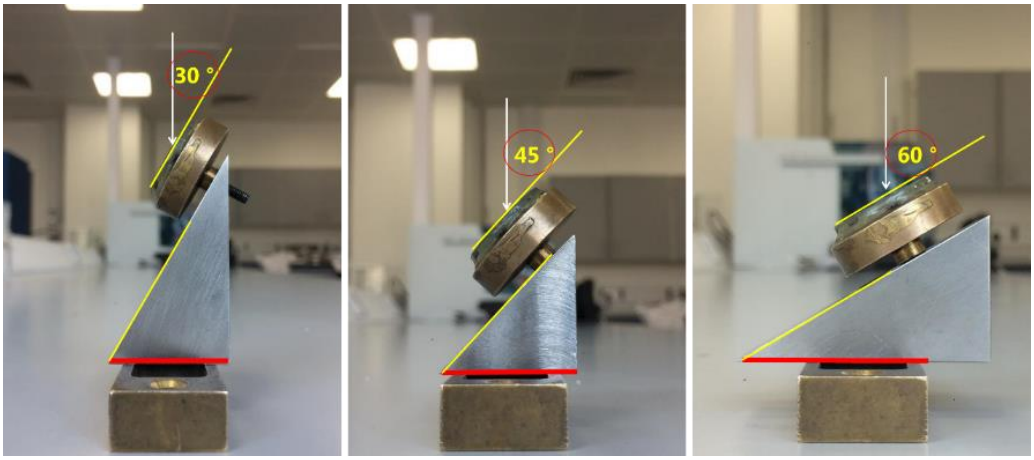

Figure 3-8. Target of SPIT inclined at 30, 25 and 60°

3.3.2 Scirocco Impact Test (SIT)

Laser diffraction is nowadays one of the most used techniques for particle size analysis. The size measurement is carried out by either wet or dry dispersion. On the Malvern Mastersizer 2000, dry dispersion of free-flowing material is obtained by means of a Venturi eductor called "Scirocco" where the air pressures can be varied from 0.1 to 4 barg. A schematic view of such system is given in Figure 3-9. Compressed air is issued from "port 2" which results in a very high velocity at the nozzle tip. The particles are slowly fed to the top inlet of the disperser, "port 1", and get rapidly accelerated as they interact with the high velocity air jet stream. The dispersion of particles takes place as they collide at the elbow. The dispersed particles exit from the outlet, "port 3", and are presented to the laser for laser diffraction measurements. As the particles are accelerated by the air jet, they are impacted on the container walls and L-bend. They are then recovered downstream of the instrument by a plastic axial cyclonic dust collector, from which the material is collected, thus the extent of breakage is analysed. Coherently with

the SPIT, the breakage results are presented in terms of R^*, R^-, R^+ and R. Attrition can also be observed from the shift in PSD of the laser diffraction results at increasing pressure. The further potential attrition contribution of the recovery cyclone is not considered as most of the breakage is assumed to be caused by the high impact velocity achieved in the Scirocco. The experiments are performed on washed F-CLC using three batches of 3 g for each condition.

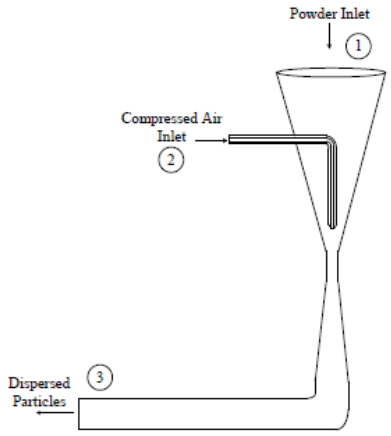

Figure 3-9. Schematic diagram of the Scirocco disperser

The particle velocity at the first impact in the Scirocco is calculated knowing the particle size, density and nozzle pressure, based on the correlation developed by Ali et al. (2015), who simulated the gas/solids flow in Scirocco using Lagrangian particle tracking for the discrete phase and the Eulerian approach for the fluid phase. Varying the nozzle pressure from 0.1 to 4 barg for CLC particles, it is possible to achieve a range of impact velocities from 18 to 59 m s^{-1}, depending on the particle size, as shown in Figure 3-10.

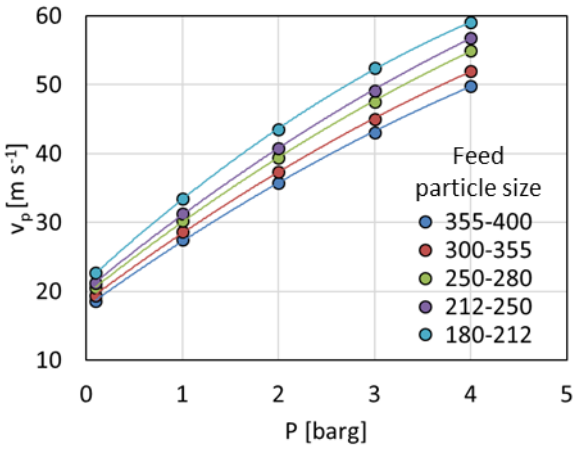

Figure 3-10. Particle impact velocities at the L-bend of the Scirocco disperser for different particle sizes as a function of air pressure

3.4 Results and Discussion

3.4.1 F-CLC

The results of the SPIT for different size cuts of non-washed F-CLC are reported in Figure 3-11 in terms of R plotted against the group $\rho_p d_p v_p^2$, following the chipping model of Zhang and Ghadiri, (2002). The unification of data points obtained for different particle sizes and impact velocities suggests a linear relationship with particle size and square dependency with the impact velocity. Furthermore, the slope of the straight line is exactly the breakability index $\alpha H/K_c^2$. However, the intercept with the abscissa is positive implying that in condition of 0 m s^{-1} impact velocity there is breakage. This is due to the presence of dust which contributes to the mass of debris by being shed off. As it will be seen later, removing the dust by washing particles resolves this problem.

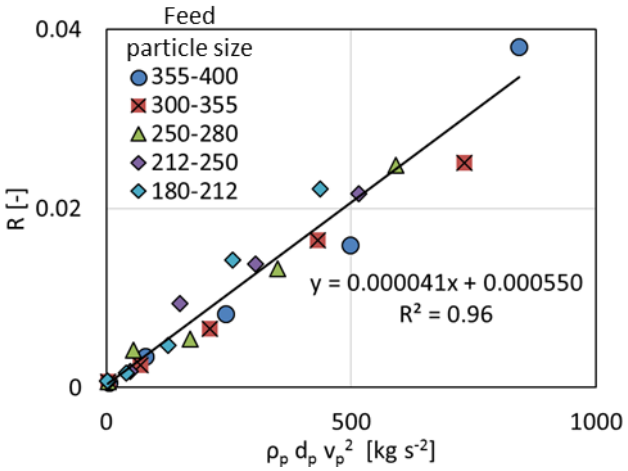

Figure 3-11. The extent of breakage "R" plotted against $\rho_p d_p v_p^2$ for non-washed F-CLC particles of different feed sizes for different impact velocities (2-26 m s^{-1}), using the SPIT

The extents of breakage R^+, R^*, R^- and R are shown in Figure 3-12 for the non-washed F-CLC. The gap between R^- and R^+ gives an indication of the degree of loss of material in the experiments. At the same time, it is not possible to establish to which source the loss belongs. If there is no loss, all the given definitions of R would give the same value. In this case the maximum error band, calculated as $(R^+ - R^-)/ R^+$, is of 23%.

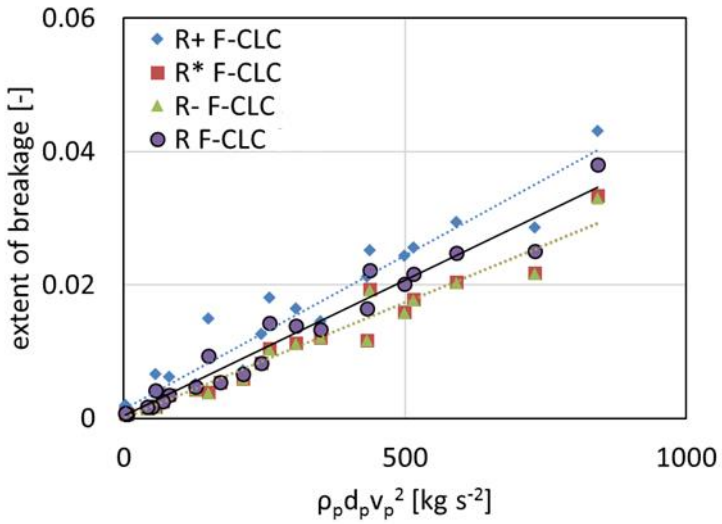

Figure 3-12. The extents of breakage "R^+", "R^*", "R^-" and "R" plotted against $\rho_p d_p v_p^2$ for non-washed F-CLC particles of different sizes for different impact velocities (2-26 m s^{-1}) using the SPIT

The angled impact tests carried out with particles of 355-400 µm are not found to agree with the magnitude of the impact velocity as well as the normal component of the impact velocity, $v_p \sin\theta$, as often suggested in literature, Figure 3-13. Not all the breakage is in

fact due to the normal component of the impact velocity, but only a fraction of it. This fraction itself should be dependent on the impact angle as the normal component is. The breakage due to the normal component is here assumed to be Rsinθ. Its complementary, R(1-sinθ) should therefore arise from the tangential component of the impact velocity $v_p \cos\theta$. This leads to a remarkable unification of the data points, as shown in Figure 3-14.

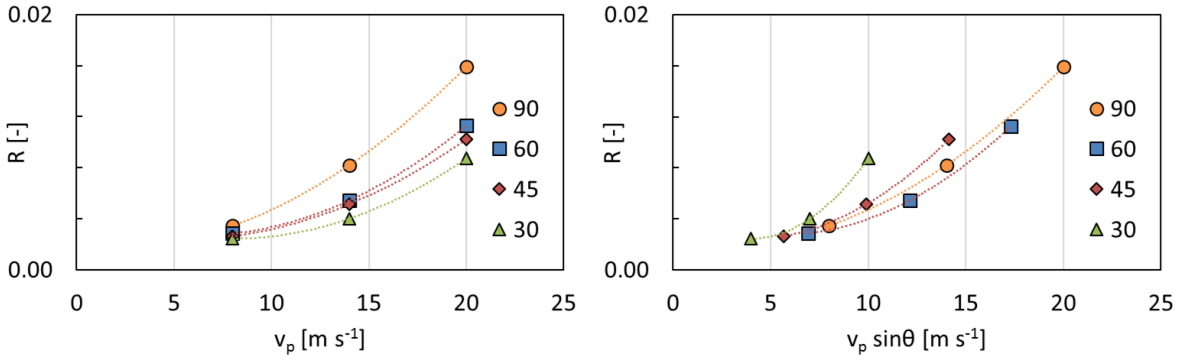

Figure 3-13. The extent of breakage "R" for F-CLC particles of 355-400 µm for different impact velocities and angles. On the left: plotted with the magnitude of the impact velocity. On the right: plotted against the normal component of the impact velocity

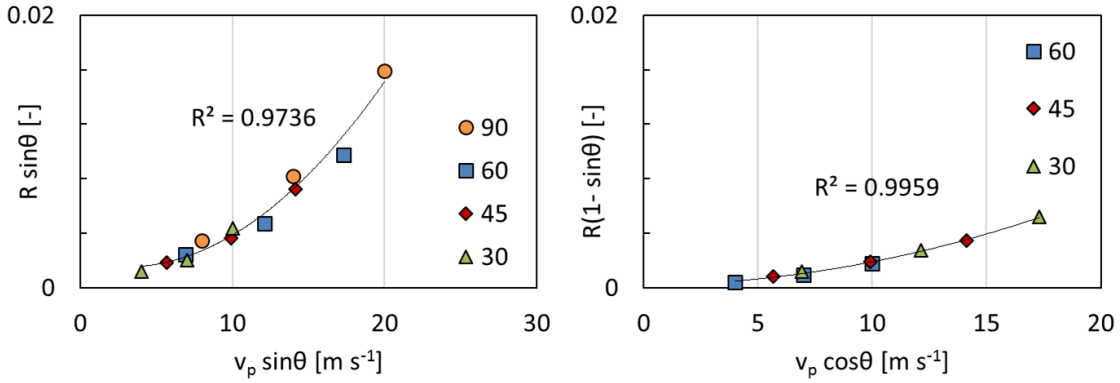

Figure 3-14. Unification of data of Rsinθ and R(1-sinθ) respectively with the normal and tangential component of the impact velocity

This analysis is purely empirical and not based on any underlying impact breakage mechanism. However, the particle breakage upon an inclined impact could actually arise from both normal and tangential components and the approach takes it into account. Given the parabolic trend observed in Figure 3-14, it can be written that, Equation. 3-12:

$$R\sin\theta \propto \left(v_p \sin\theta\right)^2 \Rightarrow R \propto v_p^2 \sin\theta \tag{3-12}$$

Hence, a linear trend would be observed if the data points are plotted as shown in Equation. 3-13

$$R \propto v_p^2 \sin\theta \tag{3-13}$$

In Figure 3-15, it is possible to see how all the data points, for both normal and inclined impacts, is on the same straight line if plotted against the group $\rho_p d_p v_p^2 \sin\theta$.

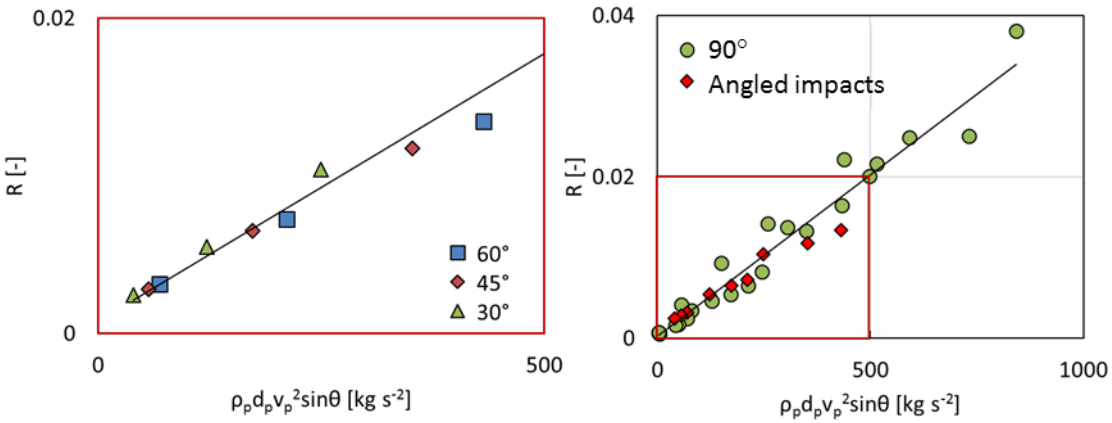

Figure 3-15. Unification of data points of "R" for F-CLC particles obtained using SPIT for different impact angles with the group $\rho_p d_p v_p^2 \sin\theta$

The results obtained for washed F-CLC, using SPIT and SIT, in terms R^+, R^*, R^- and R are shown in Figure 3-16 with a maximum error band of 28%. The solid black lines indicated the linear fitting of R.

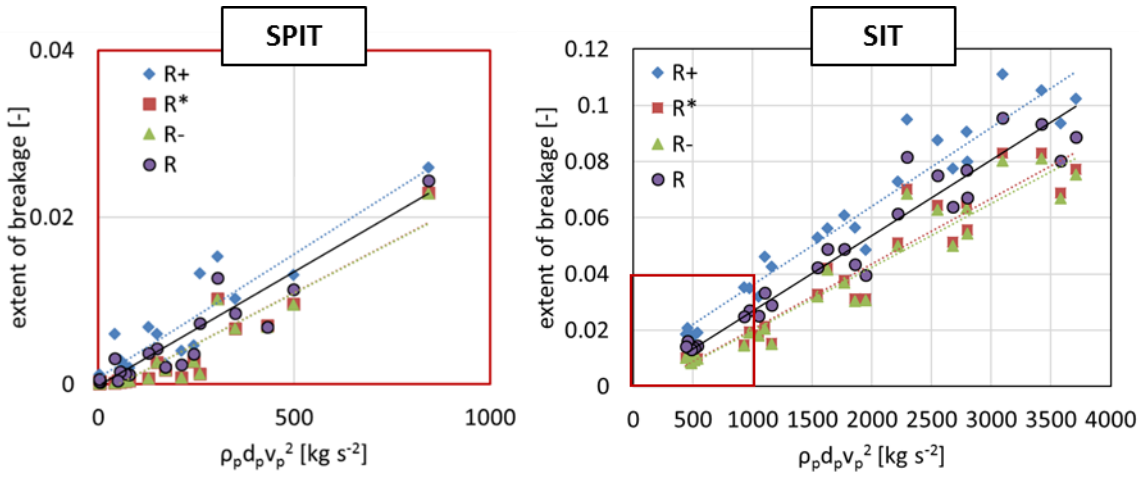

Figure 3-16. The extents of breakage "R+", "R*", "R-" and "R", obtained using SPIT (on the left) and SIT (on the right), plotted against $\rho_p d_p v_p^2$ for washed F-CLC particles of different sizes for different impact velocities

The impact velocity ranges achieved by the two techniques are somewhat complementary. All the data points are in fact plotted together in Figure 3-17 showing good agreement. This means that the "Scirocco" of the Malvern Mastersizer 2000 can be used to extrapolate the single particle breakability index of a material without recurring to the SPIT which is an in-house-fabricated equipment of property of University of Leeds.

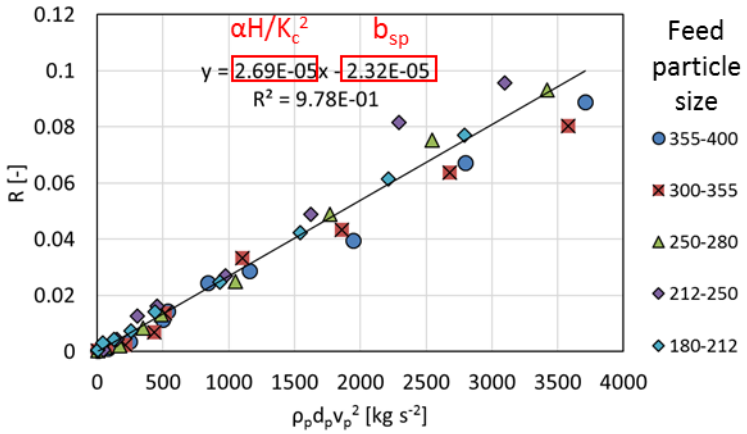

Figure 3-17. The extent of breakage "R" plotted against $\rho_p d_p v_p^2$ for washed F-CLC particles of different sizes and for different impact velocities using the SPIT and SIT methods

The intercept with the abscissa referred to as "b_{sp}" corresponds to the impact energy at the transition from no/little breakage to breakage. The impact velocity associated with this energy is $v_{p,0}$ and can be calculated according to Equation. 3-14:

$$v_{p,0} = \sqrt{\frac{b_{sp}}{\alpha \frac{H}{K_c^2} \rho_p d_p}} \tag{3-14}$$

The equation above states that the denser and larger the particle, the more energy is required upon impact to initiate breakage. It should be noted that in order to have a positive sign in the square root of Equation. 3-14, b_{sp} should be positive. This implies that its sign in the equation of the straight line should be negative. As shown by the graph below, Figure 3-11, for non-washed F-CLC, this is not true. The transition velocity for washed F-CLC is calculated for the particle sizes used, according to Equation. 3-14, and reported in Table 3-3.

Table 3-3. Breakability index, intercept with the abscissa and breakage transitional velocity for different sizes of washed F-CLC particles

F-CLC	$\alpha \frac{H}{K_c^2}$	**b_{sp}**
	2.69×10^{-5}	2.32×10^{-5}
	$v_{p,0}$ [m s^{-1}]	
355-400 µm	0.83	
300-355 µm	0.89	
250-280 µm	0.99	
212-250 µm	1.07	
180-212 µm	1.16	

By using a high-speed camera, the impact of 355-400 µm particles of F-CLC upon free fall velocity (about 1 m s^{-1}) is recorded and reported in sequence of images in Figure 3-18, showing several surface chips being produced. A direct comparison of the data points of non-washed and washed material is reported below in Figure 3-19 showing the effect of dust on the breakage results.

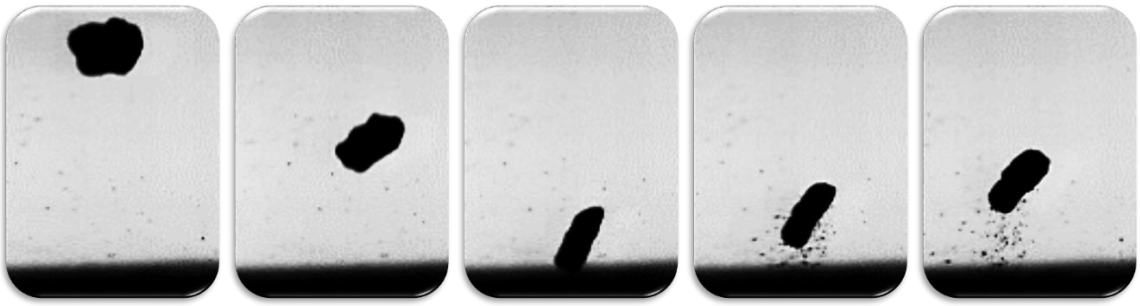

Figure 3-18. Time sequence of a single particle of 355-400 µm of washed F-CLC experiencing breakage upon free fall impact, about 1 m s^{-1}

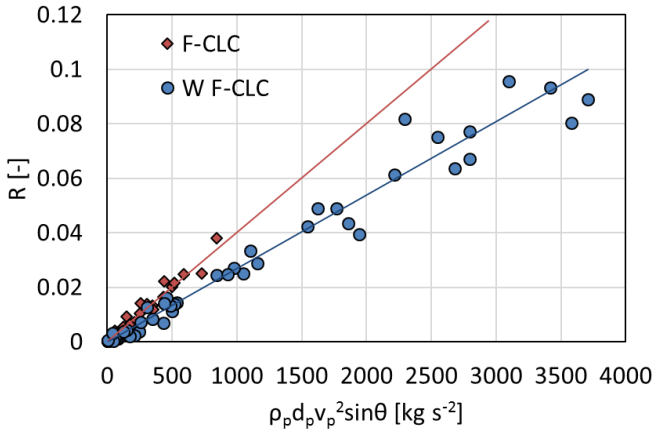

Figure 3-19. Comparison between non-washed and washed F-CLC single particle breakability

The breakage pattern is assessed using the Schumann's plot of Figure 3-20 for the same conditions, showing to be way below the fragmentation threshold.

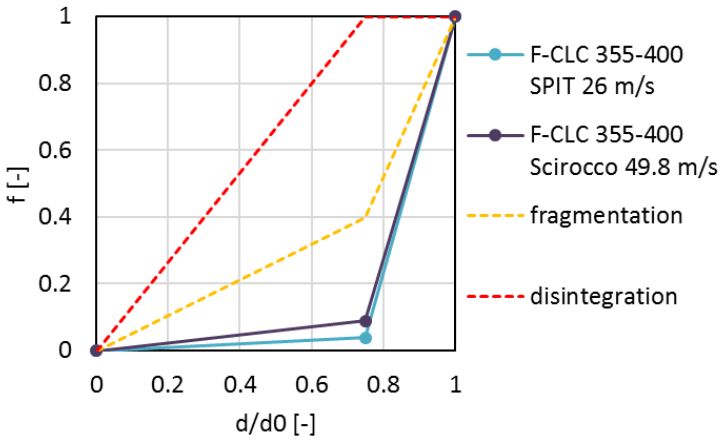

Figure 3-20. Schumann's plot of washed F-CLC 355-400 µm particles

The SEM images of the mother and debris particles obtained at the most sever conditions in Scirocco are reported for feed particles of 355-400 µm and 180-212 µm, in Figure 3-21. The figure shows that the debris particles are composed by small fines and some large ones, probably created as a result of severe chipping or fragmentation of some mother particles.

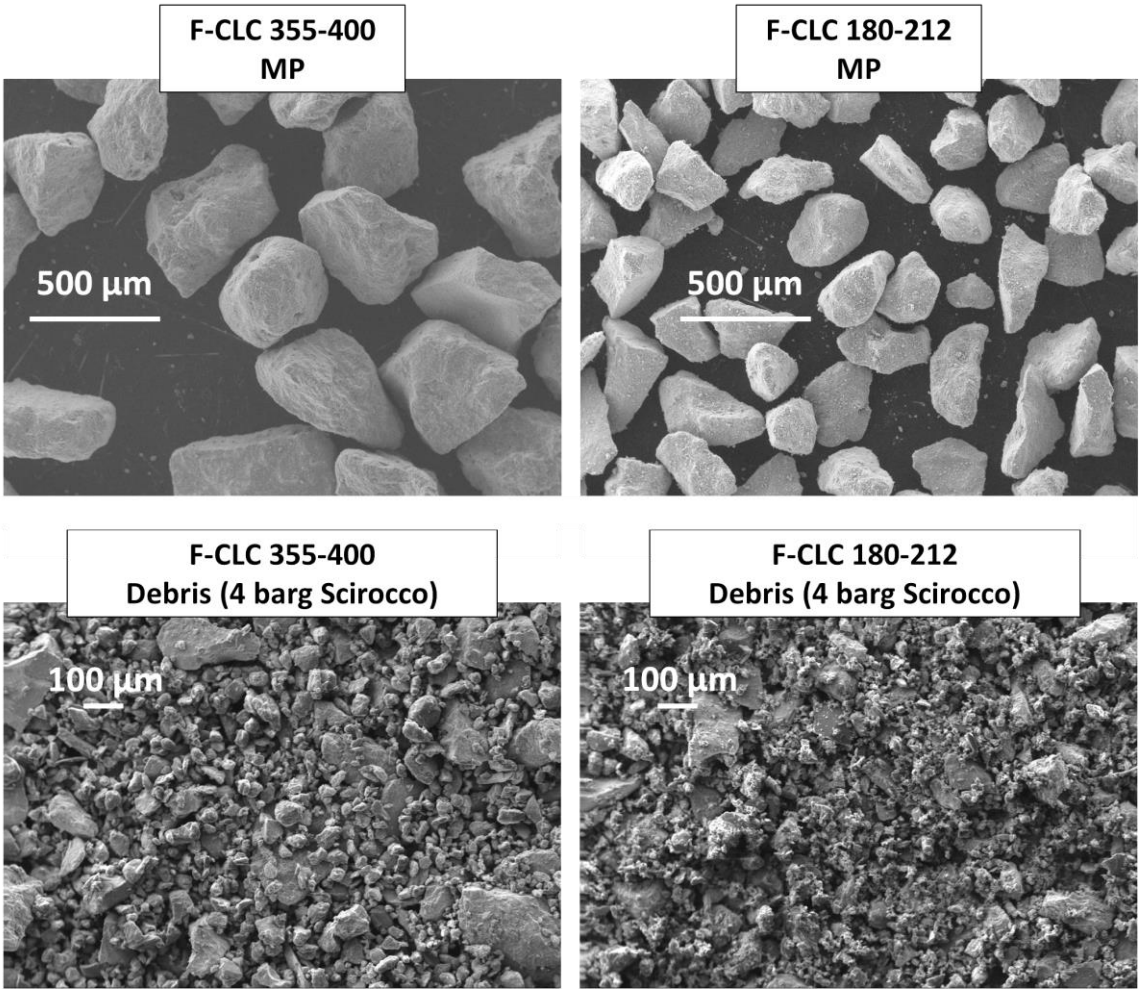

Figure 3-21. Mother and debris particles of F-CLC looked at the SEM for feed particle sizes of 355-400 µm and 180-212 µm, after attrition in the Scirocco at 4 barg pressure

The effect of fatigue is assessed by carrying out six repeated impacts at a fixed impact velocity and particle size, for both non-washed and washed material. The results, displayed in Figure 3-22, show that there is no significant effect on the number of impacts on the extent of breakage for washed material, while the non-washed material tends to have higher extents of breakage during the first three/four impacts due to the presence of

adhered dust on the mother particles surfaces. Towards the fifth/sixth impact the extent of breakage of the two materials tend to be the same.

Six impacts are probably not sufficient to make significant changes in particle breakage.

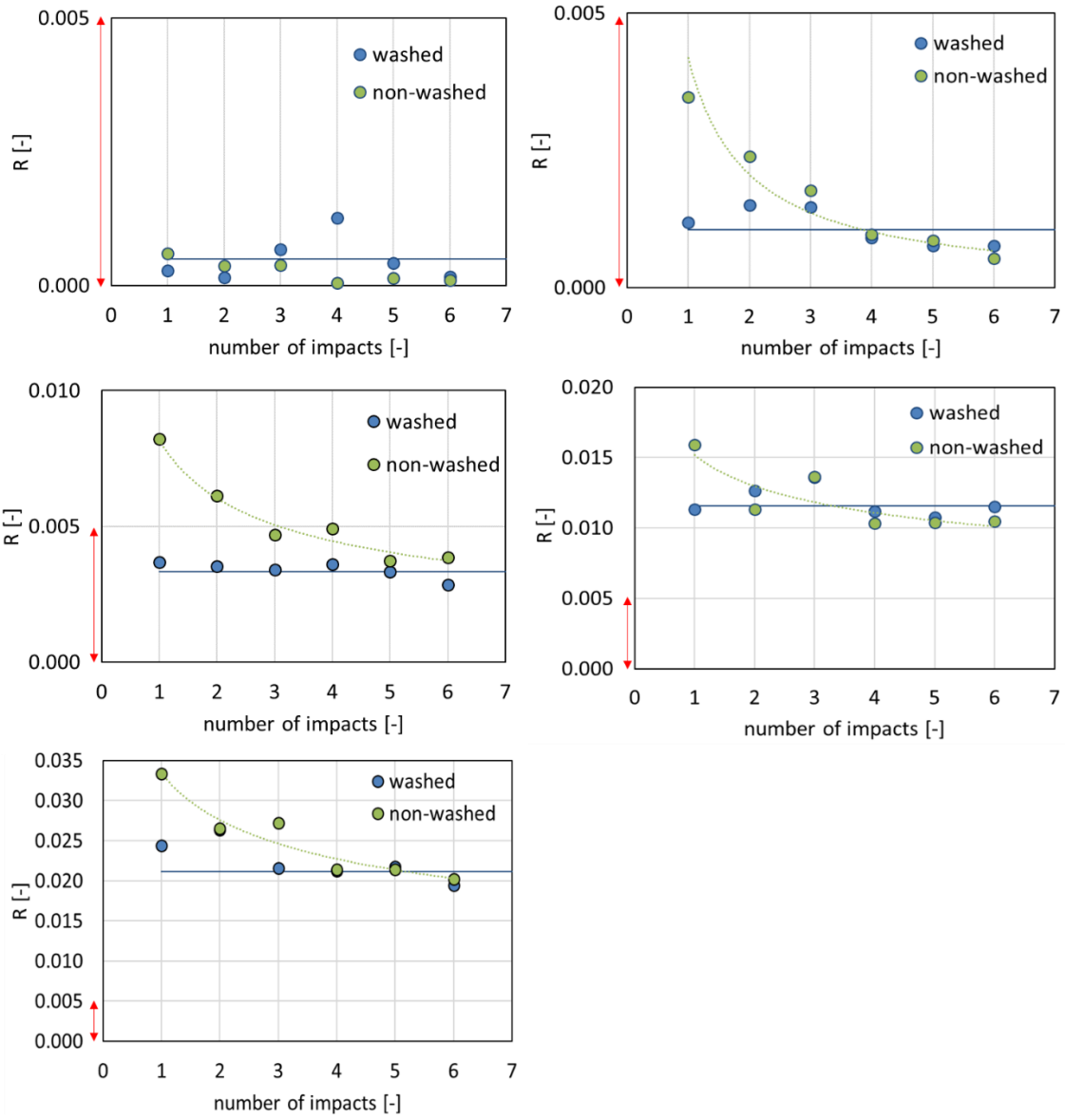

Figure 3-22. Effect of 6 repeated impacts for both washed and non-washed F-CLC particles of 355-400 µm at different impact velocities

3.4.2 E-CLC

The same analysis on the effect of particle size, impact velocity, angle of impact and fatigue is carried out for washed E-CLC particles of different sizes, using the SPIT. In

particular, the same relationship with the angle of impact found for F-CLC is obtained as shown in Figure 3-23.

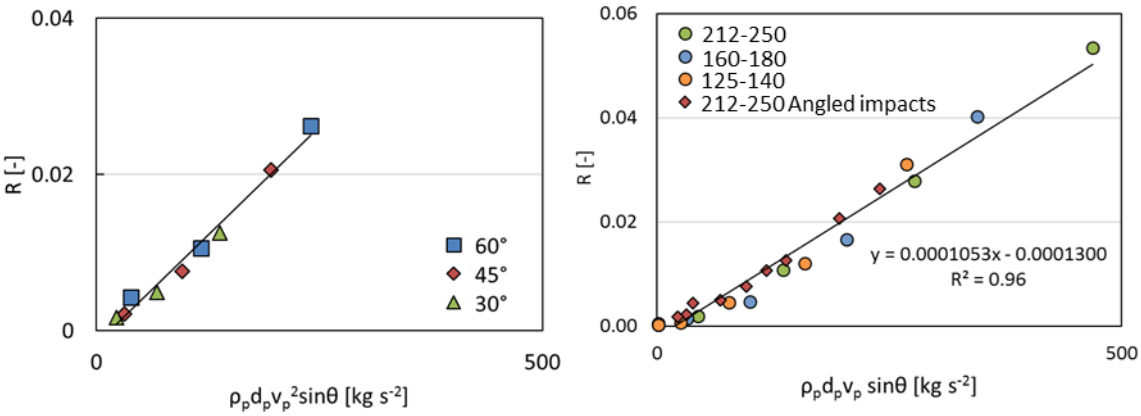

Figure 3-23. Unification of data points of "R" for E-CLC particles, obtained using SPIT, with the group $\rho_p d_p v_p^2 \sin\theta$

From the unification of the data points on a straight line, it is possible to evaluate the transitional velocity according to Equation. 3-14. These are shown in Table 3-4. They are found to be larger than those of F-CLC. The breakability index of E-CLC is much larger than that of F-CLC, implying that the former undergoes attrition to a greater extent. However, its transition velocity is also larger, as shown in Figure 3-24 meaning that equilibrium CLC particles require a higher impact energy to initiate breakage.

Table 3-4. Breakability index, intercept with the abscissa and breakage transitional velocity for different sizes of washed E-CLC particles

E-CLC sieve size [μm]	$\alpha \frac{H}{K_c^2}$	**b_{sp}**
	$1.05X10^{-4}$	$1.30X10^{-4}$
	$v_{p,0}$ [m s^{-1}]	
250-280	1.3	
160-180	1.6	
125-140	1.8	

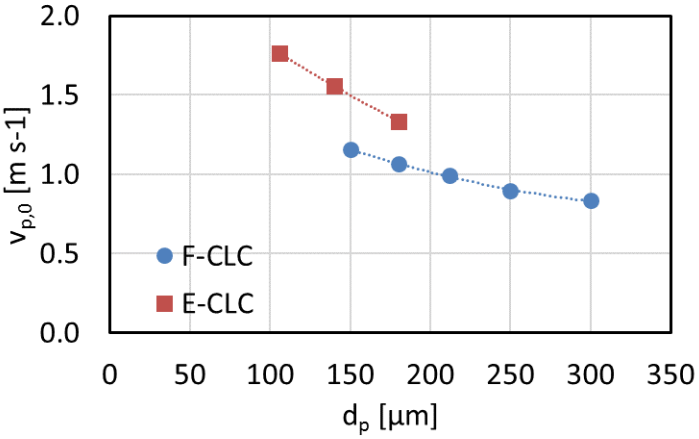

Figure 3-24. Transition velocity of F-CLC and E-CLC particles as a function of particle size

The extents of breakage obtained for all conditions, in terms R^+, R^*, R^- and R, are shown in Figure 3-25 with a maximum error band of 22%.

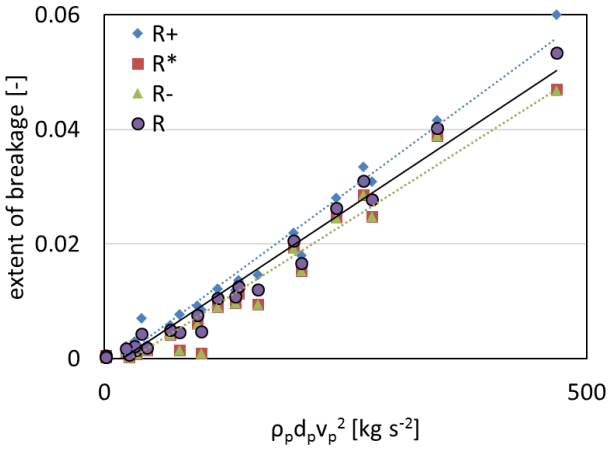

Figure 3-25. The extents of breakage "R+", "R*", "R-" and "R", obtained using SPIT, plotted against $\rho_p d_p v_p^2$ for washed E-CLC particles of different sizes for different impact velocities

Consistent with trends observed for the fresh material, the pattern of breakage for all conditions is way below the fragmentation limit, Figure 3-26. This is determined based on the mother particles becoming sufficiently small to go through the sieve size limit that defines the debris, as discussed in section 3.3.

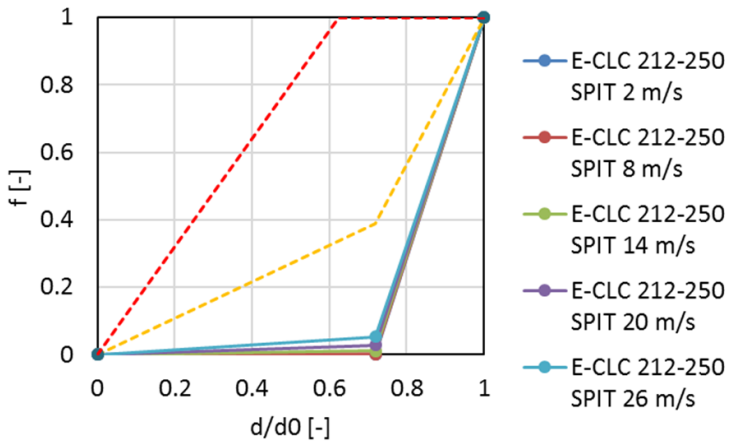

Figure 3-26. Schumann's plot of washed E-CLC

The repeated impacts carried out on washed E-CLC particles of 212-250 µm show a gradual decrease of extent of breakage at the highest velocity tested, 20 and 26 m s^{-1}. This behaviour is in contrast with what observed for F-CLC particles for which no effect of the number of impacts is observed.

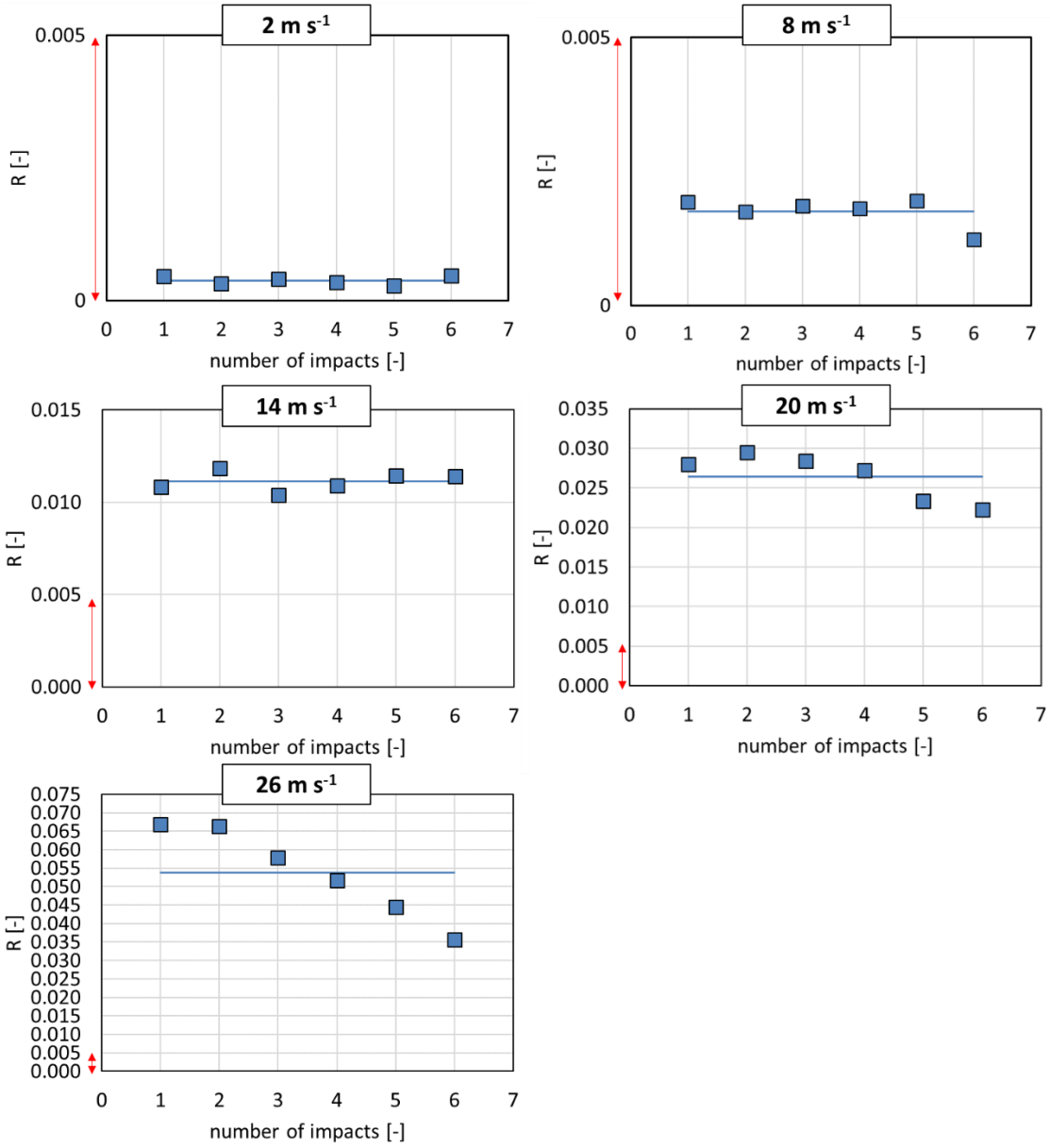

Figure 3-27. Effect of 6 repeated impacts for both washed and non-washed E-CLC particles of 212-250 µm at different impact velocities

3.5 Assessment of the Model for Inclined Impact

As mentioned above, the remarkable unification of the data points obtained at different angles for the two materials is surprising, because the model has not been derived on physical bases. Therefore, its validity is assessed here using data sets taken from literature on particle and agglomerates breakage upon angled impact. All the data presented here are reported as a function of the impact velocity magnitude, the normal component of the impact velocity and the model developed here $v_p \sin^{0.5}\theta$ (which gives a parabolic trend).

Wang et al. (2019) carried out single particle impact test using zeolite particles at different inclination, 30°, 45° and 60°. Figure 3-28 shows that the empirical model proposed here is able to capture the trend.

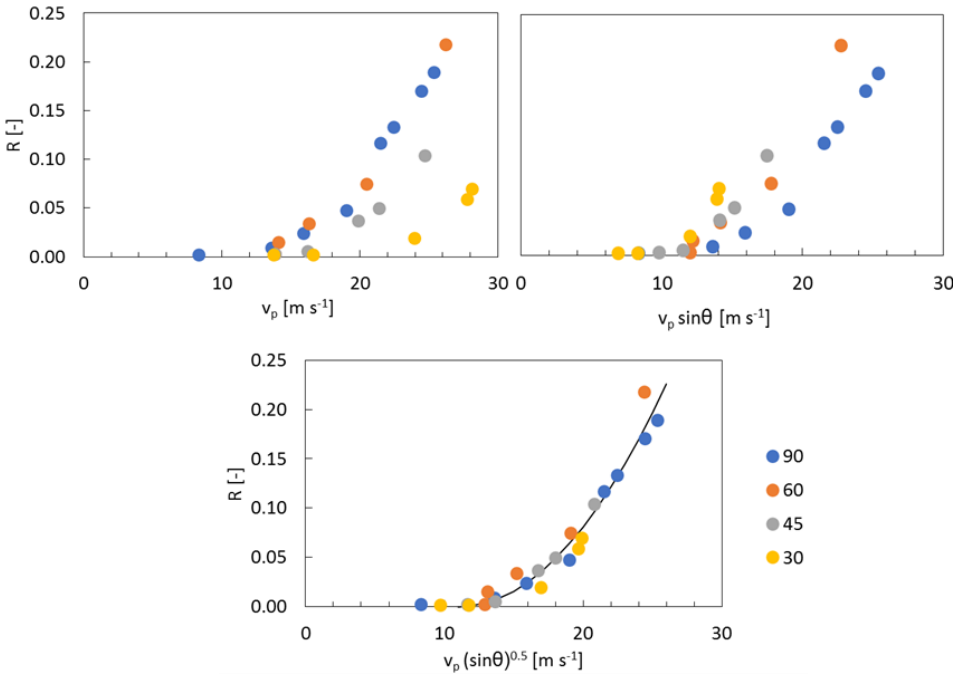

Figure 3-28. Extent of breakage of zeolite particles obtained by (Wang et al. 2019) plotted against (in order from left to right): the impact velocity magnitude, the normal component of the impact velocity and the model derived here

Salman et al. (1995) studied the effect of the angle of impact on the breakage of aluminium oxide particles of 2.8-7.6 mm. The results, reported in terms of damage ratio, i.e. mass of broken particles over the total mass, are displayed in Figure 3-29 showing again a good prediction of the model.

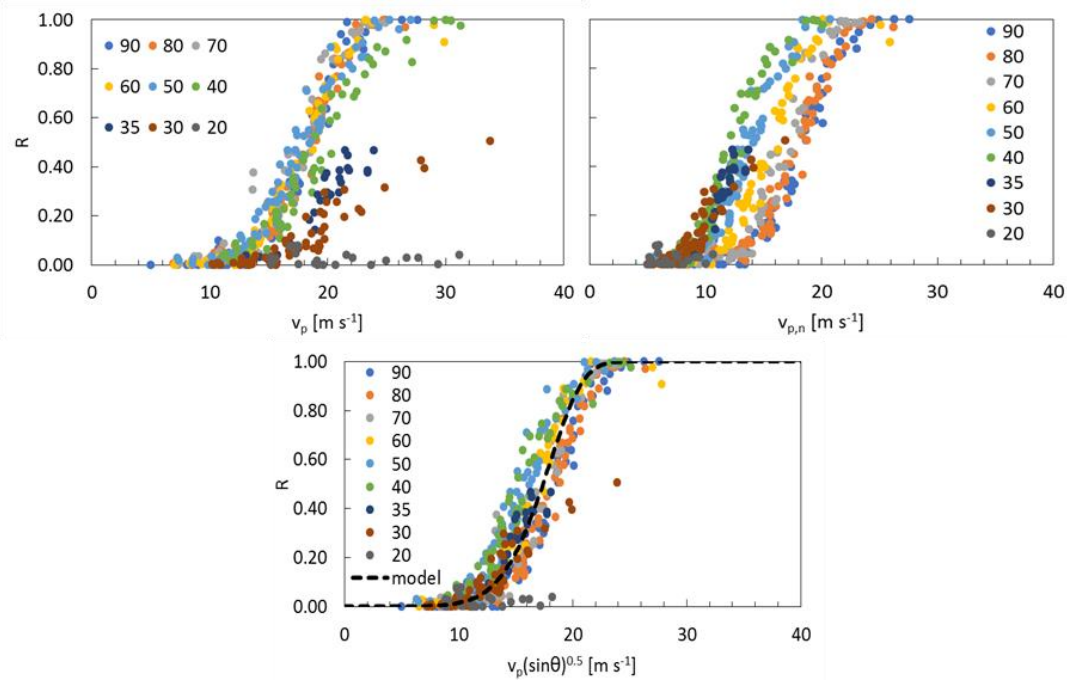

Figure 3-29. Damage ratio of aluminium oxide particles obtained by (Salman et al. 1995) plotted, in order from left to right, against: the impact velocity magnitude, the normal component of the impact velocity and the model derived here

3.6 Concluding Remarks

The single particle breakability of fresh and equilibrium CLC particles is evaluated using the single particle impact test and the Scirocco impact test with focus on the effect of particle size, impact velocity, angle of impact and number of impacts. Both materials are "washed" in order to remove the fine dust adhering to the particles surfaces so as not to influence the outcomes of the impact test. The impact breakage of non-washed F-CLC particles is also analysed and found to be higher than that of its washed equivalent.

The experimental data for all the materials agree well with the chipping model for semi-brittle material of Ghadiri and Zhang, (2002), confirming the proportionality with the impact velocity square and the particle size.

The investigation on the effect of the angle of impact leads to a dependency of the extent of breakage with the sinθ. The applicability of the latter is verified by using the data sets of particles breakage at inclined impact taken from literature, showing a good capability of prediction. However, the model has no physical basis and its true nature is to be considered yet to be discovered.

The transition velocity from little/no-breakage to breakage is assessed using the straight-line fitting of the extents of breakage against the group $\rho_p d_p v_p^2 \sin\theta$. This is found to be higher for the E-CLC than F-CLC. The breakability index $\alpha H/K_c^2$, namely the slope of the straight line, is larger for E-CLC, as shown in Figure 3-30. This is because substantial structural changes take place as a result of cyclic oxidation which produces large pores and cavities.

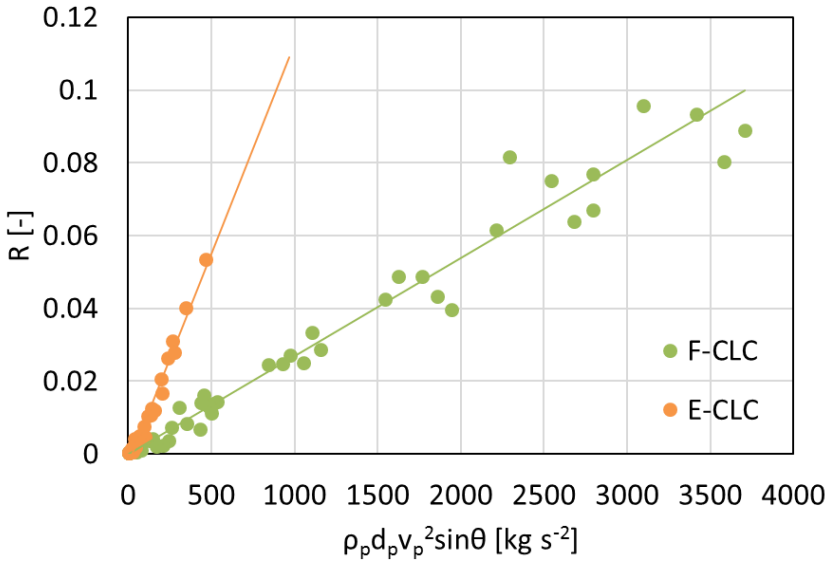

Figure 3-30. Comparison of the single particle breakage extents between washed F-CLC and washed E-CLC particles, as a function of the group $\rho_p d_p v_p^2 \sin\theta$

No significant variation of the extent of breakage is observed for washed F-CLC particles throughout six repeated impacts. The extent of breakage of non-washed F-CLC decreases during the first three/four impacts, then it tends to the same values of its washed equivalent, confirming the effect of the dust on the evaluation of breakage. Unexpectedly, the extent of breakage of E-CLC particles tends to reduce with the number of impacts at high impact velocities while at low impact velocities no significant variation is observed. In this work the extent of breakage of single particles by impact has been evaluated and described in terms of an empirical equation. This will later be used in the analysis of attrition in the jet region of the fluidised bed, the cyclone and the population balance model.

4. CYCLONE ATTRITION

CHAPTER 4

The work reported in this Chapter aims at understanding the dynamics behind particle attrition in a cyclone and at developing a correlation of attrition for F-CLC particles as a function of gas inlet velocity, particle size and solids loading. This work is divided in two main parts: experimental based and computational based. Both have been carried out at University of Leeds facilities across the 2nd and 3rd year of this PhD project.

Initially a literature review is given. Then the description of the experimental approach used to characterise attrition of F-CLC particles in a high efficiency Stairmand cyclone is presented and the results discussed.

Moreover, CFD-DEM simulations are used to simulate the particles dynamics in the same system to elucidate the mechanisms behind particle attrition and compare consistency with the experimental work. The main outcomes of the simulations are the particle-wall and particle-particle relative impact velocities, angles, frequencies, and particle-wall sliding distances, normal loads and residence times in various regions of the cyclone. In a post processing data analysis, these outcomes are coupled with two mechanistic models of single particle breakage, describing respectively chipping and surface abrasion in order to predict the overall extent of attrition in the cyclone. The former is the single particle breakage model of impact, derived in Chapter 3 for F-CLC particles, and the latter is the theoretical wear model of Archard and Charj, (1953). The results of the computational work are compared with the experimental results.

A schematic description of the work plan is reported below in Figure 4-1.

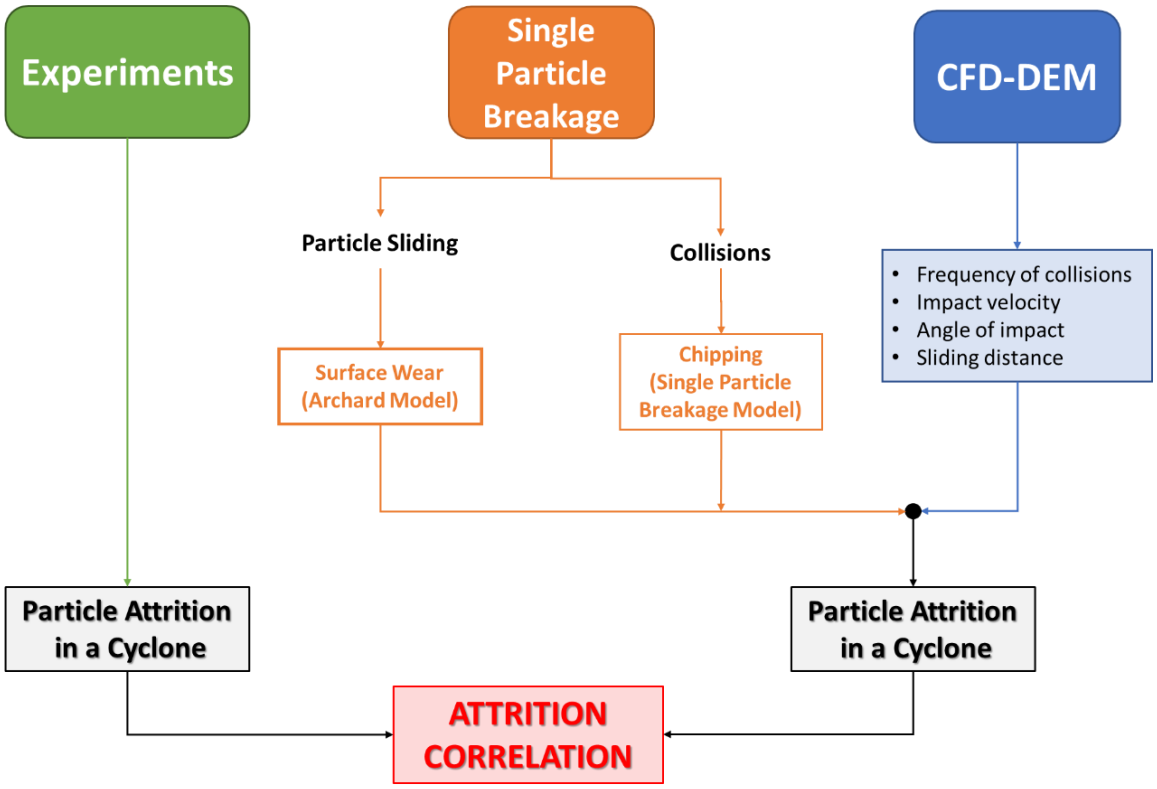

Figure 4-1. Scheme of the cyclone working plan

The CFD-DEM approach allows to be identified the relative contributions of different regions of the cyclone to the overall attrition, as well as elucidating the relative importance of different mechanisms of attrition. Initially, only CFD simulations are performed to reach mesh independency and validate the macroscopic fluid dynamic behaviour through the pressure drop, against the experimental observations. Then CFD simulations are coupled with DEM to simulate the gas/solids dynamics

The Chapter is structured in the following order: (i) background, (ii) literature review of cyclone attrition, experimental setup and results, (iii) literature review of fluid/solids dynamics in cyclones by computational approaches, CFD-DEM principles, simulations setup, results and (iv) conclusions.

4.1 Background

Cyclones are inexpensive gas/solids separation systems characterised by low pressure drops, (Yang, 2003; Gauthier et al. 2010). A strong swirling flow is established as the

fluid enters the cyclone. As a result, the particles are subjected to a centrifugal force leading them to the walls, (Yang, 2003). The flow field of a reverse cyclone is characterised by a high-pressure outer vortex moving downward and a low pressure reverse inner vortex moving upwards. This has been observed by several CFD studies, (Chu et al. 2011; Raoufi et al. 2008; Martignoni et al. 2007; Elsayed, 2015). The particles tend to move in strands towards the bottom outlet where they are collected. In fluidised and circulating fluidised bed processes, cyclones are fundamental to recover the elutriated particles and avoid great losses of material. However, the rapid shearing of the particles and their collisional behaviour lead to attrition, (Pell, 1990).

4.2 Experimental Work

4.2.1 Literature Review

The cyclone is one of the most significant contributors to particle attrition especially at high superficial gas velocities, (Werther and Reppenhagen, 2001). Particles entering the cyclone are likely to impact on the opposite side of the inlet duct and slide against the wall towards the bottom outlet. Usually, particle attrition in cyclones is surface damage dominated but when a certain threshold energy is exceeded, fragmentation can also take place. However, in normal operations, severe particle attrition is usually avoided by using an appropriate design.

Reppenhagen and Werther, (2000) developed a model of particle attrition in a cyclone for FCC catalysts under conditions of pure abrasion. They reported that the attrition rate is dependent on the material properties, gas kinetic energy, particle size and inversely proportional to the square root of the solids loading, Equation. 4-1.

$$R_{cyc} = c_{cyc} \frac{u_{cyc,in}^2}{\mu^{0.5}} d_p \tag{4-1}$$

where the solids loading, μ, is defined according to Equation 4-2

$$\mu = \frac{\dot{m}_{solids}}{\dot{m}_{fluid}} \tag{4-2}$$

The square of the velocity term is due to the kinetic energy of the particles, which is related to that of the fluid. The inverse proportionality with the square root of the solids

loading is caused by the decreasing probability of the particle to get in contact with the wall at increasing concentrations (Reppenhagen and Werther, 2000). The authors firstly analysed the relative importance of different regions of the cyclone, they looked at the erosion spots of the internal surface of the cyclone by covering it with a black painted sheet. They noticed, after several passages of the material, a highly eroded area opposite to the cyclone inlet, less eroded areas along the cylindrical body and no erosion in the conical body. They concluded that the highly eroded area is the results of particles colliding against the wall experiencing chipping/fragmentation, as further suggested by the SEM images of the mother particles. At the same time, they observed that surface abrasion occurs mainly in the cylindrical body. Moreover, they verified successfully the validity of the model by testing nine different cyclone geometries, at the same process conditions. This can be explained by the fact that attrition, in such systems, is mainly due to particle collisions at the entrance and therefore strongly dependent on the entrance conditions.

It is critical to understand the conditions under which a certain mechanism of attrition is dominant. The particle dynamics in a cyclone is thus the key to understanding this phenomenon. At low solids loading, for instance, particle collisions against the wall of the cyclone can be the main cause of attrition. Bayham et al. (2017) carried out an analytical study on the steady state particle attrition in cyclones under conditions of pure abrasion, considering the wear model of Archard and Charj, (1953). They assumed that the particle dynamics in the cyclone is not affected by the solids loading when this is low. On these bases, by mathematically manipulating the wear model, they managed to express the cyclone attrition constants as a combination of two parts: one dependent on the material properties and the other on the cyclone geometry. Nevertheless, they generalised their model by including the dependency of the solids loadings. They also recognised the need of developing a model able to capture both surface abrasion and chipping.

In this work, the effect of gas inlet velocity, solids loading and particle size is analysed by using an experimental setup similar to that used by Werther and Reppenhagen, (1999), thus their methodology and results are discussed here.

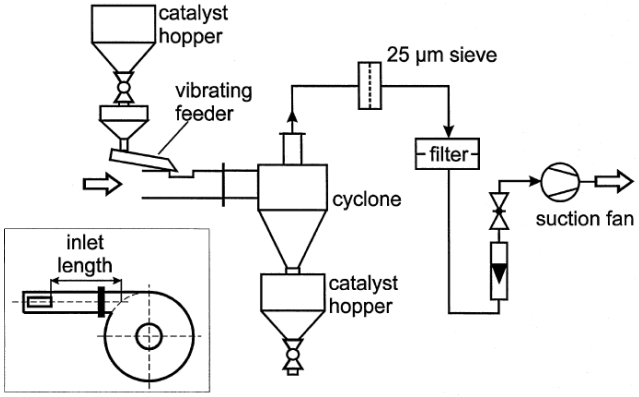

Figure 4-2. Experimental set up of (Reppenhagen and Werther, 2000)

Their system, reported in Figure 4-2, operates in suction mode, the full PSD of the material is fed by mean of a vibratory feeder in order to achieve the desired solids loading. The material is recovered at the bottom of the cyclone and reprocessed through the cyclone for about 34 times. Attrition is measured by the increase of the weight of the filter and calculated as the ratio of mass of fines collected with the feed mass. This criterium is consistent with the definition of attrition as the steady state mass loss but, it does not allow to consider attrition by chipping or fragmentation. The surface chips and fragments are unlikely to be carried away at the top outlet. This is the reason why their model is purely abrasion based.

Some characteristic results, obtained for an equilibrium FCC catalyst, are reported in Figure 4-3, showing a high loss rate at the beginning and a sudden decrease to steadier values after 3-4 passes. This occurrence is explained by the presence of very small fines attached to the surfaces of larger particles that are removed after few passes.

According to the same figure, after steady state is reached, the gas velocity is increased, and a new steady state is reached after a transient of 10 passes. Each steady state corresponds to a certain concentration of fines, produced by attrition, which is equal to the loss. They have also reported a decrease of the loss rate by prolonging the experiments to 500 passes, as caused by the particle reduction in size due to attrition, in agreement with the model.

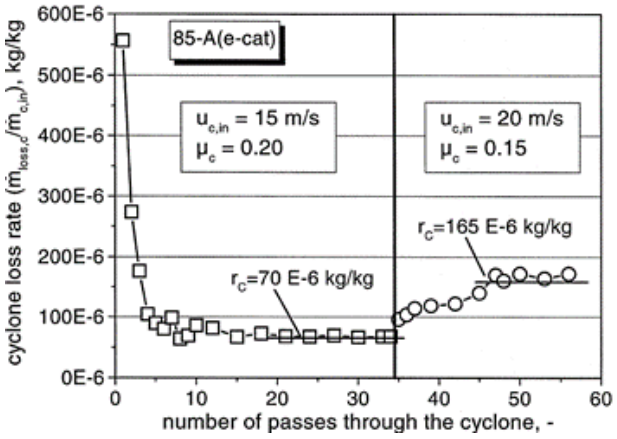

Figure 4-3. Extent of attrition for equilibrium FCC catalyst at different passes of (Reppenhagen and Werther, 2000)

4.2.2 Motivation and Objectives

Cyclones are major contributor to particle attrition. According to the work reported above, it is mainly dictated by the gas inlet velocity (which directly influences the particle impact velocities), the solids loading and the particle size. The inverse effect of the solids loading is believed to represent the likelihood of the particles to impact against the wall, higher at low solids loading. However, when the concentration of particles is high, particle-particle collisions might represent a significant contribution to the overall attrition. Heavy and large particles, such as those used here, might lead to different conclusions as compared to FCC catalyst because of their inertia towards being carried away with the gas. Moreover, the attrition analysis cannot be limited to only the elutriated fines because it might not be sufficient to fully understand the particles pattern of breakage. In this chapter, particle attrition is measured using the elutriated fines as well as by sieving the material collected in the catch pot so to consider any pattern of breakage.

4.2.3 Setup, Methodology and Experimental Conditions

Particle attrition in the cyclone is evaluated experimentally for washed F-CLC particles (to avoid that the dust adhered on the particle surfaces could affect the attrition results) at different conditions of gas inlet velocity, solids loading and particle sizes. The setup, methodology and experimental conditions are discussed here.

The experimental setup is similar to that used by Reppenhagen and Werther, (2000) and is shown in Figure 4-5. The cyclone rig has been built specifically for this research project. It operates in suction mode using two industrial vacuum cleaners mounted in

parallel, providing a total flow rate of 0.076 m^3 s^{-1} (Nilfisk, 1854). The solids are fed by means of a vibratory feeder at the beginning of the inlet pipe from a top-facing trough; the length of the inlet pipe is 0.33 m and it has a rectangular section which coincide with the cyclone slotted inlet. A cartridge filter of 2 µm pore size is mounted at the top exit of the cyclone in order to capture the fines escaping particles. A rotameter is used to measure the air flow rate and a needle valve to regulate it. The pressure drop is measured across the cyclone by means of a digital manometer, as shown in Figure 4-4 and schematically in Figure 4-5, to check consistency with the simulations. These values will be reported in the CFD-DEM section. The catch-pot is provided with a "chinese hat" to help inducing the reverse flow and minimise the interference between the collected material and the fluid. The cyclone design is a Stairmand high-efficiency type made of stainless steel, fabricated by the University of Leeds mechanical workshop; the dimensions are reported in Figure 4-4.

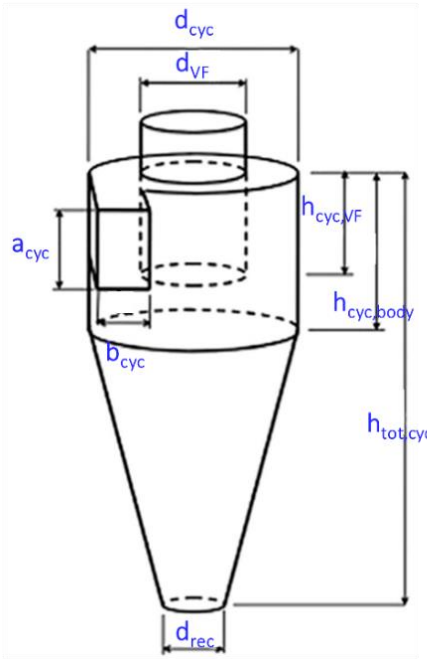

a_{cyc}	0.02
b_{cyc}	0.01
d_{cyc}	0.04
d_{rec}	0.01
d_{VF}	0.02
$h_{tot,cyc}$	0.16
$h_{cyc,body}$	0.08
$h_{cyc,VF}$	0.03

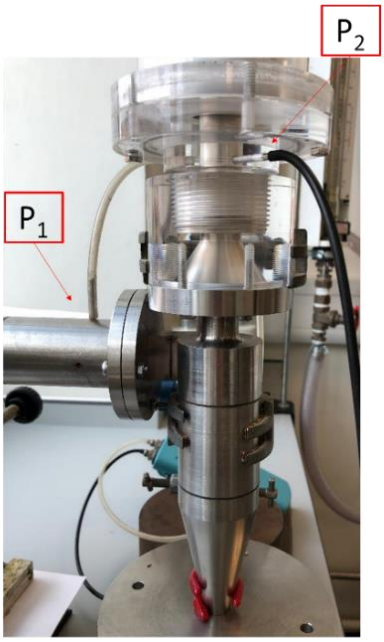

Figure 4-4. Cyclone dimensions in [m]

A total amount of 15 g of washed particles is used to run each test. The vibratory feeder is calibrated beforehand, in terms of mass discharged divided by the discharging time. The desired solids loading, defined as shown in Equation 4-2, is achieved by setting a certain solids and gas flow rate. The solids flow rate is regulated by the frequency of the vibratory feeder while the air flow rate by the opening of the needle valve.

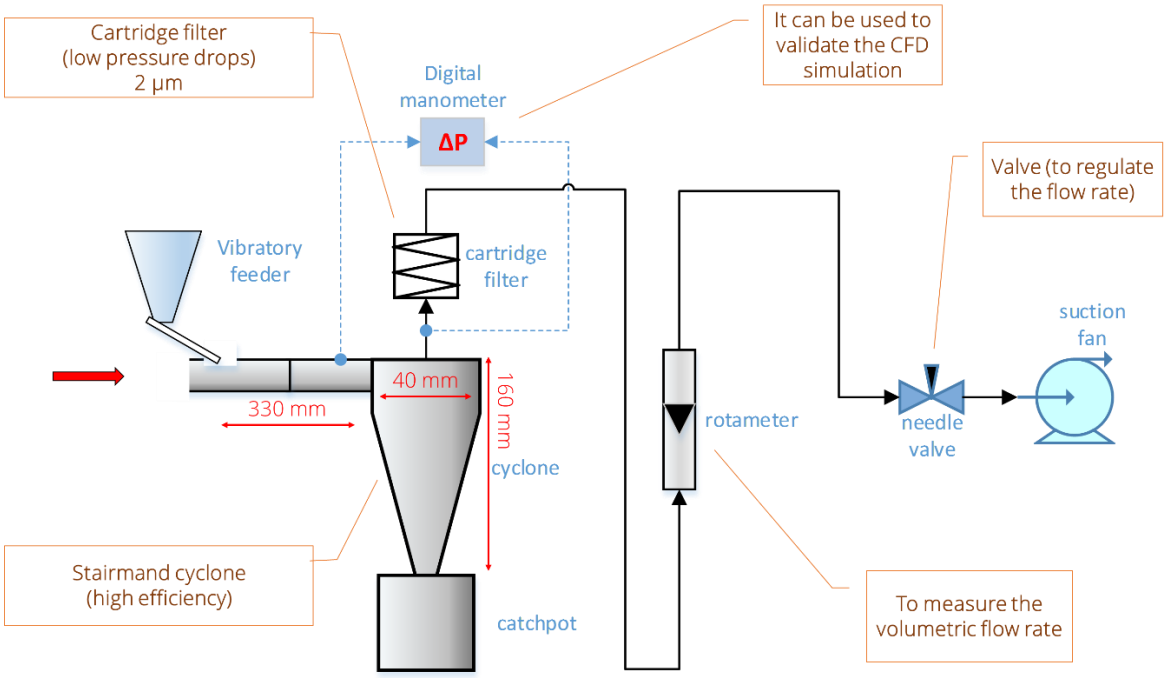

Figure 4-5. Experimental setup for cyclone induced attrition testing

The extent of attrition is evaluated as the average of R^- and R^+ which are defined in Equation. 3-6 and Equation. 3-7, respectively, after each pass through the cyclone, according to the same gravimetric analysis carried out for the single particle impact tests, i.e. the mother particles are separated from the debris by using a sieve mesh size of two sizes below the feed size; the cut-off sieve sizes are indicated in Table 2-2. In addition, the mass increase of the filter is also considered as debris. A total of 20 passes are carried out; for each run, only the mother particles of the previous pass are fed to the cyclone. The breakage pattern is assessed by means of the Schumann's plot and by the evaluation of the PSD of the debris particles by laser diffraction technique.

For a sample with a particle size range of 355-400 µm, prepared by sieving, the gas inlet velocity is varied from 12 to 24 m s^{-1} and solids loading is varied from 0.1 to 1, while the effect of particle size is evaluated under conditions of constant gas inlet velocity of 20 m s^{-1} and solids loading of 0.1. All the tests conditions are schematically reported in Table 4-1.

Table 4-1. Experimental conditions for washed F-CLC particles. The simulation conditions are the same except for the case at 12 m s^{-1}

Particle sieve size range used for experiments [µm]		**355-400**				**300-355**	**250-280**	**212-250**	**180-212**
Particle size used for simulations (arithmetic mean of above) [µm]		**377.5**				**327.5**	**265**	**231**	**196**
Solid loading ratio [kg_{solid} kg_f^{-1}]		**0.1**	**0.3**	**0.6**	**1**	**0.1**			
Gas inlet velocity [m s^{-1}]	**12**	exp	exp	exp	exp	-	-	-	-
	16	exp & sim	exp & sim	exp & sim	exp & sim	-	-	-	-
	20	exp & sim	exp & sim	exp & sim	exp & sim	exp & sim	exp & sim	exp & sim	exp & sim
	24	exp & sim	exp & sim	exp & sim	exp & sim	-	-	-	-

4.2.4 Results and Discussion

4.2.4.1 Effect of Gas Inlet Velocity and Solids Loading

The extents of attrition R^+, R^*, R^- and R for washed F-CLC particles of 355-400 µm at the conditions of 20 m s^{-1} of gas inlet velocity and 0.1 of solids loading are reported below in Figure 4-6. In this case, and all other cases, there is a large discrepancy between the lower and upper limit of breakage, R^- and R^+ respectively, related to the mass loss during the test and handling procedure. The loss could be related to the fines as well as mother particles, so the results hereinafter are presented and discussed in terms of R.

All the results of the experiments carried out with the particle size of 355-400 µm for different gas velocities and solids loading are shown in Figure 4-7. The figure shows a great scatter of the data points at low gas inlet velocity so no clear trend can be distinguished. At the lowest gas inlet velocity, 12 m s^{-1}, the quantity of debris measured is the same as the balance resolution (10^{-4} g) so the results are not considered for further analysis as they are subjected to high uncertainty. The low attrition extent can be

explained by the fact that such heavy particles at such low gas velocity would simply fall by gravity in the catch-pot not experiencing any remarkable stress. As the gas velocity is increased to 16, 20 and 24 m s^{-1} a trend becomes distinguishable. In fact, it is possible to notice that the attrition extent increases with the gas inlet velocity and decreases with the solids loading. At progressing number of passes the extent of attrition seems to linearly decrease. This was initially associated with the presence of surface asperities which would be gradually lost. In order to further investigate the effect of number of passes on cyclone attrition, at a later time during the project, the mother particles of the 20th pass, at the conditions of 20 m s^{-1} and solids loading of 0.1, are used to continue the test until 40 passes. The surprising results are shown in Figure 4-8. The figure shows that from 20th to 40th pass the same initial trend is re-observed obtaining, in this way, almost two parallel straight lines. The only difference between the 20th and 21st pass is that the cyclone was cleaned from the fines deposited on the walls created as a result of attrition. It is assumed that the building layer of fines on the walls might have had a mitigating effect on attrition. This has not been proven and further investigation is needed.

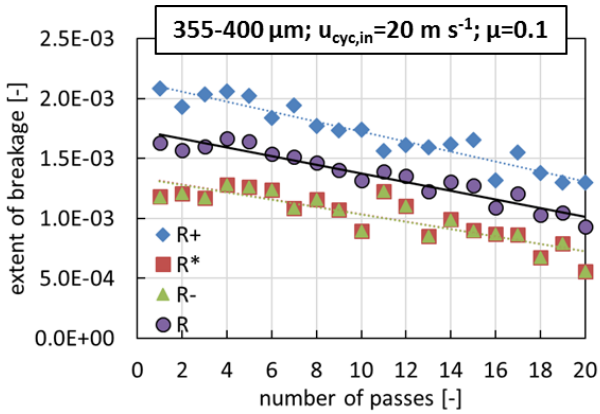

Figure 4-6. Extents of breakage R^+, R^*, R^- and R of washed F-CLC particles of 355-400 µm for 20 passes through the cyclone

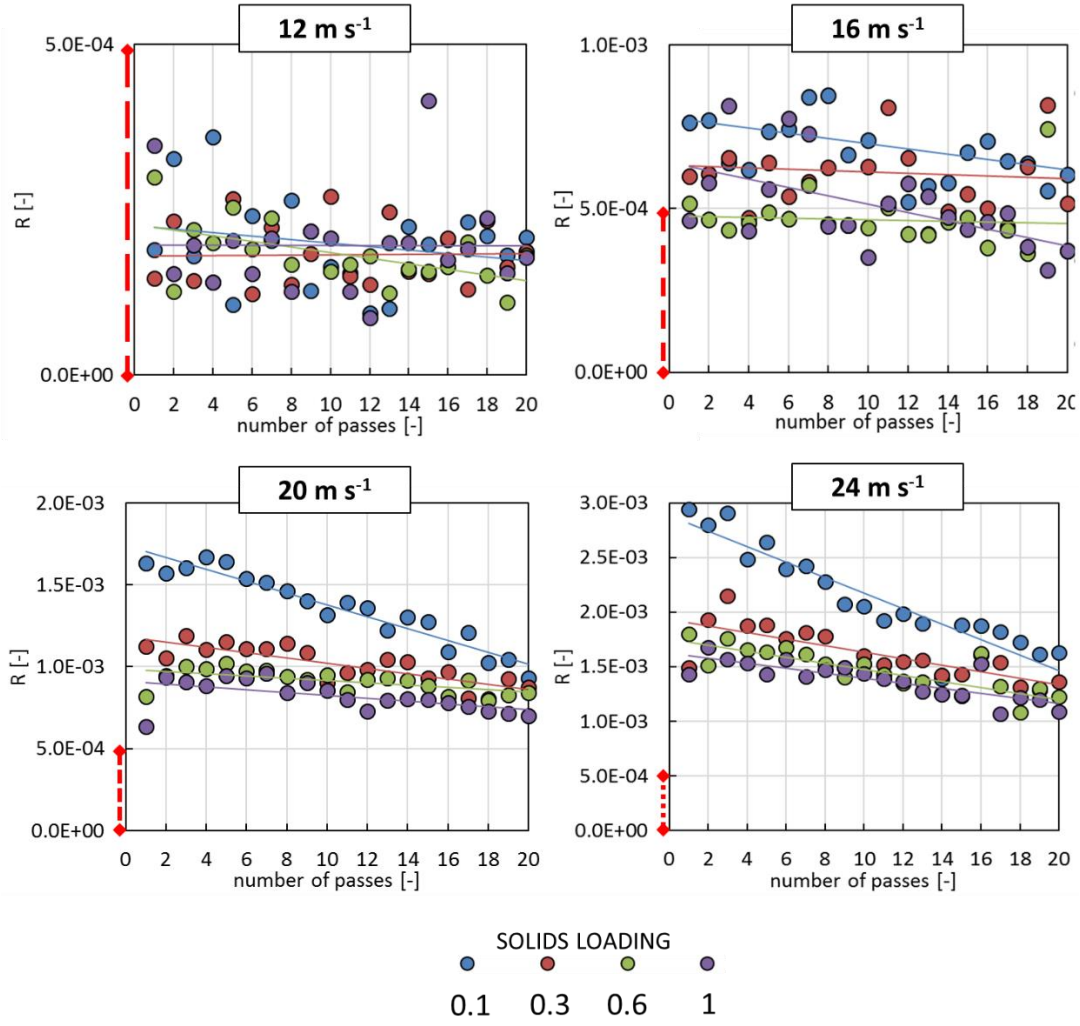

Figure 4-7. Extent of attrition, R, for a constant particle sieve size of 355-400 µm of washed F-CLC and at different values of gas inlet velocity and solids loading for 20 passes through the cyclone

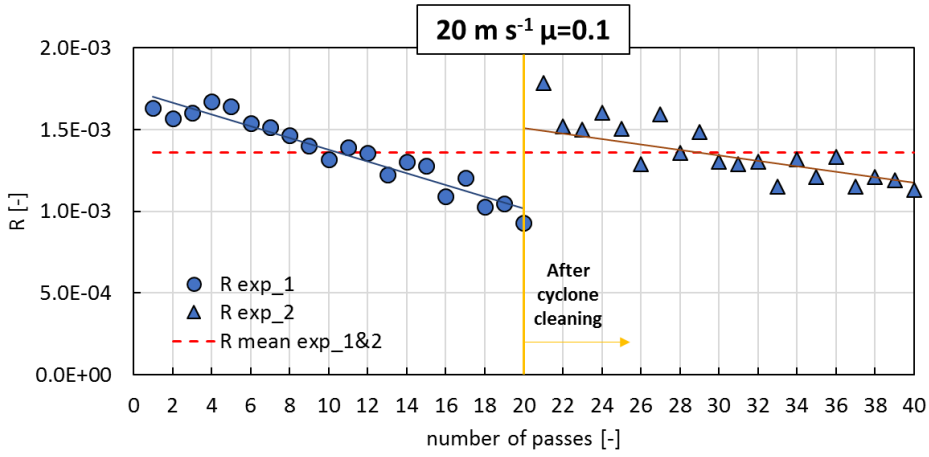

Figure 4-8. Cyclone-induced extents of attrition for a fixed particle size of 355-400 µm for an inlet gas velocity of 20 m s^{-1} and a solids loading of 0.1, throughout 20 passes

4.2.4.2 Effect of Particle Size

At 20 m s^{-1} and at 0.1 of solids loading the effect of size is investigated. The results, in terms of the extent of attrition, are shown in Figure 4-9. The results show that the attrition extent decreases with particle size. This is in contrast with the model of Reppenhagen and Werther, (2000) who observe a linear dependency with particle size, and also counterintuitive, because it has been established experimentally that particle breakage, upon impact, increases linearly with particle size following the model of Zhang and Ghadiri, (2002). This can be explained though by considering the entrance effect; small particles might accelerate faster and enter the cyclone at higher velocity as compared to large particles. This effect is enhanced in case of very dense particles, such as those used here. The length of the pipe might have been insufficient to accelerate the particles to a similar velocity. A CFD-DEM study is eventually carried out to investigate the importance of the entrance effect of particles of different sizes, mono-dispersed and poly-dispersed, at different solids for different pipe lengths.

The same linear reduction with the number of passes is observed for all the particle size tested.

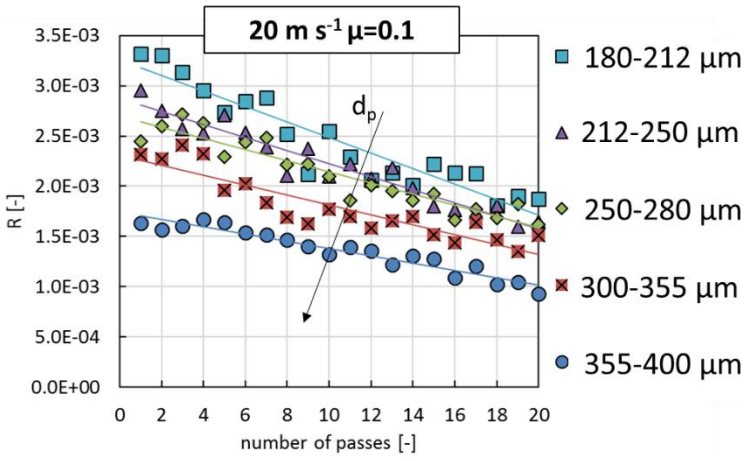

Figure 4-9. Cyclone-induced extents of attrition for different particle sizes, at 20 m s^{-1} gas inlet velocity and 0.1 solids loading

4.2.4.3 Breakage Pattern

By referring to the most severe conditions of attrition, namely low solids loading and high gas inlet velocity, the pattern of breakage is assessed by means of the Schumann's plot. Figure 4-10 shows the Schumann's plot for the cyclone attrition for two particle sizes,

355-400 µm and 180-212 µm at 24 m s^{-1} and solids loading of 0.1 in comparison with their breakage upon a normal impact at 26 m s^{-1}. In all cases, being below the fragmentation limit, the dominant breakage pattern is due to surface abrasion and chipping.

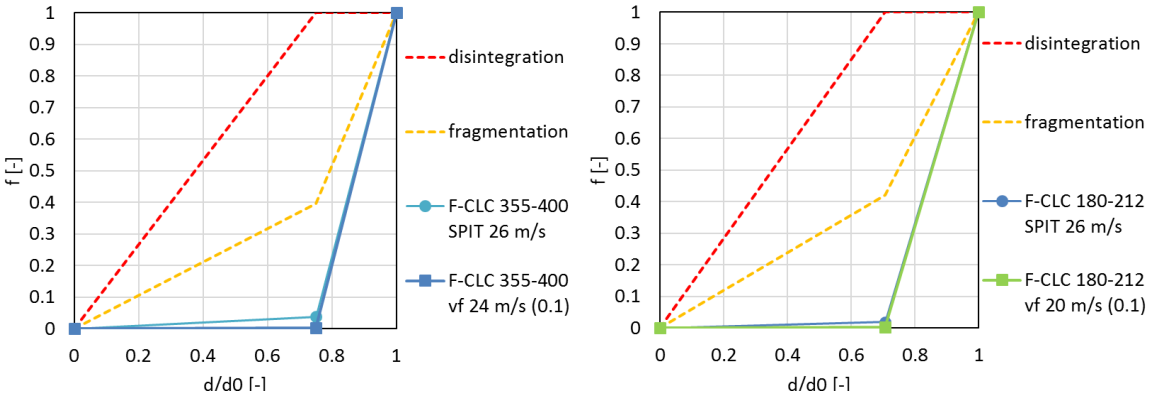

Figure 4-10. Schumann's plot of the attrition in cycloen in comparison with the single particle attrition upon a normal impact. On the left, for the particle size fo 355-400 µm and on the right, for the particle size of 180-212 µm

More insights can be given by the PSDs of the debris particles, reported in Figure 4-11. The PSDs are obtained with the laser diffraction technique using the Malvern Mastersizer 3000 with dispersion by the Aero S at 4 barg air pressure. The figure shows the PSD of the feed particles and the debris particles in terms of volume fraction for all the particle sizes studied. The debris size distribution presents in general four modes, the first three are in common for all the cases; they are about 0.6, 5 and 30 µm, whilst the fourth one, i.e. the highest, varies from 62 to 135 µm with increasing particles feed size. The presence of these relatively large particles is associated with particle fragmentation. As suggested by the Schumann's plot the general pattern of breakage is way below the fragmentation regime, but at the same time it is probable that few particles might have undergone fragmentation. Since the laser diffraction techniques give the volume-based PSD, the contribution of the latter is significant.

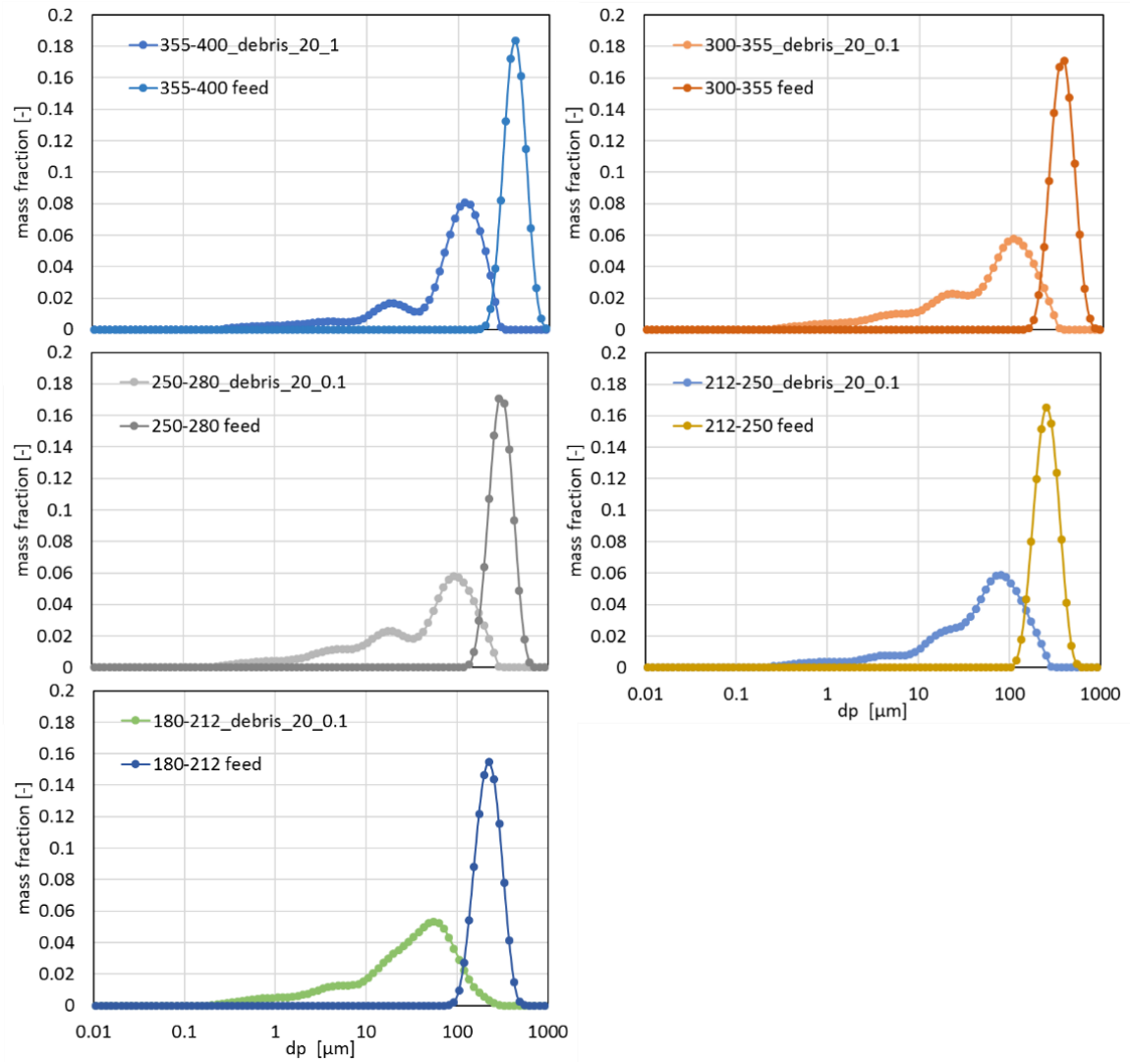

Figure 4-11. Feed and debris PSD, as obtained by laser diffraction technique, after 20 passes through the cyclone at 20 m s^{-1} and solids loading of 0.1 for different particle size

4.2.4.4 Overall Results

The average extents of attrition, out of 20 passes, are used to investigate the effect of the three main variables: gas inlet velocity, solids loading and particle size. They are reported in Figure 4-12 showing that attrition increases with the gas inlet velocity but decreases with the gas solids loading and particle size. The latter is probably due to the different entrance velocities for different particle sizes.

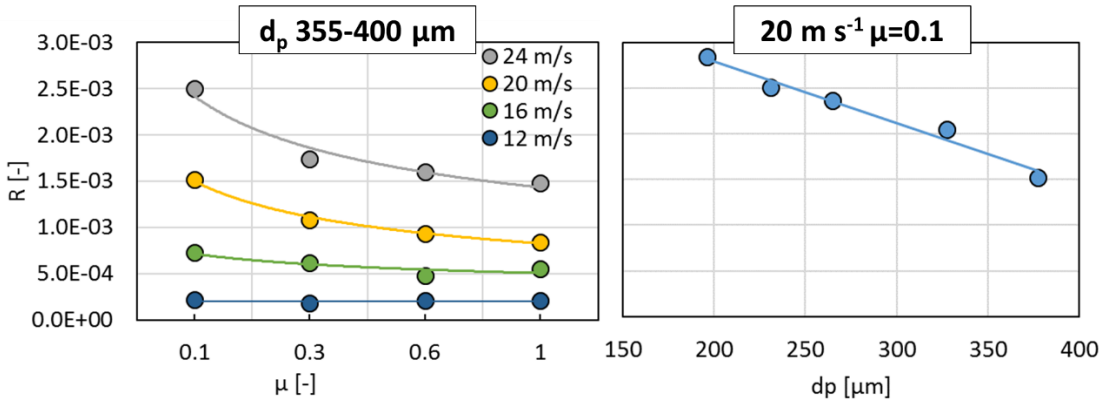

Figure 4-12. Extent of attrition in the cyclone, on the left: for particle size of 355-400 µm as a function of solids loading at different gas inlet velocity; on the right: at 20 m s^{-1} and solids loading of 0.1 for different particle sizes.

By assuming power functionality with the three variables studied, the power indices are evaluated by fitting the data points in the following way:

- for the gas velocity power dependency, the solids loading and particle size are kept constant, (the points obtained 12 m s^{-1} are excluded from this analysis)
- for the solids loading power dependency, the inlet gas velocity and particle size are kept constant
- for the particle size power dependency, the inlet gas velocity and solids loading are 20 m s^{-1} and 0.1, respectively.

The exponents are reported in Table 4-2, showing general disagreement with those of Reppenhagen and Werther, (2000). The power index of the gas inlet velocity, solids loading and particle size are respectively 2.75, -0.21 and -0.87 as compared to 2, -0.5 and 1 for Reppenhagen and Werther, (2000). The dependency on the particle size might be just an artefact of the experimental set up allowing smaller particles to accelerate faster than larger ones. Further analysis by CFD-DEM on the particle velocity at the cyclone entrance will be discussed in the CFD-DEM section. The confrontation with Reppenhagen and Werther, (2000) should be carefully done as both particles type and attrition assessment method are different.

Table 4-2. Power dependencies of the gas inlet velocity, solids loading and particle size obtained from the experimental data set of attrition

material	comments	d_p^	$u_{cyc,in}$^	μ^
FCC (full PSD)	(Reppenhagen and Werther, 2000) Experimental	1	2	-0.5
MnO_2 (constant particle size)	Experimental	**-0.87** CV=n.a.	**2.75** CV=12%	**-0.21** CV=26%

A unification of all the data points, in terms of R, is achieved and shown in Figure 4-13 against the lumped parameter $\alpha \frac{H}{K_c^2} u_{cyc,in}^3 d_p^{-1} \mu^{-0.2}$. The parameters c_{cyc} and b_{cyc} are the cyclone attrition constant (slope of the straight line) and constant term, respectively.

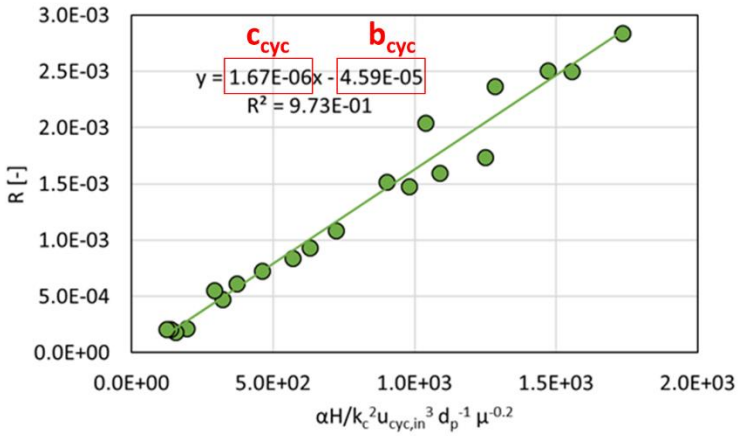

Figure 4-13. Cyclone-induced extent of attrition plotted against the lumped parameter $\alpha H/k_c^2 \cdot u_{cyc,in}^3 \cdot d_p^{-1} \cdot \mu^{-0.2}$ showing unification of data points

The correlation of extent of attrition in the cyclone can be written as shown below in Equation 4-3 where $u_{cyc,0}$ is the gas inlet velocity at the incipient of breakage, namely "the cyclone transitional velocity".

$$\begin{cases} R = \alpha \frac{H}{K_c^2} c_{cyc} \frac{u_{cyc,in}^3}{d_p \mu^{0.2}} \\ u_{cyc,in} > u_{cyc,0} \end{cases} \quad (4\text{-}3)$$

By exploiting the fitting of the straight line, the intercept with the abscissa gives the cyclone transitional velocity, where attrition is null, as a function of particle size and solids loading, as shown below in Equation 4-4:

$$u_{cyc,0} = \left(\frac{b_{cyc} d_p \mu^{0.2}}{\alpha \frac{H}{K_c^2} c_{cyc}} \right)^{-\frac{1}{3}} \tag{4-4}$$

4.3 CFD-DEM Work

4.3.1 Literature Review

Factors contributing to cyclone attrition are the particle dynamics in combination with the particle physical properties. Coupling the dynamics of particle motion in a certain system with a single particle breakage model can give an estimate of the overall attrition. This approach was proposed by Ghadiri and Boerefijn, (1996) who predicted the attrition of FCC catalysts induced by a single jet in a fluidised bed. The same approach is used by Fries et al. (2013); they evaluated the growth rate by agglomeration in a fluidised bed granulator by extrapolating the particle impact velocity and frequency, respectively, using CFD-DEM simulations.

Computational modelling has been used extensively to characterise the flow inside cyclones with fair agreement in predicting the fluid behaviour, (Safikhani et al. 2010). Many articles are available on CFD simulations of cyclones, (Raoufi et al. 2009; Gao et al. 2019; Elsayed and Lacor, 2010), few on 4-way coupled CFD-DEM simulations, (Chu et al. 2009; Chu et al. 2011; Wei et al. 2017). The majority of studies are based on one-way or two-way coupling and therefore limited to dilute systems, (Derksen, 2003; Derksen et al. 2008; Elsayed and Lacor, 2016; Mousavian et al. 2009; Park et al. 2012).

The main focus of the works mentioned above is the understanding of the behaviour of such complex systems, so spherical particles are usually used, and the fluid is treated as incompressible. By introducing the particles, the pressure drop reduces because the tangential velocity, and thus the turbulences, is reduced, (Bernardo et al. 2006). Therefore

even at low solids loading the presence of the particles might affect the fluid dynamic, (Derksen et al. 2008).

When the concentration of particles is high or when the emphasis of the study is on the particles micro-behaviour, then particle-particle interactions should also be taken into account. In this case, the global interaction between continuous and discontinuous phase is more pronounced and so are the inter-particles interactions, (Chu et al. 2011). This means that particle-particle collisions might become more and more significant to the overall attrition. It should be noted though that the average force acting on a single particle decreases because of the reduction in kinetic energy.

In this work, the focus is on the particle-wall and particle-particle interactions to better elucidate the underlying dynamics leading to attrition, thus 4-way coupled CFD-DEM simulations are used here to simulate the dynamics of F-CLC particles in a high efficiency Stairmand cyclone, (Haig et al. 2014).

Chu et al. (2011) studied the effect of the solids loading in a cyclone and concluded that the highest collision intensity is found at the opposite of the cyclone entrance at all loadings. This agrees with what was found experimentally by Reppenhagen and Werther, (2000). Past this region, the authors also found high particle-wall interactions in the conical region, because of the building solids concentration, and in particular a higher sliding distance at low solids loading, as shown in Figure 4-14. This is, on the other hand, in disagreement with Reppenhagen and Werther, (2000) as they have observed experimentally that particle-wall interactions are significant at the opposite of the cyclone entrance and the cylindrical body.

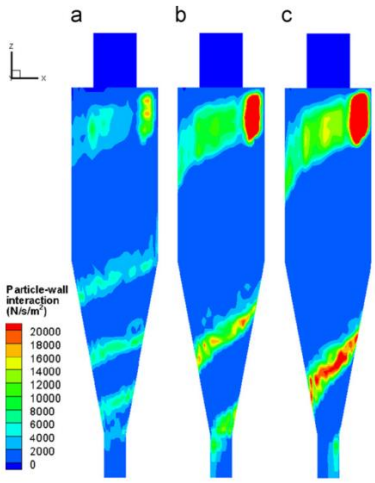

Figure 4-14. Particle-wall time-averaged collision intensity under different solids loadings: (a)0.5; (b)1.5; (c)2.5 (Chu et al. 2011)

4.3.2 Motivation and Objectives

Computational approaches have proven to be an efficient mean to understand the particle dynamics in cyclones. They dictate attrition along with the particle physical and mechanical properties. The authors mentioned in the previous section remark the significant impact of the solids loading on the number of turns that the particles perform before exiting and on the magnitude of particle-wall interactions. Yet, this effect has not been fully assessed and explicitly related to particle attrition. Also, the effect of particle-particle interactions at increasing solids loading has not been considered as a potential source of attrition. In this section, the relative contributions of different regions towards particle attrition from any source, as given by CFD-DEM simulations, is quantified with the aim of gaining an understanding of the particle dynamics in a cyclone.

4.3.3 CFD-DEM Background

The Computational Fluid-Dynamics (CFD) is a method for solving on the computer momentum, mass and energy equations for fluids by numerical algorithms while, the computational study of distinct bodies is achieved by the implementation of Discrete Elements Method (DEM). This method is based on the equations of motion for individual bodies and their explicit numerical integration; in such systems many different interactions are relevant, including particle-particle and particle-wall interactions.

The CFD-DEM is the combination of these techniques. It is used to simulate multiphasic flow field and, in particular, the particle motion when there is a strong interaction with

the fluid. The way CFD and DEM are combined together can be of different kind and referred to as "coupling", as shown in Figure 4-15.

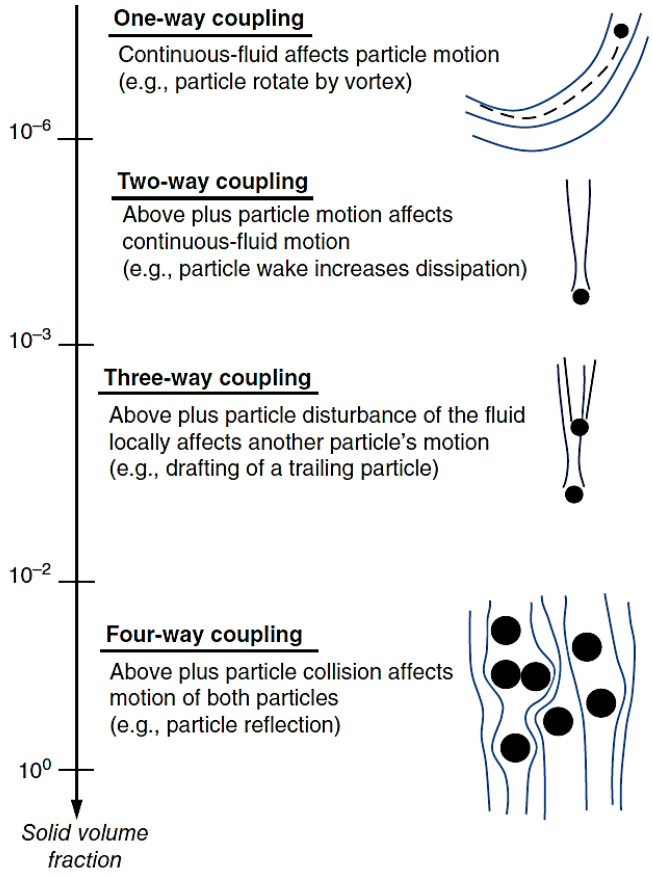

Figure 4-15 Coupling types, as indicated by **(Norouzi et al. 2016)**

The type of coupling chosen depends on the strength of the mutual interaction between the two phases. A dimensionless group, defined as the "momentum coupling number", helps indicating the type of coupling needed, (Norouzi et al. 2016). The momentum coupling number Π_m is defined as follows, Equation. 4-5:

$$\Pi_m = \frac{\text{Total drag force due to the solid phase}}{\text{Convective momentum flux of the fluid phase}} = \frac{C_{solids}}{1+St_m} \qquad (4\text{-}5)$$

where C_{solids} is the solids concentration and St_m is the particle Stokes number defined, as shown in equation 4-6:

$$St_m = \frac{\text{Momentum response time of the particle}}{\text{Characteristic time of the fluid flow field}} \qquad (4\text{-}6)$$

The momentum coupling number is much lower than 1 either when the solids concentration is low and/or the particle size is small due to their immediate response with the fluid velocity. In this instance, the fluid-dynamics resolution of the system is carried out separately before solving the particles motion (one-way coupling): i.e. the fluid affects the solids motions but not vice versa.

On the other hand, when the momentum coupling number is much higher than 1, the fluid dynamic does not affect the solids motion. This occurs either at high solids concentrations and/or when the particles response time is much higher than the fluid characteristic time. In this case the resolution of the solids dynamic can be separately carried out before solving the fluid-dynamic.

The most generic case is an interacting system where the fluid flow field and the particles motion cannot be calculated separately. In this case, the form of the fluid conservation equations changes to account for the solids-fluid exchange terms. No significant heat and mass transfer as well as reactions are present in the analysed case, the main equations will be the continuity and momentum conservation.

The flow regime inside cyclones is usually turbulent and, in this case, the resolution of the conservation equations is achieved by describing an average behaviour by means of the Reynolds-Averaged Navier Stokes model (RANS) along with a turbulence model instead of the classic NS equations, (Wilcox, 1993). The reason being the great difficulty into accounting for the exact fluctuations of properties caused by the turbulent flow regime.

The fluid mass conservation on a fixed quasi-infinitesimal volume, in the presence of solids material, leads to Equation 4-7, (Norouzi et al. 2016):

$$\frac{\delta \rho_f \varepsilon_f}{\delta t} = -\vec{\nabla} \cdot \left(\rho_f \varepsilon_f \vec{u} \right) \tag{4-7}$$

The equation states that the accumulation of the fluid inside the control volume, per unit of volume, $\frac{\delta \rho_f \varepsilon_f}{\delta t}$, has to be equal to the net entering gas flowrate per unit of volume given by $-\vec{\nabla} \cdot \left(\rho_f \varepsilon_f \vec{u} \right)$.

The momentum conservation for the fluid phase on a fixed quasi-infinitesimal volume, in the presence of solids material, leads to Equation 4-8, (Norouzi et al. 2016):

$$\frac{\delta\rho_f\varepsilon_f\vec{u}}{\delta t}+\vec{\nabla}\cdot\left(\rho_f\varepsilon_f\vec{u}\vec{u}\right)=-\varepsilon_f\nabla P-\varepsilon_f\vec{\nabla}\cdot\underline{\underline{\tau_f}}+\rho_f\varepsilon_f\vec{g}-\vec{f}_{f-s} \quad (4\text{-}8)$$

where the terms are, on a volume base:

- $\frac{\delta\rho_f\varepsilon_f\vec{u}}{\delta t}$, the accumulation of the momentum
- $\vec{\nabla}\cdot\left(\rho_f\varepsilon_f\vec{u}\vec{u}\right)$, the advective momentum transport term
- $\varepsilon_f\nabla P$, the momentum change induced by the pressure gradients
- $\varepsilon_f\vec{\nabla}\cdot\underline{\underline{\tau_f}}$, the momentum change induced by viscous and turbulent stresses
- $\rho_f\varepsilon_f\vec{g}$, the gravity or sum of external forces
- $\vec{f}_{f-s}$, force exerted by the fluid on the solid phase.

The main differences of Equation 4-8 with the classical RANS are the presence of (i) the term $\vec{f}_{f-s}$ which is the direct effect of the solids presence in the system, and (ii) the fluid volume fraction ε_f. The fluid stress tensor, $\underline{\underline{\tau_f}}$, because of the turbulences, includes the Reynolds stresses in the three directions $\left(\rho_f u_i' u_j'\right)$. The turbulence model is needed here to link these new six independent unknowns to the mean flow variables.

Several turbulence models are based on the Boussinesq hypothesis, i.e. the Reynolds stresses are treated as the viscous stresses by introducing the concept of eddy viscosity. The turbulence models based on Boussinesq hypothesis are found to not be able to predict correctly the fluid flow field in cyclones, (Hoekstra et al. 1999), while the Reynolds Stress equation model is widely used to predict curve swirling flows and capture the anisotropy of the fluid flow field, (Kozołub et al. 2017; Sommerfeld and Ho, 2003; Chu et al. 2011).

Generally two methods can be used for the computation of the fluid-particle interaction, (Norouzi et al. 2016): (i) the resolved Surface CFD-DEM and (ii) the unresolved Surface CFD-DEM. In the former case, the fluid-particle interaction is directly calculated by integrating the stress tensor around the particle surface, so the fluid cell size has to be very small, several times smaller than the particle itself. This demands a high

computational cost that does not allow to simulate more than few hundred particles (Norouzi et al. 2016). In this work, this procedure is not feasible. Using the latter approach, $\vec{f}_{f-s}$ is computed by the use of semi-empirical correlations. In this way, the local values of the properties around the particles are not needed. Equation 4-8 is used to obtain average behaviour of the fluid properties in the fluid cell and not local values. In this case, if the cell-size of the fluid is too small, the average will be not meaningful: the rule of thumb is 2-3 times the particles diameter, (Müller et al. 2009). At the same time, if the fluid cell size is too large, the fluid resolution would lose accuracy.

The force exerted by the fluid on the solid phase, $\vec{f}_{f-s}$, is generally subdivided into three parts, (Norouzi et al. 2016), as shown in Equation 4-9, where $N_{p,cell}$ is the number of particle in the fluid cell and V_{cell} the volume of the latter:

$$\vec{f}_{f-s} = \frac{1}{\delta V_{cell}} \sum_{i=1}^{N_{p,cell}} \left(\vec{F}_i^{d} + \vec{F}_i^{u} + \vec{F}_i^{l} \right) \tag{4-9}$$

where

- $\vec{F}_i^{d}$ is the steady drag force exerted by the fluid on the particles when the flow is steady
- $\vec{F}_i^{u}$ is the unsteady drag force caused by the evolution in time of the boundary layer around the particles
- $\vec{F}_i^{l}$ is the lift force caused by the fluid pressure gradient around the particle, because of the non-homogeneous fluid velocity field around it.

Particle positions and velocity field are needed to solve the fluid equations: this is done by the DEM solver. DEM is based on the application of Newton's laws of motion. By assuming that the mass of the particle does not change, the equations of the single i-th particle can be expressed as follows:

-translation, Equation 4-10

$$\vec{F}_i = m_i a_i = m_i \frac{d\vec{v}_i}{dt} = m_i \frac{d^2\vec{s}_i}{dt^2} \tag{4-10}$$

-rotation, Equation 4-11

$$\vec{M}_i = I_i \alpha_i = I_i \frac{d\vec{\omega}_i}{dt} = I_i \frac{d^2\vec{\varphi}_i}{dt^2} \quad (4\text{-}11)$$

where:

- $\vec{F}_i$ is the resultant of all forces acting on the i-th particle
- m_i is the mass of i-th particle
- $\vec{a}_i$ is the particle acceleration that can be expressed as the time derivative of the velocity, $\frac{d\vec{v}_i}{dt}$, or the time second derivative of the position vector, $\frac{d^2\vec{s}_i}{dt^2}$
- $\vec{M}_i$ is the resultant of all torques acting on the i-th particle
- I_i is the moment of inertia of i-th particle relative to an axis passing through the centre
- α_i is the particle angular acceleration that can be expressed as the time derivative of the angular velocity, $\frac{d\vec{\omega}_i}{dt}$,or the second time derivative of the angular position, $\frac{d^2\vec{\varphi}_i}{dt^2}$

Forces and torques generally do not only depend on the properties of the considered particle but also on the values describing the state of the other particles and the fluid, thus, according to Norouzi et al. (2016), for a particle "i", they are expressed as shown in Equation 4-12 and Equation 4-13, respectively:

$$\vec{F}_i = \sum_{j \in C} \vec{F}_{i-j} + \vec{F}_{fluid-i} + \vec{G} \quad (4\text{-}12)$$

$$\vec{M}_i = \sum_{j \in C} \left(\vec{M}^t_{i-j} + \vec{M}^r_{i-j} \right) + \vec{M}^{f-p}_i \quad (4\text{-}13)$$

where:

- $\sum_{j \in C} \vec{F}_{i-j}$ is the resultant of particle-particle interactions
- $\vec{F}_{fluid\text{-}i}$ is the force exerted by the fluid on the particle
- $\vec{G}$ is the resultant of external field forces, the gravitational force in this case
- $\sum_{j \in C} \left(\vec{M}^t_{i-j} + \vec{M}^r_{i-j} \right)$ is the resultant of tangential torques applied on the i-th particle by collision with the other j-th particle and the opposing rolling resistant torques

- $\vec{M}_i^{f-p}$ is the rotational drag of the fluid on the particle
- C is the total number of particles interacting with the i-th particle.

The fluid-particle force $\vec{F}_{fluid\text{-}i}$ can be expressed as follows, Equation 4-14:

$$\vec{F}_{flud-i} = \vec{F}_i^d + \vec{F}_i^u + \vec{F}_i^l \tag{4-14}$$

which terms are presented in Equation 4-9.

In the most common two-phase flow systems, a single particle can undergo multiple collisions and the time during which a particle collides is not negligible; for these systems, the soft sphere model is used. The soft sphere model is based on the assumption that particles are never permanently deformed, and the contact forces are well described by force-displacement laws (or contact models) which link the displacement to the physical and kinematic parameters of the colliding bodies, (Norouzi et al. 2016).

Generally, particle interactions may be of different nature. In this work only physical non-cohesive/adhesive interactions are considered (given the relatively large size of the particles simulated). The physical interaction, as dictated by the contact model, causes a deformation of the contacting surfaces. Deformation is opposed by an elastic force which, at its peak, causes the rebounding of the two particles in order to re-establish the condition of no-deformation. It should be noted that the elastic deformation does not actually occur, but rather it is described as the overlap between the particle original geometries.

Both forces and overlaps have normal and tangential components. The normal direction is the one linking the two centres of the particle while the tangential direction is perpendicular to the normal at the contact point. The overlap corresponding to the normal deformation is called normal overlap, δ_n, and is defined as the variation of the distance between the centres of the two particles along the normal direction, Equation 4-15:

$$\delta_n = r_{p,i} + r_{p,j} - \left|\vec{x}_j - \vec{x}_i\right| \tag{4-15}$$

r_p is the radius of the spherical particle and $\vec{x}$ is the position vector of the centre where the subscripts identify the i-th and the j-th particle. On the other hand, the tangential overlap, δ_t, is caused by the tangential component of velocity once the particles are in normal overlap. If t_0 is the initial time, when the particles are in contact only through a contact point, the tangential overlap will be given by Equation 4-16:

$$\delta_t = \int_{t_0}^{t} v_{ij}^t dt \tag{4-16}$$

where v_{ij}^t is the tangential component of the relative velocity.

The collision force is expressed as the sum of normal and tangential component as follows, Equation 4-17:

$$\vec{F}_{ij} = \vec{F}_{ij}^n + \vec{F}_{ij}^t \tag{4-17}$$

For the third law of motion, Equation 4-18:

$$\vec{F}_{ij} = -\vec{F}_{ji} \tag{4-18}$$

Where $\vec{F}_{ij}$ is the force exerted by the i-th particle on the j-th particle.

Analytically, a contact model is an expression that links the force to the displacement, usually in the following form, Equation 4-19, Equation 4-20 and Equation 4-21:

$$\vec{F}_{ij}^n = \vec{F}_{ij}^{n,el}(\delta_n) + \vec{F}_{ij}^{n,dis}(\delta_n, v_{ij}) \tag{4-19}$$

$$\vec{F}_{ij}^t = \vec{F}_{ij}^{t,el}(\delta_t, \vec{F}_{ij}^n) + \vec{F}_{ij}^{t,dis}(\delta_t, \vec{F}_{ij}^n, v_{ij}) \tag{4-20}$$

$$\vec{M}_{ij}^r = \vec{M}_{ij}^{r,el}(\vec{\omega}_{ij}, \vec{F}_{ij}^n) + \vec{M}_{ij}^{r,dis}(\vec{\omega}_{ij}, \vec{F}_{ij}^n) \tag{4-21}$$

where each force and torque are seen as the sum of an elastic and a dissipative term, indicated respectively, with the suffix “el” and “dis”; the latter is responsible for the transformation of the elastic energy into heat. The explicit numerical integration of the laws of motion gives the trajectories and the velocity field of the particles; it usually consumes the major computational energy because it requires a very small time-step. The choice of the time-step is subjected to some limitations according to Rayleigh criterion, (Burns and Hanley, 2017), as it will be discussed later on. A single time-step of the particle does not significantly affect the fluid resolution, so several particle time-steps can be performed for each fluid time step. At the beginning of the fluid time step, information about particle positions and velocity field is taken from the DEM solver and passed onto the CFD solver, the inter-phase forces are calculated so the fluid dynamics is solved; in the following step the new data and forces are used by the DEM software to solve the particle motion and calculate the new positions and velocity field.

4.3.4 Turbulence model

The selection of the turbulence model is critical in the fluid resolution. A perfect turbulence model does not exist so different models have to be tested in order to find the one that best describes the actual behaviour. In the case of cyclones, researchers have applied different turbulence models for CFD and CFD-DEM simulations; Large Eddy Simulation (LES) and Reynolds Stress equation Model (RSM) are largely suggested for strongly swirling flows and anisotropic behaviour, as compared to other models based on the definition of the eddy viscosity such as k-ε and k-ω, (Raoufi et al. 2009; Elsayed and Lacor, 2016; Park et al. 2012; Chu et al. 2009). In this work, RSM is used, given its lower computational cost as compared to LES.

In Reynolds Stress equation Model, each of the six independent components of the Reynolds stress tensor is calculated using its transport equation, where diffusion, production and dissipation terms are present. The transport equations for the Reynold stresses are obtained by manipulating the NS equations, but new 22 unknowns are generated.

A general way to represent the transport equations for the Reynolds stresses is the following, Equation 4-22, (ANSYS Inc, 2014):

$$\frac{\delta\left(\rho_f u_i' u_j'\right)}{\delta t} + C_{ij} = D_{T,ij} + D_{L,ij} + P_{ij} - \Phi_{ij} + \Sigma_{ij} + F_{ij} \tag{4-22}$$

where:

- C_{ij} is the advective transport term
- $D_{T,ij}$ is the turbulent diffusion transport term
- $D_{L,ij}$ is the molecular diffusion transport term
- P_{ij} is the stress production
- Φ_{ij} is the pressure strain
- Σ_{ij} is the dissipation term
- F_{ij} is the production by system rotation.

The terms C_{ij}, $D_{L,ij}$, P_{ij} and F_{ij} do not introduce new unknowns while $D_{T,ij}$, Φ_{ij} and Σ_{ij} need to be modelled to reduce the number of unknowns. Several assumptions allow to express them as a function of the mean flow field variables, except for Σ_{ij} which is obtained by its transport equation. As a result, 7 new transport equations have to be solved in order to obtain a solution for the flow field in the turbulent regime.

The use of the RSM will be validated, for the present work, by comparing the experimental pressure drop with that predicted by the simulation. Of course, this does not imply validation of the flow field inside the cyclone, but real validation of the RSM model for cyclones has already been carried out by other authors, (Balestrin et al. 2017; Fraser et al. 1997) who compared the local rather than global behaviours.

When the CFD resolution is coupled with the DEM, the RSM have to be changed in order to take into account the presence of solids in the system by introducing the fluid volume fraction as well as the interaction between the continuous and discrete phase. The modified RSM is then referred to as "RSM Dispersed Turbulence Model", (ANSYS Inc., 2013).

4.3.5 Contact Models

The CFD-DEM simulations are carried out by the coupling of a CFD solver (ANSYS FLUENT ® V18/19) with a DEM solver (EDEM® 2017/2018).

The models reported below are the contact models that describe particle-particle and particle-wall physical contacts. They are already implemented in the software EDEM®.

4.3.5.1 Normal Force

The Hertz model of elastic contact deformation is commonly used for the normal component of the contact. Hertz studied the contact between perfectly elastic spheres, (Dintwa et al. 2008; Hertz, 1881; Thornton and Ning, 1998), assuming that: (i) the contact surfaces only undergo normal forces caused by collision and they are very small respect the total body surface, (ii) the material is isotropic and linearly elastic in nature, (iii) the contact is frictionless and causes only slight deformations as compared to the radius of the spheres. With these assumptions and positioning the origin of the system in the first

contact point, Hertz formulated an ellipsoidal distribution of the pressure on the contact area and proposed the following equation for the normal force:

$$F_{ij}^{n,el} = \frac{4}{3} E^* \sqrt{r^*} \delta_n^{\frac{3}{2}} \equiv K_{Hertz} \delta_n^{\frac{3}{2}} \tag{4-23}$$

where K_{Hertz}, E^* and r^* are the nonlinear Hertzian-spring stiffness, the effective Young's modulus and the effective radius, respectively. The latter two are defined as shown below in Equation 4-24 and Equation 4-25:

$$\frac{1}{E^*} = \frac{1-\nu_i^2}{E_i} + \frac{1-\nu_j^2}{E_j} \tag{4-24}$$

$$\frac{1}{r^*} = \frac{1}{r_{p,i}} + \frac{1}{r_{p,j}} \tag{4-25}$$

$E_{i/j}$, $\nu_{i,j}$ and $r_{p,i/j}$ are Young's modulus, Poisson's ratio and the radius of the i/j-th colliding particle, respectively. This force is valid only for the linear component of the normal collision force, while the dissipative viscous force, $\vec{F}_{ij}^{n,dis}$, is defined according to Tsuji et al. (1992) as shown in Equation 4-26:

$$F_{ij}^{n,dis} = \eta_n \delta_n^{\frac{1}{4}} \left(\vec{v}_{ij} \cdot \vec{n}_{ij} \right) \tag{4-26}$$

Thus, the normal collision force can be expressed as the sum of the Hertzian contribution and dissipative (or damping force), according to Equation 4-19, as shown below in Equation 4-27:

$$\vec{F}_{ij}^{n} = \vec{F}_{ij}^{n,el} + \vec{F}_{ij}^{n,dis} = -\left(\frac{4}{3} E^* \sqrt{r^* \delta_n^{\frac{3}{2}}} \right) \vec{n}_{ij} - \left[\eta_n \delta_n^{\frac{1}{4}} \left(\vec{v}_{ij} \cdot \vec{n}_{ij} \right) \right] \vec{n}_{ij} \tag{4-27}$$

The typical damping factor of the model η_n is usually expressed in terms of particle properties and the normal restitution coefficient e_n, as shown in Equation 4-28, (Tsuji et al. 1992; EDEM, 2014).

$$\eta_n = -\frac{2.236 \ln(e_n)}{\sqrt{(\ln(e_n))^2 + \pi^2}} \sqrt{m^* K_{Hertz}} \tag{4-28}$$

where e_n is the ratio between the impact normal relative velocity and that of rebound given in Equation 4-29 and m^* is defined by Equation 4-30:

$$e_n = -\frac{\vec{v}_{ij,imp} \cdot \vec{n}_{ij}}{\vec{v}_{ij,rbnd} \cdot \vec{n}_{ij}} \tag{4-29}$$

$$m^* = \left(\frac{1}{m_i} + \frac{1}{m_j} \right)^{-1} \tag{4-30}$$

4.3.5.2 Tangential force

The no-slip Mindlin model is used for the tangential component of the contact (EDEM 2.6 Theory Reference Guide), presented in Equation 4-17. This model was developed by Mindlin, (1949). Consistently with the definition given in Equation 4-20, the tangential component of the contact force is composed of an elastic and dissipative component. The elastic component is assumed to be proportional to the tangential overlap as follows, Equation 4-31:

$$F_{ij}^{t,el} = 8G^* \sqrt{r^* \delta_n} \delta_t \equiv K_t \delta_t \tag{4-31}$$

where K_t is the tangential stiffness, expressed as a function of the normal overlap as shown above in Equation 4-31; the tangential overlap is calculated according to Equation 4-16 and the effective radius r^* is evaluated using Equation 4-25, and G^* is the effective shear modulus, defined in Equation 4-32:

$$\frac{1}{G^*} = \frac{1-\nu_i^2}{G_i} + \frac{1-\nu_j^2}{G_j} \tag{4-32}$$

where $G_{i/j}$ are the shear moduli of the i-th and j-th particles.

The dissipative component is assumed to be proportional to the tangential component of the relative velocity ($\vec{v}_{ij} \cdot \vec{t}_{ij}$). Its expression is quite similar to the normal damping force, Equation 4-33:

$$\vec{F}_{ij}^{t,dis} = -\eta_t \left(\vec{v}_{ij} \cdot \vec{t}_{ij} \right) \vec{t}_{ij} \tag{4-33}$$

where the characteristic expression of the damping coefficient is given by Equation 4-34:

$$\eta_t = -\frac{1.826 \ln(e_n)}{\sqrt{(\ln(e_n))^2 + \pi^2}} \sqrt{m^* K_t} \tag{4-34}$$

According to Coulomb's criterion, the no-slip condition is only verified when the magnitude of the tangential force is less than μ_s times the magnitude of the normal force as shown in Equation 4-35, (Cundall and Strack, 1979):

$$\left|\vec{F}_{ij}^{t}\right| \le \mu_s \left|\vec{F}_{ij}^{n}\right| \tag{4-35}$$

where μ_s is the coefficient of static friction. For this critical value, $\mu_s \left|\vec{F}_{ij}^{n}\right|$, slipping occurs.

4.3.5.3 Torque

During a collision, the tangential component of the particle velocity gives rise to an angular acceleration. If the total contact force is $\vec{F}_{ij}^{c}$, then the torque caused by its tangential contribution is given by Equation 4-36:

$$\vec{M}_{ij}^{t} = r_i \vec{n}_{ij} \times \vec{F}_{ij}^{c} \tag{4-36}$$

In addition to this torque, for simulations in which rolling friction is important, a rolling resistance to the contacting surfaces must be considered. This is accounted for by applying a resistant torque, $\vec{M}_{ij}^{r}$. In this work, a constant resistant torque, as implemented in EDEM®, is used. Following DEM Solutions, (2014b), this is assumed to be proportional to the normal force as follows, Equation 4-37:

$$\vec{M}_{ij}^{r} = -\mu_r \left|\vec{F}_{ij}^{n}\right| r^{*} \frac{\vec{\omega}_{ij}}{\left|\vec{\omega}_{ij}\right|} \tag{4-37}$$

where the relative angular velocity $\vec{\omega}_{ij}$ is calculated according to Equation 4-38

$$\vec{\omega}_{ij} = \vec{\omega}_i - \vec{\omega}_j \tag{4-38}$$

And μ_r is coefficient of rolling friction, $\left|\vec{F}_{ij}^{n}\right|$ is the magnitude of the normal contact force and r^{*} is the effective rolling radius calculated based on Equation 4-25.

The reason behind the minus sign of Equation 4-37 is because the rolling resistance is always opposed to the relative angular velocity.

4.3.6 Particles-Fluid Interactions

The estimation of the particle fluid interactions is carried out through semi-empirical models. It needs to be considered that not all the forces acting on the particles have the

same relevance because the medium is air and its density and viscosity are relatively small at the working conditions, (Chu et al. 2011; Wei et al. 2017). For instance, the unsteady drag force, $\vec{F}_i^{u}$, due to the evolution of the boundary layer thickness around the particle, can be neglected because of the small thickness of the gas boundary layer and the low density of the gas. Moreover, the lift force, $\vec{F}_i^{l}$, caused by the non-homogeneous fluid velocity field around particle, is neglected because of (i) the low fluid viscosity, (ii) the absence of very high velocity gradients around the particles and (iii) not extreme angular velocities of the particles. The most relevant force that has to be modelled is then the steady drag force, $\vec{F}_i^{d}$. Generally, two approaches are used to model the drag force for solids-fluid systems, (Norouzi et al. 2016):

-correction of the drag force model for isolated particles, like the model of Wen and Yu, (1966);

-packed bed based correlations, like the Ergun's equation, (Ergun and Orning, 1949).

The first approach is more accurate at low solids concentrations while the second one at high solids concentrations. The "Ergun-Wen and Yu correlation" is used here to estimate the drag force acting on the particles, as available in ANSYS FLUENT®. The reason being, the correct evaluation of the drag force in the initial dilute phase as well as the dense phase, which is expected to form in the conical part in proximity of the wall of the cyclone. The model comprises of Wen and Yu equation for a fluid volume fraction higher than 0.8 and Ergun equation otherwise, (ANSYS Inc., 2014). Following what reported by Norouzi et al. (2016), it is common practice to normalize the drag force, $\vec{F}_i^{d}$, by the corresponding force for an isolated sphere in the Stokes flow regime, Equation 4-39:

$$\vec{N}_i^{d} = \frac{\vec{F}_i^{d}}{3\pi\mu_f \varepsilon_f d_{p,i} \left|\vec{w}_i\right|} = \frac{\left|\vec{F}_i^{d}\right|}{3\pi\mu_f \varepsilon_f d_{p,i} \left|\vec{w}_i\right|} \cdot \frac{\vec{w}_i}{\left|\vec{w}_i\right|} \tag{4-39}$$

where $\vec{N}_i^{d}$ is the normalized drag force, $d_{p,i}$ is the particle diameter, $\vec{w}_i$ is the fluid-particle relative velocity defined as follows, Equation 4-40:

$$\vec{w}_i = \vec{u}_{cell} - \vec{v}_{p,i} \tag{4-40}$$

where $\vec{v}_{p,i}$ is the particle velocity and $\vec{u}_{cell}$ is the fluid velocity inside the fluid cell, in which the particle is located.

According to "Ergun-Wen and Yu model", the normalised drag force is expressed according to Equation 4-41:

$$\left|\vec{N}_i^d\right| = \begin{cases} \dfrac{150(1-\varepsilon_f)}{18\varepsilon_f^2} + \dfrac{1.75}{18\varepsilon_f^2}\mathrm{Re}_p & \text{for } \varepsilon_f \le 0.8 \\ \dfrac{C_D}{24}\mathrm{Re}_p\,\varepsilon_f^{-3.65} & \text{for } \varepsilon_f > 0.8 \end{cases} \tag{4-41}$$

while the drag coefficient C_D is given by Equation 4-42:

$$C_D = \begin{cases} \dfrac{24}{\mathrm{Re}_p}\left(1+0.15\mathrm{Re}_p^{0.687}\right) & \text{for } \mathrm{Re}_p \le 1000 \\ 0.445 & \text{for } \mathrm{Re}_p > 1000 \end{cases} \tag{4-42}$$

where Re_p is the characteristic particle Reynolds number defined as shown in Equation 4-43:

$$\mathrm{Re}_p = \frac{\left|\vec{w}_i\right| d_{p,i}\varepsilon_f\rho_f}{\mu_f} \tag{4-43}$$

4.3.7 Analysis of Attrition

In the following CFD-DEM simulations, the spherical particles, do not change their size in the cyclone and do not lead to the formation of other particles (debris). The reason being, the huge computational cost required to simulate the large number of small debris produced and the remarkable interactions that the system would have. A cheaper alternative would be to consider changes in the parameters describing the interactions into the system, such as sliding and rolling friction as well as the attrition parameters. Further investigation is needed in this regard. Moreover, the mother particle size would slightly change after one pass through the cyclone, thus it does not affect the fluid-dynamic of the system. For the reasons mentioned above, the simulations are carried out with mono-dispersed spherical particles and attrition is implemented post-simulation.

As reported in the literature review, particle attrition in cyclones occurs following different mechanisms in different regions. Here, attrition is treated locally dividing the body of the cyclone into regions of interest where different mechanisms of breakage can

be applied based on the particle dynamics. In particular, referring to Figure 4-16, chipping is considered at the entrance regions (Region 1 and Region 2) due to the high velocity particle impact (particle-particle and particle-wall) while surface wear elsewhere (Region 3 - 7) due to particles sliding against the walls towards the bottom outlet. These regions are reported below in Figure 4-16.

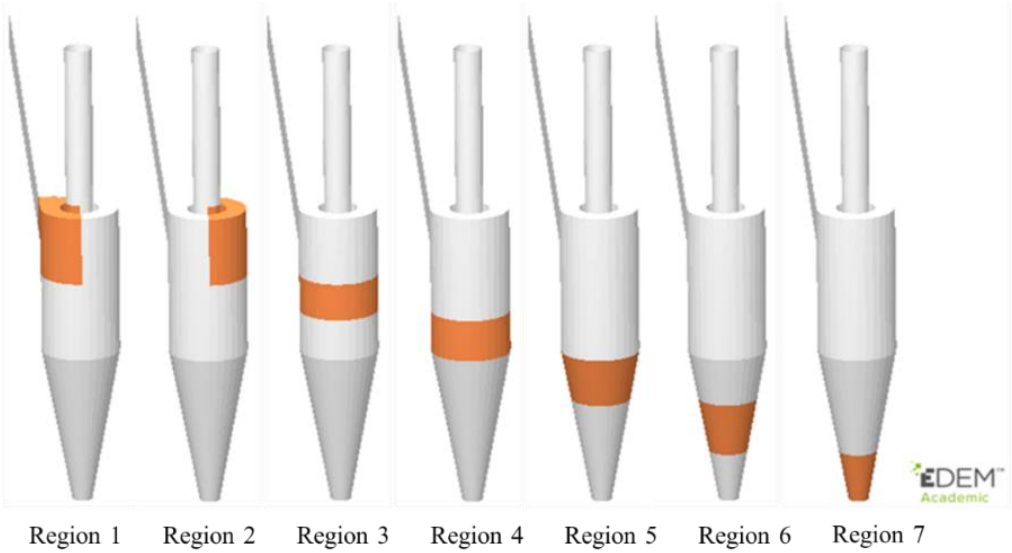

Figure 4-16. Cyclone sub-division in regions of interest

The attrition analysis is carried out using a set of simulation outcomes which are evaluated at each time step, for each region of interest, and under steady state conditions, throughout a fixed observation time. They are listed below:

- the number of particles N_p
- the number of particles actually in contact with the walls $N_{p,w}$ (this is given by the difference of the total number of particles in the region with the total number of particles in an internal region having a gap with the walls equal to the particle size)
- the number of particle-wall (P-W) and particle-particle (P-P) collisions N_{col}
- the single P-W and P-P relative velocity of collision v_p
- the single P-W and P-P normal component of relative collision velocity v_p^n
- the average normal load acting on a particle F^n

the extent of attrition of a k-th region is referred to as R_k while the overall cumulative extent of attrition, R, can be seen as a series of n-attrition events, where n is the total number of regions, as reported below in Equation 4-44.

$$R = 1 - \prod_{k=1}^{n}(1 - R_k) \sim \sum_{k=1}^{n} R_k \tag{4-44}$$

4.3.7.1 Collisional Attrition

Collisional breakage is computed using the chipping model of single particle breakage upon impact developed experimentally for washed F-CLC particles, shown below in Equation 4-45:

$$\begin{cases} R_{chip} = \alpha_{chip} \dfrac{H}{K_c^2} \rho_p d_p v_p^2 \sin\theta \\ v_p > v_{p,0} \end{cases} \tag{4-45}$$

where $v_{p,0}$ is the transition velocity from no-breakage to breakage, Equation 4-46.

$$v_{p,0} = \sqrt{\frac{b_{sp}}{\alpha_{chip} \dfrac{H}{K_c^2} \rho_p d_p \sin\theta}} \tag{4-46}$$

Referring to a k-th region, the extent of attrition by chipping $R_{chip,k}$ can be expressed as the summation of the P-W and P-P contribution, as shown in Equation 4-47. It is here assumed that P-P collisions would lead to the same breakage of a single particle impacting on a fixed rigid target at a velocity equal to their relative impact velocity. According to Ghadiri and Zhang, (2002) the contact force upon impact determines the extent of breakage, therefore the assumption mentioned above holds on the basis that P-P collisions would happen between a slow-moving particle and a faster moving particle. In such case the collision contact force would approach that of a single particle impacting on a fixed target:

$$R_{chip,k} = R_{chip,pw,k} N_{col/p,pw,k} \eta_{col,pw,k} + 2R_{chip,pp,k} N_{col/p,pp,k} \eta_{col,pp,k} \tag{4-47}$$

The equation reported above is evaluated using the steady state values of:

a) collision relative velocity square v_p^2 (present in $R_{chip,pw}$ and $R_{chip,pp}$)

b) angle of collision θ (present in $R_{chip,pw}$ and $R_{chip,pp}$)

c) number of collisions per particle $N_{col/p}$

d) efficiency of collision η_{col}

The last two parameters of the list account for the fact that the particle can undergo respectively, multiple collisions and ineffective collisions (if occurring at velocities below the transition velocity).

Following the order of the previous list:

a) the collision relative velocity square is simply obtained by averaging the square of the collision relative velocities above $v_{p,0}$, throughout the observation time

b) the angle of collision is obtained by averaging the angles of collisions occurring above $v_{p,0}$, throughout the observation time.

   For a single impact, it can be expressed as shown in Equation 4-48:

$$\theta = \arcsin\left(\frac{v_p^n}{v_p}\right) \tag{4-48}$$

c) the number of collisions per particle $N_{col/p}$ is obtained by averaging the number of collisions per particle throughout the observation time.

   For a single time step, it is defined as the ratio of the frequency of collisions ($\dot{N}_{col}$) with the number flow rate of particles entering the cyclone ($\dot{N}_{p,in}$), as shown below in Equation 4-49:

$$N_{col/p} = \frac{\dot{N}_{col}}{\dot{N}_{p,in}} \tag{4-49}$$

   where the frequency of collisions, $\dot{N}_{col}$, is expressed as the number of collisions divided the time step, Equation 4-50:

$$\dot{N}_{col} = \frac{N_{col}}{\Delta t} \tag{4-50}$$

d) The efficiency of collision η_{col} is obtained by averaging the efficiency of collisions throughout the observation time.

For a single time-step, it is defined as the total number of collisions occurring above the transition velocity over the total number of collisions, as shown below in Equation 4-51:

$$\eta_{col} = \frac{N_{col}\big|_{v_p > v_{p,0}}}{N_{col}} \tag{4-51}$$

4.3.7.2 Surface Wear

Breakage by surface wear, caused by particles sliding against the walls, is evaluated using the model of Archard and Charj, (1953), presented in Equation. 3-2 in terms of detached volume as a function of a detachment efficiency factor, the normal load acting on the particle, the travelling distance and the material hardness. Still, referring to a k-th region, the extent of attrition by surface wear $R_{wear,k}$ can be obtained by dividing both sides of the Equation. 3-2 by the particle volume, obtaining Equation 4-52:

$$R_{wear,k} = \alpha_{wear} \frac{F_k^n \Delta s_k}{H} y_k \tag{4-52}$$

It needs to be noted that by expressing the equation in terms of extent of breakage, the constant α_{wear} is no longer less than 1.

The parameter y_k is the steady state fraction of particles actually contributing to wear as in direct contact with the wall, due to probable multilayering at high solids loadings. It is defined according to Equation 4-53:

$$y_k = \frac{N_{p,w,k}}{N_{p,k}} \tag{4-53}$$

while the steady state sliding distance is evaluated as the product of the regional residence time τ_k with the steady state particle velocity $v_{p,k}$, as shown in Equation 4-54:

$$\Delta s_k = \tau_k v_{p,k} \tag{4-54}$$

where the regional residence time, τ_k, is evaluated as the ratio of the number of particles in the region with the number flow rate entering the region, as shown in Equation 4-55:

$$\tau_k = \frac{N_{p,k}}{\dot{N}_{p,in}} \tag{4-55}$$

The constant α_{wear} is unknown. Therefore, this is extrapolated from the experimental data point obtained at 20 m s^{-1} and 0.1 of solids loading for F-CLC particles of 355-400 µm, using the parameters "F^n", "Δs" and "y" given by the simulations. The hardness, "H", needed for Equation 4-52, is evaluated experimentally for several F-CLC particles by means of the nano-indentation technique, as shown in Chapter 2, and equal to 5.2 GPa. The value of α_{wear} is estimated to be 5.38×10^{10}.

4.3.8 Setup and Simulation Conditions

The setup of the CFD-DEM simulations is discussed next, with focus on the geometry, meshing, criterion of convergence, particle and fluid properties, boundary conditions, time step and studied conditions.

4.3.8.1 Cyclone Geometry

The geometry of the cyclone is that used for the experimental tests, Figure 4-4, given by Haig et al. (2014). The geometry is reported schematically in Figure 4-17.

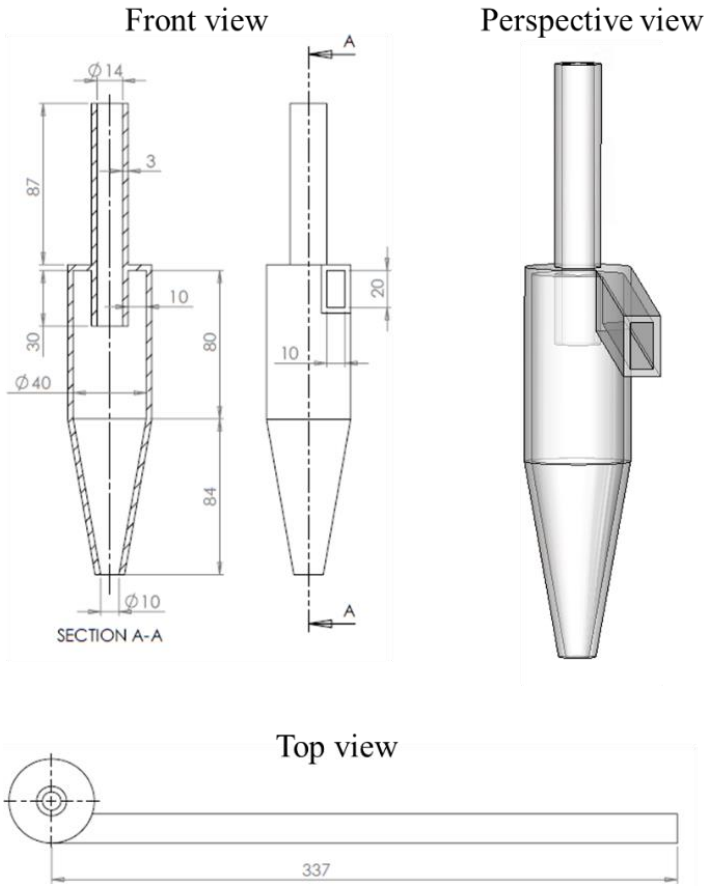

Figure 4-17. Cyclone geometry: front, perspective and top view. Units in [mm].

4.3.8.2 Cyclone Meshing

To ensure an appropriate volume fraction of the cell, a cell size of at least 2-3 times the particle size should be used. In this case, the meshing has been quite challenging, given the relatively small dimension of the cyclone and the relatively large particles, in the range of [180-400] μm, especially considering that in the conical part the cells tend to be smaller because of the reduced section. For these reasons, a hexahedral structured mesh with cells aligned with the cyclone circumference is used. This allows to have a better fluid resolution with a smaller number of cells, (Slack, 2012).

The type of mesh adopted is the so-called butterfly mesh where a square core is surrounded by a hexahedral mesh which adapts to the geometry. Moreover, the body is subdivided into 14 zones meshed independently in order to keep control on the cell size, as reported in Figure 4-18, using Fluent Meshing Tool®.

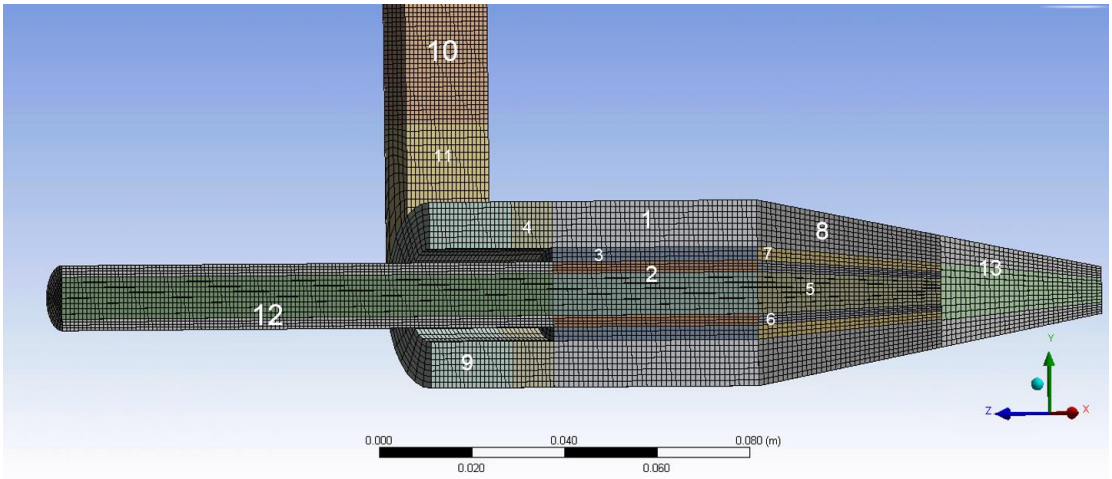

Figure 4-18. Internal structure of the mesh

The conical body, being defined as an independent part of geometry, is connected with the rest by means a fluid interface where the CFD solver interpolates among their nodes.

The basic mesh used here is made of 112832 hexahedral cells. Other two meshes are obtained by consecutive refinement of the previous one for the sake of the mesh independency analysis.

Three meshes with different number of elements are produced by this procedure in order to test the mesh independency of the results. The details of the three meshes are reported in Table A-1.

4.3.8.3 Methods and convergence criterion

High order discretisation schemes are used for the equations. The hexahedral mesh allows to use the "Quadratic Upwind Interpolation scheme for Convective Kinematics" (QUICK) that is a weighted average of a second order upwind scheme and a central scheme.

For the continuity equation, the PREssure STaggering Option (PRESTO) is used, as suggested by Slack, (2012), in order to better capture the expected high radial pressure gradients. The convergence criterion used here is the decrease of the normalised scaled residuals, as defined in Fluent, of three orders of magnitude. The initial iterations are carried out using the steady state solver, after which it is switched to transient, using a time step less than 1% of the fluid residence time, (Slack, 2012). Four-way coupling with the DEM solver is introduced by enabling the Dense Discrete Phase Model (DDPM)

which allows to account for the presence of the solids, by introducing the fluid volume fraction, into the Reynolds Averaged NS. Moreover, the Node Based Averaging is enabled to smoothen out the distribution of variables in the fluid resolution grid by mean of a Gaussian distribution with a width factor equal to 6, as defined in the Fluent User Guide, (ANSYS Inc., 2013).

4.3.8.4 Particle and fluid properties

For the present work, the P-P and P-W contact properties, such as coefficient of restitution and sliding friction are taken from the work on iron ore particles of Li et al. (2004) and Lu, (2015), respectively. The rolling friction coefficient is set to be relatively high, 0.5, because of the irregular shape of the particles, as suggested by Lu, (2015). No sensitivity analysis is carried out on the effect of these parameters, thus further studies are needed in this regard. The stiffness of the particles is often reduced from the real material properties to increase the time step in case of dry, non-adhesive and relatively coarse particles where only the contact force is dominant, (Kobayashi et al. 2013; Hærvig et al. 2017; Chu et al. 2011). Therefore, here, the particle Young's modulus is set to 10^7 Pa, as compared to the value calculated by nano-indentation equal to $2X10^{11}$ Pa, in order to use a larger time-step.

Because of the low absolute pressure change, the fluid properties can be considered to be uniform in the fluid domain and incompressible.

All the parameters are reported below in Table 4-3.

Table 4-3. Particle and fluid parameters used in the CFD-DEM simulations

Description	**Value**	**Unit**
Particle and wall properties		
Particle density	3300	kg m^{-3}
Particle diameters	[196, 231, 265, 327.5, 377.5]	µm
Particle Young's modulus	10^7	Pa
Particle Poisson's ratio	0.30	-
Steel density	7800	kg m^{-3}
Steel Young's modulus	$2X10^{11}$	Pa
Steel Poisson's ratio	0.30	-
Particle and wall contact properties		
Particle-Particle restitution coefficient	0.40	-
Particle-Particle friction coefficient	0.60	-
Particle-Particle rolling friction coefficient	0.50	-
Particle-Wall restitution coefficient	0.35	-
Particle-Wall friction coefficient	0.50	-
Particle-Wall rolling friction coefficient	0.50	-
Fluid properties (air)		
Density	1.225	kg m^{-3}
Viscosity	$1.789X10^{-5}$	Pa s

4.3.8.5 Boundary Conditions

The boundary conditions for the fluid are listed below:

a) no-slip wall boundary condition
b) fixed inlet velocity at the entrance of the inlet pipe
c) the closed-wall/no-slip condition at the bottom outlet
d) the pressure outlet at the exit of the vortex finder

Along with the inlet velocity, the turbulence intensity and the hydraulic diameter of the inlet section are computed according to the definition provided by ANSYS Inc., (2014). About the last two points of the list (c and d), the bottom outlet can be approximated to a closed-wall due to obstructive effect of the catch-pot and the apex cone used in the actual system. Scalable wall functions are used for the near-wall treatment in order to have a

good resolution regardless of the position of the computational cells next to the wall (ANSYS Inc., 2014).

At the fluid outlet, a uniform constant gauge pressure is fixed to 0 Pa; the absolute pressure does have any effect on the fluid properties, having considered incompressible gas. The length of the vortex finder is kept very large in order to have a minimum effect of the boundary condition of point "d" on the fluid dynamics inside the domain of interest.

Consistent with the configuration of the actual system, the cyclone pressure drop is evaluated between the sections "B" and "C", as shown in Figure 4-19 in terms of surface weighted average.

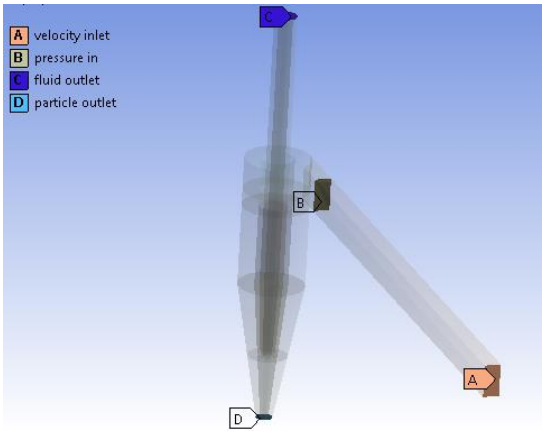

Figure 4-19. Main boundary sections

The initial condition in the cyclone is the steady state fluid flow-field without solids. The particles are generated in random positions in a fixed volume in proximity of the section "A", next to the gas inlet. The initial particle velocity will be set to 0 m s^{-1}, in order to replicate the experimental condition. The solids loading is achieved by fixing the solids generation rate in EDEM®. When the particles reach the bottom outlet, they escape the system, likewise if they reach the fluid outlet, but this is not expected.

4.3.8.6 Time step

The movement of a single particle within an assembly of particles is not only affected by the forces and torques originated by contacts with its immediate neighbouring particles, but also by disturbance propagations from particles not directly in contact. The particle displacement calculation, carried out within the time step, should be such that the disturbance wave does not propagate further than the immediate neighbour particle,

(Cundall and Strack, 1979). The speed of propagation is evaluated using the Rayleigh surface wave speed, based on the physical properties of the particle. By knowing the particle size and speed of propagation, the time of propagation can be calculated. This is referred to as Rayleigh time step, (Norouzi et al. 2016), shown in Equation 4-56:

$$T_R = r_p \pi \left(\frac{\rho_p}{G} \right)^{0.5} \frac{1}{0.1631\nu + 0.8766} \tag{4-56}$$

where r_p is the particle radius, ρ_p is the density, G is the shear modulus and ν is Poisson's ratio of the particle. To prevent numerical instability and ensure a realistic force transmission the solids time step should be smaller than this value. For dense systems with high coordination numbers (4 and above) a typical time-step of about 20% of T_R is appropriate, (EDEM, 2014). Here, the solids time step is set to 2.5×10^{-6} s (13% T_R) while the fluid time step is set to be 40 times higher (10^{-4} s). No sensitivity analysis has been conducted on the time step.

4.3.8.7 Studied Conditions

Consistently with the experimental work, the CFD-DEM study aims at elucidating the effect inlet gas velocity (16, 20, 24 m s^{-1}) and solids loading (0.1, 0.3, 0.6, 1), for mono-dispersed particles of size of 377.5 μm, on the particle dynamics in the cyclone. Moreover, by fixing the gas inlet velocity at 20 m s^{-1} and the solids loading at 0.1, the particle size effect is studied by using mono-dispersed particles of size of 196, 231, 265, 327.5 and 377.5 μm. The conditions are schematically indicated in Table 4-1.

4.3.9 Results and Discussion

4.3.9.1 Mesh Independency and Pressure Drop Validation (CFD)

In order to check the mesh independency, three different meshes of mean cell size of about 1.25, 1.05 and 0.89 mm are checked in absence of the solid phase. The parameter of interest is the global pressure drop. The pressure drops predicted for the three cases are respectively equal to 59.1, 61.7 and 62.3 mbar. The error between the coarsest and finest mesh is about 5%, reasonable considering the huge difference in number of cells. As a result, the coarser mesh is used for the CFD-DEM simulations. The main characteristics of the fluid flow are qualitatively and quantitatively maintained as it can be seen for the tangential component of the fluid velocity reported in Figure 4-20.

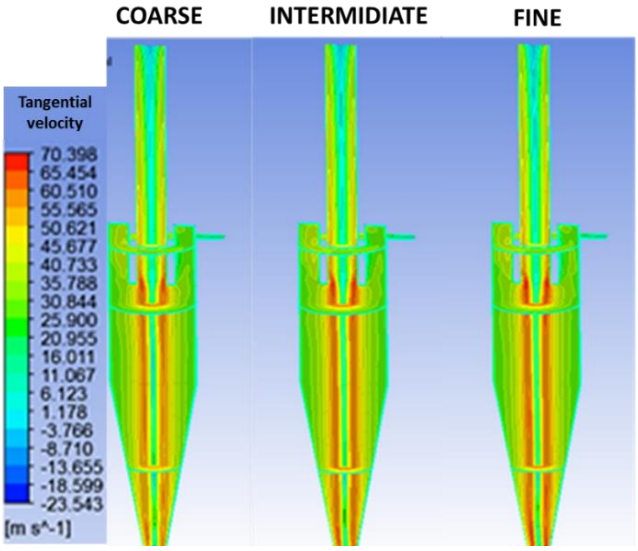

Figure 4-20. Comparison of the tangential velocity contours for differently refined meshes (inlet air velocity of 24 m s^{-1})

Validation is usually achieved by the comparison of easily measurable macroscopic trends. In this case, the pressure drop is used as reference parameter for the comparison with the measurements carried out on the actual system at different inlet gas velocity. Furthermore, the correlation of Shepherd and Lapple (1939) for pressure drop in a Stairmand cyclone, Equation 4-57, is used to check consistency. The results are reported in Figure 4-21 showing a global agreement.

$$\Delta P = \frac{0.16 a_{cyc} b_{cyc} \rho_f \frac{u_{cyc,in}^2}{2}}{d_{VF}^2} \tag{4-57}$$

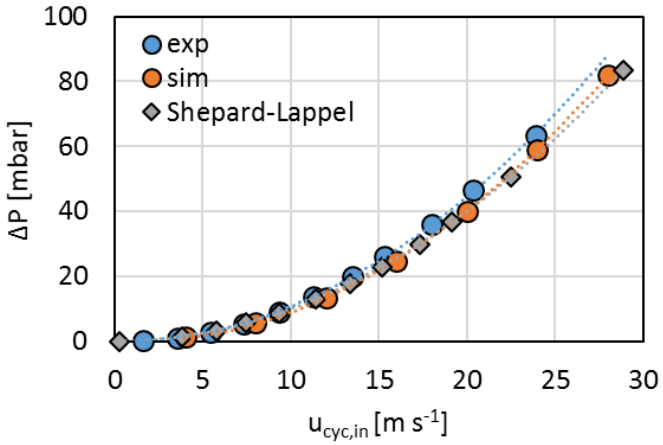

Figure 4-21. Pressure drop (only fluid) obtained from experiments, simulation and the correlation of (Shepherd and Lapple, 1939)

4.3.9.2 Fluid Dynamic Verification (CFD)

By analysing the tangential velocity profile on a central line of a section of the cylindrical body of the cyclone (section "C" of Figure 4-23), the typical wing trend is observed. This is related to the presence of the vortex in the outer wing and the forced reversed vortex at the core, Figure 4-22. This has been observed in literature by Slack, (2012), Slack et al. (2000), Raoufi et al. (2009), Liu and Liptak, (2013) and Elsayed and Lacor, (2016). In particular Liu and Liptak, (2013) reported that the trend of outer wing can be described by the following Equation 4-58:

$$u^t r^{n_v} = \text{const} \tag{4-58}$$

where n_v is found experimentally to be between 0.5 and 0.9. In this case, n_v lies in the correct range being between 0.65 and 0.71.

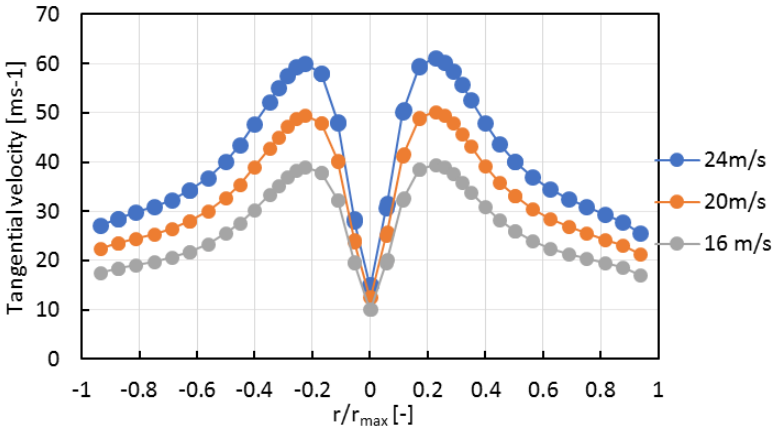

Figure 4-22. Profiles of the time averaged tangential velocity for different fluid inlet velocities

When increasing the inlet gas velocity, a larger flow rate has to circulate in the cyclone. Due to presence of the outer vortex, the inner vortex is forced into a smaller radius region. For the momentum conservation, if the same fluid is forced to spin at a lower radius, an increase of the tangential velocity is expected. This is what commonly happens in the reverse-flow cyclones, (Song et al. 2016), and is observed here in Figure 4-23.

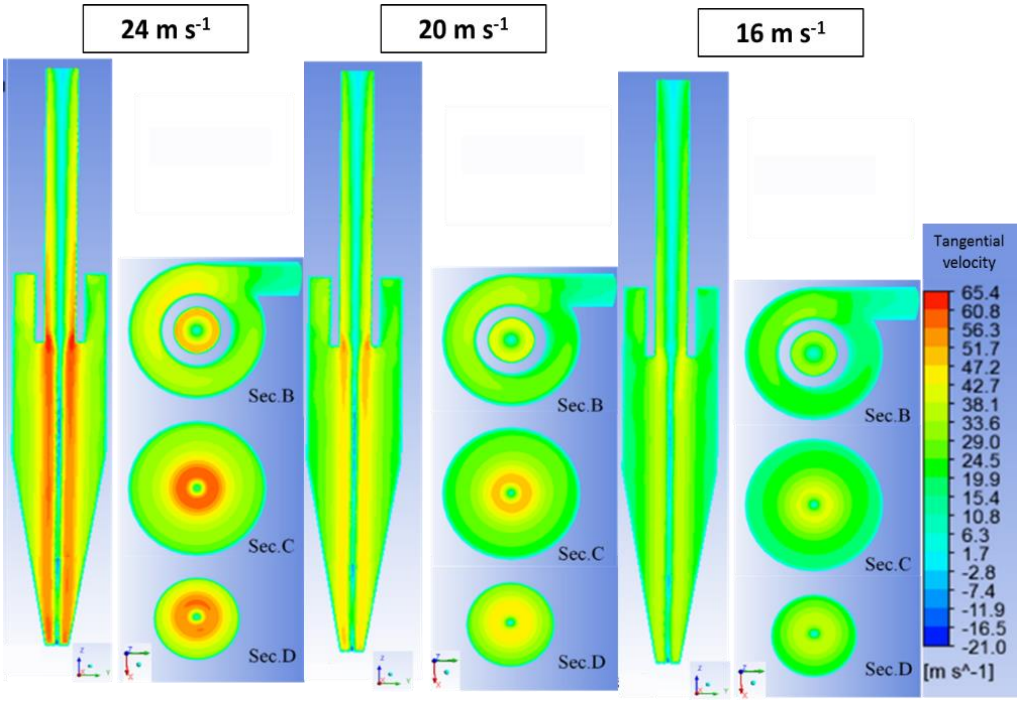

Figure 4-23. Tangential velocity at three different inlet gas velocity

A low-pressure core is also observed at all velocities, as well as high pressure near the walls which increases at increasing gas velocities, Figure 4-24. This is in agreement with Chu et al. (2011), Elsayed, (2015), Martignoni et al. (2007) and Raoufi et al. (2008) who found that that the pressure gradient is mainly established in the radial direction. The higher magnitude of static pressure observed at high velocity is due to higher inertia of the vortices, induced by its high tangential velocity, which makes the fluid escape tangentially.

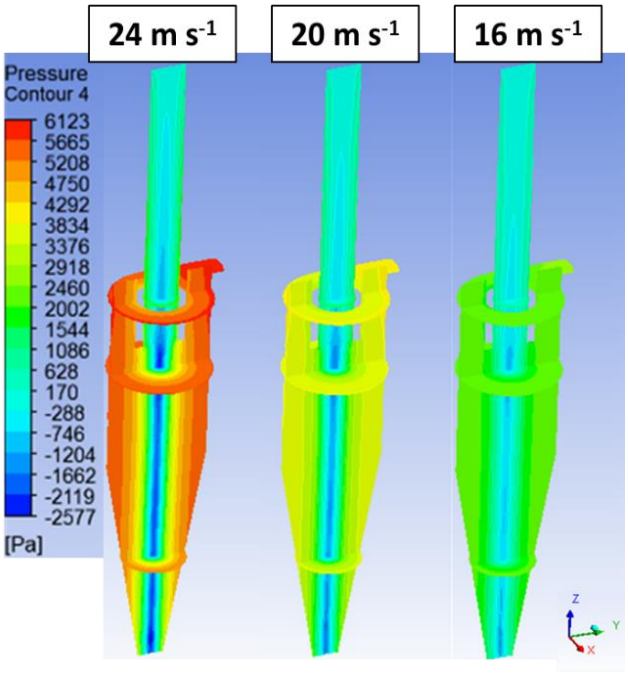

Figure 4-24. Contours of the gauge pressure for the three cases of inlet gas velocity

By referring to the axial velocity contours of Figure 4-25, it is possible to notice the reverse flow of the inner vortex and the alternation of orientation of the radial velocity as reported by Song et al. (2016).

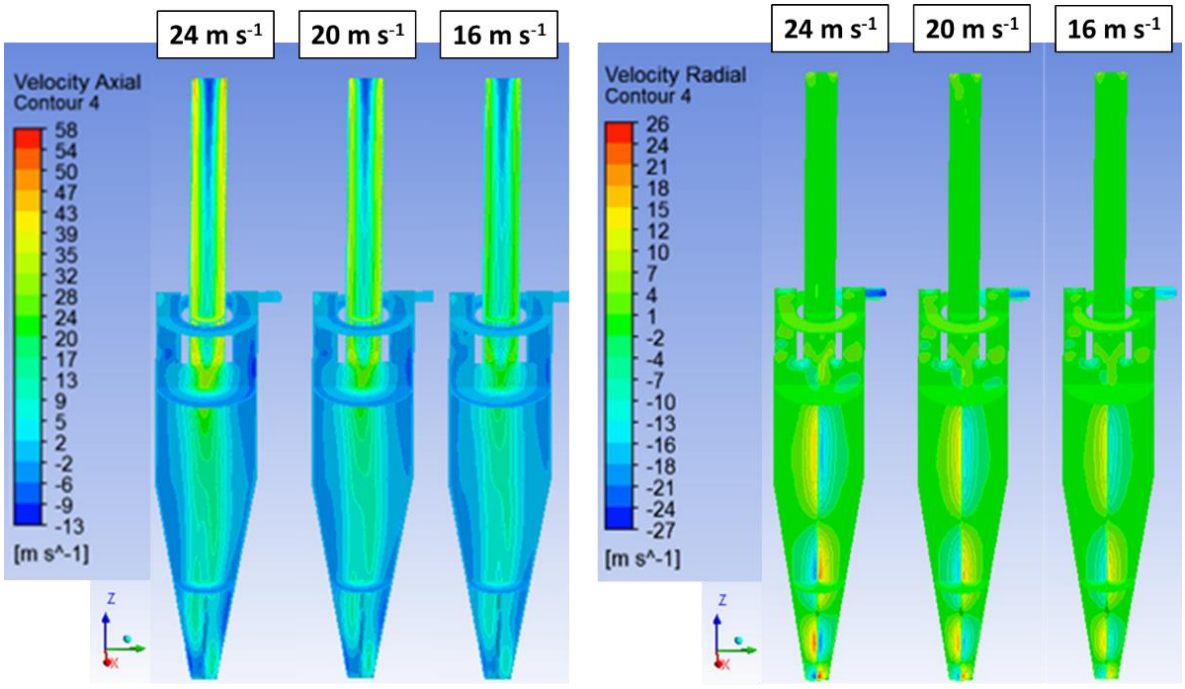

Figure 4-25. Axial and radial velocity contours at different inlet gas velocity

4.3.9.3 Fluid and Particles Dynamic (CFD-DEM)

4.3.9.3.1 Transient

At the start-up, the system is empty thus a transient period is expected where the number of particles, the global pressure drop and the coupling force (the drag forces acting on the particles) changes. They are reported in Figure 4-26, for the case of 24 m s^{-1} for different solids loadings. The steady state is considered to be reached when these three variables do not change considerably with time. This coincides roughly with the average particle residence time through the cyclone.

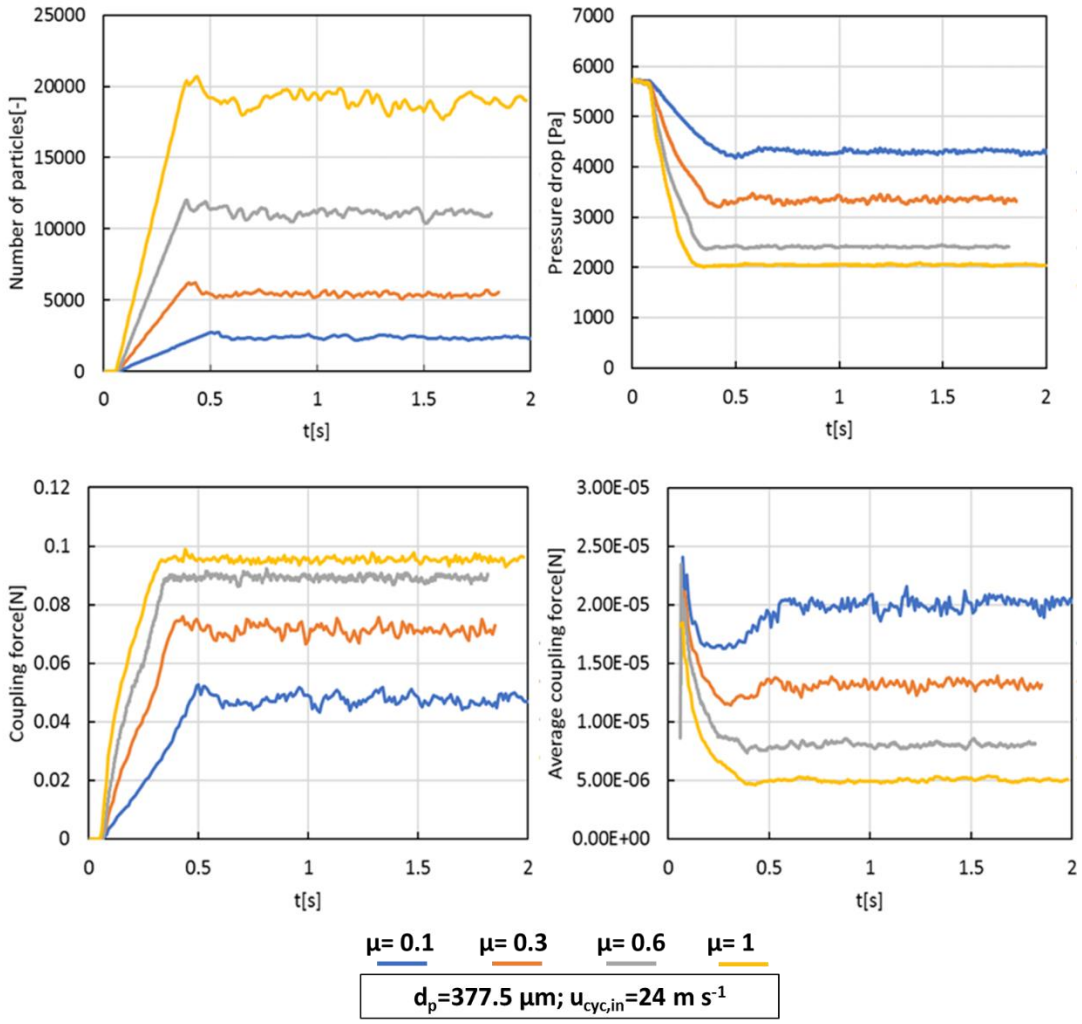

Figure 4-26. From left to right: number of particles, global pressure drop, total and average coupling force for the case at 24 m s^{-1} at different solids loadings, as a function of time.

By referring to Figure 4-26, the increase of number of particles in the cyclone is expected for higher solids loading. Moreover, the decrease of the pressure drop at high solids

loading is also expected due to the high interaction with the solid phase and consequent reduction in the tangential velocity (the main contributor of the kinetic energy), (Chu et al. 2011). This is furtherly confirmed by the total coupling force which increases at increasing solids loading. However, the average coupling force (attributable to the single particle) decreases. When the system is diluted, the average coupling force is higher thus the particles are going to have higher tangential velocities and reside in the cyclone for a longer period, as seen from Figure 4-26. This might have severe implications on attrition as both impact velocity and sliding distance would increase. Similar trends are observed at 16 and 20 m s^{-1}.

For the reasons mentioned above, referring to the case at 24 m s^{-1}, for solids loading of 0.1 and 1, steady state is reached respectively at about 0.5 and 0.3 s. The observation time window where the attrition analysis is carried out is then set to be between 1 and 1.5 s.

4.3.9.3.2 Steady State

Here, the total number of particles in the cyclone, pressure drop (in comparison with the experimental results), the total coupling force and the average coupling force, at steady state is reported and discussed for different gas velocities and solids loading.

As observed in the previous section, higher number of particles in the cyclone is expected at increasing solids loading. This also observed at increasing gas velocity, as shown in Figure 4-27.

In the same figure, the pressure drops, as predicted by the simulations for different inlet gas velocities, are compared with that obtained by experiments showing a great discrepancy at increasing solids loadings. This disagreement may be due to experimental error during the measurements or simply the way the pressure drop is measured.

Again, referring to Figure 4-27, the average coupling forces appear to reduce by reducing the inlet gas velocity and increasing the solids loading. In other words, the single particle interphase force is greater when the system is diluted and the gas velocity is high; on the other hand, this is weak when the system is concentrated, and the gas inlet velocity is low. The trend of the total coupling force can be explained by combining the trend of the average coupling force and the number of particles.

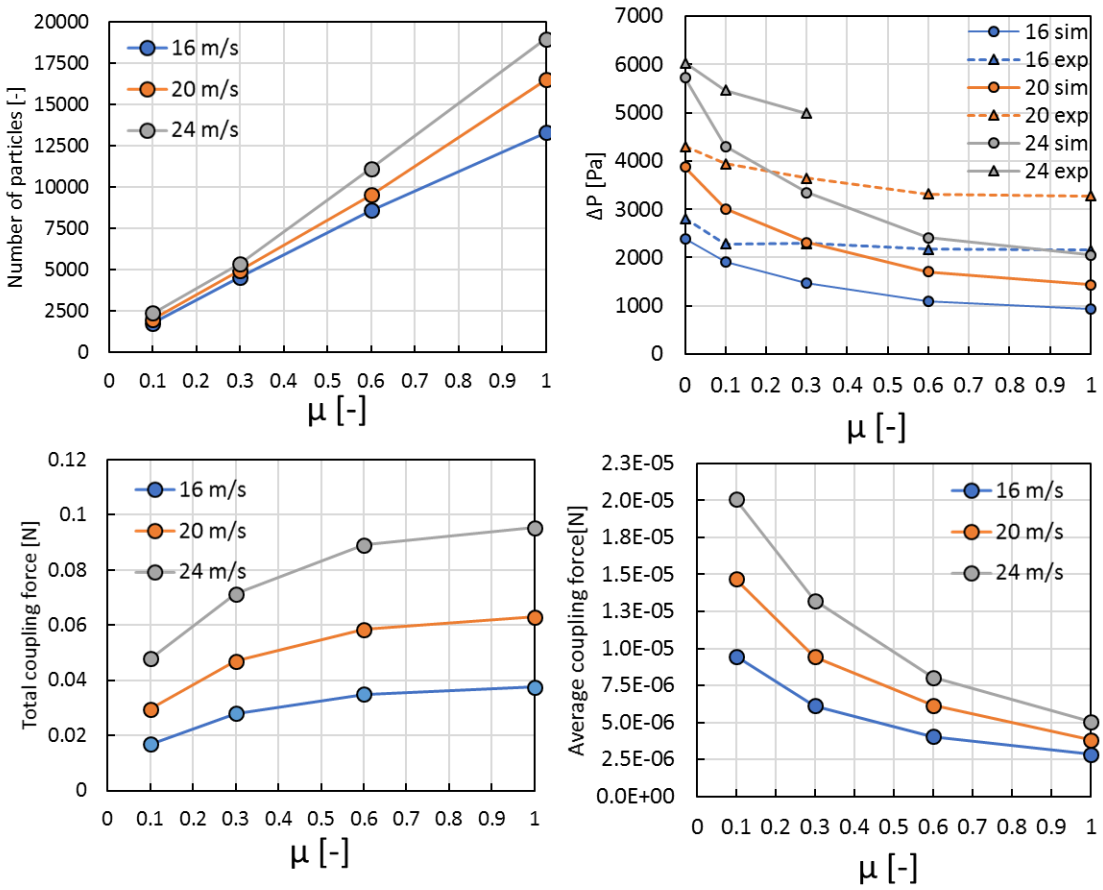

Figure 4-27. Under conditions of steady state, form UP left to BOTTOM right: the number of particles in the cyclone, the global pressure drop (EXP vs SIM), the total coupling force and the average coupling force.

4.3.9.3.2.1 Fluid Flow Field

In this section the trend of the tangential, axial and radial velocities and static pressure are discussed, at different solids loading and inlet gas velocities. By referring to the case at 24 m s^{-1}, when increasing the solids loadings, the solids have a stronger dampening effect on the fluid tangential velocity as shown in Figure 4-28. This phenomenon is similarly occurring at different inlet gas velocity, as shown by Figure A-1. A dampened tangential velocity would have an impact on the particle impact velocities.

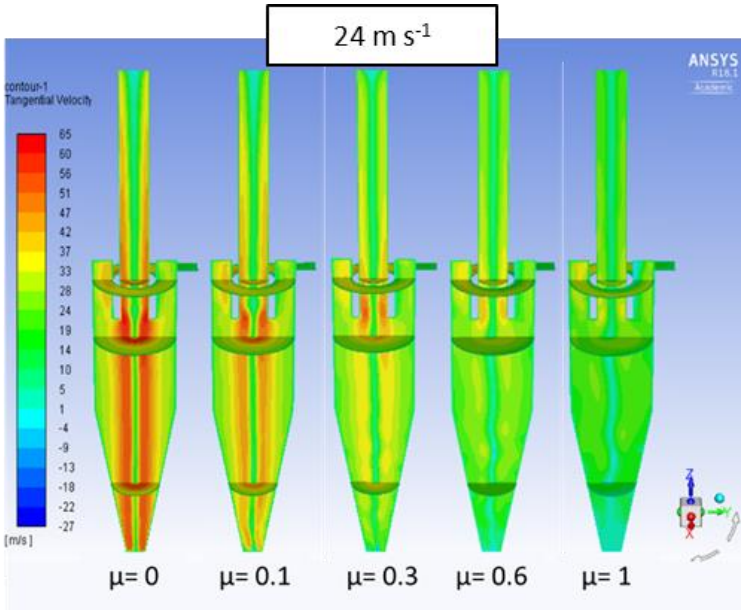

Figure 4-28. Tangential gas velocity at steady state at 24 m s^{-1} of gas inlet velocity at different solids loading.

The pressure drop is dependent on the fluid kinetic energy, therefore the changes in the pressure contours are strongly related to the changes of tangential velocity field inside the cyclone, as shown in Figure 4-29. The pressure drop for the other cases are reported in the appendix in Figure A-2.

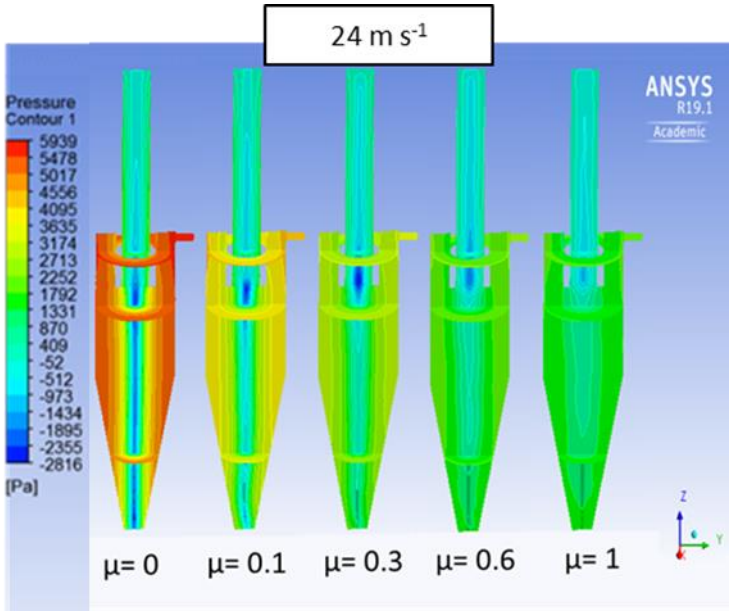

Figure 4-29. Static pressure at steady state at 24 m s^{-1} of gas inlet velocity at different solids loading.

The radial velocity contours, at all velocities and solids loading, are reported in the appendix section in Figure A-3.

The axial velocity contours, at all velocities and solids loading, are also reported in the Appendix section, Figure A-4, showing, at increasing solids loadings, an increase in the axial gas velocity due to the concentration of particles present in the conical region preventing the fluid to escape downwards.

4.3.9.3.3 Solids Flow Pattern

The particle-flow pattern, obtained from the CFD-DEM simulation, is reported and analysed here.

As shown in Figure 4-30, the particles, once accelerated in the inlet pipe, enter the cyclone and hit the walls with an angle. Here, they most probably experience the most stressful event. The initial impact slows them down so, as a result, they tend to congregate at the walls causing important interparticle interactions. Afterwards, they start their stranded spiral-like descent towards the bottom outlet, sliding against the wall.

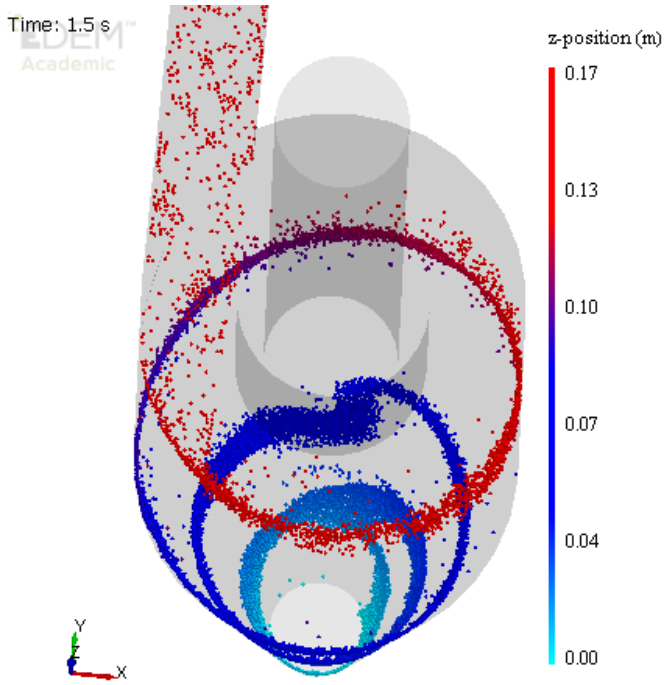

Figure 4-30. Top view of a cyclone CFD-DEM simulation (case at inlet gas velocity of 16m s^{-1} and LR of 0.6)

As shown by Figure 4-31, the number of turns of the particle strands tends to reduce in case of high solids loading. Therefore, the sliding distance is expected to be greatly affected by solids loading. Similar trends are observed at 16 and 20 m s^{-1} of inlet gas velocity, Figure A-5.

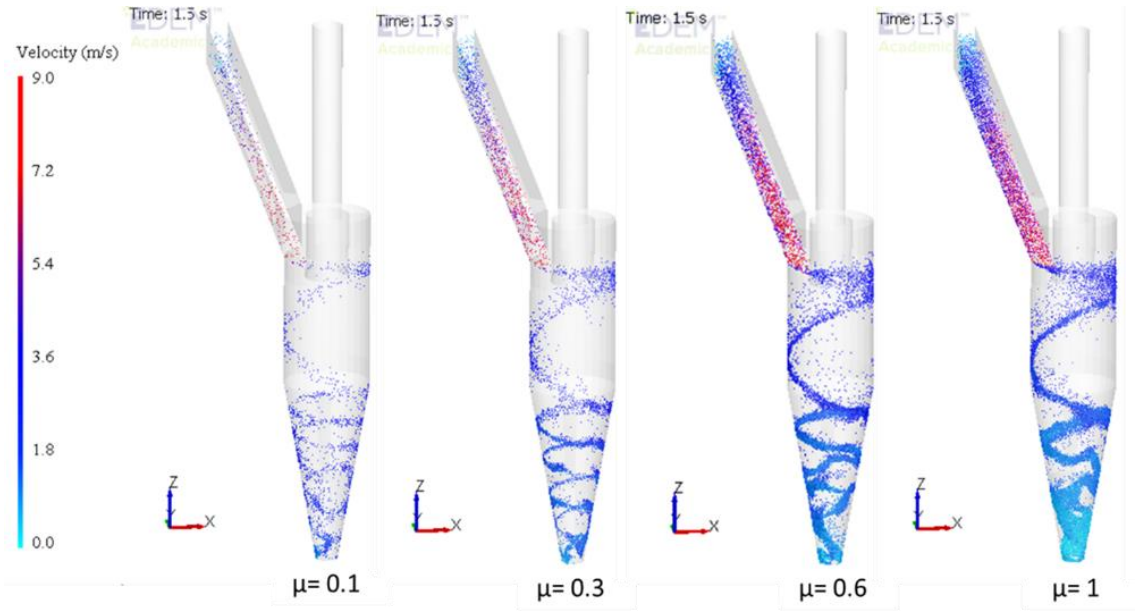

Figure 4-31. Solid flow pattern, at 24 m s^{-1}, and different solids loadings.

4.3.9.4 Attrition Results

4.3.9.4.1 Parametric Analysis

As mentioned in section 4.3.7.1, for a certain material and a fixed particle size, the parameters influencing collisional attrition are: (i) the impact energy, proportional to $v_p^2 \sin\theta$, (ii) the number of impacts per particle $N_{col/p}$ and (iii) the efficiency of the impact η_{col}. In this section, these parameters are reported and discussed for the impact dominated regions, "1" and "2" for both P-W and P-P collision.

The parameters influencing surface wear are: (i) the normal load acting on the particle F^n, (ii) the sliding distance Δs and (iii) the fraction of wearing particles "y". These parameters are reported and discussed here for the sliding dominated regions, "3 - 7".

4.3.9.4.1.1 Effect of Gas Inlet Velocity and Solid Loading Ratio

- **Region 1**

  Figure 4-32 allows to have an overview of the collisional behaviour of "Region 1". In case of P-W collisions: (i) the impact energy increases with the gas inlet velocity and decreases with the solids loading, as expected, (ii) the number of collisions per particle appear to be slightly higher at lower gas inlet velocity and not to be affected by the solids loading, (iii) the efficiency of collision is higher for higher gas inlet velocity and low solids loading.

The most severe conditions are therefore found at high gas velocity and low solids loading.

In the case of P-P collisions: (i) the impact energy increases with the gas inlet velocity and decreases with the solids loading, (ii) the number of collisions per particle greatly increases with the solids loading and appear to be independent of the gas inlet velocity, (iii) the efficiency of collisions is higher for higher gas inlet velocity and low solids loading.

In "Region 1", the most severe conditions are then expected to be at high gas inlet velocity and intermediate/high solids loading.

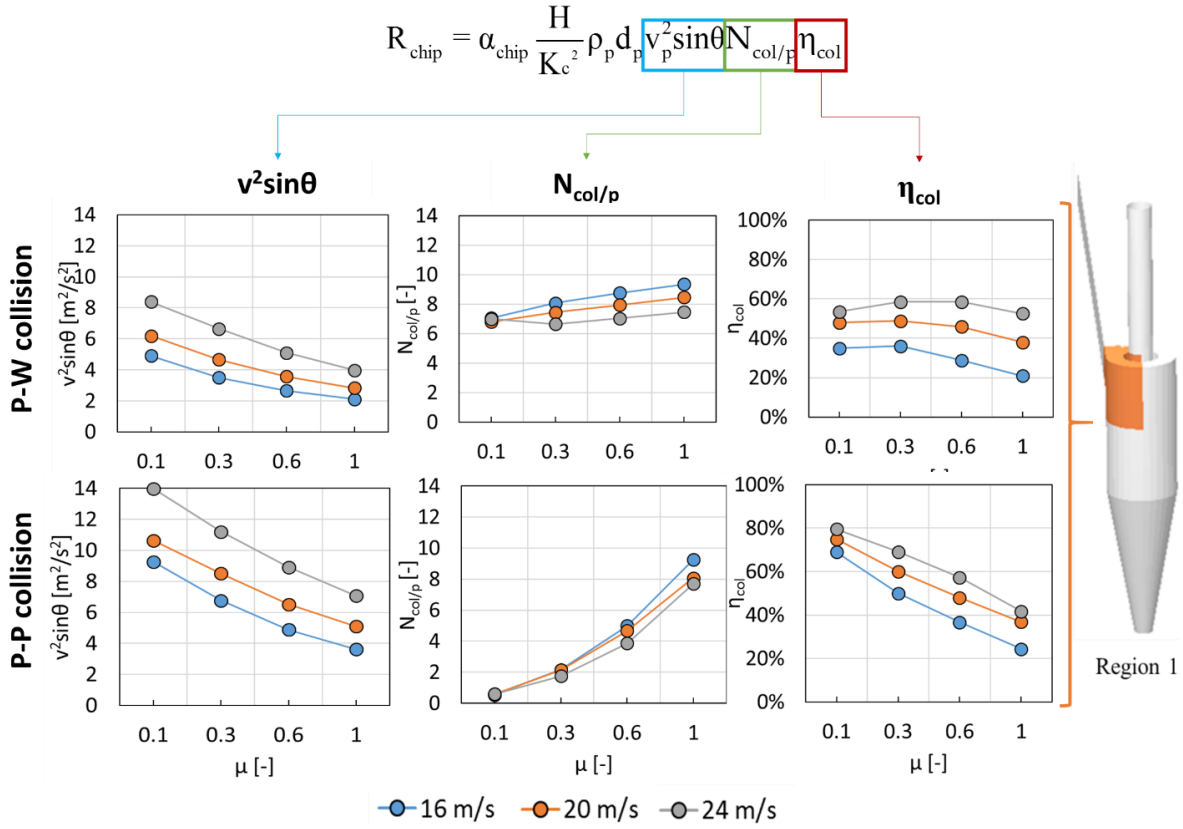

Figure 4-32. Collisional parameters at different velocities and solids loadings, for both P-P and P-W impact, in the "Region 1"

- **Region 2**

For the "Region 2", the same parameters are reported in Figure 4-33.

In the case of P-W collisions: (i) the impact energy is much lower as compared to "Region 1" and constant, (ii) the number of collisions per particle appears to be slightly higher at lower gas inlet velocity and at low solids loading, (iii) the

efficiency of collision is mainly dependent on the gas inlet velocity, as shown by the great discrepancy between 16 and 24 m s^{-1}, also slightly decreases with the solids loading.

In the case of P-P collisions: (i) the impact energy is constant, as low as the P-W case, and much smaller than in "Region 1", (ii) the number of collisions per particle slightly increases with the solids loading and appears to be independent of the gas inlet velocity, (iii) the efficiency of collision is in general very low (below 40%), slightly higher for higher gas inlet velocity and low solids loading. Severe conditions of attrition are not meaningful given the low impact energy, number of collisions and efficiency of collisions.

In "Region 2", the most severe conditions are therefore found at high gas velocity and low solids loading.

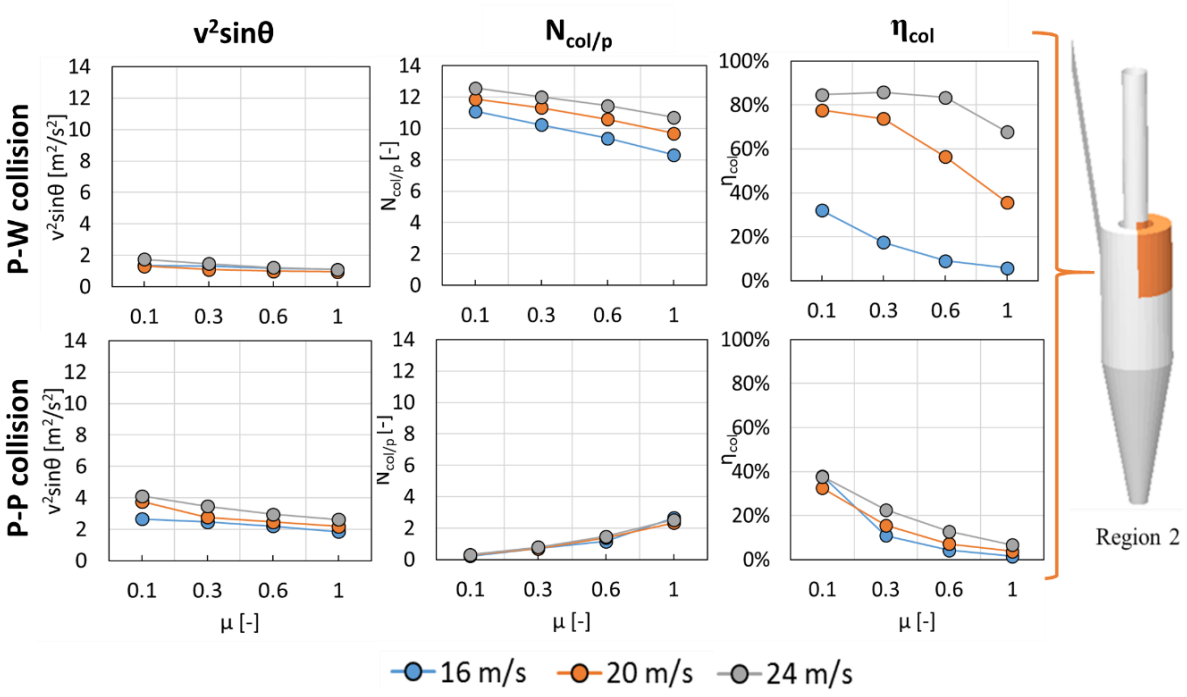

Figure 4-33. Collisional parameters at different velocities and solids loadings, for both P-P and P-W impact, in the "Region 2"

- **Region 3 – 7**

Referring to Figure 4-34, at any conditions of inlet gas velocity, the average normal load which depends on the particle momentum and fluid tangential velocity, seem to slightly increase towards the last regions. At the same time, for

a solids loading equal to "1", in "Region 7", the normal load drops dramatically due to the increasing concentration of solids.

The larger the centrifugal force, as compared to the sum of gravity and normal component of the drag force, the longer the mean path of the sliding. The sliding distance is in fact, larger at low solids loading and less significant at increasing gas inlet velocity. This effect is enhanced in the conical area due to the reaction of the inclined walls.

Multilayering is expected at high solids loading. Therefore, the fraction of wearing particles decreases with the solids loading, and towards the bottom outlet because of the building concentration of solids.

For the "Region 3-7", the most severe conditions of attrition are found to be at low solids loading and high gas inlet velocity.

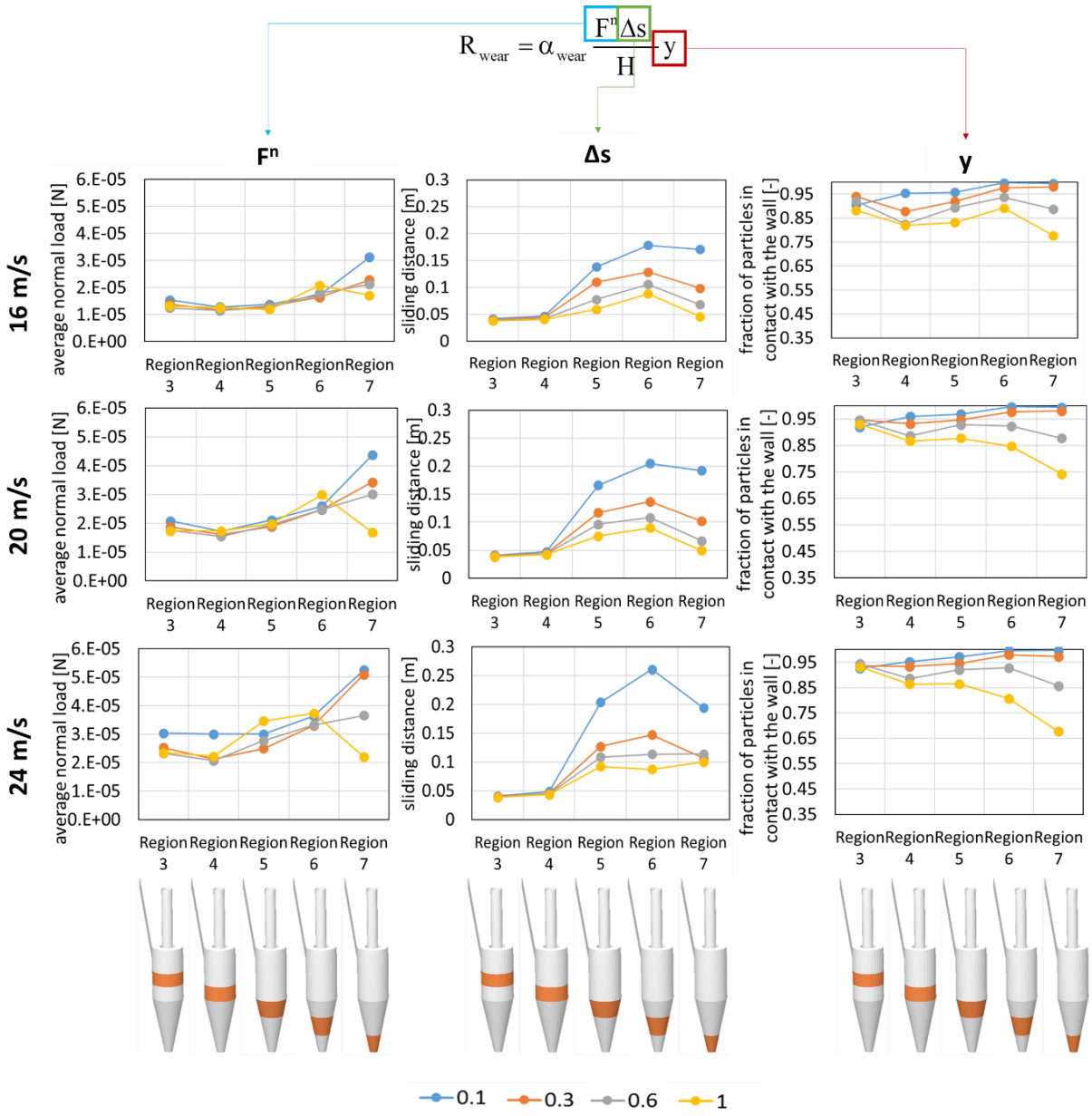

Figure 4-34. Surface wear parameters at different velocities and solids loadings, for the Regions "3-7"

4.3.9.4.1.2 Effect of Particle Size

The effect of particle size on the parameters discussed in the previous section are reported and analysed here, for the case of 20 m s^{-1} gas inlet velocity and 0.1 solids loading.

- **Region 1**

  In the case of P-W collisions, small particles have a higher impact energy as well as a higher collision efficiency. In terms of number of collisions, it seems that there is no great difference between particles of different sizes.

P-P collisions are less significant in terms of actual number of collisions experienced (around 1), due to the diluted system. Even though both particle impact energy and the efficiency of collision are high. The former is higher for smaller particles.

For "Region 1", the most severe conditions are expected for small particle sizes.

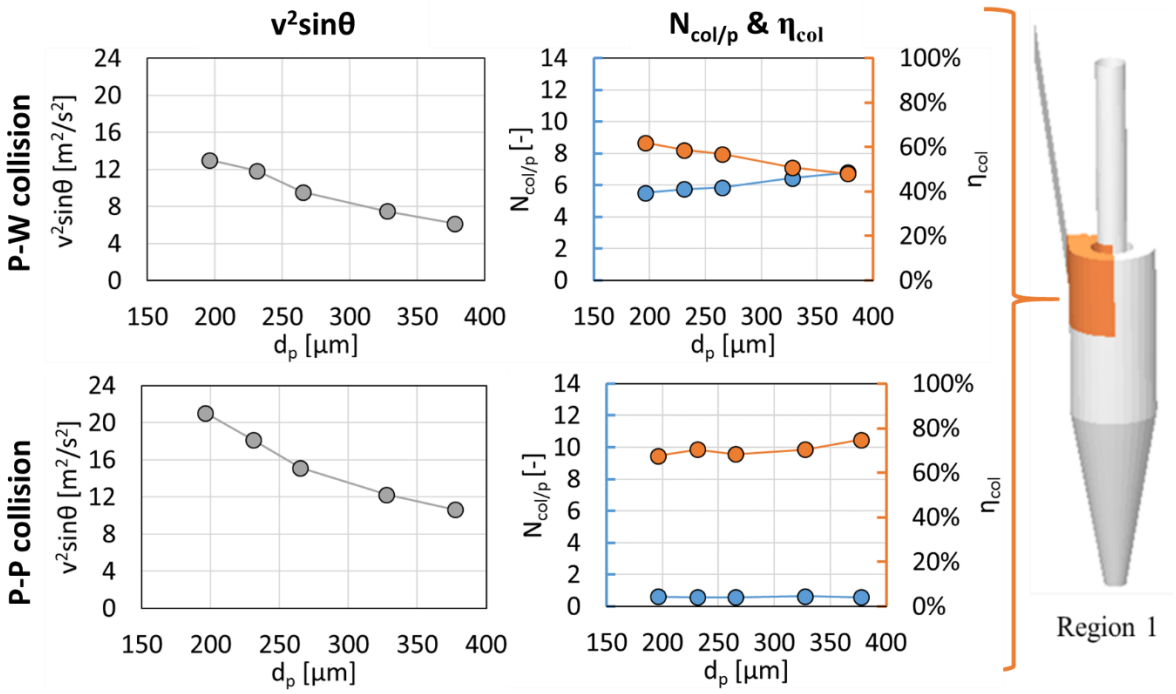

Figure 4-35. Collisional parameters for different particle sizes, at 20 m s^{-1} and 0.1 solids loading, for both P-P and P-W impact, in the "Region 1"

- **Region 2**

In "Region 2" the impact conditions are even less severe than "Region 1", in particular, the impact energy is low for both P-W and P-P cases, still slightly dependent on the particle size. The number of P-W collisions is high as well as their efficiency. The opposite trend is observed for P-P case.

For "Region 2", the most severe conditions are expected for small particle size.

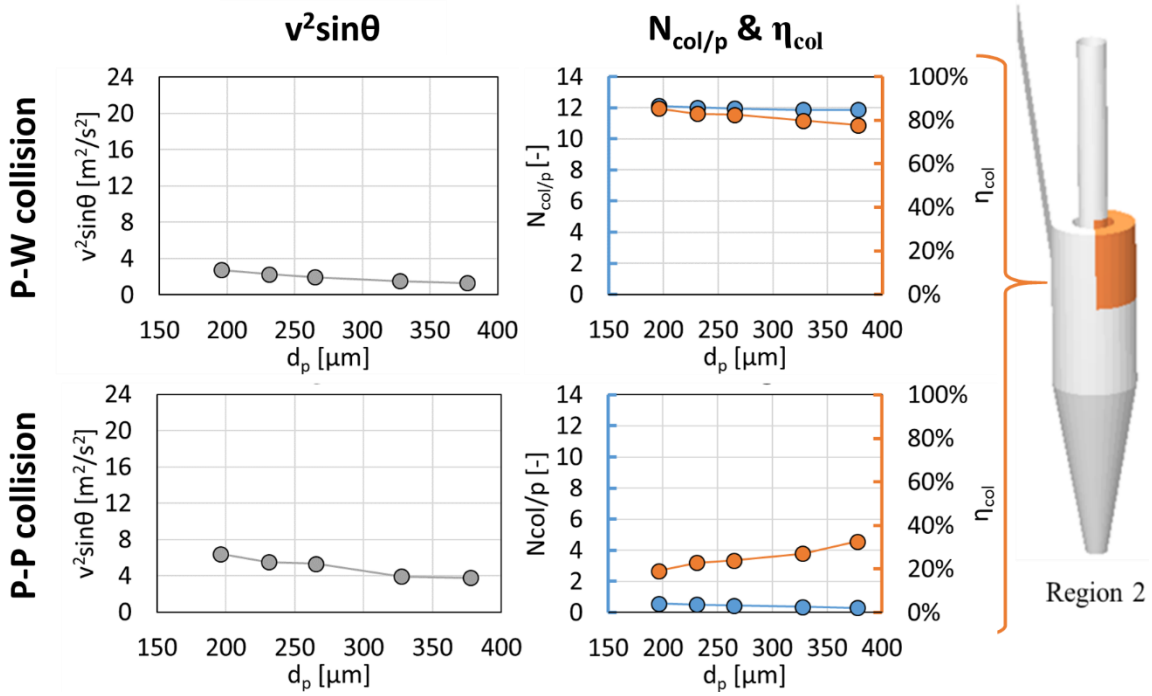

Figure 4-36. Collisional parameters for different particle sizes, at 20 m s^{-1} and 0.1 solids loading, for both P-P and P-W impact, in the "Region 2"

The strong dependency with the particle size on the impact conditions, particularly in the "Region 1", is elucidated in the next section by the particle velocity analysis in the inlet pipe of the cyclone.

- **Region 3-7**

  Analysing the parameters responsible for surface wear as induced by particle sliding against the walls, for different particle sizes, it appears that the average normal load acting on the particle is greater for larger particles. This is expected because of their higher mass; the normal load tends to increase towards the bottom as well as the sliding distance due to the axial component of the wall reaction. The sliding distance seem to have no dependency with the particle size. A great difference is noticed instead for the fraction of wearing particles, much higher for larger particles, again due to their mass, they are more effectively pushed onto the walls. Small particle sizes tend to accumulate on the walls in the conical region as shown in the figure.

  For "Region 3-7", the most severe conditions are expected for large particle sizes at the towards the conical body of the cyclone.

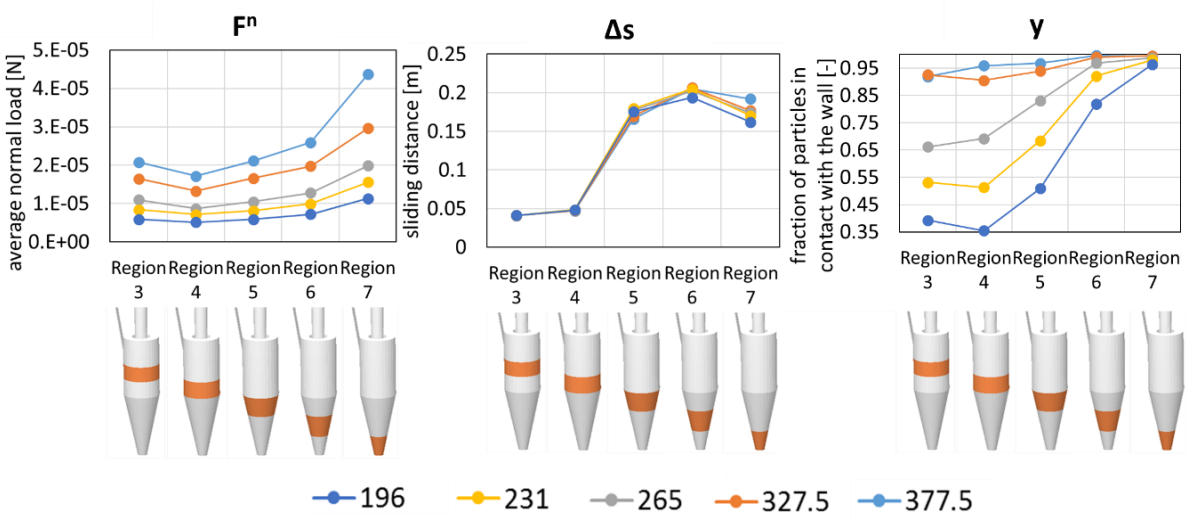

Figure 4-37. Surface wear parameters for different particle sizes, at 20 m s^{-1} and 0.1 solids loading, for the Regions "3-7"

4.3.9.4.1.3 Effect of Pipe Length and Particle Size on Particle Velocity at the Entrance of the Cyclone

The higher impact energy of the small particles is caused by entrance effects. They arrive at the cyclone with a higher velocity. A CFD-DEM study is carried out to evaluate the influence of the inlet pipe length for different solids loadings, for a mixture of particles with different sizes and density equal to that of F-CLC. The analysis revealed that the particles are subjected to acceleration at the beginning of the inlet pipe and then slowly increases their velocity, as shown below by Figure 4-38.

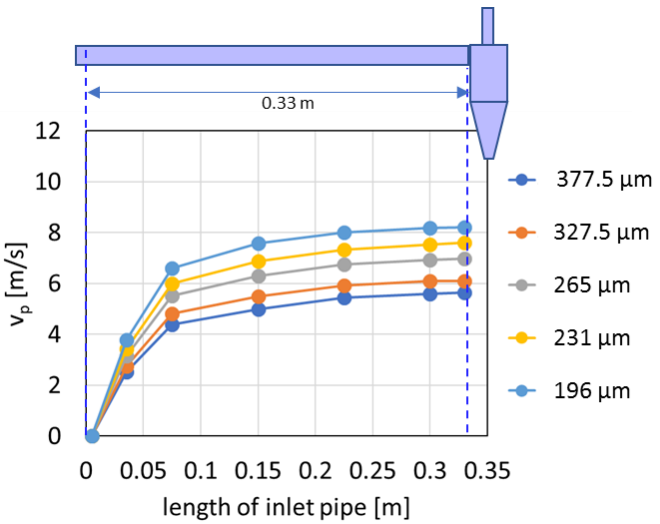

Figure 4-38. Average particle velocity in the inlet pipe for different monodispersed particle sizes (from 196 to 377.5 µm), at 20 m s^{-1} and solids loading of 0.1

CFD-DEM investigation demonstrated that this takes place at both low and high solids loading, as shown by Figure A-6 and Figure A-7; the figures show the particle average velocity for a mixture of different sizes (196 to 377.5 μm) for a solids loading of 0.1 and 10, respectively. For the particle density and size range used, the analysis shows that there is a difference in particle velocity for different particle size regardless of the solids loading and whether they are in a mixture or not. This has inevitable implications on the collisional attrition as demonstrated from the parametric analysis discussed above.

Using the particle velocities of different particle sizes, for different gas inlet velocities, at different length of the inlet pipe, a correlation is developed using the mathematical form of the model of Micaelis & Menten kinetic rate for enzymatic reactions, (Dowd and Riggs, 1965), because of the mathematical similarity of the particle acceleration zone and the its maximum entrance velocity (length independent), with the substrate dependent kinetic rate and its maximum value (substrate concentration independent). The correlation is shown below in Equation 4-59:

$$v_{p,cyc,in}\left(d_p\right) = u_{cyc,in}\left(\frac{A_p(d_p)\,L/L_{max}}{B_p(d_p) + L/L_{max}}\right) \tag{4-59}$$

where A_p and B_p are function of particle size in the following way

$$A_p\left(d_p\right) = 1.134\ d_p^{-0.136} \tag{4-60}$$

$$B_p\left(d_p\right) = 1.186\times10^{-4} d_p^{1.181} \tag{4-61}$$

and L_{max} is equal to 1 m. The correlation is represented by the continuous red line in Figure 4-39 while the markers are the CFD-DEM velocities values for different particle sizes at 20 m s^{-1} of gas inlet velocity. Figure 4-40 shows the particle velocity at $L=L_{max}$, for different particle sizes and gas inlet velocities as predicted by the correlation. The latter does not consider the effect of the solids loading and particle density so its applicability should be limited for similar particle densities and sizes to those used here.

By insertion of Equation 4-59 into the experimental model of particle attrition in the cyclone, shown in Equation 4-3, the particle extent of attrition in the cyclone can be expressed as a function particle entrance velocity (which is a function of particle size). In this way the particle size power index would change from -1 to 3.

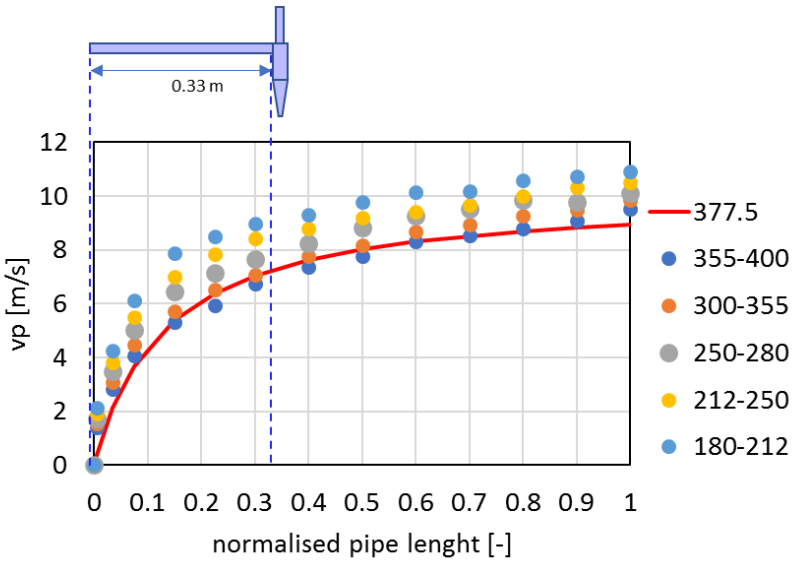

Figure 4-39. The markers represent the average particle velocity in the inlet pipe of the cyclone at 20 m s-1 and 0.1 solids loading and different particle size. The continuous line represents the correlation Equation 4-59

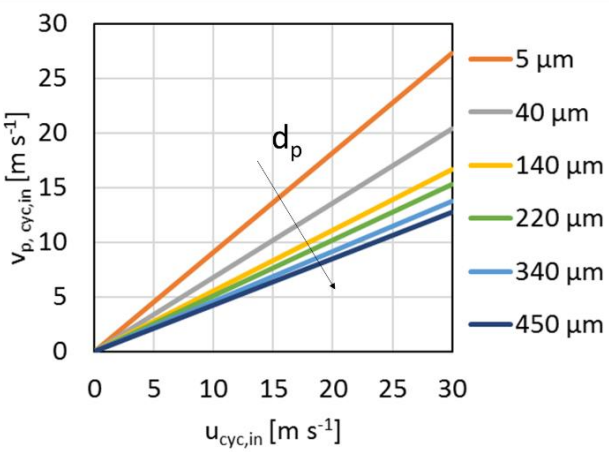

Figure 4-40. Particle entrance velocity at the cyclone for different particle sizes and gas inlet velocity as predicted by the correlation

4.3.9.4.2 Regional Attrition

Recalling the parametric analysis of the previous section, an increase of attrition with the gas velocity and at low solids loading is expected. In this section, the extent of attrition of each region is reported as a function of these two variables to check their relative importance. In particular, in Figure 4-41, R_k is shown for a fixed particle size of 377.5 µm. It is clear that the "Region 1" appears to be the region with the most severe conditions, at any solids loading and gas inlet velocity. This is expected given the high particle velocity at the entrance. A decrease of attrition is observed towards the end of the

cylindrical body of the cyclone (Region 3 and 4). These are in fact regions of transition, where the impact velocity is always ineffective towards breakage and the particles begin their sliding towards the bottom outlet as strands of solids. Attrition tends to increase in the conical body of the cyclone because the particles are travelling along longer paths experiencing extensive surface abrasion. For all cases, the collisional attrition is much larger than surface abrasion.

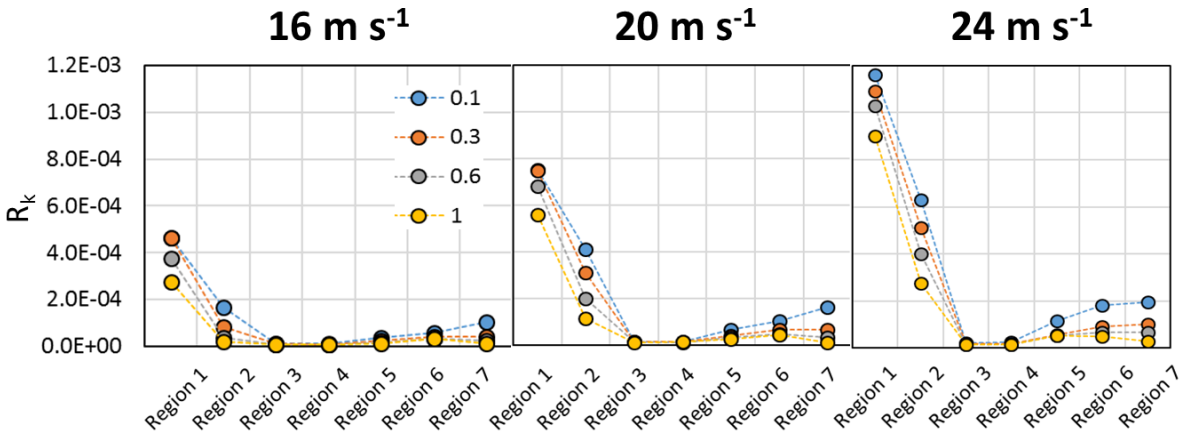

Figure 4-41. Regional extent of attriiton, R_k, for a particle size of 377.5 µm and as a function of gas inlet velocity and solids loading

Figure 4-42 shows the regional attrition for different particle sizes, from 196 to 377.5 µm at 20 m s^{-1} and 0.1. The graph elucidates the strong dependency with the particle size. Attrition in the impact dominated regions decrease with the particle size while the opposite is observed in the sliding dominated regions. The magnitude of the collisional attrition is about one order of magnitude larger than surface abrasion. The dependency with particle size of the overall attrition in the cyclone is then expected to resemble that of the dominant mechanism, in this case chipping upon particle impacts.

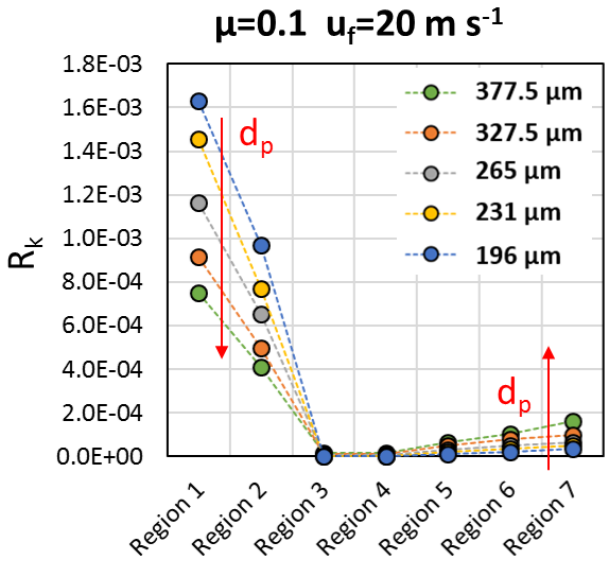

Figure 4-42. Regional extent of attriiton, R_k, for different particle sizes at 20 m s^{-1} gas inlet velocity and 0.1 solids loading

4.3.9.4.3 Main Causes of Attrition

Another important aspect is to understand the proportional contribution to attrition as induced from P-W and P-P collisions and surface abrasion, at different conditions of gas inlet velocity and solids loadings. Below, in Figure 4-43, this is reported in terms of percentage fraction for the case of the fixed particle size of 377.5 μm.

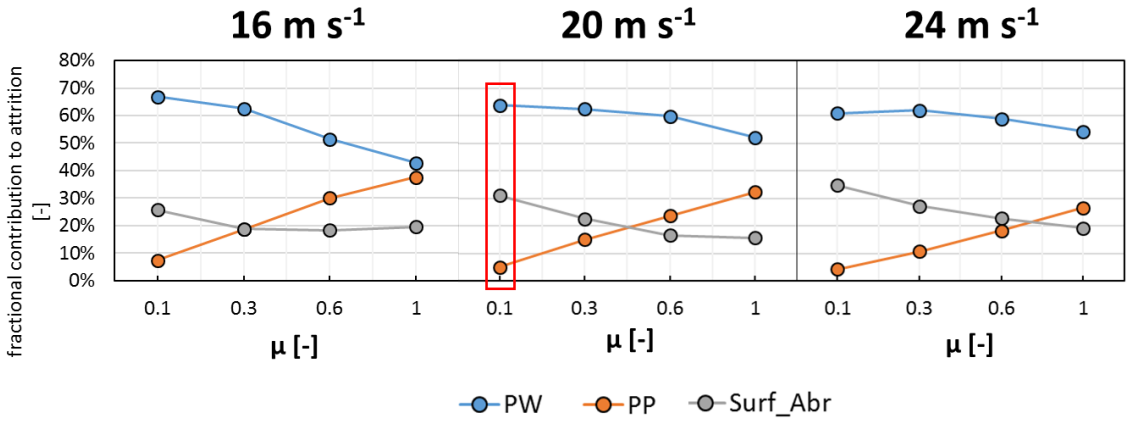

Figure 4-43. Percentage fraction of attrition contribution from different sources: P-W and P-P collisions and surface abrasion, as a function of gas inlet velocity and solids loading for a fixed particle size of 377.5 μm

It is clear that, at all conditions, the P-W collisions are the main cause of attrition. When increasing the solids loading, as it could be expected, the P-P collisions become more

significant, taking over the contribution given by surface abrasion. The latter is the second main cause of attrition at low solids loading.

The same analysis is carried out for different particle size and reported in Figure 4-44. The figure shows that the contribution given by P-W collisions increases by reducing the particle size. This is a direct consequence of the particle entrance velocity for different particle sizes, as explained previously. The contribution of surface abrasion, on the other hand, reduces by reducing the particle size.

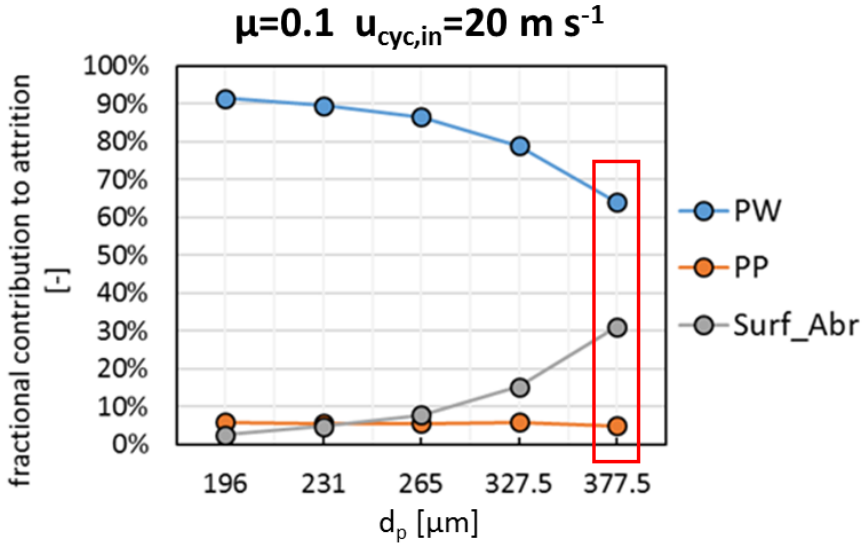

Figure 4-44. Percentage fraction of attrition contribution from different sources: P-W and P-P collisions and surface abrasion, at 20 m s^{-1} of gas inlet velocity and 0.1 of solids loading, for different particle sizes, from 196 to 377.5 μm

The overall attrition in the cyclone can be further analysed by considering the collisional and abrasion sources separately as a function of the gas inlet velocity, the solids loading and particle size. Figure 4-45 shows the extent of attrition induced by the two sources for a fixed particle size of 377.5 μm confirming the collisional attrition to be the dominant mechanism because of its higher order of magnitude.

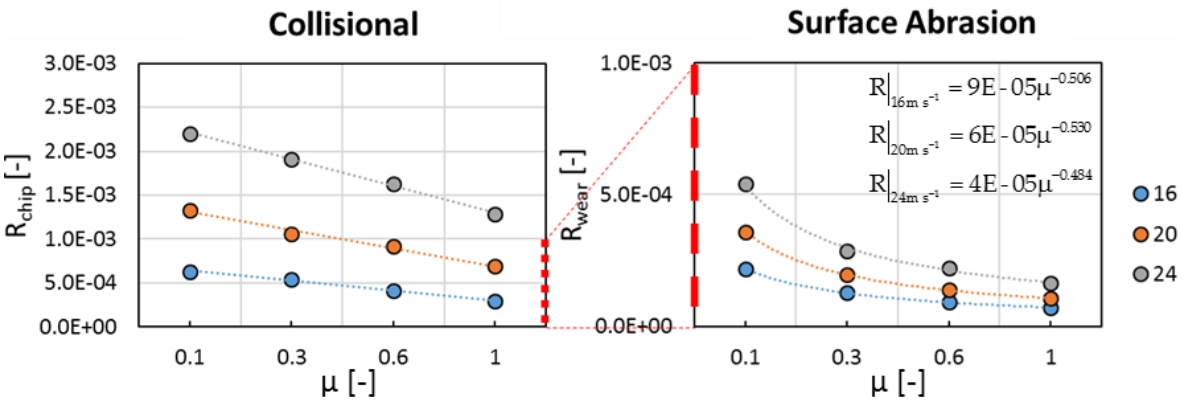

Figure 4-45. Collisional and surface abrasion attrition as a function of gas inlet velocity and solids loading for a fixed particle size of 377.5 μm

Attrition caused by both particles collisions and surface abrasion by sliding against the walls always increases with gas inlet velocity and with decreasing solids loading. If a power function is fitted to the attrition induced by surface abrasion with the solids loading, a power index of about -0.5 is obtained. This is comparable with the dependency reported by Reppenhagen and Werther, (2000).

As far as the dependency on particle size is concerned, as explained previously, it is inversely proportional to the collisional attrition and linearly proportional to the surface abrasion, Figure 4-46.

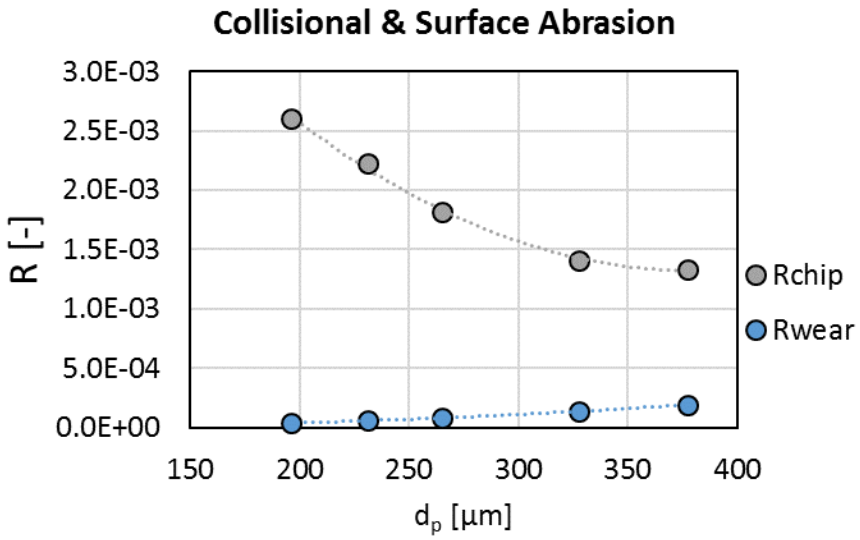

Figure 4-46. Collisional and surface abrasion attrition at 20 m s^{-1} of gas inlet velocity and 0.1 of solids loading, for different particle sizes, from 196 to 377.5

4.3.9.4.4 Comparison with the Experimental Results

The overall extent of attrition in the cyclone, R, and the attrition rates are reported in Figure 4-47. The attrition rate is given by product of the extent of attrition and the inlet solids flow rate, $\dot{m}_{att,cyc} = R\dot{m}_{s,cyc,in}$.

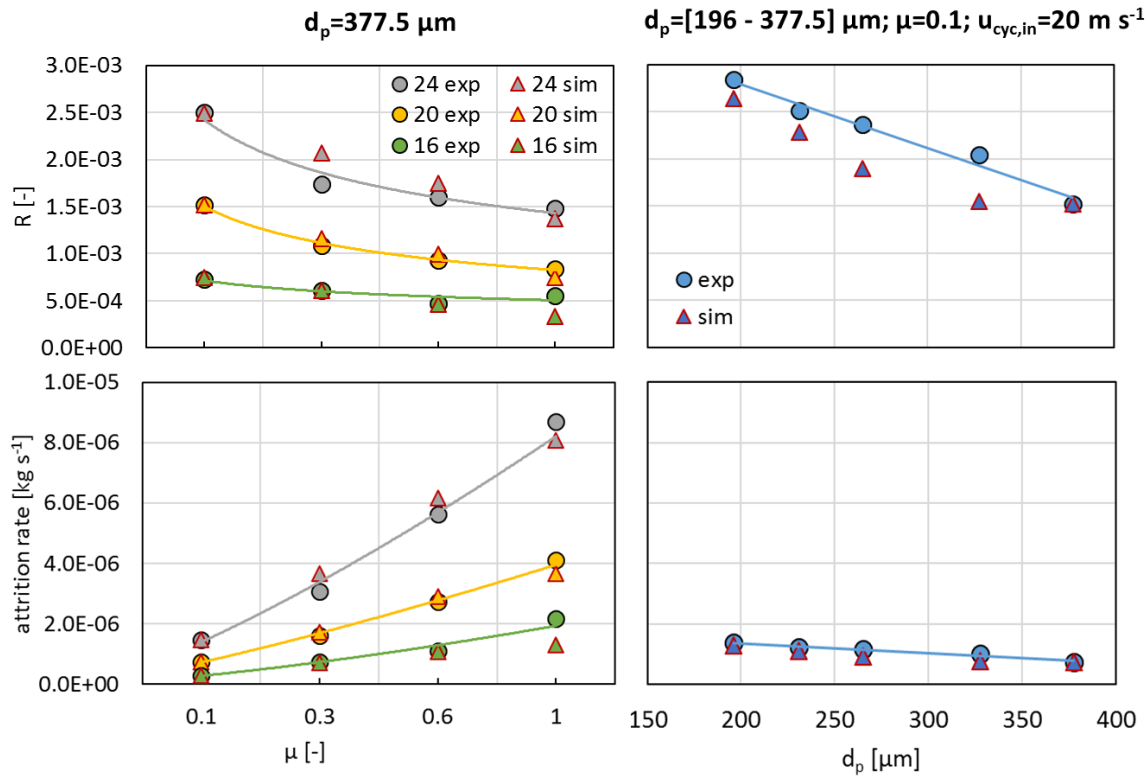

Figure 4-47. Comparison of the overall extent of attrition obtained by CFD-DEM study with the experimental results

The figure shows a fair agreement with the experimental results. This is remarkable because it confirms the validity of the methodology, the CFD-DEM simulations and the single particle models.

It is also important to understand the different trend of the extent of attrition as compared with the attrition rate. The attrition rate is higher for high solids loading simply because the rate of solids entering the cyclone is higher, therefore producing attrition more rapidly.

The power dependencies of the gas inlet velocity, solids loading and particle size are obtained and compared below, in Table 4-4, showing a remarkable agreement with the experimental results. It is important to notice the agreement of the power indices of the gas inlet velocity and solids loading of Reppenhagen and Werther, (2000) with those

obtained here by only considering the surface abrasion contribution. This can be a coincidence or better explained by recalling the way the authors measured attrition, mentioned in the literature review. They define attrition in terms of mass loss collected by the filter, therefore only the very fine particles, mainly produced by surface abrasion, are considered.

Table 4-4. Power dependency of particle size, gas inlet velocity and solids loading: as obtained from the experiments and CFD-DEM+single particle breakage in comparison with the model of (Reppenhagen and Werther, 2000)

material	comments	d_p^	$u_{cyc,in}$^	μ^
FCC (full PSD)	(Reppenhagen and Werther, 2000) Experimental	1	2	-0.5
MnO_2 (fixed size)	Experimental	-0.9	2.8	-0.2
MnO_2 (fixed size)	CFD-DEM+[Chipping, Surface Abrasion]	-0.9	2.9	-0.3
MnO_2 (fixed size)	CFD-DEM+[Chipping]	-1.2	2.9	-0.2
MnO_2 (fixed size)	CFD-DEM+[Surface Abrasion]	2.5	2.1	-0.5

The graph below, Figure 4-48, shows the extent of attrition plotted against the group $\alpha H/k_c^2 u_{cyc,in}^3 d_p^{-1} \mu^{-0.2}$ obtained by both experiments and simulations, unifying the results on a universal line. The trend is not expected to be the same if the particles of different sizes enter the cyclone at the same velocity, so the conclusion is unique to the set up and material used here.

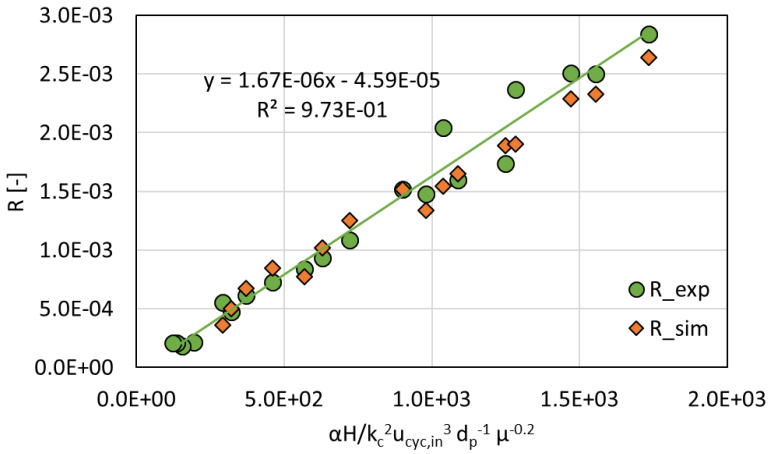

Figure 4-48. Overall cyclone extent of attrition plotted against the group $\alpha H/k_c^2 u_{cyc,in}^3 d_p^{-1} \mu^{-0.2}$: comparison between experimental and simulation results

4.4 Concluding Remarks

4.4.1 Experimental

Particle attrition in cyclone is evaluated experimentally for washed F-CLC particles using a high efficiency Stairmand cyclone. The experimental setup is similar to that used by Reppenhagen and Werther, (2000) where the cyclone is operated in suction mode so that the solids can be fed at the inlet pipe through a vibratory feeder. The extent of attrition is measured after each pass for a total of 20 passes. The effect of three main variables is studied, namely the gas inlet velocity (varied from 12 to 24 m s^{-1}), the solids loading (varied from 0.1 to 1) and the particle size (from 180 to 400 µm).

The experimental results show a decreasing of the extent of attrition with the number of passes. This behaviour is found the be the consequence of the accumulation of fines around the cyclone walls which mitigates attrition. Moreover, attrition is found to increase with the gas inlet velocity and decrease with the solids loading and particle size. The effect of particle size can be explained by accounting for the particles entrance effect, i.e. the pipe length is not sufficiently long to ensure a comparable entrance velocity for different particle sizes and as a result, small particles enter and impact with higher energy. More insights are given, in this regard, from the CFD-DEM analysis.

The Schumann's plot of the most severe cases reveal that the breakage pattern is determined by surface damage, i.e. chipping and surface abrasion. However, the PSD of debris at all conditions show the presence of some fragments.

The power indices of the gas inlet velocity, solids loading and particle size are found to be around 3, -0.2 and -1, respectively. By fitting with a straight line all data sets against the lumped parameter containing these dependencies and the single particle breakability index, the cyclone incipient velocity for attrition is defined as a function of the solids loading and particle size.

4.4.2 CFD-DEM

Four-way coupling CFD-DEM simulations of the same cyclone used for the experimental work are used to analyse the particles dynamics in such system. Mechanistic models for single particle breakage, describing breakage by chipping upon impact and surface abrasion for particles sliding against the wall, are used in combination with the

simulations to predict the local and overall attrition in the cyclone. Consistent with the experimental work, the effect of gas inlet velocity, solids loading and particle size is analysed.

A mesh independency study is carried out beforehand with reference on the global cyclone pressure drop which is found to be in good agreement with the experimental values. CFD simulations are carried out at different gas inlet velocity for verification purposes with the literature. The velocity profiles as well as the static pressure are found to have the typical established behaviour of a reverse flow cyclone. The conditions simulated in the CFD-DEM cases are the same as of the experimental work, except for the case at 12 m s^{-1}, using monodispersed spheres of same density as F-CLC.

The particle behaviour in the cyclone clearly reveals two mechanisms by which attrition occurs: (i) particle impact in the proximity of the entrance regions, and (ii) particle sliding against the wall along the cylindrical and conical body of the cyclone. The body of the cyclone is therefore subdivided into seven regions where different models of breakage are applied based on the particle dynamics at steady state. The particles dynamics are quantitatively described by the following parameters: particle impact energy and angle, number of P-W and P-P collisions, sliding distance and normal load acting on the particle.

P-W collisions in the entrance regions are found to be the main cause of attrition at low solids loading, however P-P collisions become as important as the former in case of high solids loading. Moreover, collisional attrition in the entrance region is found to decrease with the particle size. Small particles enter the cyclone at higher velocities and thus break to larger extent. A CFD-DEM analysis on the average particle velocity at the inlet pipe, at solids loading such as 0.1 and 10, for a mixture of different sizes and lengths of pipe, revealed that, although small, there is always a difference in entrance velocity for particles of different sizes. This is probably because the analysis has been carried out with relatively large and heavy particles. Thus, this conclusion is strictly valid for the range of particle sizes and density used in this work.

Particles sliding along the walls causes surface abrasion in the conical part of the cyclone mainly because the particles travel for longer paths. This occurrence is enhanced as the particle size is increased.

Collisional attrition is in general much greater than surface abrasion, dictating, in this way, the power dependencies of the three variables studied here: gas inlet velocity, solids loading and particle size. They are respectively equal to 2.9, -0.3 and -0.9, in good agreement with the experimental ones.

If only the attrition produced by surface abrasion is considered, the power indices resemble those found experimentally by Reppenhagen and Werther, (2000) who measured attrition, using FCC catalyst, as the steady state loss rate and therefore might have considered only the very fine parts of debris which are generated by surface abrasion.

5. JET ATTRITION IN FLUIDISED BEDS

CHAPTER 5

An extensive literature review about the fundamentals of jet attrition in fluidised beds is initially given. The various approaches and apparatus used to assess jet attrition are also discussed. It follows the description of the experimental setup and methodology used here to evaluate the jet attrition for F-CLC and E-CLC. The focus being establishing the dependency of jet attrition on jet velocity, orifice size and temperature. Attrition correlations are developed in order to be used later on in the population balance as breakage kernels.

This experimental work was carried out at IFP Energies Nouvelles's facilities across the 3rd and 4th year of this PhD project.

A CFD-DEM analysis of jet attrition on a small-scale simplified case is also carried out, and reported in the appendix section as incipient for further work.

5.1 Literature Review

5.1.1 Jet Induced Attrition

In a fluidised bed, the solids immediately surrounding the gas jets issuing from the perforated distributor, are entrained into the jets core. These particles are accelerated and collide with the particles near the tip of the jet. The production rate of fines for a single jet is independent of the mass of the fluidised bed surrounding it as long as is completely immersed in the bed, (Werther and Xi, 1993). Figure 5-1 depicts how the particles are peaked up and slammed into the fluidised bed, for an upwardly directed jet. Jet attrition only affects part of the bed which is limited by the jet penetration length.

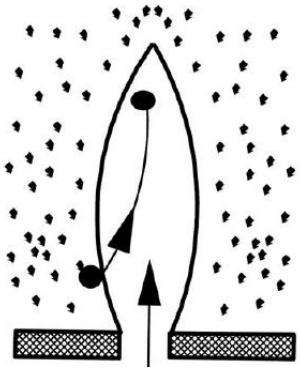

Figure 5-1. The mechanism of particle attrition in the jet region, (Karri and Werther, 2003)

It is usually difficult to separate the effect of jet attrition with that of the bubbling bed because the two phenomena are linked. Werther and Xi, (1993) tried to study the two phenomena separately. They used FCC catalyst and a Gwyn-type test apparatus, (Gwyn, 1969), where the porous plate is integrated with a fed nozzle. Measuring attrition in terms of fine loss, they fluidised the bed by the porous distributor and then by the fed nozzle and porous distributor together, keeping the same superficial velocity. Subtracting the two attrition rates, they worked out the jet induced attrition. They also found that, at steady state conditions, pure abrasion is the dominant mechanism of attrition in the jet region and thus developed a model considering the attrition rate to be a linear function of the rate of kinetic energy input of the gas equal to $\dot{m}_f \frac{u_{jet}^2}{2}$, leading to an overall dependency to the gas jet velocity of the power of 3, since $\dot{m}_f = \rho_f \frac{\pi d_{or}^2}{4} u_{jet}$. The model is shown in Equation 5-1.

$$r_{jet} = n_{or} C_{jet} d_p \rho_p d_{or}^2 u_{jet}^3 \qquad (5\text{-}1)$$

where n_{or} is the number of orifices, C_j a constant of attrition, ρ_p the particle density and d_{or} the orifice diameter.

Ghadiri et al. (1994**)** further investigated this dependency considering the jet attrition to arise from particles colliding with a slow-moving bed of particles at the top of the jet. They recognised attrition in the jet region to be the result of two fundamental contributions: (i) the particle physical properties which dictate the dependence of attrition on impact velocity, and (ii) the jet hydrodynamics which dictate the particle velocity in

the jet and rate of entrainment of the particles into the jet. Therefore, they used the single particle impact test of Zhang and Ghadiri (2002) to evaluate the single particle breakage propensity of the same FCC catalyst of Werther and Xi (1993), then calculated the jet length using the correlation of Yates et al. (1986). They used these information in combination with the model of jet hydrodynamics of Donsi et al. (1980), to work out the maximum velocity of the particles at the top of the jet length for a range of gas velocity of 25-100 m s^{-1}. Their analysis suggested a power index of the orifice velocity of 3.55 which is in fair agreement with Werther and Xi, (1993) who suggested 3.

Ghadiri et al.(1992) also studied attrition of Geldart group B particles such as common salt crystals using a Forsythe and Hertwig apparatus, (Forsythe WL, 1949), finding the power index to be different from FCC catalyst and equal to 5.1. This might be due to different particle dynamics such as rate of entrainment within the jet and frequency of collisions dictating, in this way, the overall power dependencies.

Zhang et al. (1998) and Boerefijn et al. (1998**)** studied the effect of the orifice size, d_{or}, and confirmed the assumption of Ghadiri et al. (1994), about attrition arising from inter-particle collision at the top of the jet, under the condition that the particle size is much smaller than the size of the orifice. On the contrary, when the orifice size is comparable with the particle size, the particles are subjected to rapid bulk shear. Figure 5-2 illustrates how, according to Boerefijn et al. (2000), the orifice-to-particle size ratio, d_{or}/d_p, can affect the breakage mechanism of FCC particles. In particular, they found the power of the orifice size to be 1.63 and 0.63 for fresh and equilibrium FCC catalyst, respectively. This is in contrast with Werther and Xi, (1993) and Zenz and Kelleher, (1980) who both found a power index of 2, for equilibrium FCC catalyst and fresh HA-HPV.

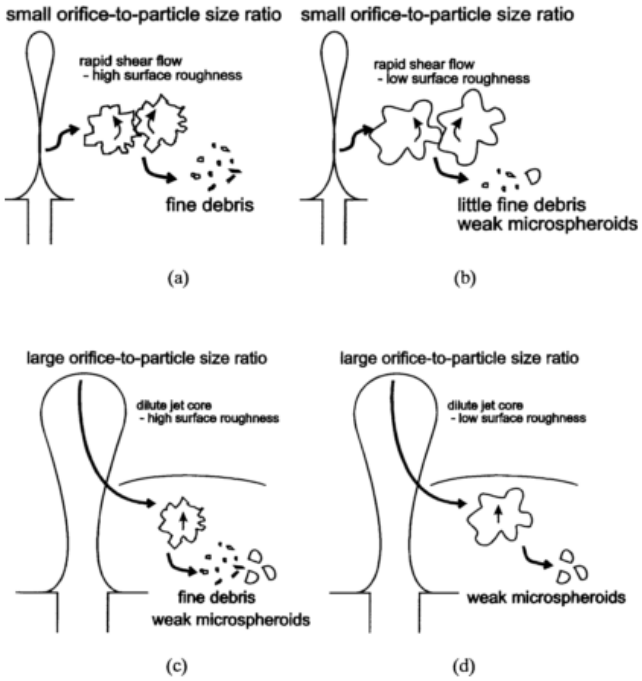

Figure 5-2. Breakage mechanism of FCC. (a) small d_{or}/d_p, fresh FCC; (b) d_{or}/d_p, used FCC; (c) large d_{or}/d_p, fresh FCC; and (d) large d_{or}/d_p, used FCC, Boerefijn et al. (2000)

Zhang et al. (2016) characterised experimentally the overall attrition rate of a fluidised bed of both group A and B particles as the summation of bubble-induced and jet-induced attrition. The jet attrition, for group B particles, was found to correlate with both the orifice velocity, and the orifice size to the power of 2, as shown in Equation 5-2.

$$r_{jet} = C_{jet} n_{or} d_{or}^2 u_{jet}^2 \tag{5-2}$$

where C_{jet} is the attrition constant.

The same square dependency on the jet velocity is found by Chen et al. (1980) who studied the jet attrition of iron ore and lignite char using the same setup of Werther and Xi, (1993), a single jet, of size range between 1.47 to 3.18 mm, at the centre of a porous distributor.

Asiedu-Boateng et al. (2016) introduced the critical jet velocity below which attrition is negligible. Depending on this value, the fitting of the experimental results can give the power index of the normalised excess jet velocity from 2 to 4. Although the particle size dependency is not in the model, they obtained more attrition for larger particles supporting the findings of Werther and Xi (1993) and Boerefijn et al. (2000) who found

a linear relationship with the particle size, d_p. This is also in accordance with Welt et al. (1977) who, like Ghadiri et al. (1994**)**, assumed jet attrition as mainly originated from particle colliding at the same velocity and hence obtain the linear dependency with particles size as given by the ratio of kinetic energy upon impact, proportional to d_p^3, and the surface area formation by particle fracturing, proportional to d_p^2. This is in contrast with Jones et al. (2017) who, using the ASTM standard attrition apparatus, found smaller particles of pumice to be more prone to attrition than large particles given their higher propensity of being entrained within the gas jet.

Temperature and pressure also effect jet attrition. When increasing the temperature, the gas jet momentum which is responsible for attrition (proportional to $\rho_f \cdot u_{jet}$) decreases, because for the same jet velocity, the gas density decreases. Thus, the jet penetration decreases and so does attrition. Similarly when the pressure is increased, the gas density increases, gas jet momentum increases and so do the jet penetration length and attrition, (Karri and Werther, 2003).

5.1.2 Bubbling Bed Induced Attrition

Particle attrition in the bubbling bed is caused by the rise of bubbles through the bed and generated by low velocity inter-particle collisions. It occurs only after the minimum fluidisation velocity is exceeded, (Arena et al. 1983). Therefore, the kinetic energy received by particles can be attributed to that portion of the gas energy exceeding minimum fluidisation. This phenomenon is enhanced in deep fluidised beds, with several meters of height, (Yang, 2003), however it is a minor source of attrition in the riser where the regime is fast fluidisation, (Kunii and Levenspiel, 1991). The most common approach to measure bubble-induced attrition is by using a porous plate as distributor avoiding any grid jets. Merrick and Highley, (1974) developed a theoretical model based on the proportionality between the rate of energy input and the rate of creation of new surface by abrasion. The total rate of input of energy to the bubbling bed is equal to $u_{sup} \cdot m_{bed} \cdot g$ and is given by the product of the volumetric flow rate (equal to $u_{sup} \cdot A_{bed}$) with the pressure drop, expressed as the weight of the bed divided the bed cross section (m_{bed}/A_{bed}). By subtracting the rate of energy needed to keep the solids fluidised, the rate of input energy available for bubble formation, and thus attrition, is given by the excess gas velocity leading to the following attrition rate expression, Equation 5-3

$$r_{bb} = C_{bb}\, m_{bed}(u_{sup} - u_{mf}) \tag{5-3}$$

where C_{bb} is an attrition constant and m_{bed} is the bed mass. Zhang et al. (2016) experimentally confirmed this model and introduced the bed diameter into the model, d_{bed}, as shown in Equation 5-4

$$r_{bb} = C_{bb}\, \gamma \frac{m_{bed}}{d_{bed}}(u_{sup} - u_{mf}) \tag{5-4}$$

where C_{bb} is an attrition constant and γ is a non-dimensional bubble-through factor. Moreover, the authors found r_{bb} to have an inverse proportionality with particle size for both Geldart group A and B particles, contradicting the direct proportionality proposed by Xi, (1993) with FCC catalyst.

Werther et al. (1999) assessed the bubbling bed attrition using a Gwyn type fluidised bed apparatus, (Gwyn, 1969), and fresh FCC catalyst finding it to be a function of the excess gas velocity to the power of 3, $(u_{sup}-u_{mf})^3$, and linearly dependent with the bed mass. The model was then improved by Xi, (1993), introducing a linear dependency on particle size, as shown below in Equation 5-5:

$$r_{bb} = C_{bb} d_p\, m_{bed}(u_{sup} - u_{mf})^3 \tag{5-5}$$

On the contrary, Donsi et al. (1981), Arena et al. (1983), Ray and Jiang, (1987), Chirone et al. (1991) found the bubbling bed attrition to be a function of the exposed surface area of the bed proportional to the mass of the bed over the bed Sauter mean diameter, $m_{bed}/d_{p,saut}$. The normalised attrition rate, $\dot{R}_{bb}$, obtained by normalising with m_{bed}, would then return an inverse relationship with particle size, as shown below:

$$\dot{R}_{bb} \propto \frac{(u_{sup} - u_{mf})}{d_p} \tag{5-6}$$

There is still a dispute though regarding the dependence of the bed height as, for example, Pis et al. (1991) found that the bed height is not influential on the attrition rate, while the models reported previously clearly show a linear dependency on the bed mass, which reflects the height of the bed.

As appeared by this literature survey, most of the bubble-induced attrition rates can be summarised in the following form:

$$r_{bb} = C_{bb} d_p^h m_{bed}^m (u_{sup} - u_{mf})^n \quad (5\text{-}7)$$

5.1.3 Assessment of Jet and Bubbling Bed Induced Attrition

Assessment of particle attrition at the bulk level due to the jet and the bubbling bed is mainly carried out in lab scale fluidised bed apparatus reasonably resembling the attrition mechanisms of a real process. Other bulk tests are useful to compare the relative attrition resistance of different material, like the jet cup. Attrition, as reported next, can be measured in different ways. In case of fluidised bed tests, it is usually given by the steady state loss rate while in many other applications either by the increase of fines extent by sieving analysis or by the increase of the surface area.

The jet cup consists of a small cup which confines the solids and provides a high velocity air flow issued tangentially into the cup for a certain period of time, Figure 5-3

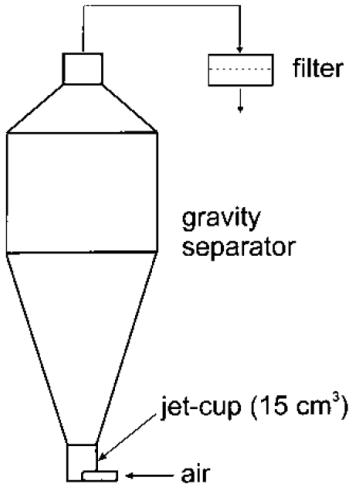

Figure 5-3. Grace-Davison jet cup, (Pell, 1990)

Dessalces et al. (1994) consider that the stress occurring in the jet cup is similar to that prevailing in gas cyclones. In the Grace-Davison type the Davison Index (DI) is determined by measuring the increase in the weight fraction of particles below 20 μm in one hour, Yang (2003). Often the jet cup is customised. Ray Cocco et al.(2010) proposed a cylindrical and conical jet cup. Amblard et al. (2015) compared the attrition results for an equilibrium FCC catalyst and fresh oxygen carrier particles using a customised Jet Cup which prevailing stresses were revealed by a CFD simulation. They defined a new attrition index that is based on the total percentage of particles generated by attrition which is called TPGI (Total Particles Generated Index). The TPGI was found to increase

at increasing air jet velocity. Further increase of the latter would lead to a more severe type of attrition as demonstrated by the change in slope of the attrition index. The experiments assessed that the oxygen carrier resulted to be more resistant than the FCC catalyst. By CFD analysis they concluded that different materials undergo the same stresses if the same volume of solids is used. Rydén et al. (2014) used a customised jet-cup to test the attrition resistance of 25 types of fresh and equilibrium CLC oxygen carriers, admitting themselves that the crushing strength is not a good index of attrition. They concluded that there is always a difference in attrition between fresh and equilibrium material, generally being the fresh material usually more prone to breakage. They refer to the normalised attrition rate as A_{tot} and A_i:

$$\begin{aligned} A_{tot} &= 100\left(m_{filter,t=60\,min} - m_{f,t=0}\right)/m_{solids} \\ A_i &= 100\frac{60}{30}\left(m_{filter,t=60\,min} - m_{f,t=30\,min}\right)/m_{solids} \end{aligned} \quad (5\text{-}8)$$

where $m_{filter,t}$ is the weight of the filter at a certain time and m_{solids} the total mass of solids used.

A_i and A_{tot} were found to have a linear trend at steady state for both fresh and equilibrium material, as shown in Figure 5-4. The difference between the fresh and equilibrium material, even though they have the same chemical composition, can be due to change in particle porosity and therefore density caused by densification due to thermal sintering.

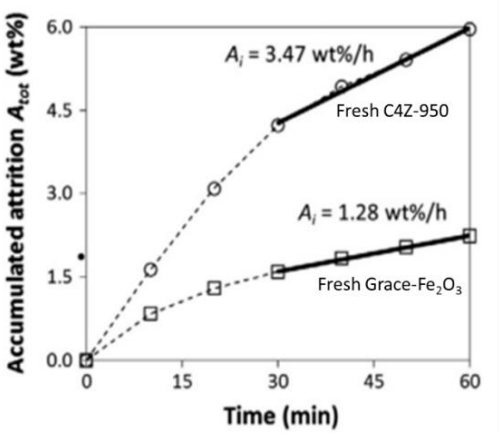

Figure 5-4. Attrition curve of fresh C4Z-950 and fresh Grace-Fe_2O_3 particles, obtained by (Rydén et al. 2014), using a customised jet cup

Fluidised bed tests are usually used for both purposes of evaluating the catalyst friability**,** Forsythe et al. (1949)**,** and investigating the attrition mechanism, Werther (1993). The

principle is to create high attrition rates in the catalyst bed by issuing high-velocity gas jets for a short period of time. It should be noted that using this method, a direct comparison between different materials is not straightforward even if the gas flow and the temperature are kept constant, because the density of the particles affects their propensity to be elutriated. The majority of tests are carried out with (i) the AJI-ASTM standard test equipment, (ASTM, 2013), (ii) the Forsythe apparatus of Forsythe et al. (1949) and (iii) the Gwyn-type apparatus of Gwyn (1969). The former and the latter are equipped with three orifices of diameter of 0.381 and 1 mm, respectively. In both cases the attrition index is given by the steady state elutriation rate. In particular the ASTM standard test defines attrition, the AJI index, as the ratio of the mass of fines collected after 5 hours of operation and the mass of sample loaded in the apparatus, as shown in Equation 5-9:

$$AJI = 100 \cdot \frac{m_{fines,5h}}{m_{solids}} \tag{5-9}$$

On the other hand, the Forsythe's apparatus is provided with a single orifice and the attrition index is given by the percentage increase of mass of particles smaller than 44 μm, obtained by sieving. The elutriated fines in this case are not removed from the system therefore might alter attrition by cushioning effect.

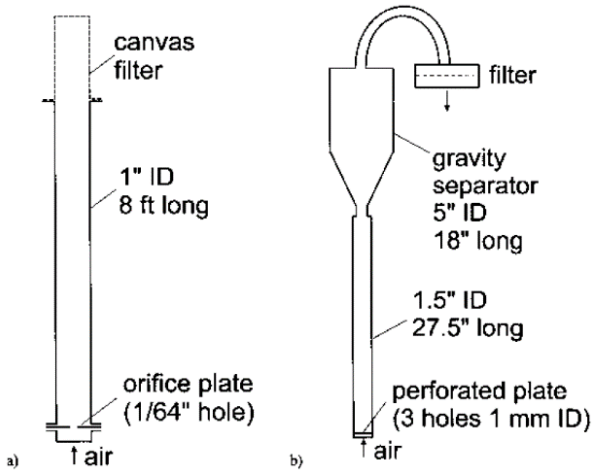

Figure 5-5. a) Forsythe and Hertwig apparatus. b) Gwyn-type jet test

It is common practice to use in-house built apparatus for attrition test. Materic et al. (2014) developed an ICFB (internally circulating fluidised bed) to evaluate particle attrition

occurring in the calcium looping sorbents. Linderholm et al. (2009) used a lab scale circulating fluidised bed at both cold and hot temperature to measure attrition.

Cabello et al. (2016) compared the attrition resistance of 23 CLC candidate oxygen carriers by testing them in a 500 W_{th} CLC hot pilot plant working out the normalised attrition rate as reported in Equation 5-10:

$$A = \frac{m_{fines}}{m_{bed}\Delta t} \cdot 3600 \cdot 100 \tag{5-10}$$

where m_{fines} is the weight of the elutriated particles of size lower than 45 μm, m_{bed} is the total weight of solids inventory in the plant and Δt is the interval of time.

They had preliminarily analysed their crushing strength using the Shimpo FGN–5X apparatus and attrition by mean the AJI-ASTM test. Using the latter, they found that the steady state attrition rate is achieved after 20 h, for the fresh copper-based oxygen carrier. In general, all the oxygen carrier types, mainly nickel, copper and iron-based show an increase in the AJI index after they have been processed in the CLC hot pilot, except for the manganese-based. This can be due change in mechanical properties caused by the chemical reaction and thermal stresses.

The fresh materials analysis reveals that three Fe-based and all Mn-based oxygen carriers resulted to be the worst candidates as determined by their low crushing strength and high AJI index.

5.1.4 Computational Modelling

Computational modelling has been widely used recently to simulate complex systems. CFD-DEM was used by Xu and Yu, (1997) to simulate a pseudo-three dimensional bed, fluidised by a central jet. Xu et al. (2014) used CFD-DEM to simulate the reduction in particle size due to attrition in a 2D jet cup by using the chipping model of Ghadiri and Zhang, (2002) and surface abrasion of Archard and Charj, (1953) calculating the new particle size after attrition as shown below:

$$d_p^{new} = d_p^{old}\left(1 - R_{GZ} - R_A\right)^{1/3} \tag{5-11}$$

and investigated the effect of the jet velocity, particle density and size. Fries et al. (2013) used CFD-DEM simulations to describe the collision dynamics in a fluidised bed

granulator, using criteria such as particle impact velocity, and frequency of particles impacts which dictates the growth rate by agglomeration.

Amblard et al. (2015) and R. Cocco et al. (2010) simulated the gas/solid behaviour in the jet-cup employing the multiphase particle-in-cell (MP-PIC) numerical method to investigate the portion of material that is hydrodynamically active. They found that to compare the attrition resistance of particles with different properties (particle size distribution, density), the jet cup test should be carried out at the same total volume of particles to have the same circulation of particles in the jet.

Zhang et al. (2008) and Pougatch et al. (2010) used instead the Eulerian-Eulerian approach (or two-fluid model), where the different phases are treated mathematically as inter-penetrating continua. The former authors looked at the fluidisation quality of Geldart type A and B particles in a 3-dimensional fluidised bed. The latter simulated particle attrition in fluidised bed induced by a supersonic gas jet by using Ghadiri and Zhang, (2002) model of chipping along with a breakage probability function assisted by the kinetic theory of granular flow (KTGF) to track particle collisions.

5.1.5 Motivation and Objectives

The gas jets and bubbling bed are major contributors to the overall attrition occurring in a circulating fluidised bed system. Several theoretical models have been proposed in the literature, most of them are based on the assumptions that the energy utilised for attrition is simply a fraction of the total kinetic energy required for the fluidisation. Some authors have confirmed this by evaluating the jet and bubbling bed attrition by experiments, using different equipment designs. Jet attrition is often evaluated as the steady state loss rate because initially some pre-existing fines of the bed inventory and the surface roughness of the fresh particles would lead to a much greater, and time-dependent, attrition rate. Moreover, it has been observed that there is always difference between the jet attrition of fresh and equilibrium catalysts, being the equilibrium less prone to attrition. This effect has not yet been studied for manganese-based oxygen carrier so in the next section a series of tests are performed on a semi-pilot scale fluidised bed in order to study their relative tendency to jet attrition, by varying the jet velocities and orifice size.

Given the relatively large scale of the fluidised bed utilised in this research project for the jet attrition assessment, the CFD-DEM approach would have been very computationally expensive and time consuming. However, a simplified case of a small fluidised bed has been simulated by CFD-DEM and reported in the Appendix for the sake of consistency with the methodology proposed in this research project.

5.2 Experimental Setup

The assessment of the jet attrition, for the two materials, is carried out on two pilot fluidised beds of the same dimensions. One runs with air, at room temperature, referred to as "COLD pilot", the other with nitrogen, is able to reach temperatures of 800°C and is referred to as "HOT pilot". The former is made of Perspex, and therefore transparent, while the latter of stainless steel. The setup is similar to that of Werther and Xi, (1993) and Chen et al. (1980): fluidisation is provided by a single jet and by a porous base which has the orifice at its centre. The dimensions and other characteristics of the COLD pilot, identical to those of the HOT pilot, are reported in Figure 5-6. The porous base through which the background fluidisation is provided, shown in Figure 5-7, is made of bronze and stainless steel for COLD and HOT pilot, respectively, and has a porosity of 5 μm. The pressure drop can be measured at different heights of the column. In particular, the value of ΔP_2 indicates the pressure drop across the whole bed and is used to characterise the fluidisation curve and estimate the minimum fluidisation velocity. The filtration system is schematically shown in Figure 5-8. The sleeve filter is held inside of a perforated aluminium shell which is itself contained in a metal housing.

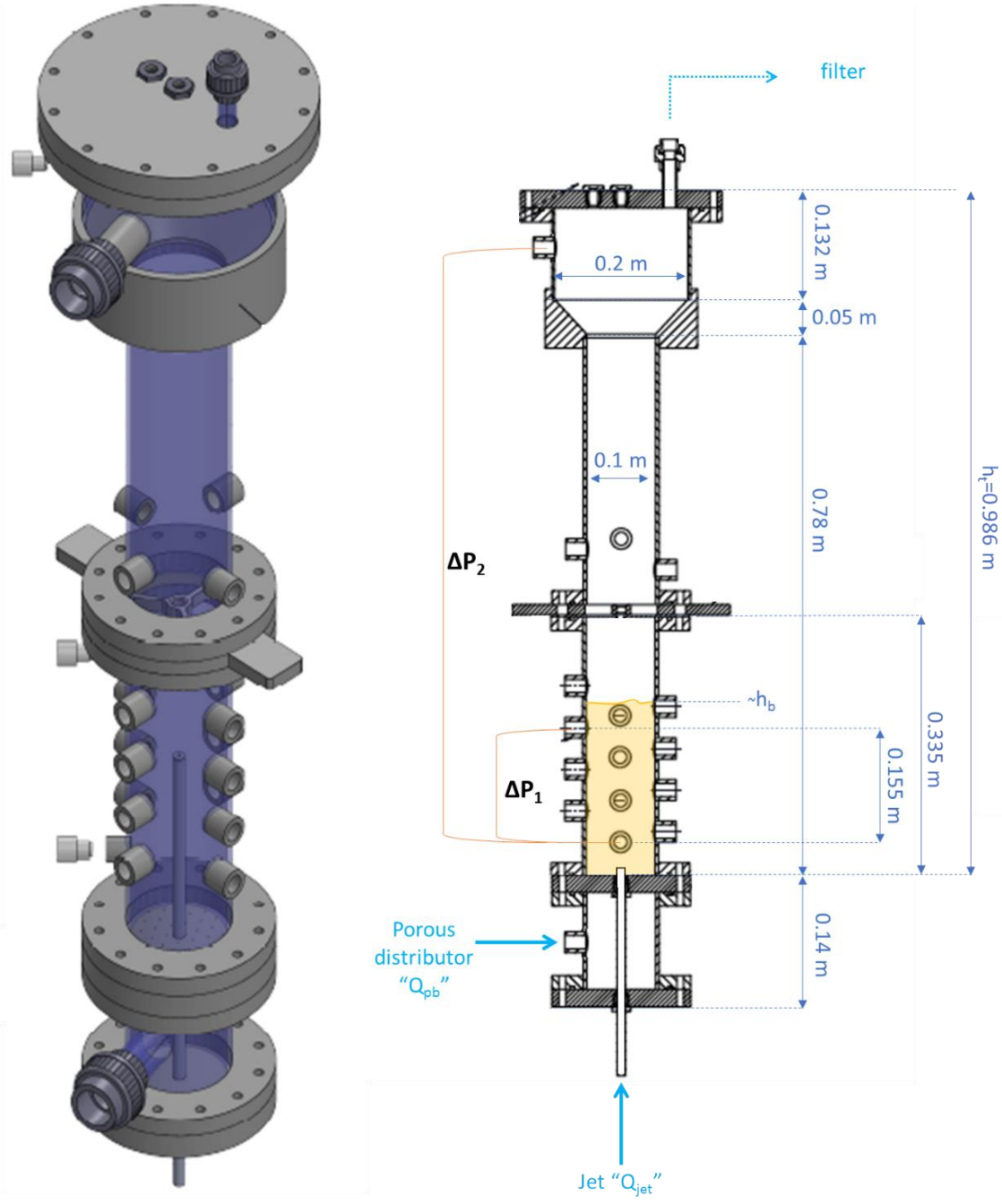

Figure 5-6. On the left: realistic representation of the "COLD Pilot". On the right: schematic representation of the "COLD Pilot"

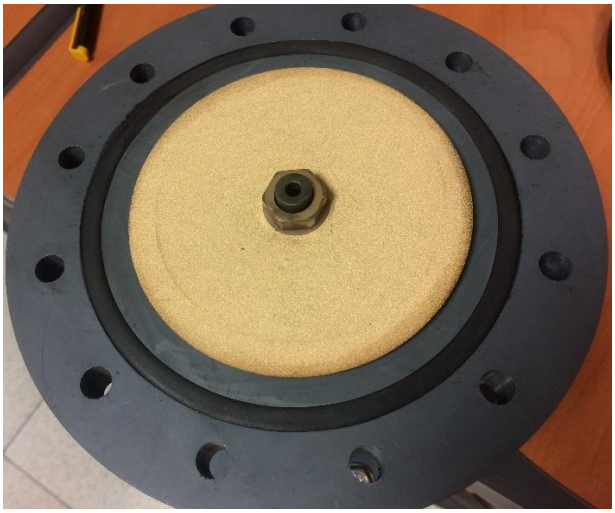

Figure 5-7. Porous distributor and the single jet of 5 mm diameter at its centre.

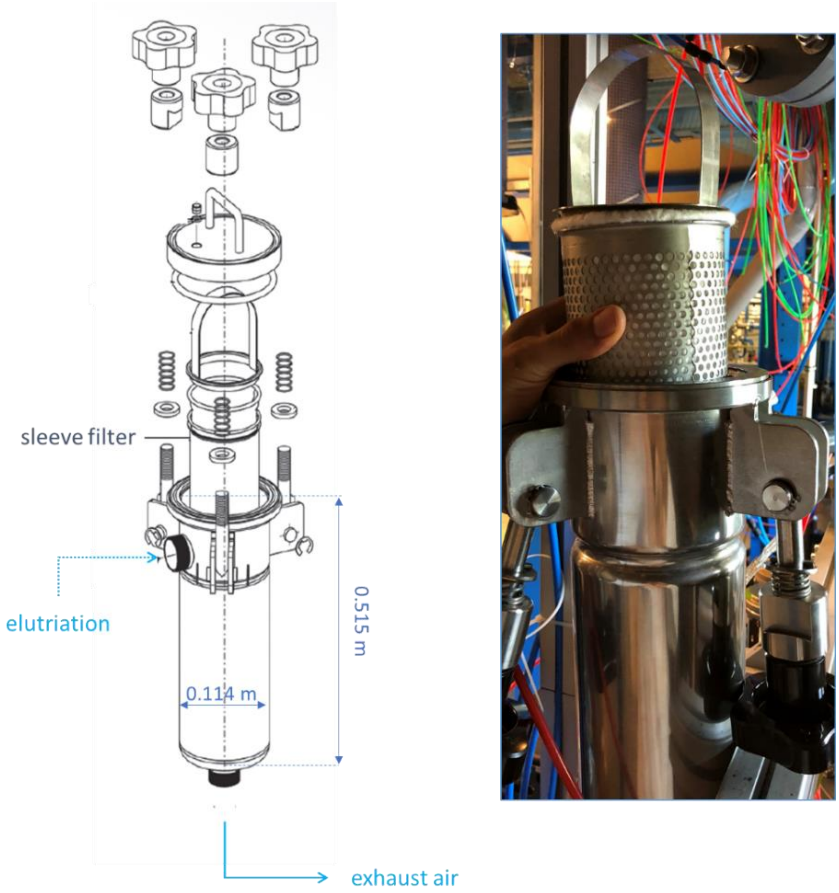

Figure 5-8. On the left: schematic representation of the filtering system. On the right: the actual filtering system.

5.3 Experimental Methodology

Attrition is characterised here as the steady state normalised loss rate, which is equal to the attrition rate provided that the TDH is exceeded, (Gwyn, 1969; Werther and Xi, 1993; ASTM, 2013; Cabello et al. 2016). The loss rate is evaluated by monitoring the increase in weight of the sleeve filter, Δm_{filter}, made of a multilayer 5 micron mesh sheet of PTFE (Polytetrafluoroethylene), mounted at the exit of the column, Figure 5-8. The normalised attrition rate, $\dot{R}_{FB}$, is then calculated as described by Equation 5-12:

$$\dot{R}_{FB} = \frac{\Delta m_{filter}}{m_{bed}\Delta t} \tag{5-12}$$

where m_{bed} is the mass of the bed inventory at the time of the measurement, calculated according to Equation 5-13:

$$m_{bed} = m_{bed,0} - \sum_{t=0}^{t} \Delta m_{filter} \tag{5-13}$$

There is no absolute way of establishing when a steady loss rates is reached. Here, the relative percentage error "*e*", of two near points of $\dot{R}$, calculated according to Equation 5-14, is considered as an indicator of the condition of steady state. When this is less than 15%, for at least two consecutive values, steady state is assumed to be reached, and the loss rate is considered as attrition. It should be noted that the value of 15% is arbitrary and chosen post experiments considering the fluctuations of the measurement. The duration of an experiment is determined by how quickly the steady state is reached (usually days).

$$e = \frac{\left|\dot{R}\big|_{t+\Delta t} - \dot{R}\big|_{t}\right|}{\text{mean}\left(\dot{R}\big|_{t+\Delta t}, \dot{R}\big|_{t}\right)} \times 100 \tag{5-14}$$

For experiments carried out at room temperature with one material and one type of fluid, the superficial velocity is kept constant by complementarily varying the gas flow rate of the jet and the porous base to achieve the desired jet velocity. In this way, the comparison of the results obtained at different orifice sizes and velocities is consistent.

The bubbling bed attrition contribution is assumed to be constant at all conditions and not as important as the jet, (Werther and Xi, 1993). Therefore, the jet-induced normalised

attrition rate is evaluated by subtracting the bubbling bed attrition, obtained by fluidising the bed only with the porous base, to the total attrition rate in the presence of the jet as shown below, in Equation 5-15:

$$\dot{R}_{jet} = \dot{R}_{tot} - \dot{R}_{bb} \tag{5-15}$$

For experiments carried out at different temperatures, fluid types and materials, keeping the same superficial velocity would not allow to compare the attrition results. In fact, since attrition here is measured as the steady state loss rate, the entrainment potential should always remain constant. For this reason, a theoretical criterion is used here: the superficial gas velocity u_{sup} is always set to be equal to the terminal velocity, $v_{p,\infty}$, of a fixed particle size, $d_{p,\infty}$, at all conditions. The motivation behind the choice of $d_{p,\infty}$ is discussed in the next paragraph 5-17. The superficial velocity associated to this critical particle size is calculated as follows, (Tilton, 2008), according to Equation 5-16:

$$u_{sup} = v_{p,\infty} = \sqrt{\frac{4 g d_{p,\infty} \left(\rho_p - \rho_f\right)}{3 \rho_f C_D}} \tag{5-16}$$

where the drag coefficient C_D is calculated as

$$\begin{cases} Re_{p,\infty} < 0.1 & C_D = \dfrac{24}{Re_{p,\infty}} \\ 0.1 < Re_{p,\infty} < 1{,}000 & C_D = \left(\dfrac{24}{Re_{p,\infty}}\right)\left(1 + 0.14\, Re_{p,\infty}^{0.7}\right) \\ 1{,}000 < Re_{p,\infty} < 350{,}000 & C_D = 0.445 \end{cases} \tag{5-17}$$

by knowing the Reynolds number, $Re_{p,\infty}$:

$$Re_{p,\infty} = \frac{\rho_f d_p u_{sup}}{\mu_f} \tag{5-18}$$

Three main batches, each 3.2 kg, comprising the full PSD of the material are used to carry out three main tests formalised as EXP 1, EXP 2 and EXP3. The former two aim at establishing the dependency on the jet velocity and orifice size for F-CLC and E-CLC, respectively. EXP 3 is carried out to check the effect of temperature on F-CLC. A summary of the three experiments is shown in Table 5-1. The choice of the amount of

test material and the experimental operating conditions is discussed in the next paragraph 5-17.

Table 5-1. Batches used for the jet-induced attrition test

	EXP 1	**EXP 2**	**EXP 3 (in the appendix)**
	Batch 1	*Batch 2*	*Batch 3*
Material	F-CLC full PSD	E-CLC full PSD	F-CLC full PSD
Assessment	effect of u_{jet} and d_{or}	effect of u_{jet} and d_{or}	effect of T
Temperature	room	room	from room to 800°
Equipment	COLD pilot	COLD pilot	HOT pilot

For "EXP 1" and "EXP 2", each time, before u_{jet} is changed, fluidisation is provided only by using the porous base. This was initially done to check the effect of fluidisation history on attrition, but later on also used as a pre-conditioning phase. Measurements are taken twice a day, one in the morning and one in the evening.

5.3.1 Optimal Experimental Conditions

The choice of the experimental conditions and the amount of test material should be coherent with the considerations presented below, where h_{tot}, h_{bed}, h_{jet}, Q_{pb} and Q_{mf} are the total height of the column, the height of the bed free surface, the jet height, the background flow rate through the porous base and the minimum fluidisation flow rate, respectively:

a) TDH < h_{tot}-h_{bed}, the freeboard height should be larger than the transport disengaging height to consistently relate the loss rate to the attrition rate as otherwise large particle could be entrained. TDH is estimated by the correlation of Sciazko et al. (1991) shown below, using the Sauter mean diameter of the bed and the superficial velocity at the expansion section of the column:

$$TDH = \frac{1500\, h_{bed}\, Re_p}{Ar} \tag{5-19}$$

where Re_p and Ar are the Reynolds and the Archimede's number defined respectively in Equation 5-18 and Equation 5-20:

$$Ar = g d_p^3 \rho_f \frac{\left(\rho_p - \rho_f\right)}{\mu_f^2} \quad (5\text{-}20)$$

This is achieved by using either a low u_{sup} and/or a small amount of solids.

b) $h_{bed} >> h_{jet}$, this allows to get a fully submerged and stable jet and the formation of a bubbling region. This is achieved by using either low u_{sup} and/or a big amount of solids. The jet height is calculated according to the correlation of Merry, (1975) who has successfully validated it for material with similar size and density as the one at hand:

$$\frac{h_{jet}}{d_{or}} = 5.2\left(\frac{\rho_f d_{or}}{\rho_p d_p}\right)^{0.3}\left[1.3\left(\frac{u_{jet}^2}{g d_p}\right) - 1\right] \quad (5\text{-}21)$$

c) u_{jet} should be as high as possible to induce attrition and obtain a measurable loss rate within a reasonable interval of time. This is achieved by using high u_{sup}.

d) h_{bed} should be less than about twice the bed diameter to avoid undesired slugging, (Yang, 2003). This is achieved by using a small amount of solids and low u_{sup}.

e) $Q_{pb} \geq Q_{mf}$, the background fluidisation, provided by the porous base, should at least be equal to the flow rate of minimum fluidisation to avoid stagnant solids. This is achieved by using high $u_{sup.}$

Some of these criteria are in conflict with each other so a window of operating conditions needs to be identified where the all the criteria are respected.

In order to comply with the point "e", the fluidisation curves of both material are found experimentally by only using the porous distributor, at room temperature, and reported for F-CLC and E-CLC, in Figure 5-9 and Figure 5-10, respectively:

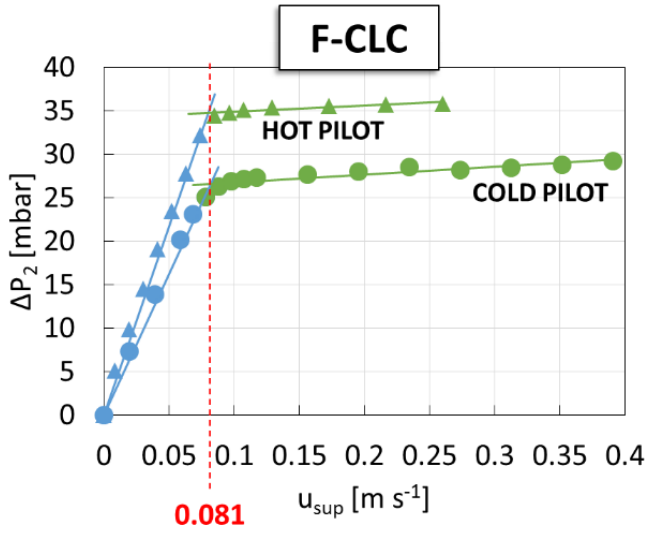

Figure 5-9. Fluidisation curve of F-CLC at room temperature

As shown, the minimum fluidisation velocity is obtained from the intercept of the curve of the fixed bed pressure drop with that of the fluidised bed. For F-CLC, the material is tested in both COLD and HOT pilot, at room temperature, showing consistent results. The cause of the different values of pressure drop for the two systems is that the base point where the pressure is measured is different, being closer to the porous distributor in case of the HOT pilot.

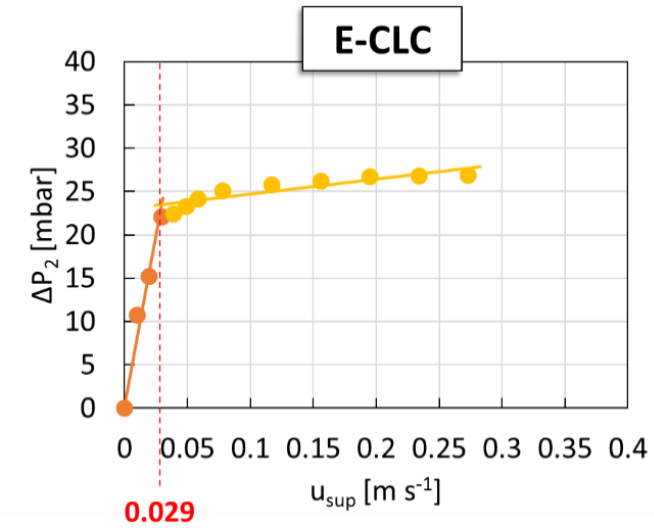

Figure 5-10. Fluidisation curve of E-CLC at room temperature

The values obtained experimentally are compared with the theoretical values calculated with the correlation of Baeyens and Geldart, (1986), given in Equation 5-22 , and reported in Table 5-2, showing a fair agreement.

$$u_{mf} = \frac{0.0009\left(\rho_p - \rho_f\right)^{0.934} g^{0.934} d_{p,saut}^{1.8}}{\mu_f^{0.87} \rho_f^{0.006}} \quad (5\text{-}22)$$

Table 5-2. Comparison between experimental and theoretical minimum fluidisation velocities for F-CLC and E-CLC at room temperature

	$Q_{mf,\,exp}$ [m^3 s^{-1}]	$u_{mf,\,exp}$ [m s^{-1}]	$u_{mf,theor}$ [m s^{-1}]
F-CLC	0.00063	0.081 m s^{-1}	0.069 m s^{-1}
E-CLC	0.00023	0.029 m s^{-1}	0.026 m s^{-1}

On the base of these preliminary observations, after 1-2 months of trials and error where different configurations are tested, the best compromise is found for a mass of 3.2 kg and a $d_{p,\infty}$ of 53 μm which, at room temperature, gives a superficial velocity of 0.243 m s^{-1}. In this way, the TDH is below the freeboard height, no slugging is observed, and the jet velocity can be set as high as 55 m s^{-1}.

For F-CLC (EXP 1) and E-CLC (EXP 2), at room temperature using the COLD pilot, the jet velocities tested are 30, 42.5, 48.75 and 55 m s^{-1} while the orifice diameters tested are 3, 4, and 5 mm. Moreover, for F-CLC, attrition tests are conducted on the HOT Pilot without jet at 200, 400 and 600°C, (EXP 3).

The details of the three tests EXP 1, EXP 2 and EXP 3 are reported in details in Table 5-3, Table 5-4 and Table A-2, respectively. In the same order, the gas flow rates of jet and porous base used for three experiments are graphically reported in Figure 5-11, Figure 5-12 and Figure A-8. It is here recalled that as the jet velocity is increased, the background gas flow rate is reduced in order to keep the superficial velocity constant.

Table 5-3. Experimental conditions for F-CLC to look at the effect of jet velocity and orifice size, at room temperature

EXP 1 (*Batch 1* full PSD F-CLC)							
T [°C]	***room***						
$\mathbf{u_{jet}}$ [m s^{-1}]	***0***	***30***	***42.5***	***48.75***	***55***		
d_{or} [mm]	5				3	4	5
h_{jet_theor} [m]	0	0.0482	0.0562	0.0597	0.0362	0.0495	0.063
Q_{jet} [m^3 s^{-1}]	0	0.00059	0.00083	0.00096	0.00039	0.0006	0.00108
Q_{pb} [m^3 s^{-1}]	0.00189	0.00130	0.00106	0.00093	0.00150	0.001209	0.00081
Q_{tot} [m^3 s^{-1}]	0.0189						
$d_{p,\infty}$ [µm]	53						
u_{sup} [m s^{-1}]	0.243						
u_{sup}/u_{mf_exp}	3						
u_{sup}/u_{mf_theor}	3.5						
$m_{bed,0}$ [kg]	3.2						
TDH_{theor} [m]	0.260						
$h_{bed,exp}$ [m]	0.243						
h_{tot}-h_{bed} [m]	0.743						

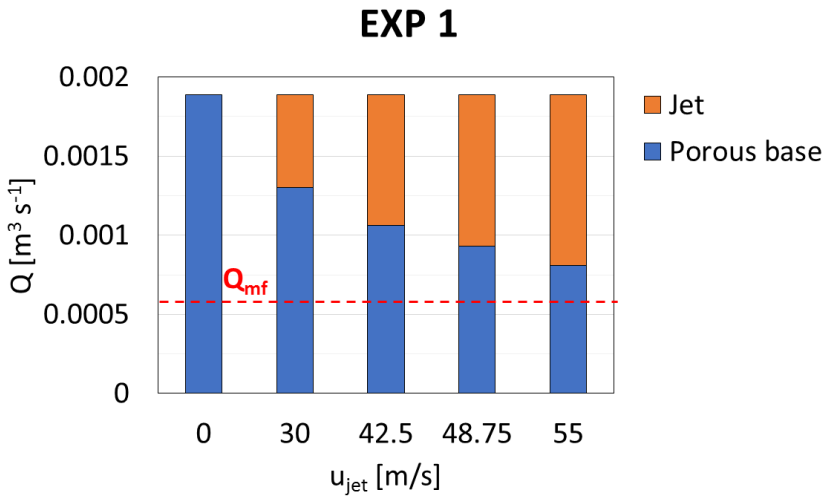

Figure 5-11. Gas flow rates for the jet and porous base for the evaluation of F-CLC jet induced attrition, at room temperature and a jet diameter of 5 mm

Table 5-4. Experimental conditions for E-CLC to look at the effect of jet velocity and orifice size, at room temperature

EXP 2 (*Batch 2* full PSD E-CLC)							
T [°C]	***room***						
$\mathbf{u_{jet}}$ [m s^{-1}]	***0***	***30***	***42.5***	***48.75***	***55***		
d_{or} [mm]	5				3	4	5
h_{jet_theor} [m]	0	0.059	0.065	0.069	0.042	0.057	0.073
Q_{jet} [m^3 s^{-1}]	0	0.00059	0.00083	0.00096	0.00039	0.00069	0.00108
Q_{pb} [m^3 s^{-1}]	0.00172	0.00113	0.00089	0.00076	0.00133	0.00103	0.00064
Q_{tot} [m^3 s^{-1}]	0.00172						
$d_{p,\infty}$ [µm]	53						
u_{sup} [m s^{-1}]	0.222						
u_{sup}/u_{mf_exp}	7.2						
u_{sup}/u_{mf_theor}	8.5						
$m_{bed,0}$ [kg]	3.2						
TDH_{theor} [m]	0.600						
$h_{bed,exp}$ [m]	0.265						
h_{tot}-h_{bed} [m]	0.721						

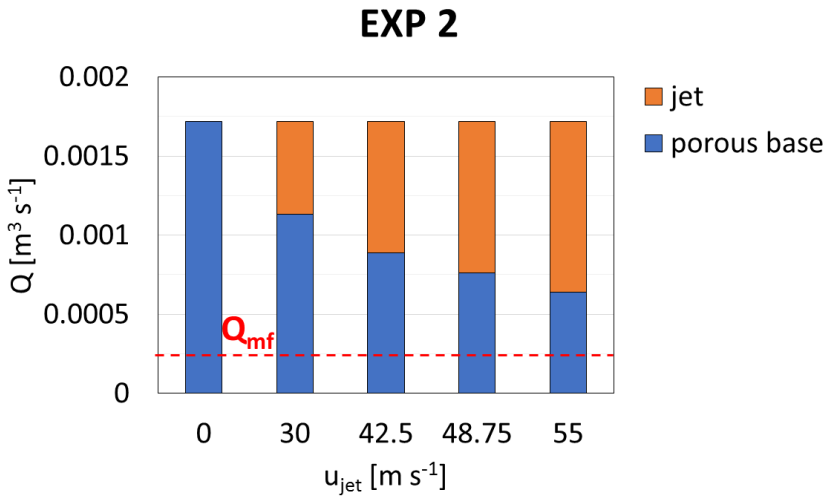

Figure 5-12. Gas flow rates for the jet and porous base for the evaluation of E-CLC jet induced attrition, at room temperature and a jet diameter of 5 mm

5.3.2 Technical Problems Experienced

The preliminary attrition tests conducted on the COLD pilot which is used for the first time for this project, during the initial 3-4 months, were not successful. The weight of the filter after a considerable interval of time (about 8 hours) was unpredictably increasing or decreasing, even at very high superficial velocity. After a thorough check of the system, few technical defects were identified: stagnant fines at the entrance of the filter and leaking of fines at the perimeter of the sleeve filter, as shown in Figure 5-13.

Figure 5-13. Respectively on the left and right: stagnant fines at the entrance of the filter housing and leaking perimeter of the sleeve filter

The first issue was solved by introducing an inlet tube at the filter entrance of smaller section and therefore providing a higher air velocity, avoiding stagnant fines, the second one, by introducing an additional rubber at the top of the sleeve perimeter providing a firmer push between the pierced cage and the lid of the filter housing.

About the HOT pilot, the first 25 days of test were conducted at room temperature at different jet velocities trying to replicate the results obtained in the COLD pilot. By using the jet, inexplicable fluctuations around the value obtained without jet were observed. No clear trend could be identified, nor the problem. Given the short period of time allocated for the usage of this equipment it was decided to only look at the effect of temperature by fluidising with the porous base which gave a good agreement in terms of minimum

fluidisation velocity with the cold pilot. The outcomes of this analysis are reported in the appendix section as incomplete work.

5.4 Results and Discussion

5.4.1 EXP 1

"EXP 1" is carried out on F-CLC particles to investigate the effect of jet velocity and orifice size at room temperature. As shown in Figure 5-14 about 10-15 days are required to reach a steady loss rate by fluidising only with the porous base. This is in fair agreement with the 10 days required for fresh HA-HPV particles to reach a steady state attrition in the fluidised bed in presence of the jet, (Werther and Xi, 1993).

This steady value is referred to as $\dot{R}_{bb}$ and used as a base line to characterise $\dot{R}_{jet}$ according to Equation 5-18.

The high loss rate at the beginning is due to the removal of the pre-existing fines and the higher attrition rate of fresh materials due to the presence of surface asperities and weak spots. Then attrition increases at increasing jet velocities and orifice sizes. The conditioning phase, performed before the jet velocity is changed, shows that there is no effect of history as attrition returns quite rapidly to the same steady value of before. With the jet, a steady value is reached quite promptly (2-3 days).

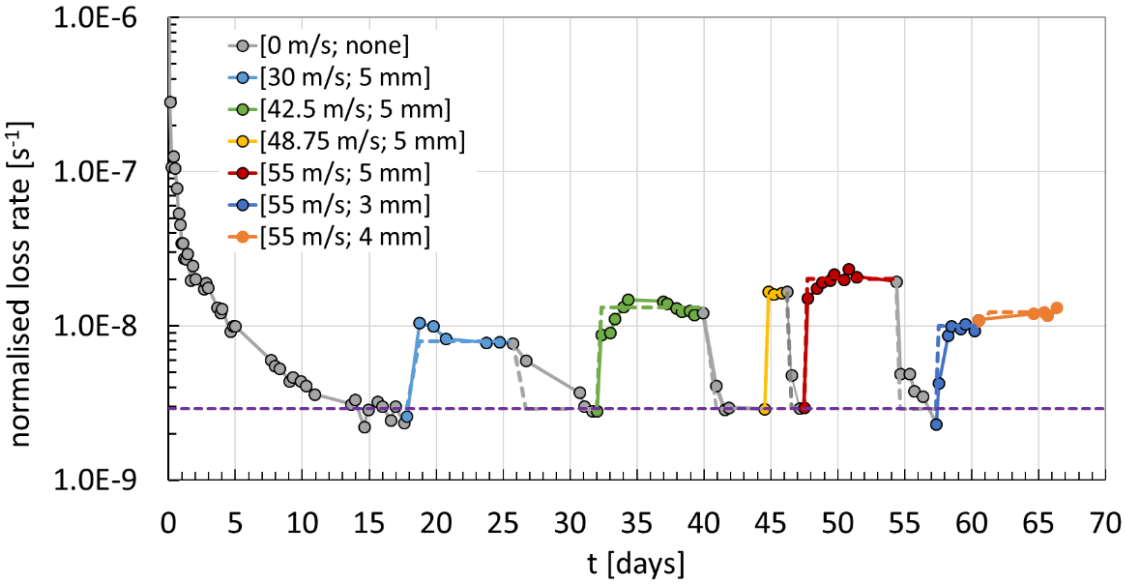

Figure 5-14. Effect of jet velocity and orifice size at room temperature for F-CLC. The legend is organised as [*jet velocity; orifice size]*

By mean of a linear regression of the values of $\dot{R}_{jet}$, the power indices of the jet velocity and orifice size are found to be 2 and 1.7, respectively. This is in good agreement with the model of Chen et al. (1980) who used a similar setup, comparable orifice sizes and material (iron ore). Here, $\dot{R}_{jet}$ is expressed as a function of the material propensity to attrition represented by the single particle breakability index, particle density and jet velocity and orifice size, according to literature. Unification of the data points of $\dot{R}_{jet}$ against the group $\alpha H/K_c^2 \cdot \rho_p \cdot u_{jet}^2 \cdot d_{or}^{1.7}$ is shown in Figure 5-15.

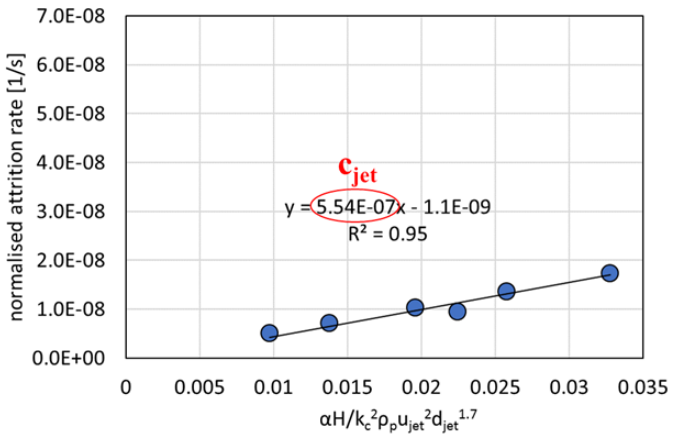

Figure 5-15. Data unification of the jet induced normalised attrition rate for F-CLC

The slope of the straight line would be the constant of the model, referred to as c_{jet}, equal in this case to $5.54X10^{-7}$. If the same power dependencies are to be found with other materials, like the E-CLC, then its constant $c_{jet,ECLC}$ is expected to be proportional to:

$$c_{jet,ECLC} \propto c_{jet,FCLC} \frac{\alpha \frac{H}{K_c^2}\Big|_{FCLC} \rho_{p,FCLC}}{\alpha \frac{H}{K_c^2}\Big|_{ECLC} \rho_{p,ECLC}} = c_{jet,FCLC} \frac{1}{K_{sp}} \tag{5-23}$$

where K_{sp} is the ratio of the single particle breakage propensities of E-CLC and F-CLC, found to be equal to 3.6 in Chapter 3, and defined here in Equation 5-24.

$$K_{sp} = \left(\frac{\alpha \frac{H}{K_c^2}\Big|_{FCLC} \rho_{p,FCLC}}{\alpha \frac{H}{K_c^2}\Big|_{ECLC} \rho_{p,ECLC}} \right)^{-1} \tag{5-24}$$

The intercept of the fitted straight line with the abscissa allows to calculate the jet transition velocity, below which no notable attrition is detected. This is found to be equal to be 13.5 m s^{-1}.

It should be noted that no analysis has been carried out on different numbers of jets; thus, it remains unknown whether the contribution of the single jet will remain the same in case of many jets.

The PSD before and after the experiment is evaluated by the laser diffraction technique using the Mastersizer 3000 and the Aero S disperser at 4 barg. The results, reported in terms of volume fraction in Figure 5-16, show a very slight shift of mother particles towards smaller sizes confirming that surface damage, such as surface abrasion and chipping, is the dominant mechanisms of breakage. Moreover, the debris PSD collected on the filter after the test for a jet velocity of 55 m s^{-1} is also reported in the same figure showing two modes, respectively at about 2 and 30 μm.

More insights are given by the SEM images of the particles after the experiment. They are reported in Figure 5-17. By comparing the particles before attrition and after EXP 1 it is hard to see a change in particle size confirming the laser diffraction outcomes. It is

also noted that the surfaces have barely smoothed out. They are instead as rough as before demonstrating a great tendency to chipping.

The SEM pictures of the debris, Figure 5-18, show that the majority of the particles are very fine (about 1 μm) and therefore clustered together. Moreover, there is the presence of rather large particles, probably responsible for the second peak of the laser diffraction results.

It is believed, but not yet proved, that the very fines are mainly the results of surface abrasion occurring due to bubbling bed attrition while the larger ones, the result of chipping occurring in the jet region because of particle impacts.

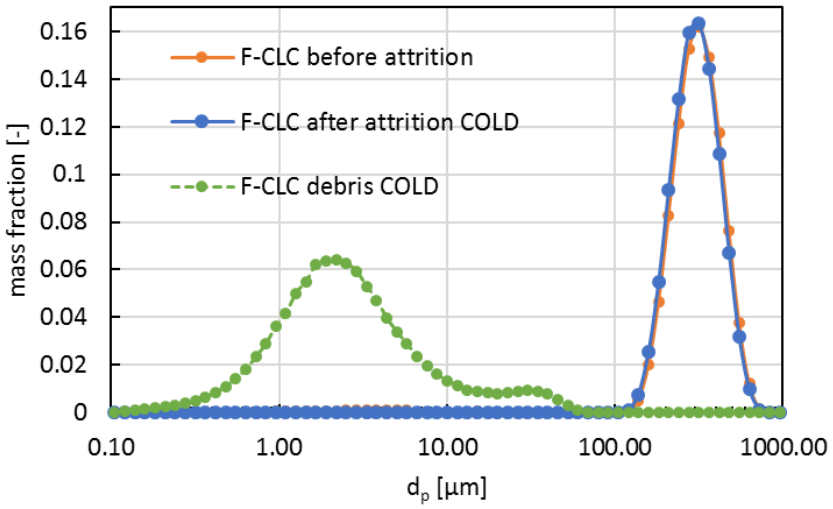

Figure 5-16. PSD of F-CLC before attrition and after attrition at room and high temperature.

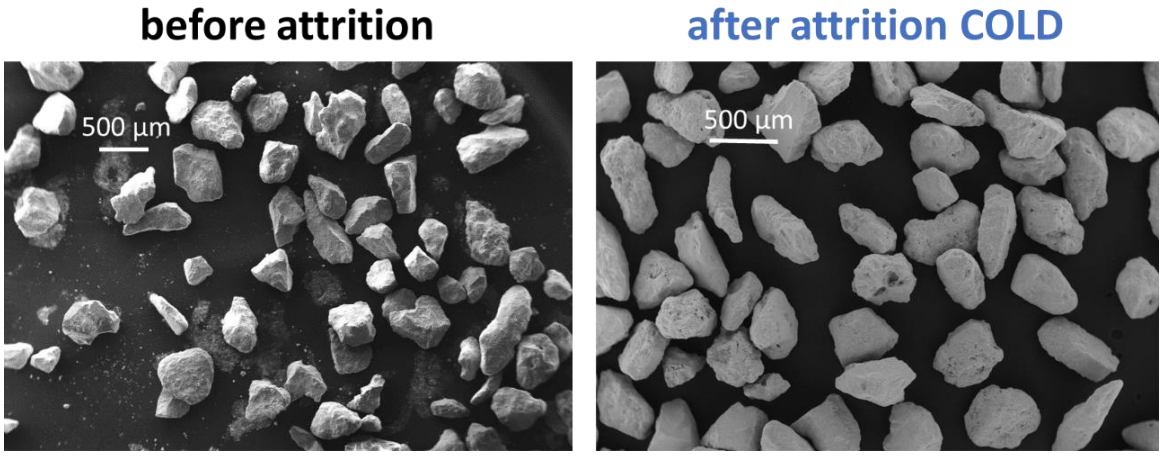

Figure 5-17. SEM images of E-CLC before and after attrition at room temperature

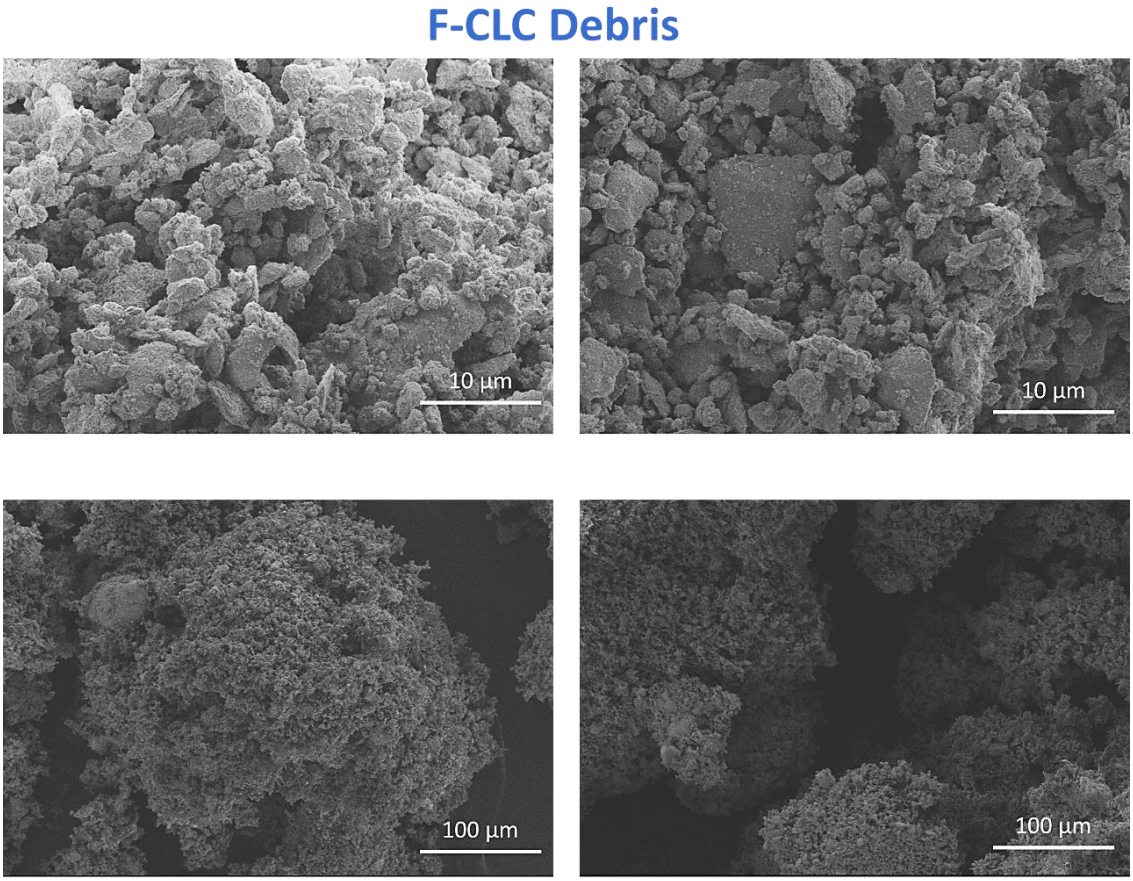

Figure 5-18. Debris particles of F-CLC collected at the filter

5.4.2 EXP 2

"EXP 2" is carried out on E-CLC to investigate the effect of jet velocity and orifice size. As shown in Figure 5-19, about 10 days are required to reach a steady loss rate by fluidising only with the porous base, quite similar to the time required for F-CLC. This result is unexpected as usually equilibrium material would require less time to reach a steady attrition. This is slightly higher than that of F-CLC confirming the findings of Chapter 3, about the single particle attrition propensity.

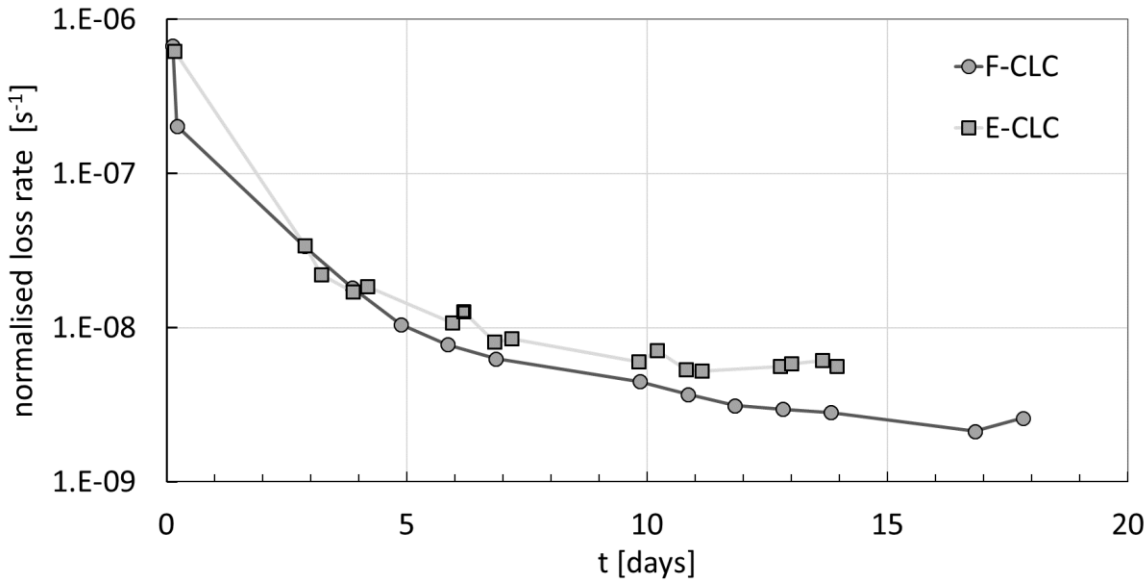

Figure 5-19. Bubbling bed attrition: comparison between F-CLC and E-CLC

As done in the previous case, this steady value is referred to as $\dot{R}_{bb}$ and used as a base line to characterise $\dot{R}_{jet}$ according to Equation 5-15.

Consistently with what seen for F-CLC, the high loss rate at the beginning is mainly due to the presence of pre-existing fines and higher initial attrition rate for the removal of weaker spots. Attrition increases at increasing jet velocities and orifice sizes. In this case much more fluctuation is observed, in particular at high jet velocities. This is, to date, not fully understood.

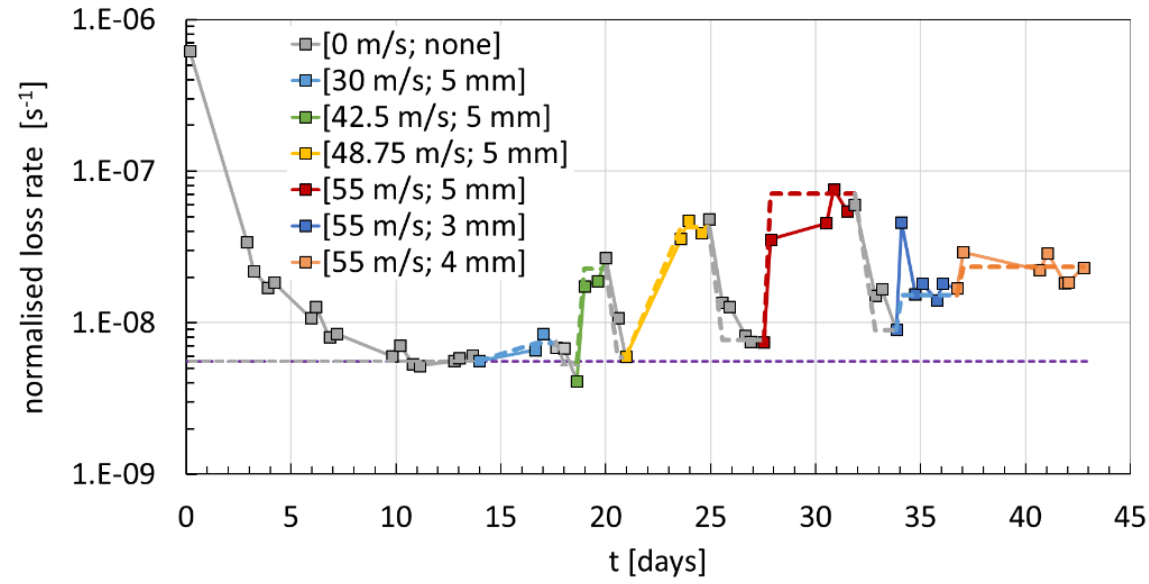

Figure 5-20. Effect of jet velocity and orifice size at room temperature for E-CLC. The legend is organised as [*jet velocity; orifice size]*

By mean of a linear regression, the power indices of the jet velocity and orifice size are obtained, they are 6 and 3.6, respectively. They are unexpectedly and greatly different from F-CLC so Equation 5-23 cannot be applied to check the direct dependency of jet attrition with the single particle breakability index. The unification of data points as a function of the lumped group made by the single particle breakability index, particle density, jet velocity and orifice size is shown in Figure 5-21. In this case, the jet constant c_{jet} is equal to 1.41×10^{-9} (not comparable with that obtained for the F-CLC because of the different power dependencies and hence having different unit measure). Moreover, the jet transition velocity is equal to 4.2 m s^{-1}, lower than F-CLC which is equal to 13.5 m s^{-1}.

The PSDs before and after the test, Figure 5-22, show a slight reduction in the mother particle size, confirming that mainly surface damage has occurred. The SEM images of the material before and after jet attrition at room temperature are reported in Figure 5-23 and show that although there has not been a remarkable change in size, the external surfaces have undergone extensive damage because of the clear larger presence of open macro-pores.

In Figure 5-22, the PSD of the mother particles before and after attrition at room temperature is reported as well as the debris PSD obtained for 55 m s^{-1} of jet velocity. The latter presents (i) two peaks at about 1 and 30 µm, like the fines of F-CLC, (but in

different proportion as shown in the comparative graph of Figure 5-25), and (ii) a third peak of large particles of about 250 µm apparently belonging to the original PSD. The presence of these large particles is confirmed by the SEM pictures of Figure 5-24. The same figure shows some very fines particles clustered together, as observed for the F-CLC.

The presence of these large particles can only be explained by the fact the EXP 2 was carried out under conditions where the freeboard height is only slightly larger than the theoretical TDH (calculated with the model of Sciazko et al. (1991)). This means that large particle could have actually been elutriated away. This might also justify the discrepancy in power dependencies between the two materials and the strong fluctuations of data points using the jet, as reported in Figure 5-20. The presence of the jet is likely to have enhanced the entrainment of large particles, as compared to the case with only the porous distributor, because of the eruption of bigger bubbles being formed at the top of the jet. This is very likely but yet to be confirmed.

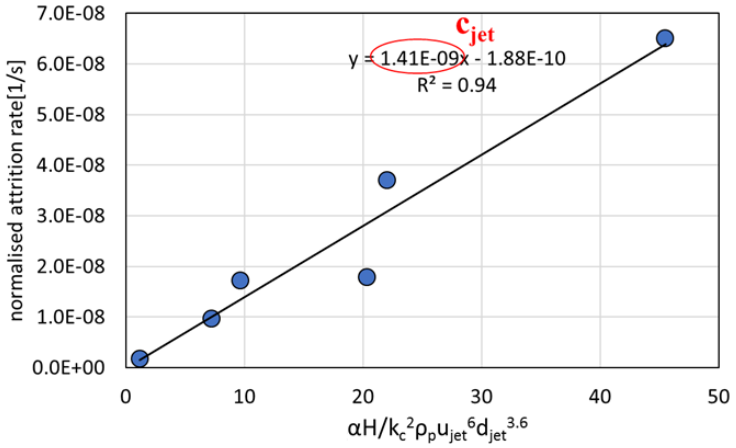

Figure 5-21. Data unification of the jet induced normalised attrition rate for E-CLC

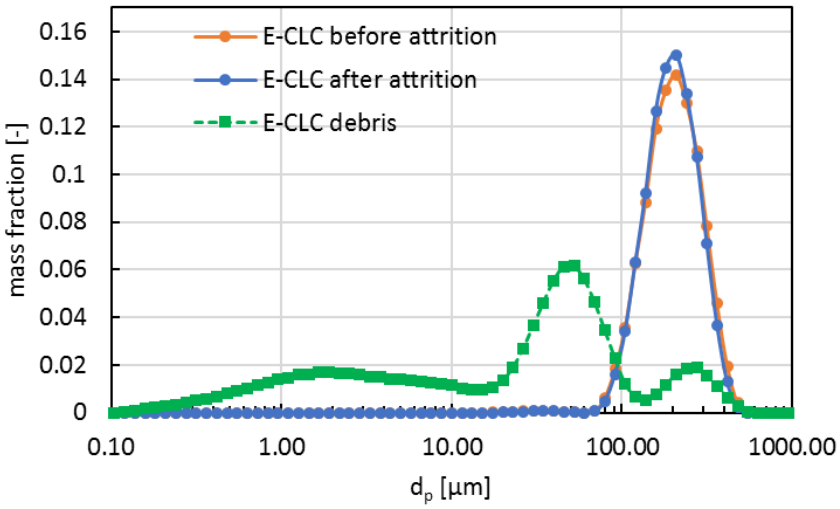

Figure 5-22. Cumulative PSD of E-CLC before and after attrition

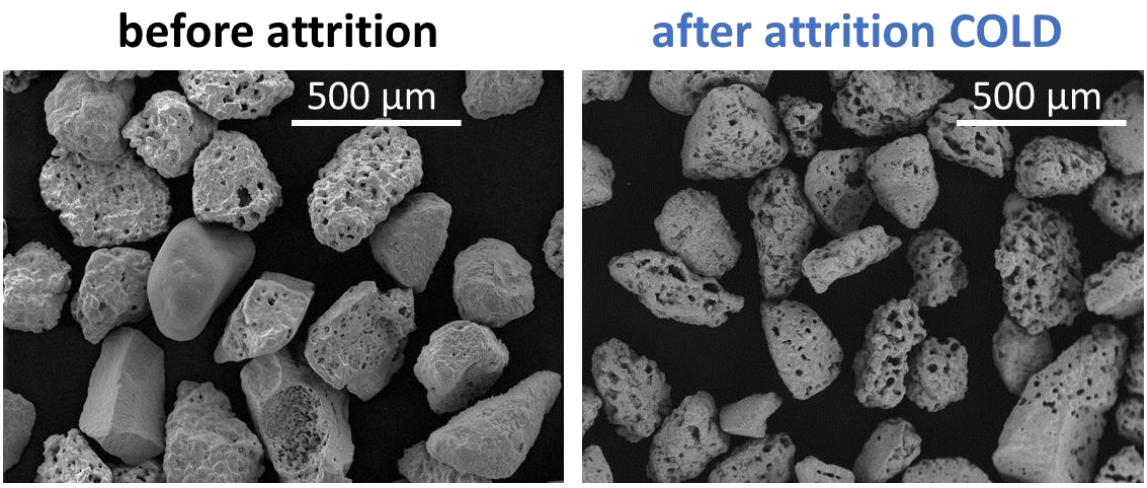

Figure 5-23. E-CLC particles before and after jet attrition at room temperature

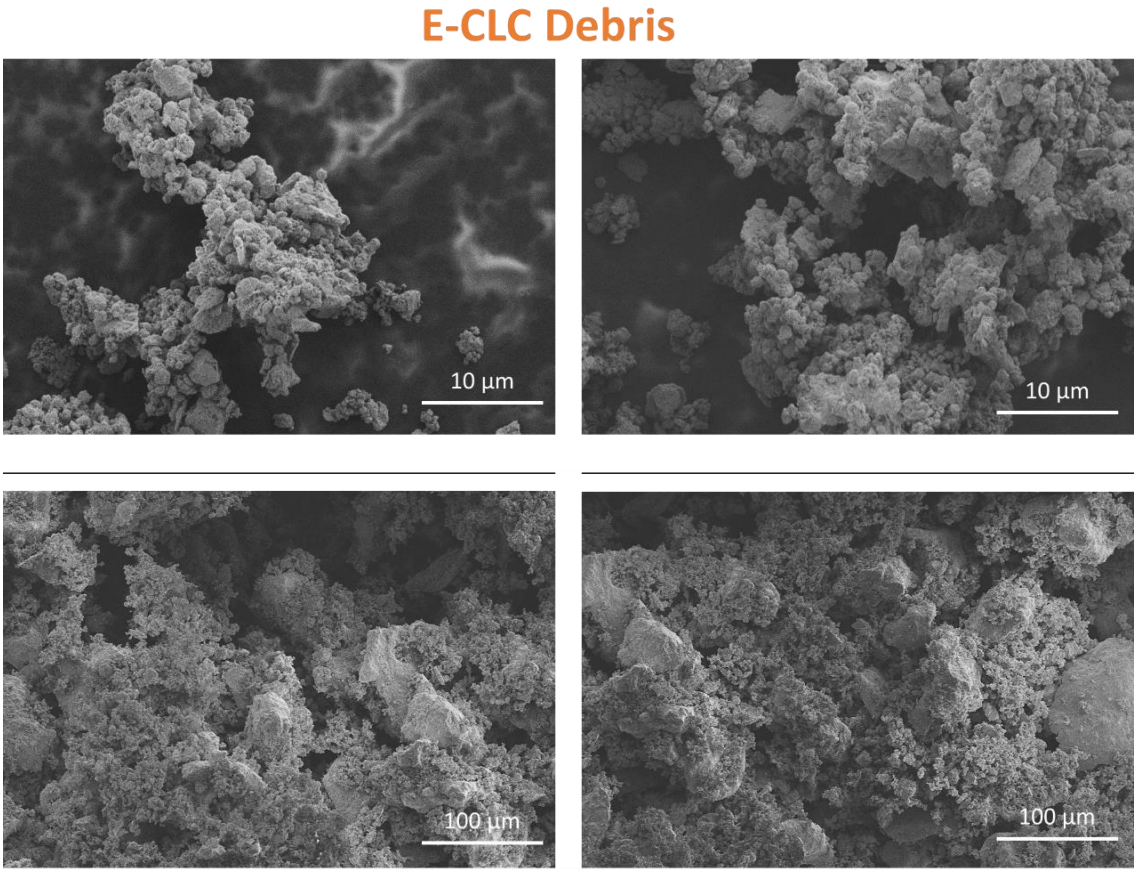

Figure 5-24. Debris particles of E-CLC collected at the filter

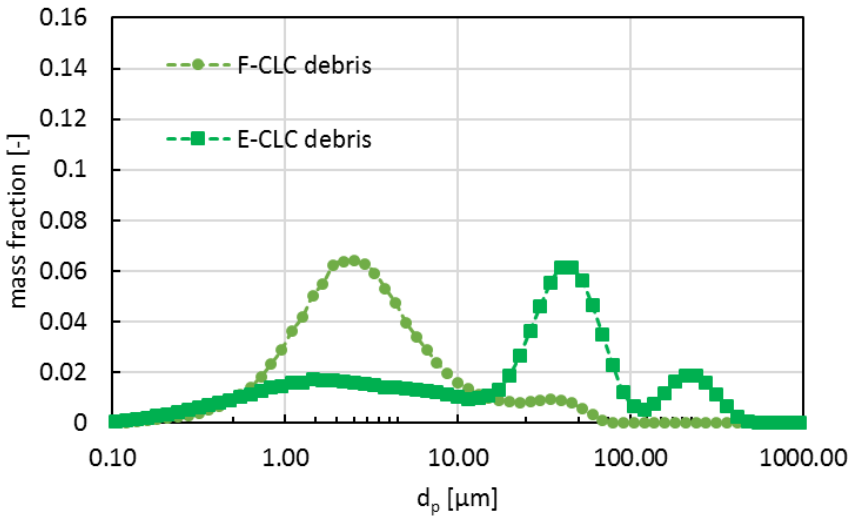

Figure 5-25. PSD of the debris particles collected at the filter of F-CLC and E-CLC

5.5 Concluding Remarks

The effect of jet velocity and orifice size on jet attrition is evaluated experimentally for F-CLC and E-CLC, using two fluidised beds with the same dimensions, able to work at room temperature and 800°C, respectively. The setup of the columns comprises of a single jet embedded in a porous distributor from which background fluidisation is also provided. Attrition is measured as the normalised steady state loss rate by monitoring the weight of the sleeve filter mounted at the top end of the column. For a given material, the gas flow rates of the jet and porous distributor are varied in order to reach the desired jet velocity, whilst keeping the superficial velocity constant. The criterium used to run tests with other materials, fluid type and temperatures are is keeping the theoretical maximum particle size elutriated constant. Therefore, the superficial velocity is equal to the terminal velocity of this given particle size. The tests are run in total for 4-5 weeks starting from the full PSD. Using only the porous distributor, therefore inducing bubbling bed attrition, during approximately 1-2 weeks of test, the loss rate undergoes a gradual decay until a steady state value is reached, called $\dot{R}_{bb}$. This value, for E-CLC, is higher than that of F-CLC (about twice). This confirms the findings of the single particle breakage propensity obtained by impact test and goes against most of the common trends for fresh and equilibrium catalyst, being the latter usually less prone to attrition. However, major structural changes in the particles, being very porous, could explain this trend.

The results obtained for F-CLC in terms of power dependencies of the orifice size and jet velocities are in good agreement with the correlation of Chen et al. (1980) who used a similar experimental setup and material. On the other hand, the results obtained for E-CLC show a discrepancy with F-CLC.

The data points are fitted with a straight line to develop a correlation for a single jet attrition which, assuming a linear relationship with the number of jets, can be expressed according to Equation 5-25, considering the single particle breakability index, a constant parameter, the particle density, the jet velocity and orifice size:

$$\dot{R}_{jet} = \alpha \frac{H}{K_c^2} c_{jet} n_{or} \rho_p u_{jet}^x d_{or}^y \qquad (5\text{-}25)$$

All the results obtained here are meant to be valid for a single jet; no analysis has been carried out on more than one jet, so there is no evidence that the correlations are directly generalised for n-jets. Further study needs to be carried out in this regard.

The intercept of the fitted line with the abscissa allows to estimate the jet velocity which causes no/little attrition. This is called jet transition velocity. The latter is reported in Table 5-5 along with the other main parameters mentioned above, for both materials.

Table 5-5. Jet attrition parameters for F-CLC and E-CLC and steady state bubbling bed attrition

Jet and bubbling bed attrition				
symbol	**description**	**F-CLC**	**E-CLC**	**Unit measure**
$\dot{R}_{bb}$	Steady state bubbling bed attrition	$2.9 X10^{-9}$	$5.6 X10^{-9}$	s^{-1}
c_{jet}	Jet attrition index	$5.5 X10^{-7}$	$1.4 X10^{-9}$	
$\hat{u}_{jet}$	Jet velocity power index	2	6	-
$\hat{d}_{or}$	Orifice size power index	1.7	3.6	-
$u_{jet,0}$	Jet transition velocity	13.5	4.2	$m\ s^{-1}$

Particle size distribution analysis and image analysis of the bed particles show that little shift in size has occurred at room temperature and there is no clear distinction between particles of before and after attrition, except for the E-CLC which expose more open macro-pores. The same analysis is carried out on the fines collected at the filter after the test of 55 $m\ s^{-1}$ of jet velocity. They are mainly composed by very small particles of about 1 μm organised in clusters but also by relatively large chips of about 30 μm. For the E-CLC, the fines are also composed by large particles of size comparable to that of the mother particle. It is possible that the test on E-CLC might be carried out below the TDH or at its very limit. This could also explain the discrepancy between the dependencies obtained for the two materials and the significant fluctuations of the loss rate.

6. POPULATION BALANCE MODEL OF PARTICLE ATTRITION IN FLUIDISED AND CIRCULATING FLUIDISED BEDS

CHAPTER 6

In this Chapter, a comprehensive literature review of the applications of the PBM for attrition in fluidised and circulating fluidised bed systems is initially given. A detailed and stepwise description of the PBM developed here is then presented. The PBM is used to simulate particle attrition occurring in a fluidised bed, and in a circulating fluidised bed. The results are discussed with a focus on the effects of the integration time step, particle breakability index and superficial velocity of fluidising gas. The PBM part of this thesis was developed at IFP Energies Nouvelles facilities in the 3rd and 4th year of this PhD project.

6.1 Literature Review

In the population balance approach, a set of mass balance equations of a generic population are inter-linked by considering streams of masses travelling to different classes of the population. It is widely applied to describe size changing mechanisms like growth, aggregation and breakage, (Ray et al. 1987; Werther and Hartge, 2004; Heinrich et al. 2003; Falola et al. 2013; Redemann et al. 2009; Rajniak et al. 2008). In literature, there are examples of PBM of particle attrition in fluidised and circulating fluidised beds due to the inevitable consequences of the particle size reduction. Furthermore, for both FB and CFB combustors, several authors consider the change in particle size due to attrition as well as the change in particle density caused by the formation of ashes, defining the particle population in both density and size classes, (Wang et al. 2003; Chirone et al. 1991). With the assumption that attrition only occurs by surface damage, several mathematical models have been formulated in the past. This assumption allows

to treat the attrition mass as made of particles of size zero that would be instantly lost, (Levenspiel et al. (1968), Chirone et al. (1991) and Arena et al. (1983)), or collected in the last size class and no longer subjected to attrition, (Hansen and Ottino, (1997), Werther and Hartge, (2004), Klett et al. (2007) and Redemann et al. (2009)). Alternatively, Rangelova et al. (2002) assume that a particle in a fluidised bed shrinks because of attrition until the point where its terminal velocity is equal to the superficial velocity and eventually is lost from the system. Many other authors support the idea that the role of the debris cannot be completely neglected depending on the application. For instance, Ray et al. (1987), Wang et al. (2003), Montagnaro et al. (2011) and Welt et al. (1977) have simulated particle attrition in a fluidised bed combustor by PBM, dividing the population into two categories: the mother and debris particles, whereas only the former undergoes attrition. The two categories are defined based on a critical particle size which functions at the same time as minimum mother particle size and maximum debris particle size. All the debris particles would have a PSD between 0 and this critical size. This value is set to 50 μm for the authors mentioned above.

Heinrich et al. (2003), simulating growth and attrition in a fluidised bed granulator via PBM, assume that only a fraction of the fines produced by attrition is lost from the system, as dictated by the operating conditions. Consequently, the complementary fraction that remains inside can contribute to the agglomeration process as nuclei. The role of the fines is then essential for such applications as well as other applications like heterogeneous or catalytic chemical reactions, i.e. CLC and FCC, respectively. According to Ray et al. (1987), the fines produced by attrition can strongly affect the efficiency of reaction due to their high specific surface area. However, the authors remark the importance of the operating conditions which determine whether the fines will be elutriated away, increasing the average particle size of the bed and causing a reduction of the reaction efficiency. In fact, the bed average particle size depends on the balance between attrition rate and elutriation rate. Ray et al. (1987) and Werther and Hartge, (2004) have found the attrition rate to be the rate-controlling step at steady state because the extent of fines inside the bed does not change considerably as they are continuously produced by attrition and promptly elutriated.

Ray et al. (1987) and Montagnaro et al. (2011) have developed a steady state PBM, in a FB combustor and a CFB combustor for SO_2 sorbent particles, respectively. In their model, they consider the debris particles to participate in the chemical reaction assuming that attrition is caused by only surface abrasion and surface abrasion/fragmentation, respectively. To describe the debris produced as a result of surface abrasion, both authors utilise the "natural grain size" concept, firstly applied in a PBM by Ray and Jiang, (1987), according to which the debris PSD is independent of the volume scale and follows a beta function. The concept, introduced by Lowrison, (1974), states that certain amorphous materials consist of grains, pores, agglomerates or particles embedded in matrix of another, thus producing a characteristic debris PSD, regardless of the mother particle size or abrasive attrition intensity.

Particle fragmentation can be implemented by defining the PSD of the particle after fragmentation, (Welt et al. (1977) and Wang et al. (2003)). Particle attrition in these systems, as considered by the majority of the authors mentioned above, is seen as a whole in the process and expressed as a function of the excess fluidisation velocity, (Arena et al. 1983), rather than considering different sources.

Werther and Hartge, (2004), Hartge et al. (2007), Redemann et al. (2009) and Klett et al. (2007) developed a time dependent PBM of attrition in CFB reactor/regenerator systems, under surface abrasion dominated conditions of FCC catalyst. Three different sources of attrition were considered: the jet region, the bubbling bed, and the cyclone. Given the close similarities with this PhD research project, their work is used here as inspirational source for the development of the PBM. Werther and Hartge, (2004) neglect the initial breakage of the fresh catalyst. On the contrary, Hartge et al. (2007), Redemann et al. (2009) and Klett et al. (2007) introduce a time dependent factor in the attrition kernels that reflects the particles age which provides an exponential decay of the attrition rate until a steady state value. They compensate for the mass loss by adding fresh catalyst, in one time-step, when the solids holdup in the reactor falls below a certain value. The masses in the standpipes are assumed to be constant during the whole calculation, i.e. in each time step, the same mass of solids fed to the standpipe leaves the standpipe. The modules of the PBM, namely the parts comprising the full cycle in the CFB, like the fluidised bed, elutriation, cyclone, regenerator and recycle, are solved in sequence during

one time step. The time step is chosen between 0.5 and 20 s ensuring that, at each time step, the mass leaving any class is significantly less than that of the respective class. Attrition in the cyclone is calculated prior to separation, as justified by Reppenhagen and Werther, (2000) who show that attrition mainly occurs at the entrance, while the separation grade efficiency is evaluated by the theory of Muschelknautz, (1997). They show that the cyclone has the highest attrition rate, while the lowest is the regenerator bubbling bed. They reported that the mean particle size of the bed inventory gets coarser despite the formation of the small fines as they are unable to be kept inside the system. Moreover, Werther and Hartge (2004) show the strong interrelation between attrition and efficiency of the solids recovery cyclone, which is able to hold and recycle the majority of particles but at the same time produces debris. In other words, the cyclone attrition increases with its efficiency.

Referring to the same authors, a remark has to be made here about the way the particle size after attrition is calculated. In their work, for each class, the attrition correlations give the amount of attrition mass produced regardless of how much populated the class is. In this way, whether the class is composed by many or few particles does not matter, and the same attrition mass would be produced. This has implications on the particle shrinkage. In fact, the attrition mass per single particle, being computed as the ratio of the attrition mass of the class and the number of particles of the same class, depends on the latter. The solution would be to use a normalised attrition rate per class or an explicit dependency with the mass fraction. As a matter of fact, Kramp et al. (2011), describing the effect of attrition in a CLC process, by means of a population balance, used the same attrition correlations but weighted with the mass fractions.

6.1.1 Motivation and Objectives

In view of this literature survey, it is clear that the population balance approach has been widely used with the intent of predicting the response of the fluidised bed process to particle attrition. Surface damage and consequent particle size reduction is considered the dominant mechanism of attrition in fluidised beds. Moreover, it has been elucidated the importance of considering the attrition of different sources as well as the formation of fines which, depending on the operating conditions, might not be simply lost and thus have a key role on the performances of the process. Moreover, the minimum mother

particle size, which determines the part of particles population undergoing attrition, has not been well defined yet. In the next section, the physical meaning of the minimum mother particle size is given based on the single particle breakage tendency. The aim of this chapter is to use the PBM to provide some insights on the effect of particle attrition on the behaviour of a circulating fluidised bed by accounting for the single particle breakage tendency, simulating different scenarios considering strong/weak particles at different operating conditions. It needs to be noted that the particle degradation due to the thermal stresses and chemical reaction is not considered in the population balance model. Hence, the model cannot accurately represent the situation in a real system.

6.2 Definition of the System

The system under study comprises of a fluidised bed, a cyclone separator and a recycle leg, as shown in Figure 6-1.

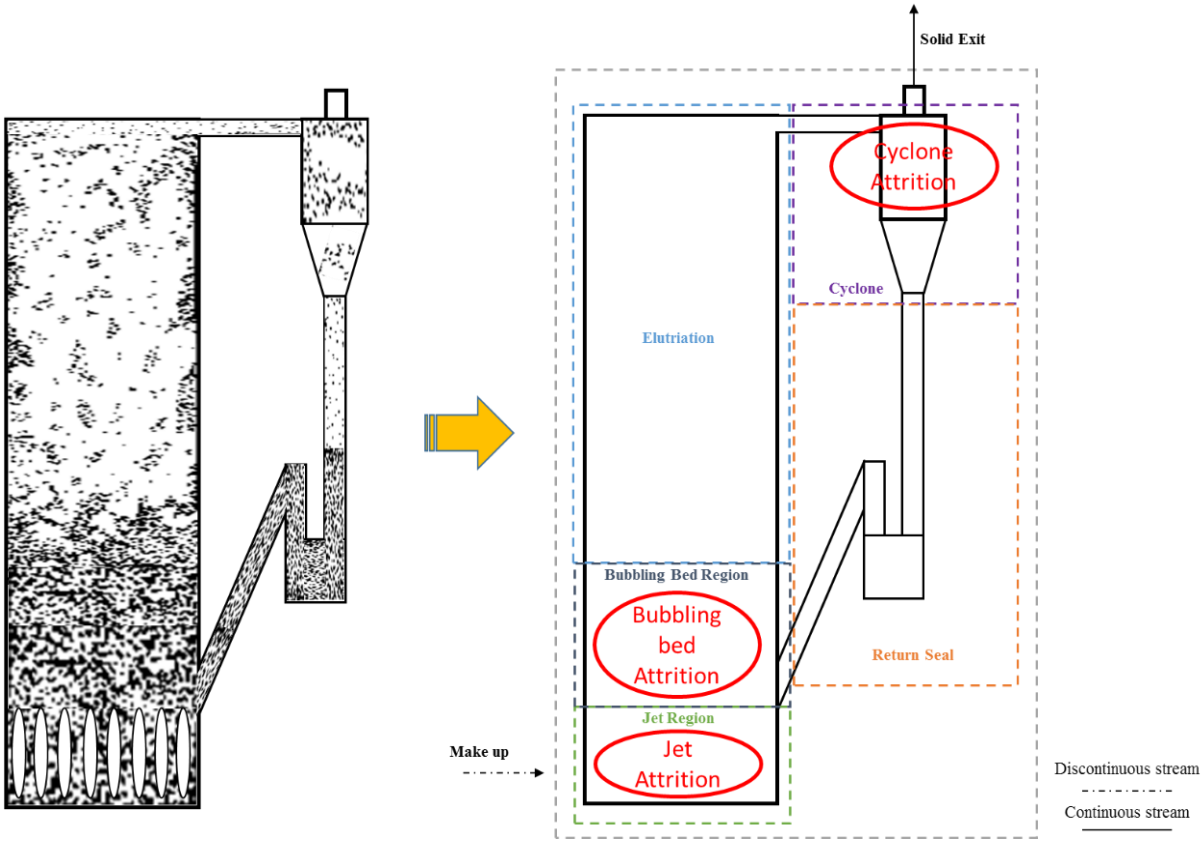

Figure 6-1. The CFB system

The sources of attrition considered here are the jet region, the bubbling bed, and the cyclone. The attrition correlations, developed experimentally, give the steady state extent of attrition rate while the PBM is time dependent. The system is divided into modules. Each module has a distinctive function and is solved separately following the direction of the solids circulation. They are, in order: jet region, bubbling bed, elutriation, cyclone and recycle. A discontinuous make-up stream provides fresh material when a certain degree of loss is reached. The ODEs constituting the PBM are discretised with time according to Euler's method, by explicitly approximating the derivative with the incremental ratio. For instance, the global mass balance on the system is reported below in Equation 5-1:

$$\begin{cases} \dfrac{dm}{dt} = \dot{m}_{make-up} - \dot{m}_{cyc,out} \\ m\big|_{t=0} = m_{bed,0} \end{cases} \tag{6-1}$$

which discretised becomes

$$\begin{cases} \dfrac{\Delta m}{\Delta t} = \dot{m}_{make-up}\Big|_t - \dot{m}_{cyc,out}\Big|_t \\ m\big|_{t=0} = m_{bed,0} \end{cases} \tag{6-2}$$

and eventually equal to:

$$m_{bed}\big|_{t+\Delta t} = m_{bed}\big|_t + \dot{m}_{make-up}\Big|_t \Delta t - \dot{m}_{cyc,out}\Big|_t \Delta t \tag{6-3}$$

The mass balances constituting the PBM have no spatial dependency, the only variables are time and particle size. The particle population is divided into fixed discretised size classes. The mass transfer between classes, as a function of particle size, is carried out post attrition by a classification function, after which the mean class properties are evaluated, as shown schematically in Figure 6-2. However, the particle size can keep decreasing within each class causing no mass transfer between size classes, (Werther and Hartge, 2004).

Figure 6-2. Logic steps of PBM

It should be noted that discretisation has some implications such as the loss of details in one of the population global properties, such as the number, the total surface and the total volume of particles. Surface and volume (or mass) are naturally linked, so it is common to come across PBMs which are either number or mass based. In the former case, the conservation of mass is not guaranteed and vice versa for the latter. This effect is enhanced when the classes are wide. Nevertheless, it has been shown that the continuity of mass and number can be achieved by a series of numerical manipulation, (Kumar et al. 2006; Bertin et al. 2016). Referring to particle attrition in fluidised beds, mass is the main interest thus, the PBM derived here is going to be mass based.

The dimensions and specifics of the process are to be defined in an Excel sheet which serves as data input source. In here, the total simulation time, integration time step, and the saving time step (within which the results are averaged) can be indicated. All the inputs are read and processed by Matlab® which performs the initialisation of the variables and the calculation of the minimum mother particle size, the particle residence times of the elutriation, cyclone and recycle module τ_{elut}, τ_{cyc}, τ_{rec} and the maximum time step allowed Δt_{max}. The default configuration is the circulating fluidised bed (CFB). However, the cyclone and recycle can be omitted from the calculation in order to simulate only the fluidised bed column (FB). The flow chart of the calculation steps is reported in Figure 6-3.

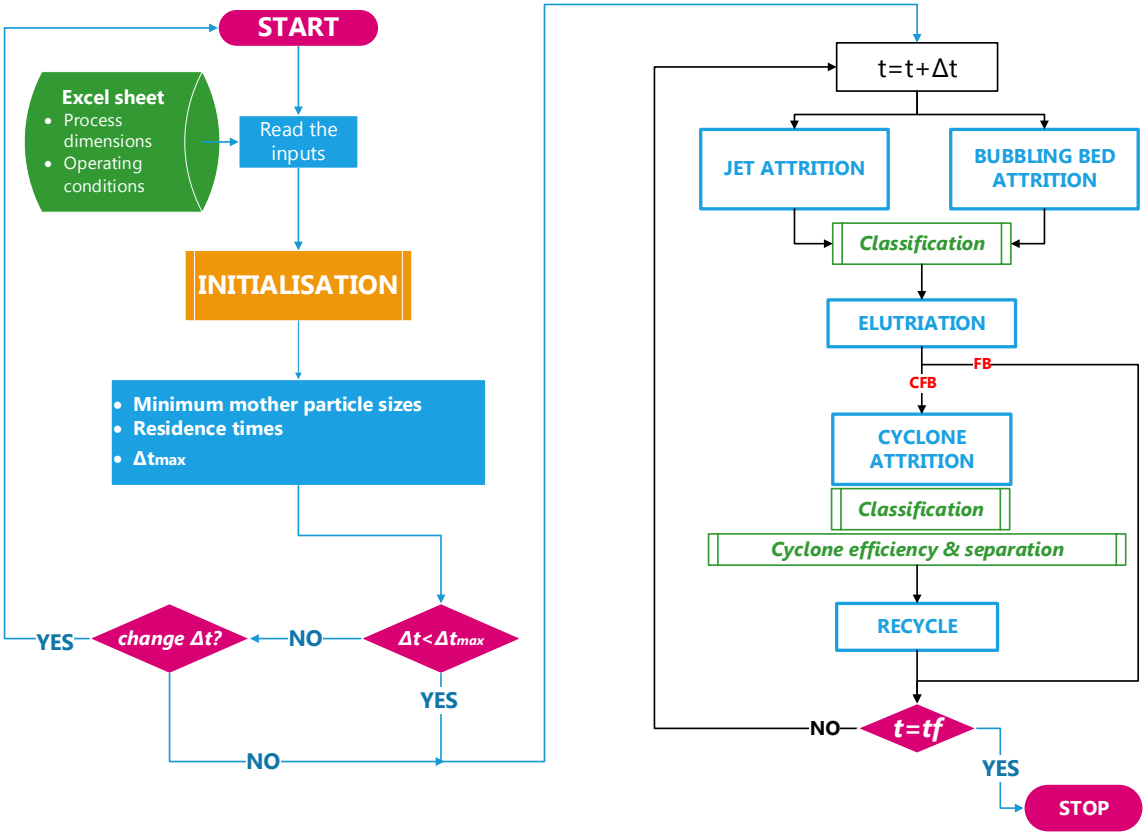

Figure 6-3. Resolution flow chart of the PBM

By definition:

- mother particles are all the particles undergoing attrition and shrinkage; they have sizes larger than $d_{p,min}^{mp}$ (minimum mother particle size). Thus, any particle size less than this value does not undergo attrition and shrinkage
- debris particles are all the particles generated in one time step as a result of attrition of the former; they have sizes smaller than $d_{p,max}^{de}$ (the maximum debris size). This value is an input of the model, in this case set on the base of experimental support.

It is possible that $d_{p,max}^{de} > d_{p,min}^{mp}$; in this instance, a debris particle can undergo attrition and shrinkage in the next calculation time step, becoming in this way a mother particle itself. On the contrary, for Ray et al. (1987), Wang et al. (2003), Montagnaro et al. (2011) and Welt et al. (1977) $d_{p,max}^{de}$ is equal to $d_{p,min}^{mp}$ so the population of mother and debris particles are separated into two never overlapping groups. The mass of debris produced

at each time step, per class, is given by the attrition correlations which at the same time dictates the shrinking rate of the mother particles. The debris particles generated in the fluidised bed and cyclone have a PSD obtained by two beta functions, (Ray and Jiang, 1987; Ray et al. 1987; Montagnaro et al. 2011), fitted with the experimental results presented in the previous chapters. Unlike Werther and Hartge, (2004), who assumed the mass in the standpipe to be constant already at time 0 s, here there is a transient period where the solids circulation entering the empty module can establish a steady state mass. An exception is made for the jet and bubbling bed regions which are themselves not empty from the start. Mother and debris particles are assumed to be spherical, the bed inventory perfectly mixed and the jet region is delineated from the bubbling bed by the jet height, (Werther and Hartge, 2004; Klett et al. 2007; Redemann et al. 2009).

6.2.1 Particle Size Reduction

For each interval of time, the mass of debris produced by the class "i", for all size classes greater than $d_{p,min}^{mp}$, is calculated according to the definition of the normalised attrition rate $\dot{R}$ given below in Equation 6-4:

$$\dot{R} = \frac{\text{mass of debris particles produced by attrition}}{\text{mass undergoing attrition} \times \text{unit time}} \tag{6-4}$$

for a class "i", it can be written Equation 6-5

$$\frac{dm_i^{de}}{m_i^{mp} dt} = \dot{R}_i, \qquad m_i^{de}(t) = 0, \qquad m_i^{de}(t+\Delta t) = m_i^{de}\Big|_{t+\Delta t} \tag{6-5}$$

By discretising and solving the above equation, knowing m_i^{mp} (the mass of a class "i"), Δt and $\dot{R}_i$, the following is expression can be obtained, Equation 6-6:

$$m_i^{de}\Big|_{t+\Delta t} = \dot{R}_i \, m_i^{mp}\Big|_t \, \Delta t \tag{6-6}$$

Equation 6-4 can be re-written for the mother particles as shown below in Equation 6-7:

$$-\frac{dm_i^{mp}}{m_i^{mp} dt} = \dot{R}_i, \quad m_i^{mp}(t) = m_i^{mp}\Big|_t, \quad m_i^{mp}(t+\Delta t) = m_i^{mp}\Big|_{t+\Delta t} \tag{6-7}$$

where $m_i^{mp}\Big|_t$ is the mass of mother particles of the class "i" at time "t".

Discretising Equation 6-7, Equation 6-8 is obtained:

$$m_i^{mp}\Big|_{t+\Delta t} = m_i^{mp}\Big|_t \left(1 - \dot{R}_i\, \Delta t\right) \tag{6-8}$$

then the mass of the class after attrition is given by Equation 6-9, by combining Equation 6-6 with Equation 6-8,:

$$m_i^{mp}\Big|_{t+\Delta t} = m_i^{mp}\Big|_t - m_i^{de}\Big|_{t+\Delta t} \tag{6-9}$$

From Equation 6-6, it is possible to derive the mother particles shrinking rate by recalling that the total mass of a class is constituted by a number of spheres of size $d_{p,i}^{mp}$:

$$-\frac{dm_i^{mp}}{m_i^{mp} dt} = \dot{R}_i \quad \Rightarrow \quad -N_{p,i}^{mp}\frac{3\pi\rho_p d_{p,i}^{2mp}}{6}\frac{dd_{p,i}^{mp}}{dt} = \dot{R}_i N_{p,i}^{mp}\frac{\pi\rho_p d_{p,i}^{3mp}}{6} \tag{6-10}$$

and eventually:

$$-\frac{dd_{p,i}^{mp}}{dt} = \frac{d_{p,i}^{mp}}{3}\dot{R}_i \tag{6-11}$$

The particle shrinking order might then vary according to the particle size dependency of $\dot{R}_i$, which is different for different sources of attrition. The mass of a single mother particle before attrition is given by the mass of the class divided by the number of particles, Equation 6-12.

$$m_{p.i}^{mp} = \frac{m_i^{mp}}{N_{p,i}^{mp}} \tag{6-12}$$

The mass of debris produced by a single mother particle is equal to mass of debris produced by the class divided by the number of particles of the class, as shown in Equation 6-13:

$$m_{p.i}^{de} = \frac{m_i^{de}}{N_{p,i}^{mp}} \tag{6-13}$$

Equation 6-9 can be then rearranged to obtain the mass of a single mother particle after attrition:

$$m_{p.i}^{mp}\Big|_{t+\Delta t} = m_{p.i}^{mp}\Big|_t - m_{p.i}^{de}\Big|_{t+\Delta t} \tag{6-14}$$

Equation 6-14 can be rewritten in terms of extent of attrition rate, Equation 6-15, and in terms of particle size, Equation 6-16.

$$m_{p,i}^{mp}\Big|_{t+\Delta t} = m_{p,i}^{mp}\Big|_{t}\left(1-\dot{R}_i\,\Delta t\right) \tag{6-15}$$

$$d_{p,i}^{mp}\Big|_{t+\Delta t} = d_{p,i}^{mp}\Big|_{t}\left(1-\dot{R}_i\,\Delta t\right)^{\frac{1}{3}} \tag{6-16}$$

As mentioned earlier, if the new particle size still falls between the limits of the class there will not be mass transfer between classes. Moreover, the total mass of debris m^{de} can be expressed as the summation of the masses of debris produced by all the classes above d_{min}^{mp}, according to Equation 6-17:

$$m^{de} = \sum_{i=i(d_{min}^{mp})}^{n} m_i^{de} \tag{6-17}$$

6.2.2 Classification

Post attrition, the masses of mother and debris particles are reallocated according to their size by means of a classification function. For "N" number of classes, where "1" is the smallest and "N" the largest, n_{min}^{mp} and n_{max}^{de} are the class numbers corresponding to $d_{p,min}^{mp}$ and $d_{p,max}^{de}$. A generic class "i" can receive mother particles from all the classes above [i+1, N], donate mother particles to any of the classes below [1, i-1], donate debris to any class between [1, n_{max}^{de}] and, if the size of the class "i" happens to be below $d_{p,max}^{de}$, it can receive debris particles too, generated from the mother particles of any of the classes [n_{min}^{mp}, N]. This is described schematically in Figure 6-4.

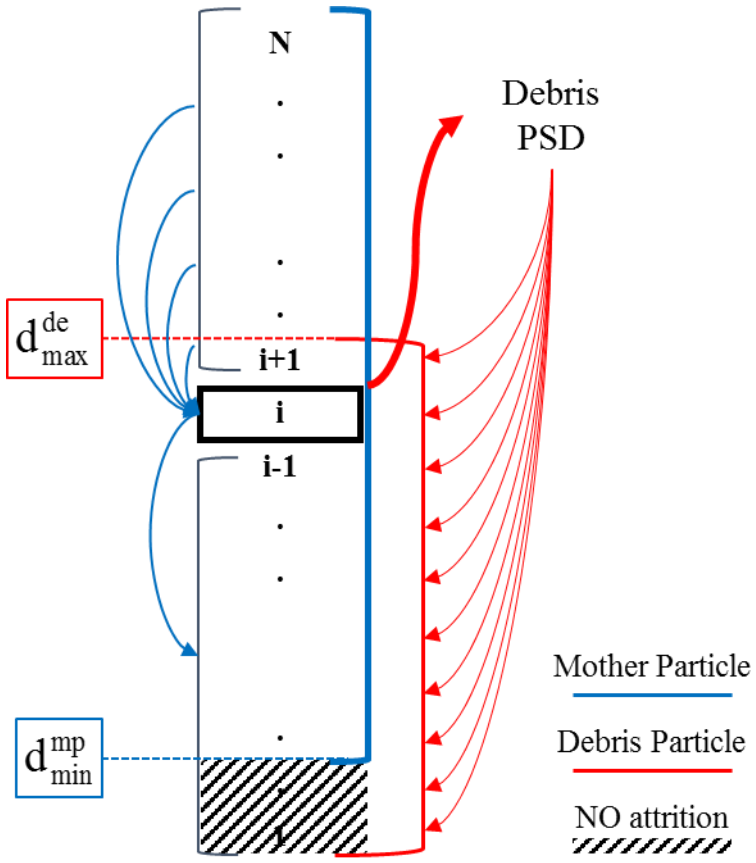

Figure 6-4. Classification of the mass of mother and debris particles.

The variation of mass in each class can be formalised in a generalised form by Equation 6-18, where the first and second indices correspond to the belonging and travelling class, respectively.

$$dm_i = \sum_{k=i+1}^{N} m^{mp}_{k,i} - m^{mp}_{i,[1\ i-1]} - m^{de}_{i,[1\ n^{de}_{max}]} + m^{de}_{[n^{mp}_{min}\ N],i} \tag{6-18}$$

Once the masses are reallocated, the new size of the class is calculated as the average size weighed on the non-travelling mass after attrition, $m_{i,i}$, and all the incoming masses, according to Equation 6-19.

$$d_{p\,av,i} = \frac{m_{i,i} d_{p\,i,i} + \sum_{k=i+1}^{N} m^{mp}_{k,i} d^{mp}_{p\,k,i} + m^{de}_{[n^{mp}_{min}\ N],i} d^{de}_{p\,[n^{mp}_{min}\ N],i}}{m_{i,i} + \sum_{k=i+1}^{N} m^{mp}_{k,i} + m^{de}_{[n^{mp}_{min}\ N],i}} \tag{6-19}$$

This diameter is then used to compute the mass of the new single particle and number of particles of the class, as shown by Equation 6-20 and Equation 6-21, respectively:

$$m_{p,i} = \pi \rho_p \frac{d_{p\,av,i}^{\,3}}{6} \tag{6-20}$$

$$N_{p,i} = \frac{m_i}{m_{p,i}} \tag{6-21}$$

Here is where the information on the number of particles before classification is lost due to averaging within the class. It is clear that the wider the size class the greater would be the discrepancy between the number of particles before and after classification.

The tendency should be to use the highest number of classes as possible in order to ensure the continuity of results. At this stage of development, no sensitivity analysis is performed here on the effect of the number of classes. Further work is needed to establish the independency of the solutions with the number of classes.

6.2.3 Minimum Mother Particle Size

Recalling the single particle breakage model, the minimum mother particle size, below which there is no attrition, can be evaluated by super-imposing conditions of no breakage, i.e. R=0, for a normal impact at a critical velocity, as shown in Equation 6-22:

$$0 = \alpha \frac{H}{K_c^{\,2}} \rho_p d_{p,min}^{mp} \, v_{p,crit}^2 - b_{sp} \tag{6-22}$$

Equation 6-22 can be re-written to obtain the minimum mother particle size, as shown below in Equation 6-23:

$$d_{p,min}^{mp} = \frac{b_{sp}}{\alpha \frac{H}{K_c^{\,2}} \rho_p \, v_{p,crit}^2} \tag{6-23}$$

The critical impact velocity needs to account for and include the most severe conditions of attrition, therefore the collisions within the jet and at the entrance of the cyclone.

In the jet, this is evaluated using the correlation of Bentham et al. (2004), developed for a fluidised bed of Geldart group B powder of 300-500 μm for a wide range of jet velocities and orifice size of 1 mm, shown in Equation 6-24.

$$v_{p,crit,jet} = 0.0719 \, u_{jet}^{0.84} \tag{6-24}$$

It is noted that the above correlation, valid for a particular size cut in this case is applied in a very simplified way to all the bed inventory.

On the other hand, the critical particle impact velocity for cyclone attrition is evaluated using a correlation based on the CFD-DEM analysis of particle velocity in the inlet pipe of the cyclone, described in detail in Chapter 4. The correlation is shown below in Equation 6-25 and gives the particle-size-dependent particle velocity at the end of the inlet pipe (referring to Equation 4-59, $L=L_{max}$):

$$v_{p,crit,cyc} = u_{cyc,in}\left(\frac{A_p(d_p)}{B_p(d_p)+1}\right) \tag{6-25}$$

where A_p and B_p are two particle-size dependent parameters, described in Equation 4-60 and Equation 4-61 of section 4.3.9.4.1.3. Using the cyclone inlet gas velocity as initial guess for $v_{p,crit,cyc}$, the cyclone minimum mother particle size can be evaluated. It should be noted that this correlation, has been developed for F-CLC particles and therefore its validity could be reasonably extended only to materials with similar size and density.

For the FB configuration, only the minimum mother particle size of the jet region is used and extended to the bubbling bed as well, while for the CFB configuration, due to the presence of the cyclone, two minimum mother particle sizes are used, one related to the jet and bubbling bed attrition, and one related to cyclone attrition. No sensitivity analysis is performed on the effect of the minimum mother particle sizes.

6.2.4 Maximum Time Step

At time t = 0 s, the system is empty except for the bottom of the column of the fluidised bed which holds the initial mass of solids, $m_{bed,0}$. At time t > 0 s the solids circulate through the modules. When the inlet solids flow rate of a module is equal to the outlet one, a constant mass is established in the module. Before this equilibrium is reached, the entering solids stream requires a time equal to the average solids residence time of the module to exit the module itself. Mathematically, this is achieved by means of the Heaviside step function which delays the exit of the solids stream of a dead time equal to the average solids residence time of the module. The solids circulation rate depends on the operating conditions so the integration time step should account for how fast the solids are travelling by knowing how long it is needed to exit any module. The modules are the "elutriation" (freeboard), the cyclone (including the inlet pipe) and the recycle (return leg). Using a time step greater than any of the residence times would not physically describe the process and the modules would be by-passed. The maximum time step

allowed is then given by the minimum between the residence times of the modules, as reported by Equation 6-26:

$$\Delta t_{max} = \min\left(\tau_{freeboard}, \tau_{cyc}, \tau_{rec}\right) \quad (6\text{-}26)$$

This value is to be taken as the very upper limit and it is therefore not suggested to be used. In general, the smaller the integration time step the more accurate the solution. Below, an estimation of the average solids residence times of each module is given:

- **Freeboard Average Solids Residence Time**

  The freeboard average solids residence time of the module "elutriation" $\tau_{freeboard}$ is calculated as the ratio between the length of the freeboard and the gas superficial velocity, which is theoretically equal to the terminal velocity of the largest particle size elutriated, Equation 6-27:

$$\tau_{freeboard} = \frac{h_{freeboard}}{u_{sup}} \quad (6\text{-}27)$$

- **Cyclone Average Solids Residence Time**

  The cyclone average residence time τ_{cyc}, including the inlet pipe, is extrapolated from the CFD-DEM analysis of F-CLC particles in a Stairmand cyclone, carried out in Chapter 4, as a function of the inlet pipe length "L", height of the cyclone "h_{cyc}" and gas velocity at the inlet, Equation 6-28:

$$\tau_{cyc} = \frac{2L + 60h_{cyc}}{u_{cyc,inlet}} \quad (6\text{-}28)$$

- **Recycle Average Solids Residence Time**

  The average solids residence time of the recycle τ_{rec} is roughly estimated as the ratio between the height of the return leg and the free fall velocity of the maximum particle size elutriated which is equal to the gas superficial velocity, Equation 6-29.

$$\tau_{rec} = \frac{h_{rec}}{u_{sup}} \quad (6\text{-}29)$$

6.2.5 Description of the Jet and Bubbling Bed Regions

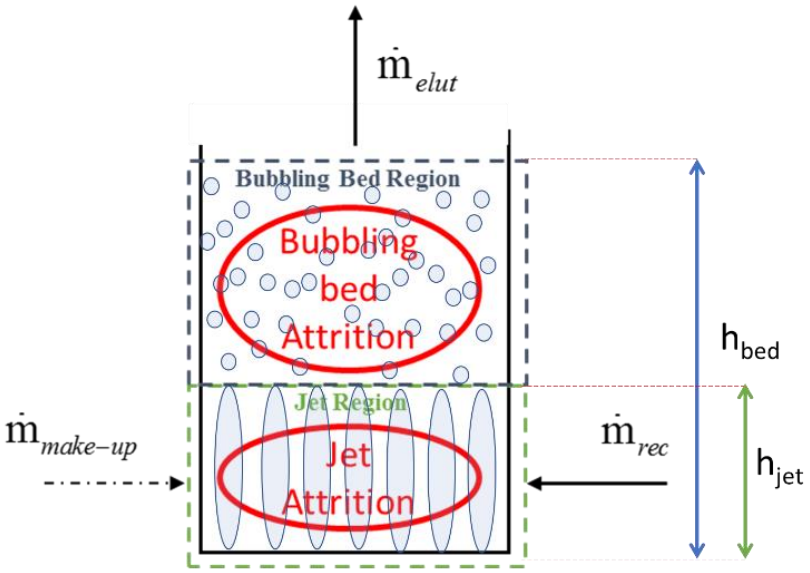

Figure 6-5. Jet and bubbling bed region

The fluidised material at the bottom of the column undergoes attrition as caused by the jets and the bubbling bed. It is common to distinguish between the two sources for three main reasons: (i) they take place in relatively well distinct areas, the former from the distributor to the jet height and the latter form the jet height till the solids bed free surface, (ii) the attrition mechanisms might differ from mainly collisional in the jet region and mainly surface wear in the bubbling bed and (iii) the magnitude of attrition is larger in the jet region than the bubbling bed. In the PBM, a planar boundary is considered dividing the two regions, with the jet penetration height evaluated with the correlation of Merry, (1975), presented in Equation 5-21. As mentioned previously, the fluidised material is assumed to be perfectly mixed so the mass which undergoes jet attrition is simply a fraction of the mass of any class, referred to as X_{jet}. This is equal to the ratio of the jet height and the bed height, as given by Equation 6-30. At the same time, the fraction of bed which is subjected to bubbling attrition is X_{bb}, Equation 6-31.

$$X_{jet} = \frac{h_{jet}}{h_{bed}} \tag{6-30}$$

$$X_{bb} = 1 - \frac{h_{jet}}{h_{bed}} \tag{6-31}$$

This is an over-simplification because jet attrition operates on the flux of entrained particles within the jet core. So, further investigation is needed here in order to improve the description of the attrition mechanisms occurring in the jet region.

Recalling Equation 6-30 and Equation 6-31, the height of the bed is given by the model of Choi et al. (1999) as a function of the minimum fluidisation bed height and velocity, ($h_{bed,mf}$, u_{mf}), and the superficial velocity u_{sup}, as shown in Equation 6-32:

$$\frac{h_{bed,mf}}{h_{bed}} = 1 - \left(1 - \frac{u_{mf}}{u_{sup}}\right)^{(1.06u_{mf}+1)/(1.06u_{mf})} \tag{6-32}$$

Assuming incompressible fluid, the superficial gas velocity is computed as the ratio of gas volumetric flow rate and area of the column, Equation 6-33.

$$u_{sup} = \frac{Q_f}{A_{bed}} \tag{6-33}$$

while the minimum fluidisation velocity is evaluated using the correlation of Baeyens and Geldart, (1986), shown in Equation 5-22.

The height of the bed at minimum fluidisation velocity, needed in Equation 6-32, is calculated from Equation 6-34:

$$h_{bed,mf} = \frac{m_{bed,0}}{A_{bed}\rho_{bed,mf}} \tag{6-34}$$

where the bed bulk density at minimum fluidisation is evaluated according to Equation 6-35, as a function of the void fraction at minimum fluidisation estimated from Ergun's equation, (Ergun, 1952; Agu et al. 2019).

$$\rho_{bed,mf} = \rho_p\left(1-\varepsilon_{mf}\right) + \rho_f\varepsilon_{mf} \tag{6-35}$$

The mass that would undergo attrition in the jet and bubbling bed can be calculated according to Equation 6-36 and Equation 6-37, respectively:

$$m_{jet} = m_{bed}X_{jet} \tag{6-36}$$

$$m_{bb} = m_{bed}X_{bb} \tag{6-37}$$

The two portions of mass will produce different amount of debris, the particles will shrink to different extents, and consequently be classified separately. Recalling Equation 6-18,

the mass balance for a class "i" for the jet/bubbling bed region can be summarised, as shown by Equation 6-38, as the combination of the jet and bubbling bed contributions:

$$dm_{bed,i} = \sum_{k=i+1}^{N} m_{k,i}^{mp,jet} + \sum_{k=i+1}^{N} m_{k,i}^{mp,bb} - m_{i,[1\ i-1]}^{mp,jet} - m_{i,[1\ i-1]}^{mp,bb} - m_{i,[1\ n_{max}^{de}]}^{de,jet} - m_{i,[1\ n_{max}^{de}]}^{de,bb} + m_{[n_{min}^{mp}\ N],i}^{de} +$$

$$-m_{elut,i} + m_{makeup,i} \tag{6-38}$$

The total extent of attrition of the fluidised bed can be expressed as the summation of that induced by the jet and bubbling bed region, as shown in Equation 6-39:

$$R_{bed} = R_{jet} + R_{bb} \tag{6-39}$$

where R_{jet} and R_{bb} are given by Equation 6-40 and Equation 6-41, respectively:

$$R_{jet} = \dot{R}_{jet}\Delta t \tag{6-40}$$

$$R_{bb} = \dot{R}_{bb}\Delta t \tag{6-41}$$

$\dot{R}_{jet}$ and $\dot{R}_{bb}$ are the attrition correlations. The total mass of debris particles generated by the fluidised bed is eventually given by:

$$m^{de} = R_{bed} m_{bed} \tag{6-42}$$

6.2.5.1 Jet Attrition

The jet attrition correlation obtained experimentally for F-CLC particles is used here, Equation 6-43:

$$\begin{cases} \dot{R}_{jet} = \alpha \dfrac{H}{K_c^2} c_{jet} n_{or} \rho_p u_{jet}^2 d_{or}^{1.7} \\ u_{jet} > u_{jet,0} \end{cases} \tag{6-43}$$

where $u_{jet,0}$ is the jet transition velocity from no attrition to attrition. The correlation has been developed experimentally by normalising the steady state mass loss with the total mass of the bed inventory, for a certain period of time, Equation 6-44.

$$\dot{R}_{jet} = \frac{\text{SS mass of debris particle due to jet attrition}}{\text{total mass of the bed solids} \times \Delta t} = \frac{m_{jet}^{de}}{m_{bed}\Delta t} \tag{6-44}$$

However, here, jet attrition is assumed to be confined to the portion of the bed limited by the jet height. Furthermore, no study has been carried out on the effect of particle size and mass fraction on the jet attrition, so it remains unknown how the attrition mass is

originated from the different size classes. Upon these reflections, the current model is corrected as shown below.

- **Correction of the Mass Used for Normalisation**

  The normalised jet attrition rate defined on its mass of interest, i.e. the mass of solids below the jet height m_{jet}, is referred to as $\dot{R}'_{jet}$ and defined in Equation 6-46

$$\dot{R}'_{jet} = \frac{\text{SS mass of debris particle due to jet attrition}}{\text{mass of the bed solids below jet height} \times \Delta t} = \frac{m^{de}_{jet}}{m_{jet}\Delta t} \tag{6-45}$$

  $\dot{R}'_{jet}$ is obtained by multiplying and dividing $\dot{R}_{jet}$ with m_{jet}, and recalling that $X_{jet}=m_{jet}/m_{bed,}$ as shown below in Equation 6-46

$$\dot{R}_{jet} = \frac{m^{de}_{jet}}{\Delta t m_{bed}} \frac{m_{jet}}{m_{jet}} = \frac{m^{de}_{jet}}{\Delta t m_{jet}} X_{jet} = \dot{R}'_{jet} X_{jet} \tag{6-46}$$

  Hence, $\dot{R}'_{jet}$ can be written as Equation 6-47:

$$\dot{R}'_{jet} = \dot{R}_{jet} \frac{1}{X_{jet}} \tag{6-47}$$

  The total mass of debris particles generated as result of jet attrition is then equal to Equation 6-48

$$m^{de}_{jet} = m_{bed} \dot{R}'_{jet} X_{jet} \Delta t \tag{6-48}$$

- **Distribution of the Total Attrition to Different Classes**

  It is intuitive to think that very populated classes would have a larger weight in contributing to the total attrition as compared to less populated ones. According to Werther and Xi, (1993), the same concept applies to large particles as compared to small ones, which is fair considering the collisional nature of jet attrition and its established linear dependency on particle size, (Ghadiri et al. 1992; Boerefijn et al. 2007; Boerefijn et al. 2000). In view of these assumptions, the total mass of debris particles produced by jet attrition is partitioned between the size classes according to the particle size and the mass fraction of the classes, as shown below in Equation 6-49:

$$m_{jet,i}^{de} = m_{jet}^{de} \frac{x_{bed,i} d_{p,i}^{mp}}{\sum_{i=n_{min}^{mp}}^{N} x_{bed,i} d_{p,i}^{mp}} \tag{6-49}$$

Dividing both sides by $m_{jet}^{mp} \Delta t$, Equation 6-50 is obtained:

$$\frac{m_{jet,i}^{de}}{m_{jet}^{mp} \Delta t} = \frac{m_{jet}^{de}}{m_{jet}^{mp} \Delta t} \frac{x_{bed,i} d_{p,i}^{mp}}{\sum_{i=n_{min}^{mp}}^{N} x_{bed,i} d_{p,i}^{mp}} \tag{6-50}$$

by considering that $m_{jet,\,i} = x_{bed,i}\, m_{jet}$, where $x_{bed,i}$ is the mass fraction of the size class "i", it is possible to derive Equation 6-51:

$$\dot{R}_{jet,i}^{'} = \frac{\dot{R}_{jet}^{'}}{x_{bed,i}} \frac{x_{bed,i} d_{p,i}^{mp}}{\sum_{i=n_{min}^{mp}}^{N} x_{bed,i} d_{p,i}^{mp}} \tag{6-51}$$

the equation above can be then written as Equation 6-52, recalling that $\sum_{i=n_{min}^{mp}}^{N} x_{bed,i} d_{p,i}^{mp}$ is the average mother particle size of the bed inventory:

$$\dot{R}_{jet,i}^{'} = \dot{R}_{jet}^{'} \frac{d_{p,i}^{mp}}{d_{p,av}^{mp}} \tag{6-52}$$

Eventually, by knowing the corrected normalised jet attrition rate of the class "i", the mass of the mother particle shrunk due to jet attrition can be calculated following Equation 6-8.

6.2.5.2 Bubbling bed Attrition

The normalised attrition rate for the bubbling bed is defined as shown below in Equation 6-53

$$\dot{R}_{bb} = \frac{\text{SS mass of debris particle due to bb}}{\text{total mass of the bed solids} \times \Delta t} = \frac{m_{bb}^{de}}{m_{bed} \Delta t} \tag{6-53}$$

According to Arena et al. (1983), Scala and Salatino, (2010) and Merrick and Highley, (1974a), the bubbling bed attrition is a linear function of the excess of fluidisation velocity, so it is here expressed as shown in Equation 6-54:

$$\dot{R}_{bb} = \alpha \frac{H}{K_c^2} c_{bb} \left(u_{sup} - u_{mf} \right) \tag{6-54}$$

As mentioned earlier for the jet attrition, the corrected normalised attrition rate for the bubbling bed would be defined according Equation 6-55

$$\dot{R}'_{bb} = \frac{\text{SS mass of debris particle due to bb}}{\text{mass of the bed solids above jet height} \times \Delta t} = \frac{m_{bb}^{de}}{m_{bb} \Delta t} \tag{6-55}$$

Below, the bubbling bed attrition rate is corrected to its mass of interest, as shown previously for the jet, and distributed to different classes.

- **Correction of the Mass Used for Normalisation**

  As done previously for the jet attrition, the corrected normalised bubbling bed attrition rate can be written as shown in Equation 6-56:

$$\dot{R}'_{bb} = \dot{R}_{bb} \frac{1}{X_{bb}} \tag{6-56}$$

- **Distribution of the Total Attrition to Different Classes**

  Not having investigated the effect of particle size, the works of Donsi et al. (1981), Arena et al. (1983), Ray and Jiang, (1987), Chirone et al. (1991) are used here as a reference to assign a particle size dependency to the debris produced by the bubbles. Their experimental evidences suggest a direct relationship with the surface of the solids (available for attrition), proportional to "$m_{bed}/d_{p,bed}$", for a wide range of materials. Therefore, the normalised attrition rate would be inversely proportional to the particle size as shown in Equation 5-6. On this base, the total mass of debris is shared between the classes according to Equation 6-57:

$$m_{bb,i}^{de} = m_{bb}^{de} \frac{m_{bb,i}^{mp} / d_{p,i}^{mp}}{\sum_{i=n_{min}^{mp}}^{N} m_{bb,i}^{mp} / d_{p,i}^{mp}} \tag{6-57}$$

  dividing both sides of Equation 6-62 by $m_{bb}^{mp} \Delta t$ and knowing that $m_{bb,i} = x_{bed,i}\, m_{bb}$, Equation 6-58 is obtained:

$$R'_{bb,i} = R'_{bb} \frac{1 / d_{p,i}^{mp}}{\sum_{i=n_{min}^{mp}}^{N} x_{bed,i} / d_{p,i}^{mp}} \tag{6-58}$$

recalling that $\frac{1}{\sum_{i=n_{min}^{mp}}^{N} x_{bed,i} / d_{p,i}^{mp}}$ is the definition of the Sauter mean diameter of the bed mother particles, the normalised bubbling bed attrition rate of the class "i" can be formalised as shown in Equation 6-61:

$$R'_{bb,i} = R'_{bb} \frac{d_{p,Saut}^{mp}}{d_{p,i}^{mp}} \quad (6\text{-}59)$$

Eventually, by knowing the corrected normalised bubbling bed attrition rate of the class "i", the mass of the mother particle shrunk due to bubbling bed attrition can be calculated following Equation 6-8.

6.2.5.3 Jet and Bubbling Bed Debris Particle Size Distribution

The PSD of the material collected on the filter under steady state attrition at 55 m s^{-1} jet velocity is used as a reference to model the size of the debris particles in the PBM. The experimental PSD is obtained by the laser diffraction technique using the Mastersizer 3000 and dry dispersion by Aero S, as shown in Chapter 5. Performing a deconvolution analysis, the bimodal trend is revealed to be composed of two Gaussians, as shown in Figure 6-6.

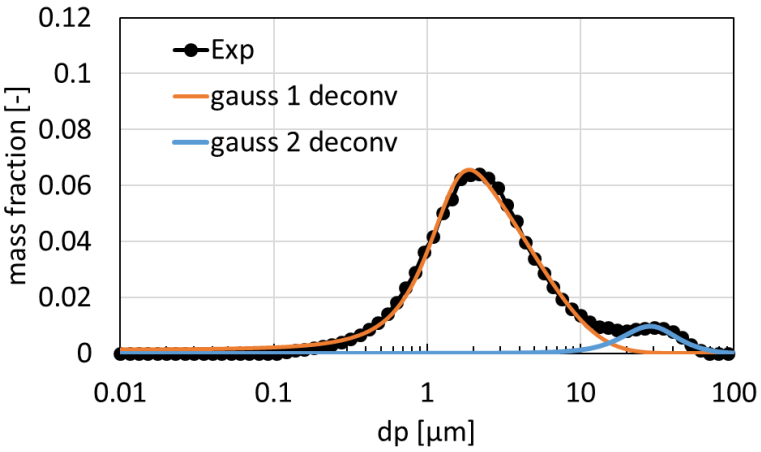

Figure 6-6. Deconvolution of the PSD of fines collected on the filter at 55 m s^{-1} of jet velocity

As indicated by Ray et al. (1987) and Ray and Jiang, (1987), it is possible to determine the mass fraction as a function of particle size using beta functions. Two symmetry parameters, e_a (right-hand) and e_b (left-hand) and an upper limit which suits well the role

of the maximum debris particle size formed by attrition, define the beta function, as shown in Equation 6-60.

$$x_{beta}^{de}(d_p) = \frac{1}{d_{p,max}^{de}} \frac{(e_a + e_b + 1)!}{e_a ! e_b !} \left(\frac{d_p}{d_{p,max}^{de}} \right)^{e_a} \left(1 - \frac{d_p}{d_{p,max}^{de}} \right)^{e_b} \quad (6\text{-}60)$$

So, the two Gaussians are fitted with two beta functions using a $d_{p,max}^{de}$ of 80 µm, as indicated by the laser diffraction results. The two beta functions are found to be convoluted by a scaling factor β= 0.92, so the mass fraction "x^{de}" can be expressed according to Equation 6-61.

$$x^{de} = \beta x_{beta1}^{de} + (1-\beta) x_{beta2}^{de} \quad (6\text{-}61)$$

The curves are shown individually in Figure 6-7, while their fitting parameters, "e_a" and "e_b" are reported in Table 6-1. They are two real numbers but only their integer part is considered for the factorials of Equation 6-60.

Table 6-1. Deconvolution fitting parameters of beta functions: e_a and e_b.

	beta 1	**beta 2**
e_a [-]	1.64	3.07
e_b [-]	49.83	4.78
$d_{p,max}^{de}$ [µm]	80	

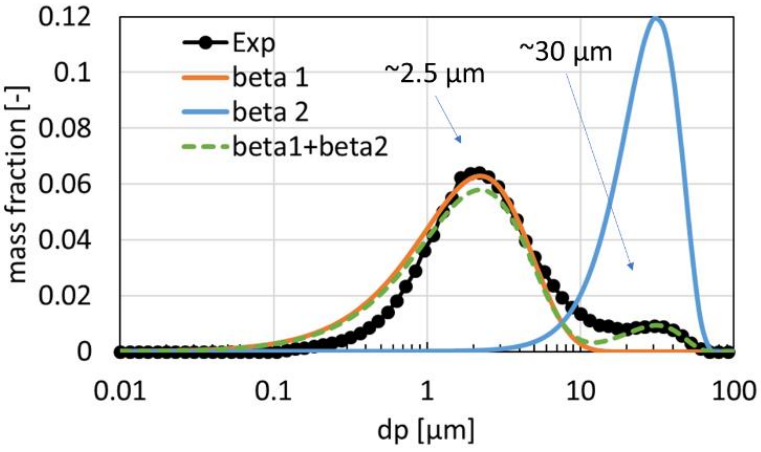

Figure 6-7. The curve beta 1 and beta 2 fitting the experimental PSD of fines collected at the filter at 55 m s^{-1} of jet velocity

The two peaks at about 2.5 and 30 μm might be the result of surface abrasion, mainly occurring in the bubbling bed, and chipping due to particle collision in the jet, respectively. This is also supported by the observations on the debris PSD of the cyclone experiments, presented in Chapter 4, which show the same two peaks, at all experimental conditions, as a result of surface abrasion due to sliding against the walls and collisions at the entrance. In view of these considerations, it is here assumed that the proportionality between the two beta functions would vary with the same proportionality that exists between the jet and the bubbling bed region, dictated by X_{jet}, through the scaling factor β, according to Equation 6-62:

$$\beta = 1 - cX_{jet} \tag{6-62}$$

where "c" is a constant found to be equal to 0.3 for an X_{jet}=0.26 and β =0.92 (at 55 m s^{-1} gas jet velocity). Various debris PSD at different hypothetical X_{jet} are reported in Figure 6-8 as example.

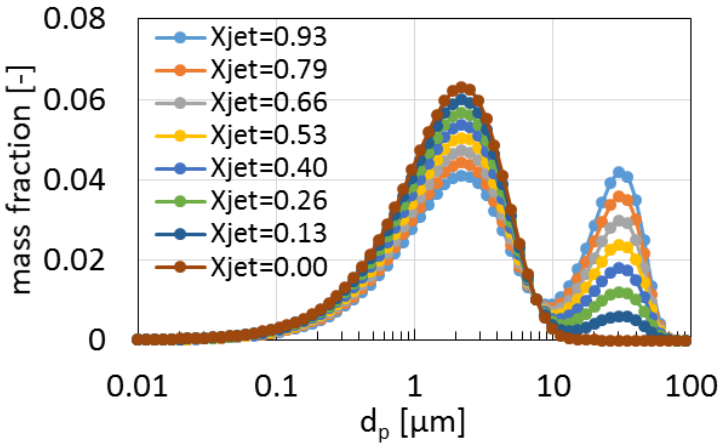

Figure 6-8. Debris size distribution for different X_{jet}

6.2.6 Entrainment

Particles are ejected from the bed free surface into the freeboard mainly by bubble eruption. Depending on the gas velocity, entrained particles can either rise or fall. So there exists a freeboard height that allows most of the particles having a terminal velocity larger than the superficial velocity to fall back in, and as a result the entrainment rate does not change appreciably thereon. This is defined as Transport Disengagement Height (TDH), (Sciazko et al. 1991; Cahyadi et al. 2015). On this basis, the entrainment rate can be seen as the summation of (i) a dispersed non-cluster flux which remains constant with the

freeboard height and (ii) and a cluster flux which follows an exponential decay with the freeboard height, (Kunii and Levenspiel, 1990; Adánez et al. 1994; Choi et al. 1999). The model of Choi et al. (1999) is used here to calculate the entrainment rate in the freeboard, (Haus et al. (2017 and 2018)). The correlation has been developed on the basis of a vast sets of experimental data obtained at different scales, bed particle size distribution, particle densities, temperature, and superficial velocities. The entrainment flux constant for a size class "i", K_i^*, is given by Equation 6-63:

$$K_i^* = K_{h,i}^* + K_{\infty,i}^* \tag{6-63}$$

where $K_{h,i}^*$ is the cluster flux which follows an exponential decay with the height of the bed while $K_{\infty,i}^*$ is the dispersed non-cluster entrainment rate independent from the freeboard height. The former is defined in Equation 6-64:

$$K_{h,i}^* = \frac{\eta}{d_{p,i}} C_D \, Re_p \exp\left(-9.12 - 0.0153a\left(h_{tot} - h_{bed}\right)\right) \tag{6-64}$$

The particle Reynolds number Re_p is defined in Equation 5-18 while the drag coefficient C_D is calculated according to Equation 6-65, (Choi et al. 1999), :

$$C_D \begin{cases} 24 / Re_p & \text{for } Re_p \le 5.8 \\ 10 / Re_p^{0.5} & \text{for } 5.8 \le Re_p \le 540 \\ 0.43 & \text{for } 540 < Re_p \end{cases} \tag{6-65}$$

On the other hand, $K_{\infty,i}^*$ is calculated as shown by Equation 6-66:

$$K_{\infty,i}^* = \frac{\eta}{d_{p,i}} Ar^{0.5} \exp\left(6.92 - 2.11 F_g^{0.303} - \frac{13.1}{F_d^{0.902}} \right) \tag{6-66}$$

Ar, F_g, and F_d are the Archimedes number (calculated according Equation 5-20), the gravity force minus the buoyancy force per projection area of the particle (calculated in Equation 6-67), and the drag force acting on the particle per projection area (calculated in Equation 6-68), respectively:

$$F_g = g d_p \left(\rho_p - \rho_f\right) \tag{6-67}$$

$$F_d = C_D \rho_f \frac{u_{sup}^2}{2} \tag{6-68}$$

In order to obtain the entrainment flux, the entrainment flux constant needs to be multiplied by the mass fraction of the bed solids.

6.2.7 Description of the Cyclone Attrition and Separation Efficiency

The correlation of particle attrition in the cyclone, obtained from the CFD-DEM study and experimental analysis on F-CLC, is used here. The cyclone has the role of separating the solids from the gas stream so they can be recycled. The two mechanisms of attrition and separation are modelled in series with attrition occurring first. It implies that the material subjected to separation has already undergone attrition, (Werther and Hartge, 2004; Klett et al. 2007; Hartge et al. 2007; Redemann et al. 2009). The separation is described according to the critical load hypothesis suggested by Muschelknautz, (1997) which divides the cyclone separation into a spontaneous separation of the surplus mass at the cyclone inlet and a subsequent inner vortex separation of the remaining critical mass.

6.2.7.1 Cyclone Attrition

The extent of attrition induced by the cyclone for a size class "i" is reported below in Equation 6-69:

$$\begin{cases} R_{cyc,i} = \alpha \frac{H}{K_c^2} c_{cyc} \frac{u_{cyc,in}^3}{d_{p,i} \mu^{0.2}} \\ u_{cyc,in} > u_{cyc,0} \end{cases} \tag{6-69}$$

where $u_{cyc,0}$ is the transition cyclone gas inlet velocity, below which no attrition is expected, as described in section 4.2.4.4 and defined in Equation 4-4.

The correlation, obtained for a narrow size cut, is assumed to be valid within a mixture as well. Further investigation is needed to support this assumption.

6.2.7.2 Cyclone Separation Efficiency

As indicated by Muschelknautz, (1997), the turbulence in the cyclone entails only a certain solids fraction which can be carried in the swirling flow. If the solids loading exceeds a critical value μ_{lim}, the excess mass fraction is removed immediately and unfractionated after the cyclone inlet by forming strands or a continuous layer at the wall.

Only a small fraction of finer particle size distribution, referred to as "inner feed", remains in the gas flow and undergoes centrifugal separation in the cyclone inner vortex.

The efficiency separation at the wall η_e is given by Equation 6-70:

$$\eta_e = 1 - \frac{\mu_{lim}}{\mu} \tag{6-70}$$

where μ is the solids loading of the feed of the cyclone, defined in Equation 4-2 as the ratio of the solids flow rate and the gas flow rate. The inner feed cumulative PSD is approximated with a Rosin-Rammler-Sperling-Bennet function (RRSB) as shown in Equation 6-71:

$$R_{Ai}(d_p) = 1 - \exp\left[\left(-\frac{d_p}{1.3 d_{50,Ai}}\right)^{1.2}\right] \tag{6-71}$$

where $d_{50,Ai}$ is a characteristic particle size. With increasing feed solids loading, the separation efficiency at the wall η_e increases as shown in Equation 6-70; the separation efficiency at the inner vortex however, declines due to the decrease of the inner tangential velocity. On the other hand, if the solids loading does not exceed the critical value all the feed will be carried away in the inner vortex.

The mass fraction of a class "i", $x_{cyc,exit,i}$, leaving from the top exit of the cyclone can be then expressed for the two cases as follows, Equation 6-72:

$$\begin{cases} x_{cyc,exit,i} = \dfrac{\mu_{lim}}{\mu} \dfrac{1-\eta_{eff,IF,i}(d_{p,i})}{1-\eta_{eff}} x_{cyc,IF,i} & \text{for } \mu < \mu_{lim} \\ x_{cyc,exit,i} = \dfrac{\mu_{lim}}{\mu} \dfrac{1-\eta_{eff,IF,i}(d_{p,i})}{1-\eta_{eff}} x_{cyc,in,i} & \text{for } \mu \geq \mu_{lim} \end{cases} \tag{6-72}$$

where $\eta_{eff,IF,i}(d_{p,i})$ is the grade efficiency of separation in the inner vortex and η_{eff} is the total efficiency of separation, given by Equation 6-73:

$$\begin{cases} \eta_{eff} = \eta_{eff,IF} & \text{for } \mu < \mu_{lim} \\ \eta_{eff} = 1 - \dfrac{\mu_{lim}}{\mu}\left(1-\eta_{eff,IF}\right) & \text{for } \mu \geq \mu_{lim} \end{cases} \tag{6-73}$$

The cyclone grade efficiency can be written as shown below in Equation 6-74:

$$\eta_{eff,i} = 1-(1-\eta_{eff})\frac{x_{cyc,exit}}{x_{cyc,in}} \quad (6\text{-}74)$$

Thus, the mass rate of the class "i" leaving the cyclone from the top and bottom exit are calculated using the grade efficiency according to Equation 6-75 and Equation 6-76, respectively:

$$\dot{m}_{cyc,exit,i} = \dot{m}_{cyc,in,i}(1-\eta_{eff,i}) \quad (6\text{-}75)$$

$$\dot{m}_{cyc,rec,i} = \dot{m}_{cyc,in,i}\eta_{eff,i} \quad (6\text{-}76)$$

6.2.7.3 Cyclone Debris Particle Size Distribution

The PSDs of the debris collected from the experimental work on cyclone attrition, as given by the laser diffraction technique using the Malvern Mastersizer 3000 and dispersion by Aero S, are used as a reference for the PBM. The debris particles are obtained from experiments carried out on F-CLC particles at different conditions of gas velocities, solids loadings, and particle sizes. The two beta functions used to fit the debris PSD in the fluidised bed, with parameters reported in Table 6-1, are applied here to describe the common modes between all the conditions tested, as seen in Chapter 4 and reported in Figure 6-9. The highest peak concerning large fragments is not considered because the PBM, as developed here, only accounts for breakage derived from surface damage which causes shrinking of the particles. Moreover, in Figure 4-10, the Schumann plots of the cyclone attrition results show that that the fragmentation limit is not reached.

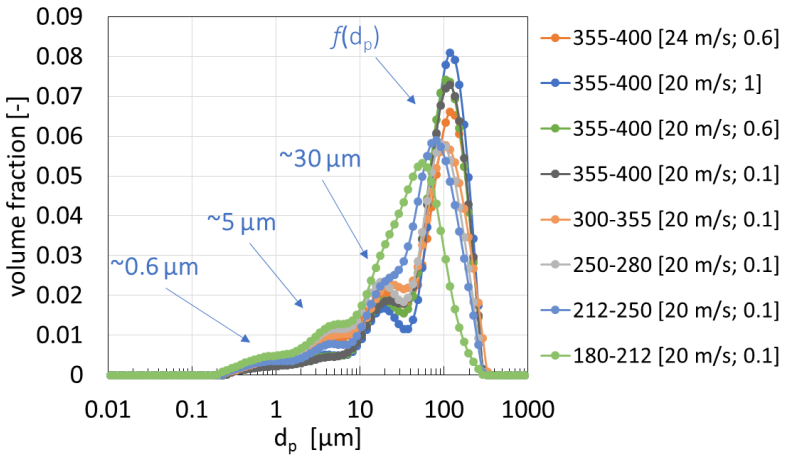

Figure 6-9. Debris PSD of the cyclone experiments obtained for different feed particle size conditions, gas inlet velocities and solids loadings. The legend is organised as shown: *feed particle size* [*gas inlet velocity; solids loading*]

A representative debris PSD curve is obtained by averaging the PSDs obtained at all conditions, truncating it at $d_{p,max}^{de}$ equal to 80 µm and rescaling to have the unitary sum of the mass fractions. By doing so, the mode concerning the fragments are excluded. This curve is shown in Figure 6-10 and referred to as "Exp". It should be noted that this would lead to an overestimation of the debris mass fraction of small sizes because of the truncation of the contribution given by the fragments. A proportionality factor of β=0.3 is found to best describe this curve by convolution of the function beta 1 and 2, by minimising the summation of the standard deviations. In particular, the function beta 1, of mode of 2.5 µm, is used to describe the bimodal behaviour shown at 0.6 and 5 µm and the function beta 2 is used to describe the peak at about 30 µm.

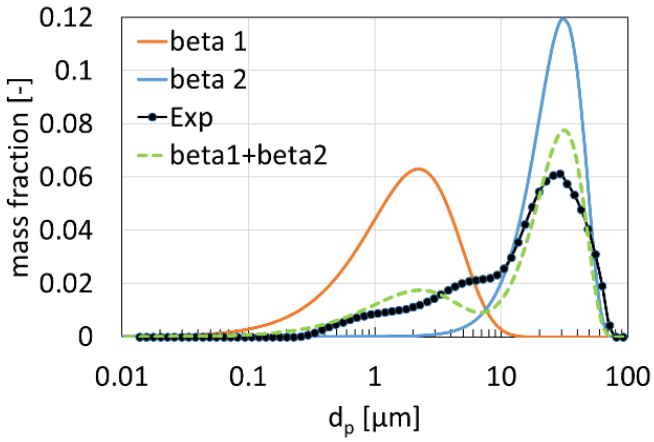

Figure 6-10. The curve beta 1 and beta 2 fitting the experimental representative PSD of debris collected from the cyclone attrition experiments.

It has to be outlined that these experimental PSDs are related to the material which was collected at the cyclone catch-pot. Therefore, the very fine particles, which have escaped the cyclone could not be considered leading to an underestimation of the finest fraction. Moreover, the debris PSDs obtained experimentally for F-CLC are the result of relatively large feed particles, from 180 to 400 µm, while the particle size of the elutriation stream, which feeds the cyclone, could be composed of smaller particles depending on the operating conditions. In the instance that the largest feed particle size is smaller than $d_{p,max}^{de}$, the debris PSD would be truncated to the largest particle size fed and rescaled to have the unitary sum of their mass fraction. This needs improvement by further

investigating the debris PSD obtained by attrition in the cyclone for much smaller feed particle sizes.

6.3 Results and discussions

6.3.1 Validation

To verify the robustness and validity of the PBM the same fluidised bed apparatus used for the jet attrition study is simulated, and the outcomes are compared with the experimental results. However, this could not be done for the circulating fluidised bed configuration, because no experiments were performed on such system, thus further investigation is needed in this matter. The jet and bubbling bed attrition rates, as well as the debris PSD, are obtained from the same fluidised bed apparatus and modelled to be implemented in the PBM, so they cannot be used as validation criteria. On the other hand, a qualitative validation can be carried out by comparing the predicted bed inventory PSD and the mass loss rate with those evaluated experimentally. For this purpose, the whole experimental history on the fluidised bed shown in Chapter 5 of F-CLC is simulated by the PBM. The error between predicted and experimental values is also computed to estimate quantitively the robustness of the PBM. The dimensions of the fluidised bed and other main simulation parameters, such as attrition constants, gas specifications and time step are reported in Table 6-2.

The jet velocities and sizes are varied to replicate the 67 days of experiment on F-CLC particles, referred to as "EXP 1" in Chapter 5. Consistent with the experiments, the porous base is also considered in the PBM as additional source of fluidising gas.

The initial particle size distribution of the bed inventory used in the PBM is that given by laser diffraction. Hence, in this case, the predefined size classes given by the laser diffraction results are used. Laser diffraction gives the PSD on the volumetric basis which is directly comparable with that predicted by the PBM, on mass basis, assuming constant particle density.

Table 6-2. Simulation specifications used in PBM for validation against experimental results for F-CLC particles

Symbol	Description	Value	Unit measure
Fluidised Bed Column			
d_{bed}	Bed diameter	0.1	m
d_{or}	Jet diameter	[3, 4, 5]	mm
h_{tot}	Total column height	0.986	m
n_{jet}	Number of jets	1	-
Gas and Solid Conditions			
ρ_p	Particle envelope density	3300	kg m^{-3}
$d_{p,Saut}$	Sauter mean diameter	126.1	µm
$m_{bed,0}$	Initial mass of solids	3.2	kg
g	Gravity	9.8	m s^{-2}
gas	AIR		
P	Pressure	101325	Pa
T	Temperature	25	C°
u_{mf} (calculated)	Minimum fluidisation velocity	0.020	m s^{-1}
u_{sup}	Superficial velocity	0.243	m s^{-1}
u_{jet}	Jet velocity	[30.00, 42.50, 48.75, 55.00]	m s^{-1}
d_{p,max_elut} (calculated)	Maximum particle size elutriated	53	µm
Attrition Parameters			
1. Single Particle			
$\alpha \frac{H}{K_c^2}$	Single particle breakability index	2.69×10^{-5}	$m^2 J^{-1}$
b_{sp}	Single particle breakage model constant	2.32×10^5	-
2. Jet attrition			

c_{jet}	Jet attrition index	5.53×10^{-7}	$m^{-0.7}\ s^{-1}$
$u^{\wedge}_{jet}$	Jet velocity power dependency	2	-
$d^{\wedge}_{jet}$	Jet size power dependency	1.7	-
u_{jet0}	Jet transition velocity	13.5	$m\ s^{-1}$
$d^{mp}_{p,min}\big\|_{v_{jet}=55\ m/s}$ (calculated)	Minimum mother particle size at 55 $m\ s^{-1}$ jet velocity	60.0	μm
3. Bubbling bed attrition			
c_{bb}	Bubbling bed attrition index	4.85×10^{-4}	$kg\ m^{-1}\ s^{-2}$
4. Debris PSD			
$e_{a,\ beta1}$	Beta 1 function constant	1.64	-
$e_{b,\ beta1}$	Beta 1 function constant	49.83	-
$e_{a,\ beta2}$	Beta 2 function constant	3.07	-
$e_{b,\ beta2}$	Beta 2 function constant	4.78	-
d^{de}_{max}	Maximum debris size	80	μm
Simulation Parameters			
Δt	Integration time step	0.5	s
Δt_{save}	Saving time step	40	s
$d_{p,max}$	Maximum particle size considered	735	μm
N	Number of classes	82	-
span	Class span	variable	μm
t_{tot}	Total simulation time	67	days

The comparison between the experimental normalised loss rate of "EXP 1", described in section 5.4.1, with that given by the PBM at all the conditions of jet velocities and orifice sizes is reported in Figure 6-11. As shown, the normalised loss rate given by the PBM reflects the experimental outcomes. This is expected as the attrition correlations are developed based on the steady state loss rate of the same experiments. The main

discrepancy between the two is shown in the initial transient period where fluidisation is provided only by the porous base. This is mainly due (i) to the initial degree of pre-existing fines which are immediately elutriated together with the debris produced by attrition. It is intuitive to think that the higher the initial extent of elutriable fines the longer it would take to reach a stationary loss rate which, at this point, is going to be directly dictated by attrition. Another possible reason is that, (ii) in reality, the initial attrition rate of fresh material is higher due to the removal of the surface irregularities. If this effect is accounted for, by introducing an age factor into the attrition correlation, (Redemann et al. 2009), the transient period would be even more delayed. Moreover, (iii) the given extent of pre-existing elutriable fines, in this case all the particles below about 53 μm, is given by laser diffraction analysis and therefore inevitably dependent on the accuracy of the measurement technique. It needs to be further considered that (iv) entrainment is here immediate while it is itself not an immediate phenomenon.

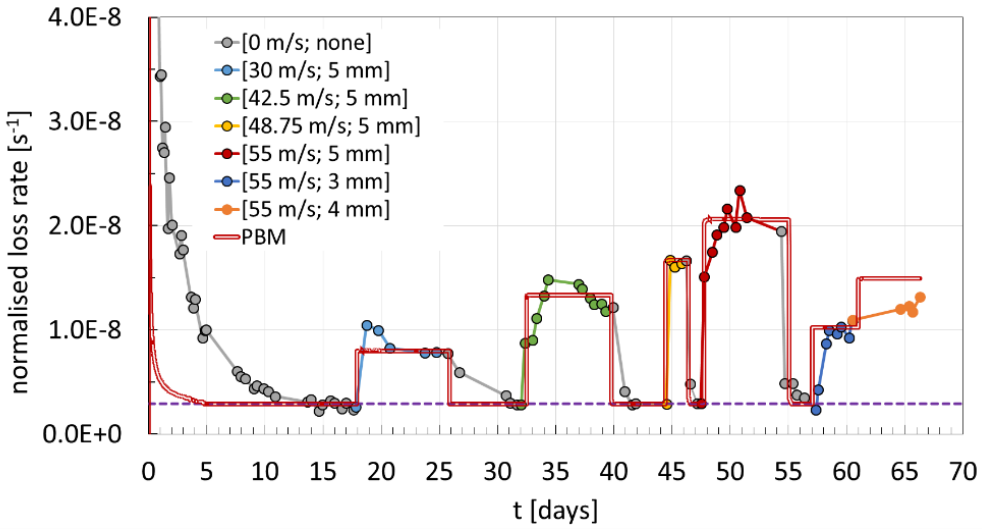

Figure 6-11. Comparison of the experimental normalised loss rate from the fluidised bed for F-CLC with that predicted by the PBM for different jet velocities and orifice sizes. The legend is organised as [*jet velocity; orifice size*].

A more robust idea of the ability of the PBM to simulate an actual system can be given by comparing the cumulative PSD predicted by the PBM with that of the bed inventory at the end of the experiment, reported in Figure 6-12, showing a very good agreement. The arithmetic mean diameter and the Sauter mean diameter of the bed are reported and compared in Table 6-3. The percentage error is also calculated according to Equation 6-77 and reported in the same table to quantify the predictive ability of the PBM. As shown,

the prediction in terms of arithmetic average bed solids diameter does not exceed 2% while the Sauter mean diameter of the bed solids seems to be also well predicted, as the error remains below 6%. A more robust validation of this PBM could be given by comparing its outcomes with different materials and on an actual circulating fluidised bed systems. More work is needed on this matter.

$$e = \frac{\left|d_{p,exp} - d_{p,sim}\right|}{d_{p,exp}} \times 100 \tag{6-77}$$

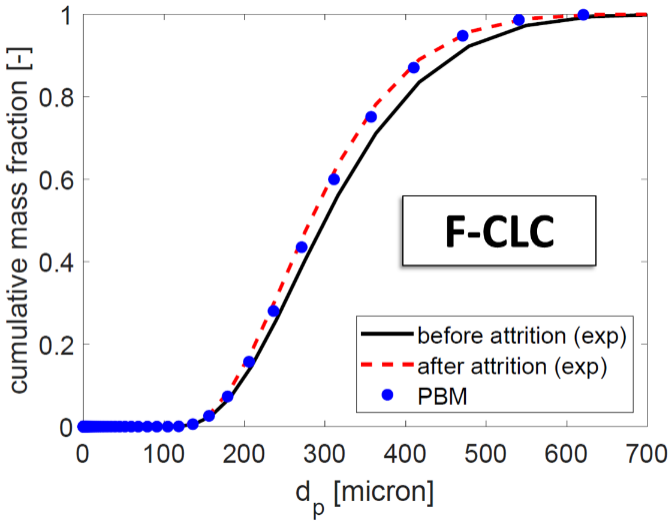

Figure 6-12. Comparison of the experimental PSD with the simulation at the end of the experiments for F-CLC

Table 6-3. Comparison of the bed average diameters

Characteristic particle size [µm]	before attrition (exp)	after attrition (exp)	PBM	*error* exp vs PBM, [%]
$d_{p,av,bed}$	321.5	316.3	320.9	1.4
$d_{p,Saut,bed}$	109.4	286.5	270.8	5.5

6.3.2 Simulation of Particle Attrition in a Fluidised bed and a Circulating Fluidised Bed

Several simulations are performed for both a fluidised bed and a circulating fluidised bed to elucidate the dynamic response of the process to particle attrition as originated from the bubbling bed, jet region, and cyclone. Results and discussion are presented next for

the fluidised bed and circulating fluidised bed configurations. Particular attention is paid to the effect of jet velocity, the single particle breakability, and the integration time step. The simulations time is 10 days while the default time step used is 0.5 s. Under these conditions, the simulation real time is about 3.2 hours, using a single core of 3.2 GHz, performing 150 time-steps per second. However, the simulation speed can be highly affected by the saving time step, here set to 40 s, and the number of classes set to 490 (from 0 to 735 μm with a narrow constant span of 1.5 μm to increase the stability of the resolution as well as improving the continuity of the results). The dimensions of the column of the CFB system replicate the fluidised bed apparatus used for the experimental work on jet attrition, except for the bed porous plate gas distributor which is not used in this case, so only the jet provides the fluidisation gas determining directly the superficial velocity, assuming a homogeneous fluidisation in the bubbling regime. Regarding the cyclone, the dimensions are those of the Stairmand type used for the experimental work on cyclone attrition. More specifications on the dimensions of the system and the operating conditions are reported below, in Table 6-4.

Table 6-4. Simulation specifications

Symbol	Description	Value	Unit measure
Fluidised Bed Column			
d_{bed}	Bed diameter	0.1	m
d_{or}	Jet diameter	0.005	m
h_{tot}	Total column height	0.986	m
n_{jet}	Number of jets	1	-
*Cyclone (*Figure 4-4*)*			
a_{cyc}	inlet height	0.02	m
b_{cyc}	inlet base	0.01	m
d_{cyc}	Cyclone diameter	0.04	m
d_{rec}	Bottom exit diameter	0.01	m
d_{VF}	Diameter vortex finder	0.02	m
$h_{cyc,\ body}$	Height of cylindrical body	0.08	m

$h_{cyc,\ body,\ VF}$	Height of vortex finder within the cylindrical body	0.03	m
$h_{tot,cyc}$	Total height of the cyclone	0.16	m
$L_{cyc,\ inlet}$	Inlet pipe length	0.35	m
Return Leg			
h_{rec}	$h_{tot-}\ h_{tot,cyc}$	0.826	m
Default Case Operating Conditions			
m_{bed0}	Initial mass of solids	3.2	kg
g	Gravity	9.8	$m\ s^{-2}$
gas	AIR		
P	Pressure	101325	Pa
T	Temperature	25	°
$d_{p,saut}$	Initial Sauter mean diameter	294.7	μm
u_{mf}	Minimum fluidisation velocity	0.086	$m\ s^{-1}$
Attrition Parameters			
$\alpha \frac{H}{K_c^2}\Big\vert_{F-CLC}$	Single particle breakability index	$2.69x10^{-5}$	$m^2\ J^{-1}$
b_{sp}	Single particle breakage model constant	$2.32\ x10^{-5}$	-
b_{cyc}	Cyclone attrition constant term	$4.95\ x10^{-5}$	s^{-1}
b_{jet}	Jet attrition constant term	$1.10\ x10^{-9}$	s^{-1}
c_{bb}	Bubbling bed attrition index	$1.25\ x10^{-3}$	$kg\ m^{-1}\ s^{-2}$
c_{cyc}	Cyclone attrition index	$1.67\ x10^{-6}$	$kg\ s\ m^{-2}$
c_{jet}	Jet attrition index	$5.53\ x10^{-7}$	$m^{-0.7}\ s^{-1}$
$e_{a,\ beta1}$	Beta 1 function constant	1.64	-
$e_{b,\ beta1}$	Beta 1 function constant	49.83	-
$e_{a,\ beta2}$	Beta 2 function constant	3.07	-
$e_{b,\ beta2}$	Beta 2 function constant	4.78	-
d_{max}^{de}	Maximum debris size	80	μm
Standard Case Simulation Parameters			
Δt	Integration time step	0.5	s

Δt_{save}	Saving time step	40	s
$d_{p,max}$	Maximum particle size considered	735	µm
N	Number of classes	490	-
span	Class span	1.50	µm
t_{tot}	Total simulation time	10	days

The initial particle size distribution of the bed inventory is that given by laser diffraction of F-CLC adapted to the classes of the PBM by means of a Gaussian fitting, given in Figure 6-13, which returns a Sauter mean diameter equal to 294.7 µm and arithmetic mean particle size of 338.8 µm.

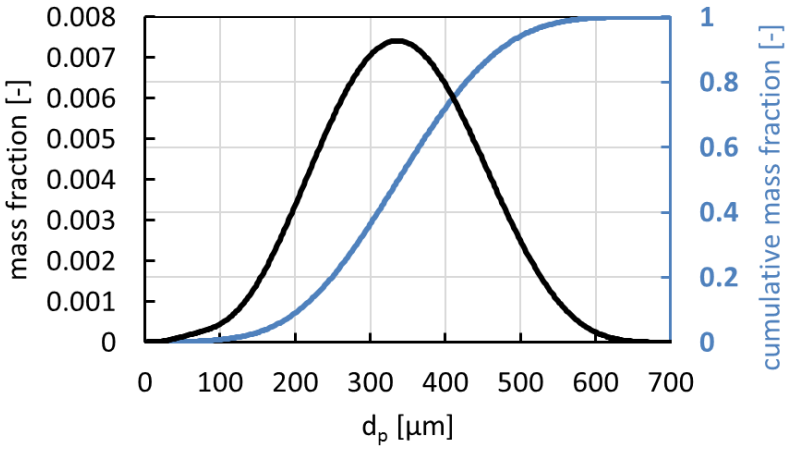

Figure 6-13. PSD of F-CLC used for validation of the PBM against experimental results

6.3.2.1 Fluidised Bed configuration

Referring to Table 6-5, several fluidised bed simulations are performed to look at the effect of time step, 0.1, 0.5 and 1 s, (cases 1, 2, 3, respectively), jet velocity, 55, 75, 95, 115 m s^{-1} (cases 2, 4, 5, 6, respectively) and the effect of particle breakability by setting 0.01, 0.1, 1, 10 and 100 times the breakability index of F-CLC (cases 2, 7, 8, 9, 10, respectively). As mentioned, each jet velocity corresponds to a superficial velocity, thus using the values mentioned above it is possible to fluidise the bed from 1.7 to 3.4 times u_{mf}. Neither make-up stream nor cyclone is considered for this configuration. Initially, the results obtained from the default conditions of case "2" are analysed and reported below.

Table 6-5. Simulations of fluidised bed (default case highlighted)

FB configuration							
#	**Δt** [s]	u_{jet} [m s^{-1}]	**u_{sup}** [m s^{-1}]	**u_{sup}/u_{mf}** [-]	**t_{tot}** [days]	$X\left(\alpha \frac{H}{K_c^2}\Big\vert_{F-CLC}\right)$	**loss tolerance** [%]
1	0.1	55	0.139	1.7	10	1	100
2	0.5	55	0.139	1.7	10	1	100
3	1	55	0.139	1.7	10	1	100
4	0.5	75	0.190	2.2	10	1	100
5	0.5	95	0.240	2.8	10	1	100
6	0.5	115	0.291	3.4	10	1	100
7	0.5	55	0.139	1.7	10	0.01	100
8	0.5	55	0.139	1.7	10	0.1	100
9	0.5	55	0.139	1.7	10	10	100
10	0.5	55	0.139	1.7	10	100	100

6.3.2.1.1 Default Case Fluidised Bed

Under the conditions of the default case, the minimum mother particle size is calculated to be 60 µm. As shown in Figure 6-14, the jet attrition rate is nearly one order of magnitude larger than that of the bubbling bed. The former is in fact about 94% of the total attrition rate.

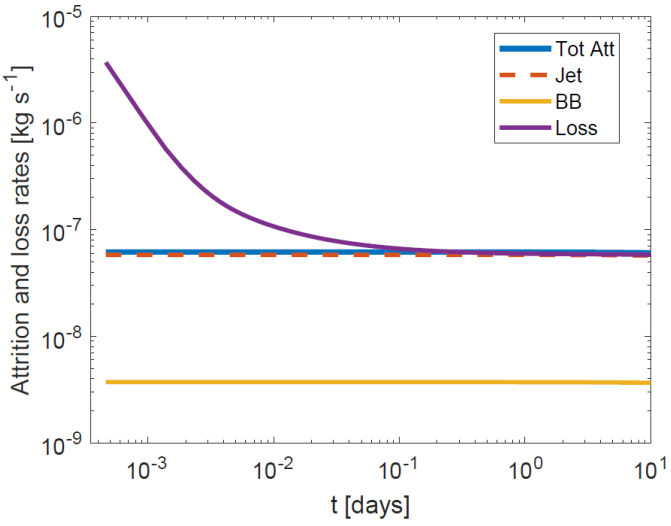

Figure 6-14. Attrition rates and loss rate for the FB

The rate of loss of material from the system, which is in this case equal to the elutriation rate, is initially extensively higher than the attrition rate, and requires about a day to reach a steady state. This is shown in Figure 6-15 in terms of magnitude of the difference between loss and attrition rate. Having the typical form of the absolute value function, the discontinuity represents the point where the loss and attrition rates intercept. Referring to Figure 6-16, it is clear how the PSD of the elutriation stream gradually shifts from the pre-existing fines to that of the debris produced by attrition (much finer). It follows that the average particle size of the bed inventory initially increases due to the removal of the pre-existing fines and later on decreases as a result of attrition, at this point dictating the loss rate. This is shown in Figure 6-17. The bed inventory PSD after 10 days is reported in Figure 6-18, showing a slight shifting towards smaller sizes for the larger particles and loss of the finer fractions.

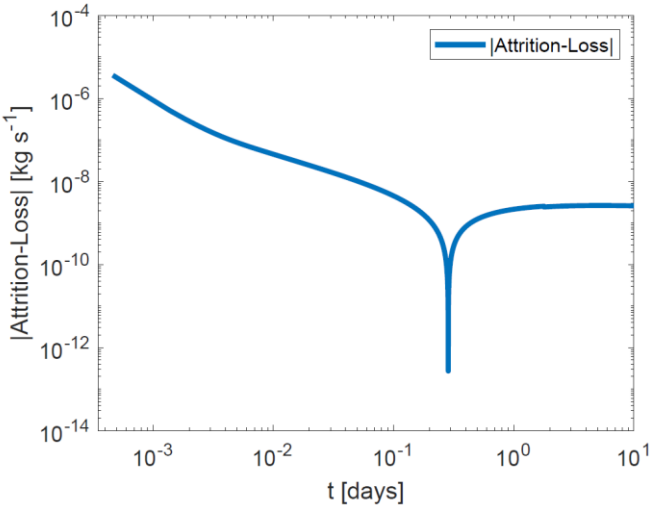

Figure 6-15. Magnitude of difference between loss rate and attrition rate as a function of time for the FB

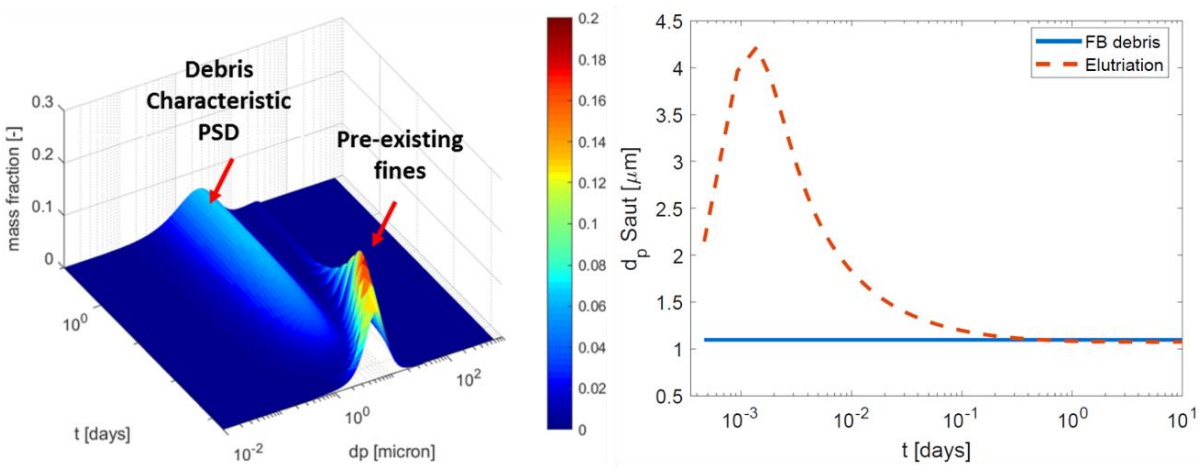

Figure 6-16. Sauter mean diameter of the debris produced in the FB by attrition and the elutriation rate as a function of time

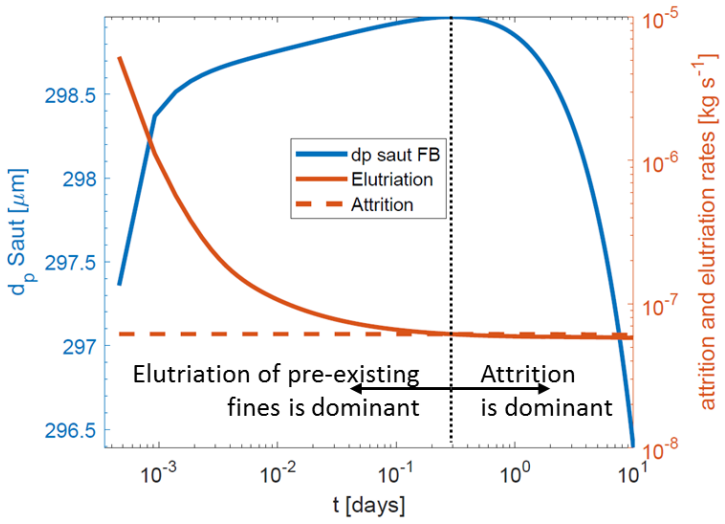

Figure 6-17. Bed inventory Sauter mean diameter, elutriation, and attrition rate as a function of time for the FB

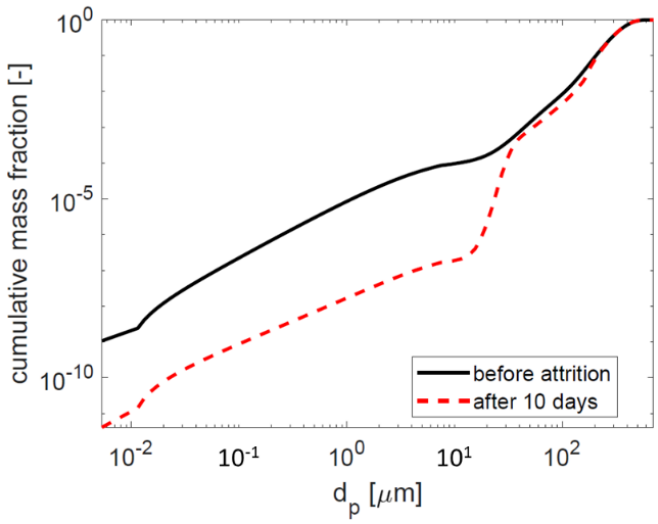

Figure 6-18. Cumulative PSD of the bed inventory before and after attrition for the FB

6.3.2.1.2 Effect of Time Step

Three different time steps of 0.1, 0.5 and 1 s, are used in order to check their influence on the simulation results shown in Figure 6-19. The three are within the maximum allowed time step, which is equal to 5.5 s.

It is clear that no effect is observed on the mass loss rate and the cumulative mass loss, as the curves are overlapping. However, for the bed Sauter mean diameter, shown in Figure 6-20, it appears that the time step has had some influence. This can be explained by considering that different time steps would lead to different patterns of travelling masses, smoother or coarser, for smaller and larger time steps, respectively, influencing in this way the development of the PSD. However, the error between the Sauter mean diameter corresponding to 0.1 and 1 s after 10 days is of 0.3% and therefore not significant.

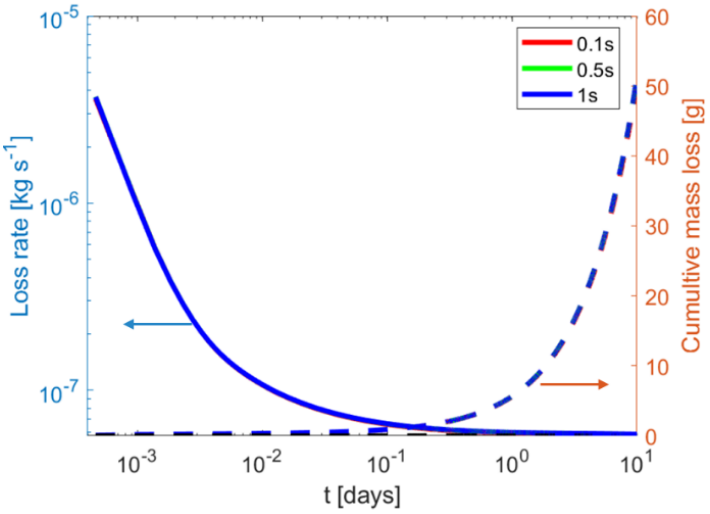

Figure 6-19. Loss rate and cumulative mass loss for a FB as a function of time for a time step of 0.1 s, 0.5 s and 1s

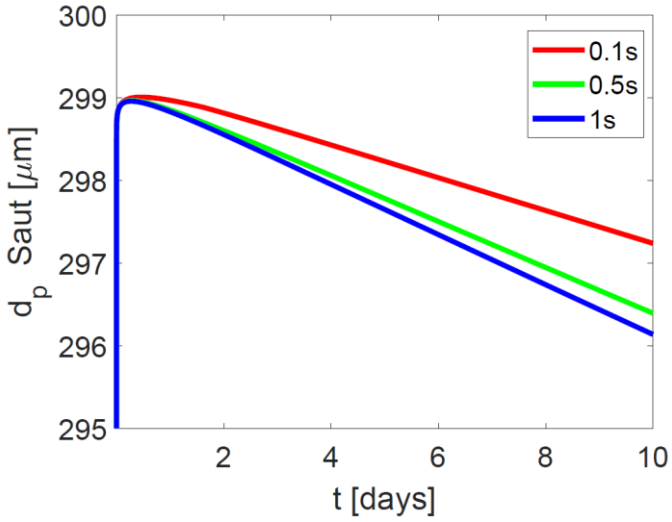

Figure 6-20. Sauter mean diameter of the bed inventory as a function of time for a time step of 0.1 s, 0.5 s and 1s for the FB

6.3.2.1.3 Effect of Jet Velocity

With increasing jet velocity, attrition is expected to increase. The jet velocity dictates the overall volumetric gas flow rate within the column and therefore the superficial velocity. This leads to an increase in: (1) the elutriation rate, (2) the maximum particle size eligible for entrainment, (3) the jet attrition and (4) the bubbling bed attrition. Thus, the response of the system is not obvious as there are two main competing mechanism depending on the same variables: attrition and entrainment. Another main effect of the jet velocity is on the estimation of the minimum mother particle size $d_{p,min}^{mp}$, according to Equation 6-23,

and the mass fraction of the bed present in the jet region X_{jet}, calculated according Equation 6-30, as the jet length increases with the jet velocity. They are shown in Figure 6-21.

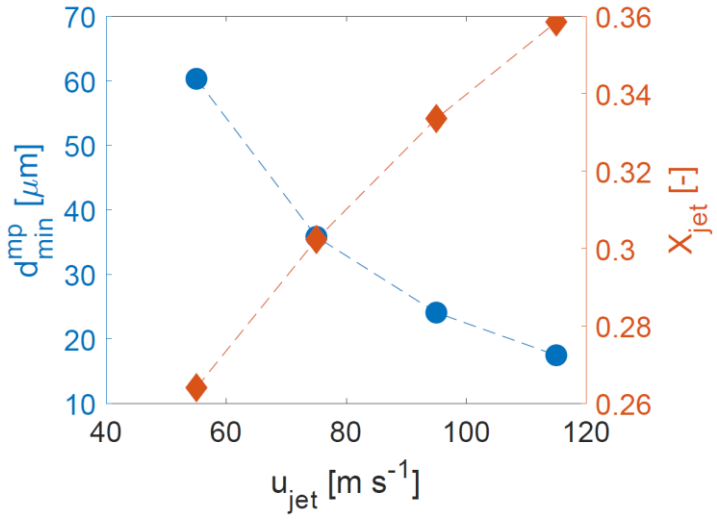

Figure 6-21. X_{jet}, mass fraction of the bed subjected to jet attrition for the FB

From Figure 6-22, it is evident how the loss rate links to the attrition rate in the same manner but at different times. In particular, increasing the jet velocity, the steady state conditions are delayed for the reasons mentioned in point (1) and (2). This is confirmed by the Sauter mean diameter of the elutriated material, shown in Figure 6-23. At the initial time, this is mainly determined by the presence of the pre-existing fines, while later on it reflects the size of the debris produced by attrition (much finer than the pre-existing fines). At the initial time, the removal of pre-existing fines would lead to an increase of the bed Sauter mean diameter, more pronounced for higher jet velocities because of larger fractions of fines being removed and more promptly. At later times, when the rate of removal of pre-existing fines becomes less important than the attrition rate, the bed Sauter mean diameter decreases, more pronouncedly for higher jet velocities, due to the higher attrition rate. This is shown in Figure 6-24.

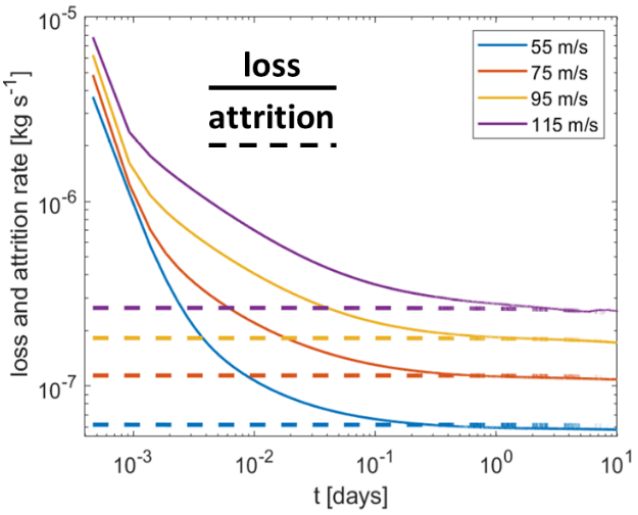

Figure 6-22. Attrition and elutriation rate of the FB for different jet velocities

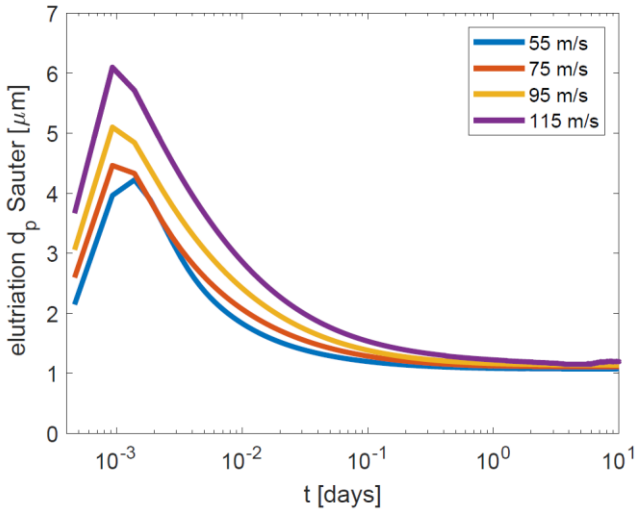

Figure 6-23. Elutriation stream Sauter mean diameter for different jet velocities for the FB

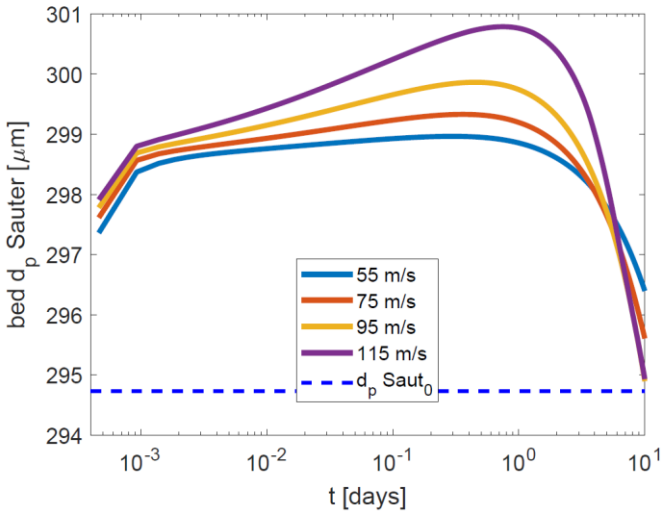

Figure 6-24. Bed inventory Sauter mean diameter for different jet velocities for the FB

It is important, at this point, to consider that attrition analysis needs to be carried out at steady state. For example, referring to the case of 115 m s^{-1} of Figure 6-24, if the simulation stopped before 1 day it could have been mistakenly concluded that the effect of attrition on the system is to coarsen the bed inventory. The cumulative PSD of the bed inventory after 10 days is given in Figure 6-25 showing at increasing jet velocities that: (i) the shrinking of large particles slightly increases (80-700 µm), (ii) the content of relatively large fines (15-80 µm, which roughly corresponds to the minimum mother particle sizes) decreases and (iii) the content of small fines increases (0-15 µm).

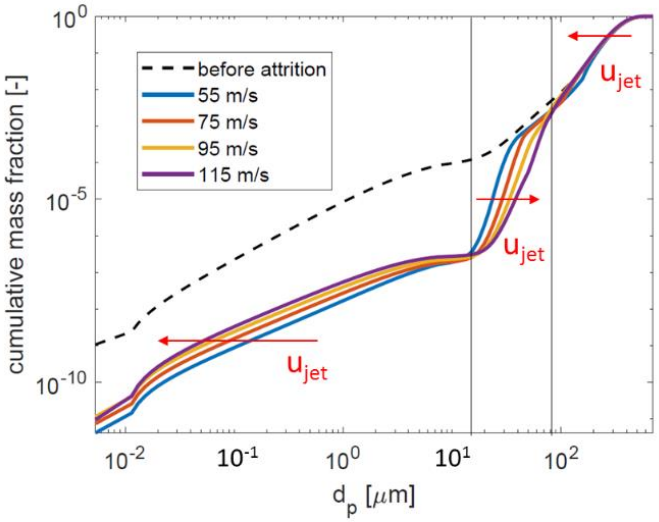

Figure 6-25. PSD of the bed inventory after 10 days for the FB

6.3.2.1.4 Effect of Single Particle Breakability Index

The single particle breakability index of F-CLC, $\alpha \frac{\mathbf{H}}{\mathbf{K_c^2}}\Big|_{\mathrm{F-CLC}}$ and constant term $\mathbf{b_{sp}}$, which are presented in Figure 3-17, are the reference values to study the effect of single particle breakability on the system by artificially manipulating them. Thus, the reference values are multiplied by a proportionality factor, called $X_{breakability}$, equal to 0.01, 0.1, 1, 10 and 100. This allows to check the effect of attrition propensity at constant conditions of jet velocity, 55 m s^{-1} (superficial velocity 0.14 m s^{-1}). Several implications are expected by manipulating the breakability index, for instance by increasing it: (1) the jet attrition linearly increases, (2) the bubbling bed linearly increases, (3) leading to a reduction in bed particle Sauter mean diameter, (4) the transient period where the pre-existing fines are removed by elutriation is shorter due to the overwhelming high attrition rate (5) affecting in this way the PSD of the elutriated fines. It should be noted that the minimum mother particle size, below which there is no attrition, remains constant for all the conditions tested as both breakability index and constant term are multiplied by the same proportionality factor not affecting Equation 6-23. Referring to Figure 6-26, it is clear that for low breakability indices, the loss would be dictated by the elutriation of the pre-existing fines as compared to very high particle breakability, where attrition dictates the loss since the beginning, confirming point (4). The gradual decrease observed for the "x100" case is due to the reduction of the bed inventory mass given by the high degree of loss. The implications on the PSD of the elutriated material are shown in Figure 6-27 in terms of Sauter mean diameter. It is evident that an elutriation stream poor in debris particles produced by attrition, like in the case of X0.01, would be coarser due to the dominant presence of the pre-existing fines, (i.e. the pre-existing fines are coarser than the characteristic debris PSD), as compared to one saturated of debris particles produced by attrition, like in the case of X100.

It is also intuitive to think that higher breakability indices would lead to a much greater reduction in size of the bed particles. The cumulative PSD of the bed inventory after 10 days is reported in Figure 6-28, confirming the remarkable shrinkage at high single particle breakability indices.

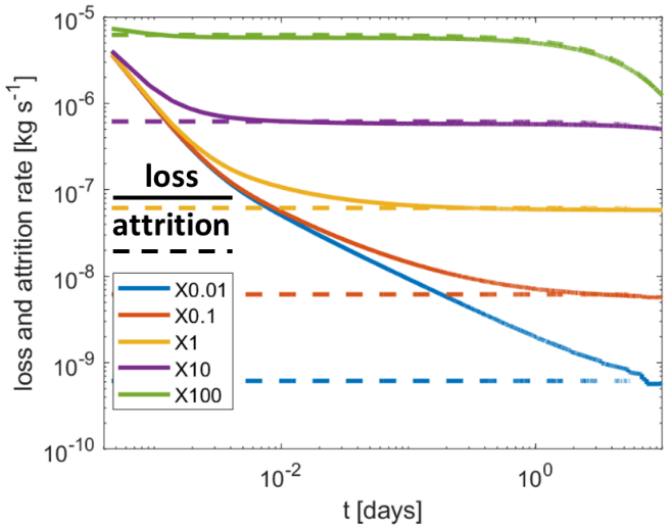

Figure 6-26. Attrition and elutriation rate for different single particle breakability for the FB

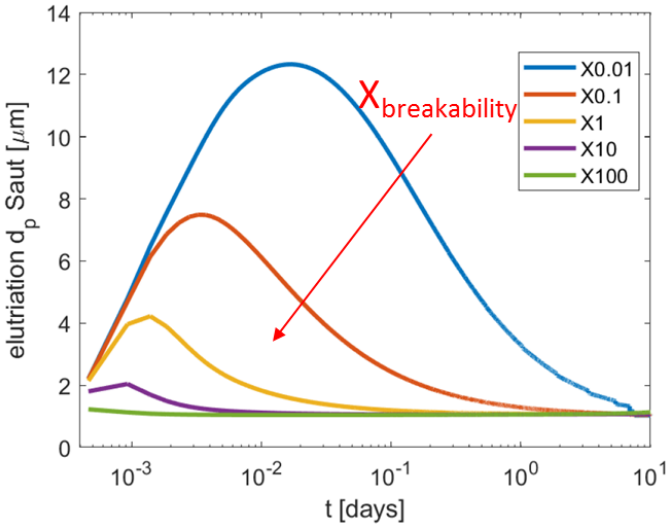

Figure 6-27. Sauter mean diameter of the elutriated material for different particle breakability indices for the FB

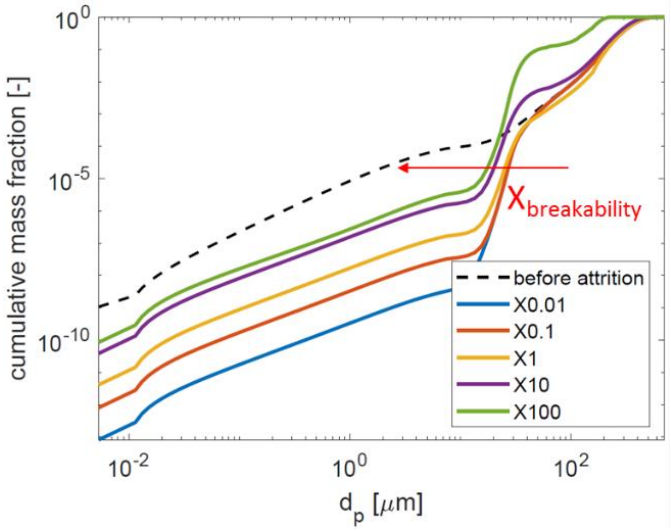

Figure 6-28. PSD of the bed inventory for different particle breakability indices for the FB

6.3.2.2 Circulating Fluidised Bed Configuration

Similar with the study conducted on the fluidised bed, referring to Table 6-6, several CFB simulations are performed in order to investigate the effect of time step, 0.1, 0.25, 0.5 and 1s, (respectively cases 1, 2, 3, 4) leading to the same conclusions obtained for the FB case. Furthermore, the effect of the jet velocity is investigated by varying it as 55, 75, 95, 115 m s^{-1} (respectively cases 3, 5, 6, 7), as well as the effect of particle breakability, X0.01, X0.1, X1, X10, X100 times the breakability index of F-CLC (respectively cases 3, 8, 9, 10, 11). All the cases are featured with a discontinuous make up stream of fresh material when 0.5% of the total mass of the process is lost. Moreover, case 12 is used to study the start-up behaviour by simulating 0.2 days by increasing the sampling rate, using a saving time step equal to the integration time step, this analysis is reported in the Appendix section. As mentioned previously in Table 6-6, each jet velocity corresponds to a superficial velocity. The results obtained from the default case are analysed and reported in the next section.

Table 6-6. Simulations of circulating fluidised bed (default case highlighted)

CFB configuration							
#	**Δt** [s]	u_{jet} [m s^{-1}]	u_{sup} [m s^{-1}]	u_{sup}/u_{mf} [-]	t_{tot} [days]	$x\left(\alpha \frac{H}{K_c^2}\Big\|_{F-CLC}\right)$	loss tolerance [%]
1	0.1	55	0.139	1.7	10	1	0.5
2	0.25	55	0.139	1.7	10	1	0.5
3	0.5	55	0.139	1.7	10	1	0.5
4	1	55	0.139	1.7	10	1	0.5
5	0.5	75	0.190	2.2	10	1	0.5
6	0.5	95	0.240	2.8	10	1	0.5
7	0.5	115	0.291	3.4	10	1	0.5
8	0.5	55	0.139	1.7	10	0.01	0.5
9	0.5	55	0.139	1.7	10	0.1	0.5
10	0.5	55	0.139	1.7	10	10	0.5
11	0.5	55	0.139	1.7	10	100	0.5
12	0.5	55	0.139	1.7	0.2	1	0.5

6.3.2.2.1 Default Case Circulating Fluidised Bed

The minimum mother particle sizes are in this case equal to 60 and 15 μm for the jet\bubbling bed region and cyclone, respectively.

As shown in Figure 6-29 , the jet attrition rate is nearly one order of magnitude larger than that of the bubbling bed, under these conditions. At the same time, the cyclone is the source of attrition which contributes less with respect to the formers.

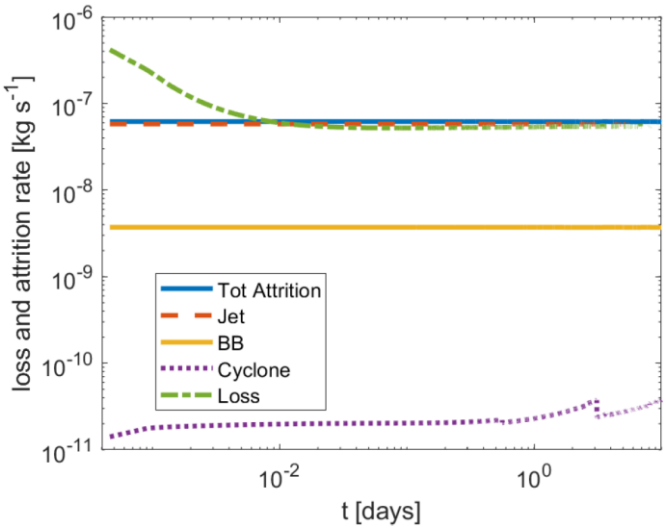

Figure 6-29. Attrition and loss rates for the CFB

The rate of loss of material from the system is limited by the cyclone efficiency, so the system requires less time, as compared to the FB configuration, to reach the steady state loss rate, as confirmed by Figure 6-30 which shows the magnitude of the difference between the loss and attrition rate. From the same figure it is possible to see two peaks at about 3.4 and 6.8 days related to the make-ups. The make-up peaks are the result of the presence of newly fed particles, of which fines, being immediately elutriated, would be lost from the system increasing, in this way, momentarily the loss rate.

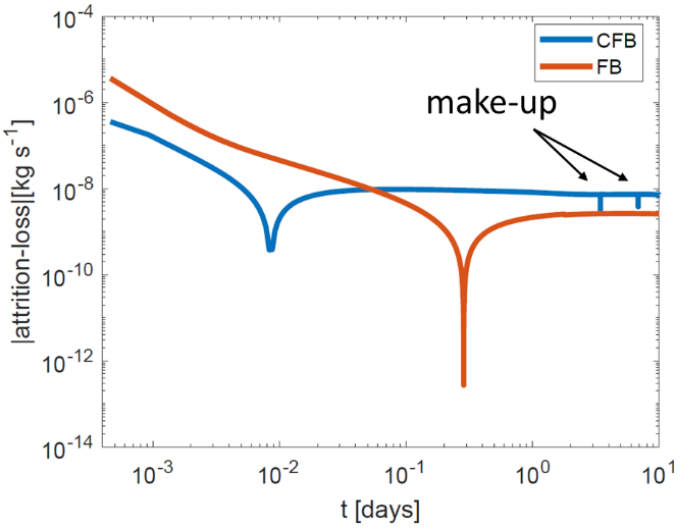

Figure 6-30. Magnitude of the difference between attrition and loss rate as a function of time for the CFB

By analysing Figure 6-31, it seems that the Sauter mean diameter of the elutriated material increases with time. This is due to the accumulation of a fraction of relatively large fines

which are captured by the cyclone and recycled back to the fluidised bed. However, the Sauter mean diameter of the debris particles produced in the fluidised bed and cyclone by attrition is constant, of about 1 μm. The Sauter mean diameter of the material exiting the cyclone is less than that of the debris particles produced by attrition, meaning that not all them would be lost. Referring to the same figure, it is possible to notice that the elutriation and recycle stream get coarser in two phases: the first being the start-up, thanks to the sudden accumulation of relatively large fines from the pre-existing fines which are captured and recycled, the second being due to accumulations of relatively large debris, which are as well captured and recycled during the regime where the loss is dictated by the attrition rate. It implies that the solids circulation rate would increase with time and be much greater than the attrition and loss rates, as shown in Figure 6-32. The average particle size of the bed inventory initially increases due to the removal of a fraction of the pre-existing fines and later on decreases as a direct result of attrition. The decrease is more pronounced for the CFB as compared to the FB due to the recycle of relatively large fines. The bed solids Sauter mean diameter, along with the elutriation, recycle and attrition rate, are reported in Figure 6-33. Due to the coarsening of the elutriation stream for the reasons mentioned above, the cyclone separation efficiency increases with time, as shown in Figure 6-34. The bed inventory PSD after 10 days is reported in Figure 6-35, showing a slight reduction from the initial condition as well as an increase of those size fractions continuously accumulating in the process of range about 5-53 μm.

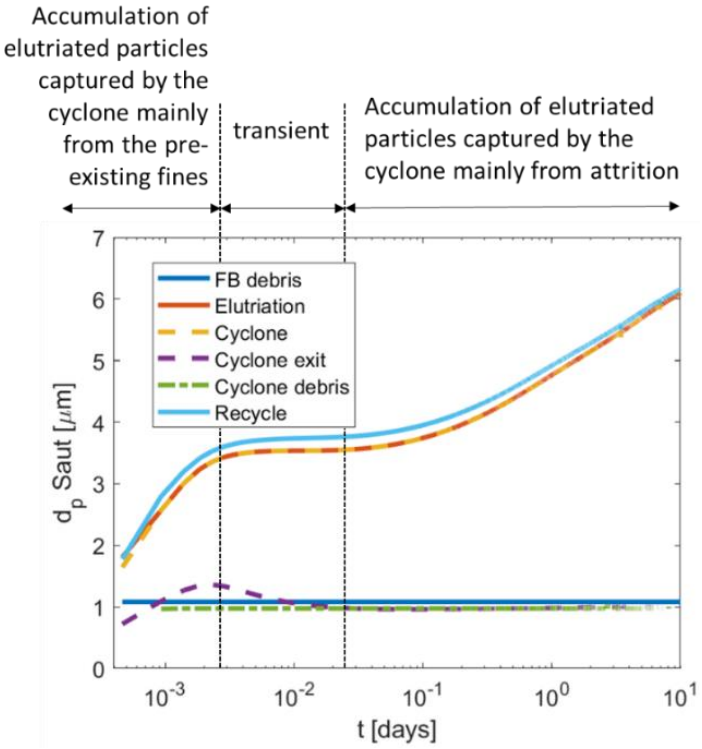

Figure 6-31. Sauter mean diameter of the debris produced in the CFB by attrition and the elutriation rate as a function of time

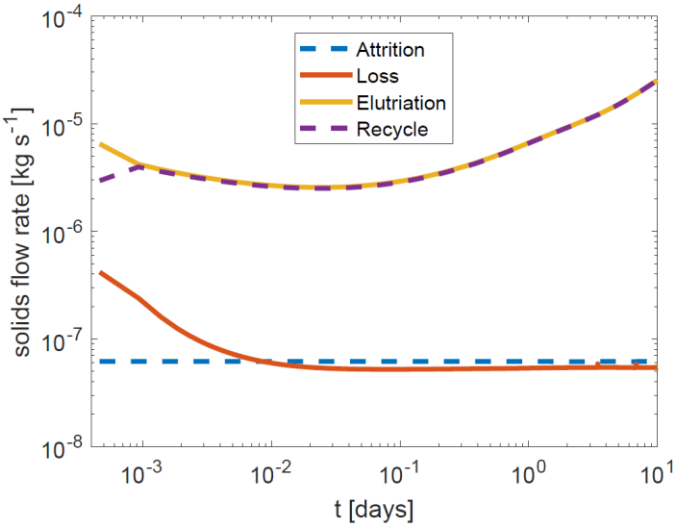

Figure 6-32. Attrition, loss, elutriation and recycle rate for the CFB

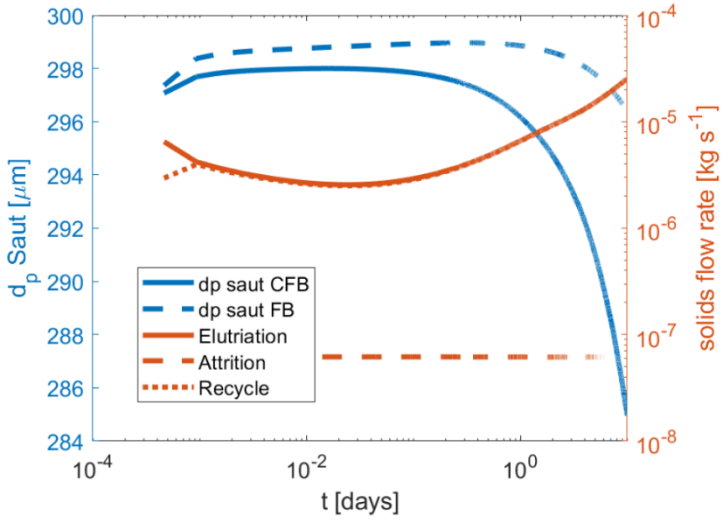

Figure 6-33. Bed solids Sauter mean diameter, elutriation, and attrition rate as a function of time for the CFB

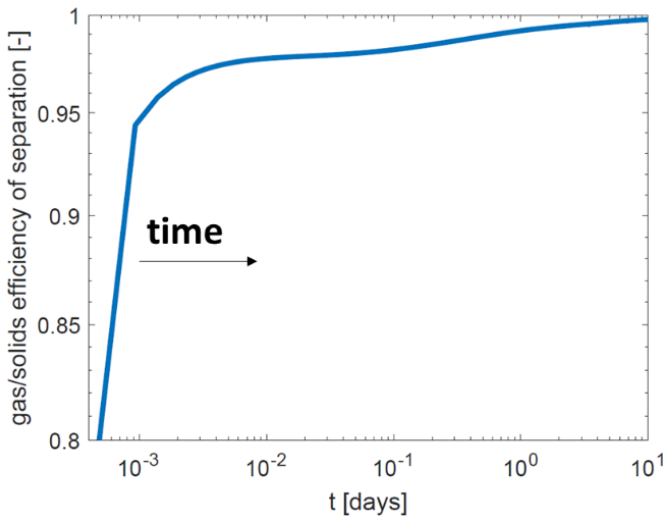

Figure 6-34. Gas/solids temporal separation efficiency for the CFB default case

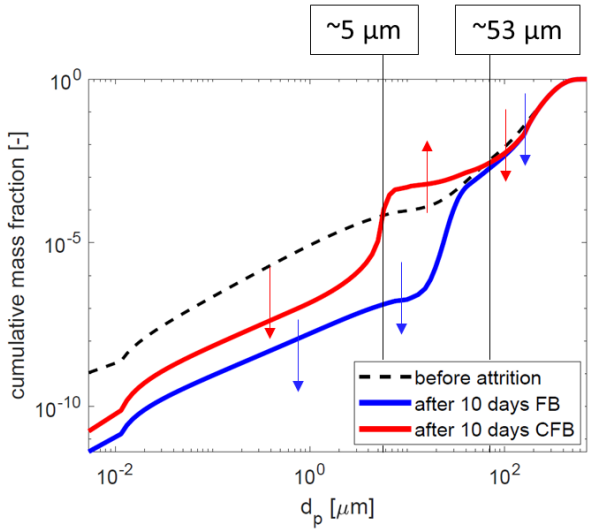

Figure 6-35. cumulative PSD of the bed inventory before and after attrition for the CFB

6.3.2.2.2 Effect of Jet Velocity

With increasing jet velocities, attrition is expected to increase. At the same time, the jet velocity dictates the overall volumetric gas flow within the column and therefore the superficial velocity. The main implications would be the increase of: (1) the solids circulation rate, dictated by the elutriation and the recycle, (2) the maximum particle size eligible for entrainment, (3) the jet attrition, (4) the bubbling bed attrition, (5) the cyclone attrition along with (6) the cyclone efficiency. Thus, the response of the system is complex, as there are three main competing mechanisms: attrition, the entrainment/recycle, and the efficiency of the solids separation. The minimum mother particle size, below which there is no attrition, is estimated for the jet/bubbling bed regions and the cyclone and reported in Figure 6-36.

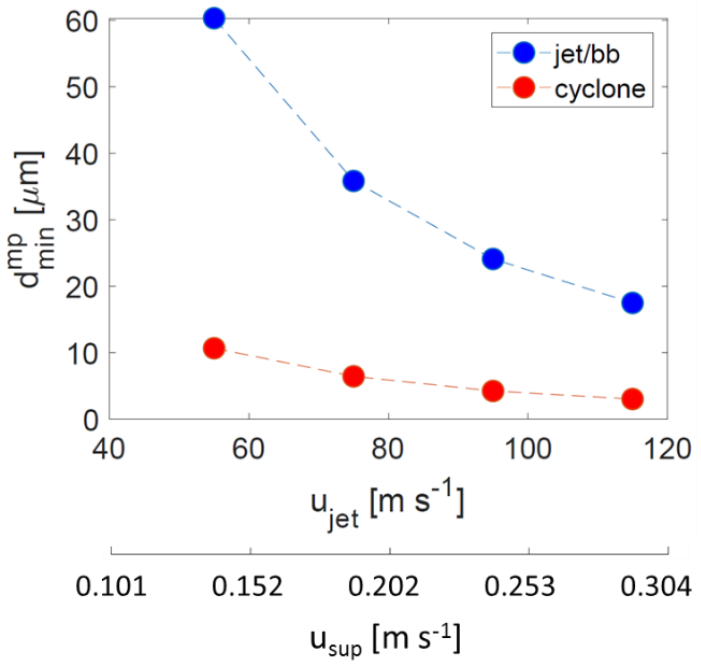

Figure 6-36. Minimum mother particle size of the CFB

According to Figure 6-37, the jet region is in all cases the main source of attrition. On the other hand, cyclone and bubbling bed are the second main source at high and low superficial velocities, respectively, in agreement with the work of Werther and Reppenhagen, (1999).

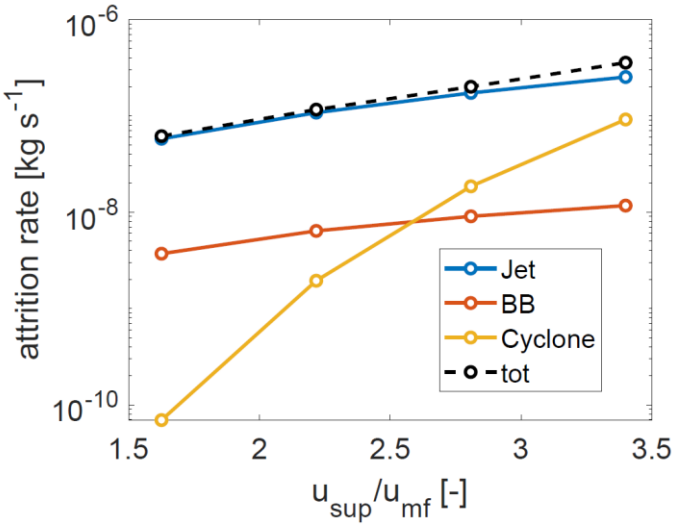

Figure 6-37. Attrition rates as a function of u_{sup}/u_{mf} for the CFB at the 10th day

The loss rate is directly linked to attrition but is controlled by the efficiency of the cyclone so, it is expected that by increasing the jet velocity, and therefore the superficial velocity,

the attrition rate would increase more significantly than the loss rate because the system produces more debris particles than fines escaping the cyclone. This is shown in Figure 6-38 in terms of ratio of the loss and attrition rate. The figure shows that the ratio is way below 1 for higher jet velocity (and superficial velocity).

The high attrition rate achieved at higher jet velocities would "force" the solids circulation rate to an equilibrium, as it would be mainly composed by the debris particles produced by attrition, this phenomenon is reported in Figure 6-39 in terms of solids loading of the elutriation stream. As a result of what mentioned above, the Sauter mean diameter of the elutriated material is not expected to vary significantly as shown in Figure 6-40. On the contrary, the slow attrition rate established at lower jet velocities would give leverage to the elutriation to accumulate relatively large particles in the system, therefore the mean particle diameter of the circulated material increases, as shown in Figure 6-40. Thus, the solids circulation rate slowly increases with time delaying in this way the reach of the equilibrium, as shown in Figure 6-39. The efficiency of the gas/solids separation increases with time as the solids loading increases. This effect is enhanced at high superficial velocity (which determines the cyclone gas inlet velocity), as depicted in Figure 6-41. The PSD of the bed inventory after 10 days, given in Figure 6-42, is radically changed and reflects the interplay between attrition and solids re-circulation which determines the accumulation of certain fractions of particle sizes. After 10 days, the total mass lost from the system is greater for larger jet velocities, in particular by nearly doubling the jet velocity from 55 to 115 m s^{-1} the mass loss increases by 4.1 times. The number of make-ups goes from 2 to 11, again for the lowest and highest jet velocities used (superficial velocities), respectively. This is shown in Figure 6-43.

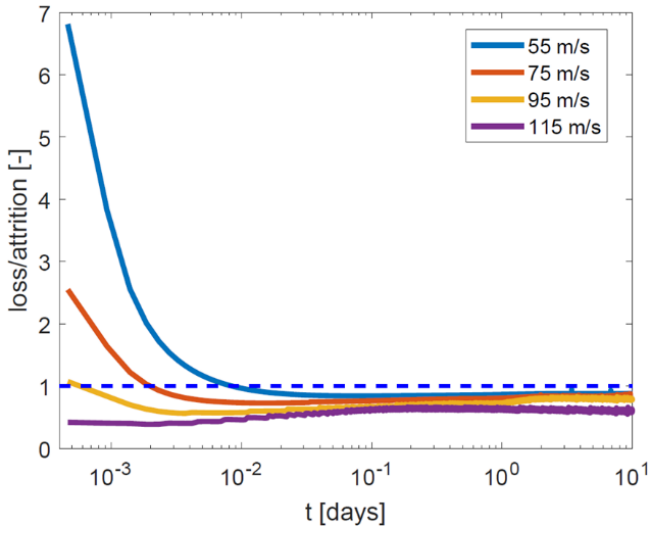

Figure 6-38. Attrition and elutriation rate of the FB for different jet velocities for the CFB

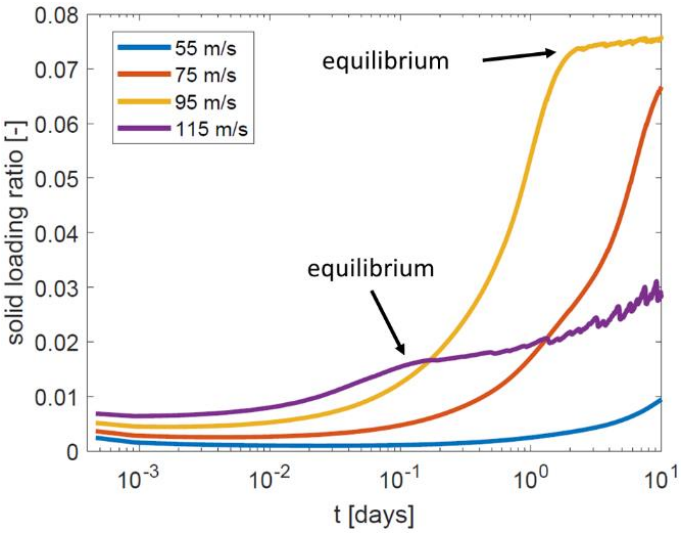

Figure 6-39. Solids loading of the entrainment rate for different jet velocities (superficial velocities) for the CFB

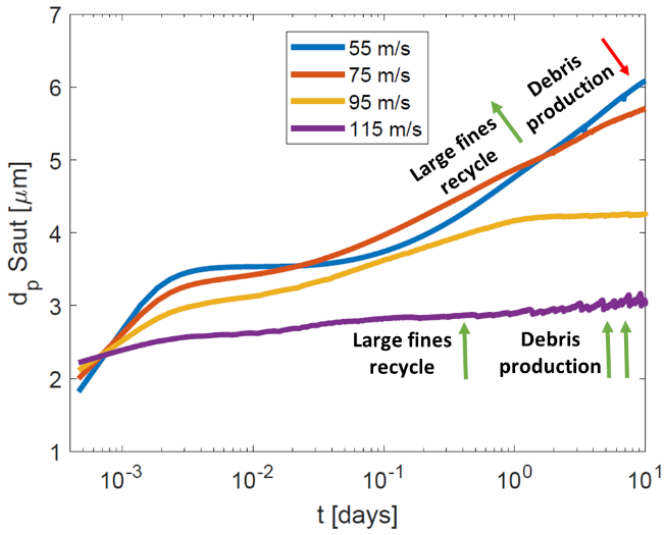

Figure 6-40. Sauter mean diameter of the elutriated material for different jet velocities (superficial velocities) for the CFB

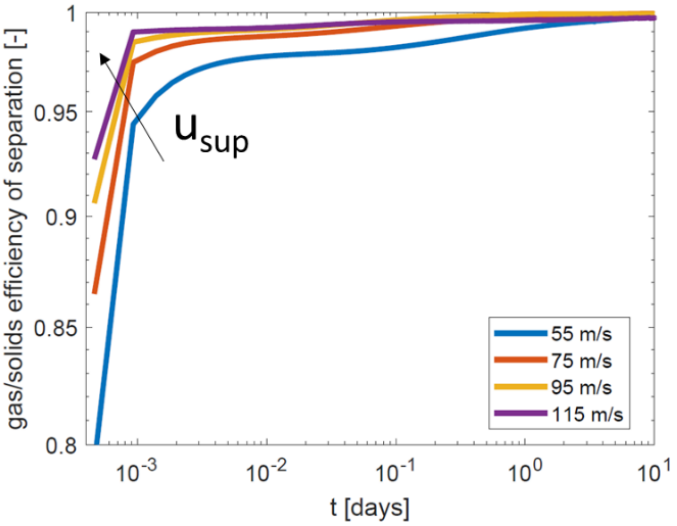

Figure 6-41. Temporal efficiency of gas/solids separation for different jet velocities (superficial velocities) for the CFB

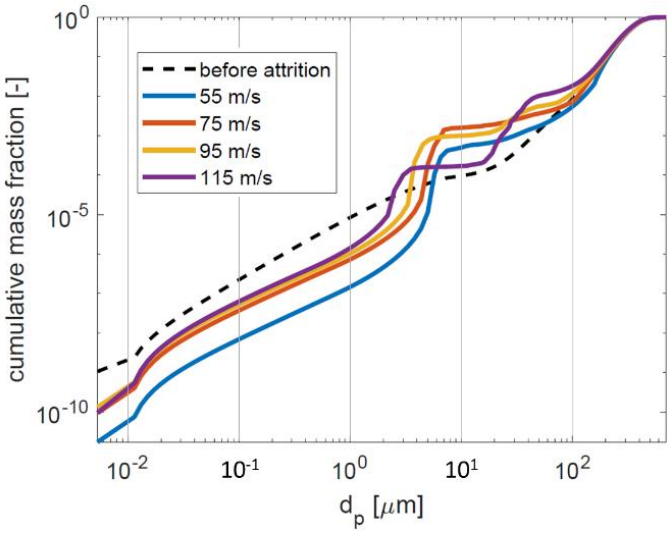

Figure 6-42. PSD of the bed solids inventory after 10 days for the CFB

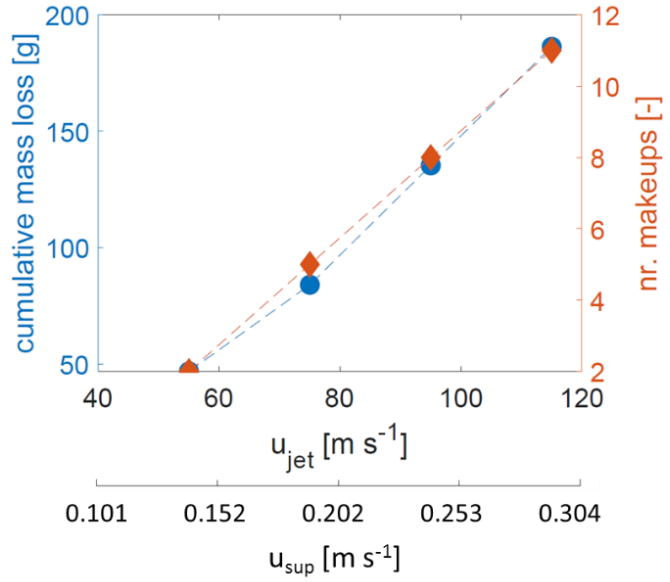

Figure 6-43. Mass lost at different jet velocities for the CFB, after 10 days

6.3.2.2.3 Effect of Single Particle Breakability Index

Similar to the FB configuration, the reference values of $\alpha \frac{H}{K_c^2}\Big|_{F-CLC}$ and b_{sp} are multiplied by a proportionality factor of 0.01, 0.1, 1, 10 and 100 to study the effect of the single particle breakability index on the CFB behaviour. The jet velocity is set to 55 m s^{-1}, which gives a superficial velocity of 0.14 m s^{-1}. Several implications are expected by manipulating the breakability index: by increasing it (1) the jet attrition linearly increases, (2) the bubbling bed linearly increases, (3) the cyclone attrition linearly increases, (4) the

solids circulation rate increases because the system is overwhelmed by the production rate of debris particles (5) affecting the PSD of the elutriated and lost solids, (6) the gas/solids separation efficiency reduces due to a much finer feed and (9) the bed inventory gets finer in size. The minimum mother particle size, below which there is no attrition, remains constant for all the conditions tested as both breakability index and constant term are multiplied by the same proportionality factor, not affecting Equation 6-23.

At low breakability indices, the initial loss is dictated by the elutriation of the pre-existing fines while at high breakability indices the loss is strongly determined by the debris produced by attrition. This is shown in Figure 6-44 in terms of ratio between loss and attrition rate. It is intuitive that, at constant superficial velocity, a higher attrition rate would increase the solids circulation rate. This is reported in Figure 6-45. The Sauter mean diameter of the elutriated material tends to reflect the debris particle size produced by attrition (about 1 μm) at high breakability indices, and the particle size of the pre-existing fines (coarser than the debris particle) at low breakability indices, as shown in Figure 6-46. Being at constant superficial velocity, the gas/solids separation efficiency is affected by the solids loading and feed particle size. At high breakability indices the gas/solids separation efficiency is low due to the small feed particles elutriated but increases with time because of the increasing solids loading, as shown in Figure 6-47. The PSD of the bed inventory after 10 days is reported in Figure 6-48 showing deviation from the initial conditions by depletion and enrichment of fine particles at low and high breakability indices, respectively. As expected, the total mass lost after 10 days increases linearly with the breakability indices as well as the need of make-ups, as shown in Figure 6-49.

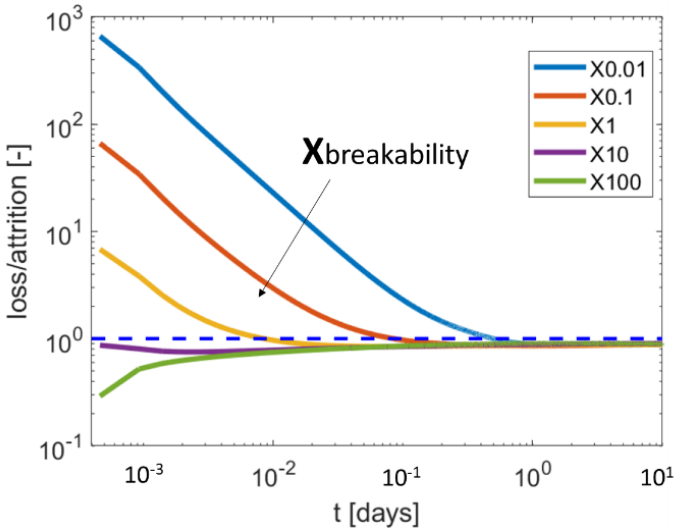

Figure 6-44. Attrition and elutriation rate for different single particle breakability for the CFB

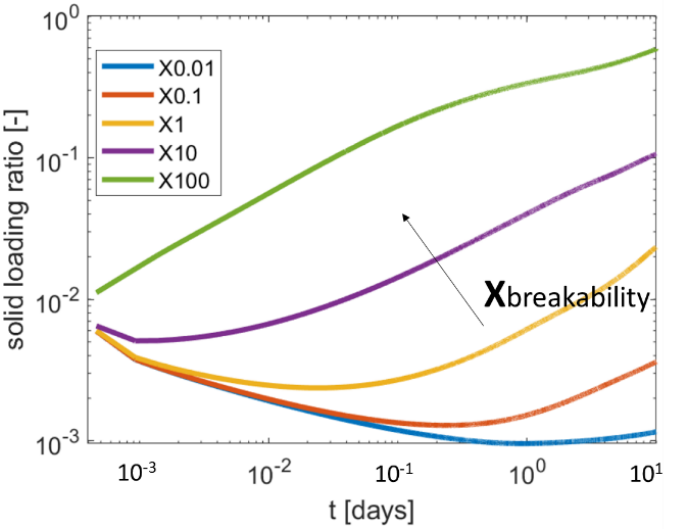

Figure 6-45. Solids loading for different breakability indices for the CFB

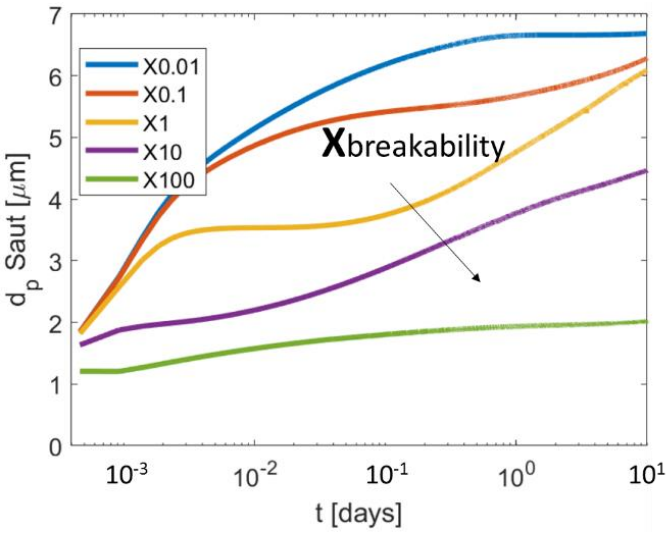

Figure 6-46. Sauter mean diameter of the elutriated material for different particle breakability indices for the CFB

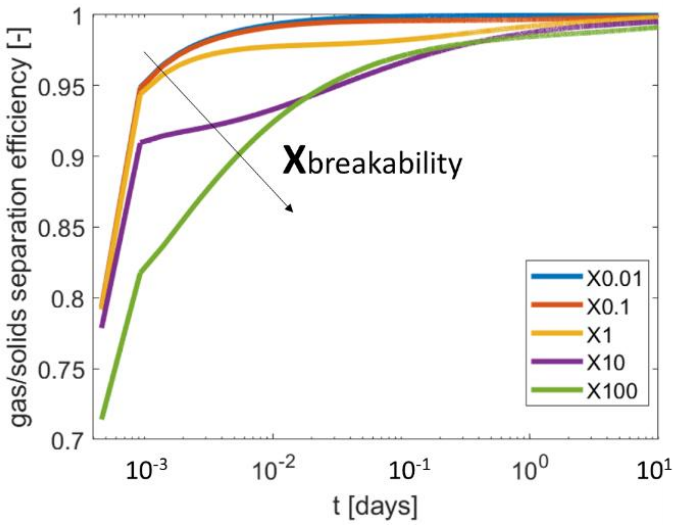

Figure 6-47. Gas/solids temporal separation efficiency for different breakability indices for the CFB

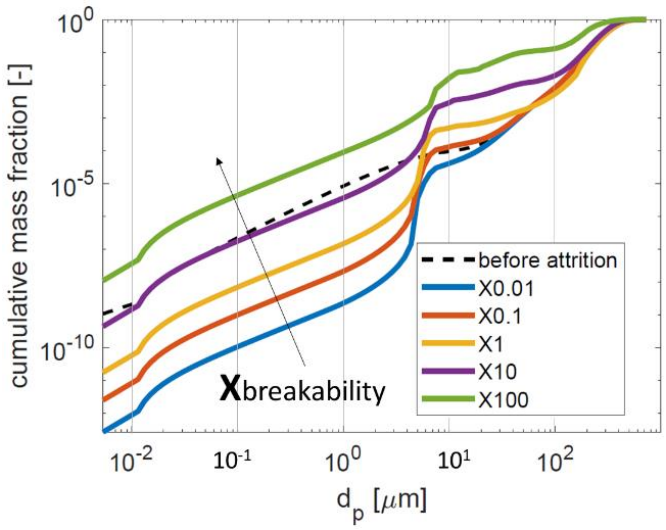

Figure 6-48. Cumulative PSD of the solids bed inventory after 10 days for the CFB

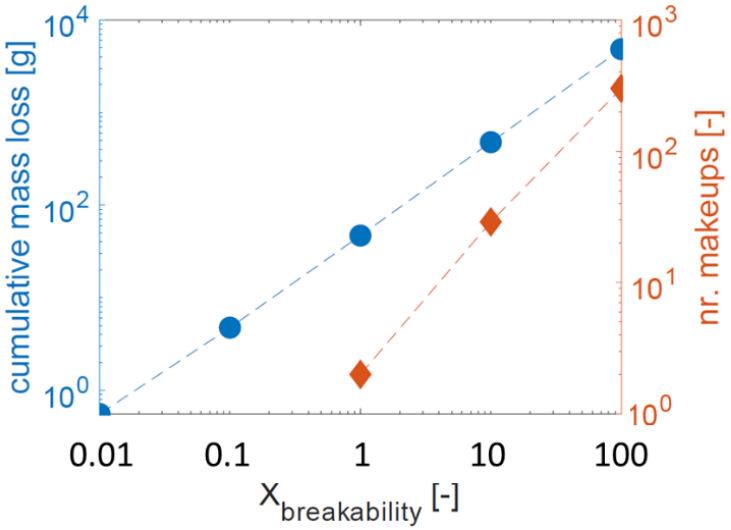

Figure 6-49. Mass lost and number of makeups at different Xbreakability index for the CFB, after 10 days

6.4 Concluding Remarks

The effect of particle attrition on the dynamic behaviour of a fluidised and a circulating fluidised bed is studied by means of a mass-based population balance. The reduction in size of the mother particles and the formation of debris particles is accounted for by using attrition kernels developed in this research project for F-CLC and E-CLC, by both experimental and computational approaches. The sources of attrition are the jet (acting as the gas distributor), the bubbling bed region, and the cyclone. Only a part of the particle population, having sizes greater than the minimum mother particle size, undergoes

attrition while the formation of debris is modelled according to the experimental results carried out on the fluidised bed and cyclone attrition tests. The minimum mother particle size, below which there is no attrition, is estimated using the model of single particle impact breakage by identifying a critical impact velocity, for the regions of interest. The PBM is written and solved in Matlab®. The study is carried out on two systems, a fluidised bed, and a circulating fluidised bed with make-up (which is a fluidised bed with a cyclone and a recycle line), at different conditions of jet velocities and single particle breakability indices. The simulations describe the dynamic behaviour throughout 10 days of operation. The analysis focuses on the effect of jet velocities (giving the superficial velocities as no background fluidisation is used), the effect of single particle breakability index and time step. The latter is found to have a negligible influence, within the allowed range. Concluding remarks are presented for the FB configuration in section 6.4.1 and CFB configuration in 6.4.2.

6.4.1 Fluidised Bed Configuration

The results of the PBM, for a fluidised bed configuration, show that jet attrition is the main source of attrition. Moreover, the existence of two regimes is established where the loss is dictated by the elutriation of the pre-existing fines and the attrition rate, in order. The bed inventory coarsens and undergoes size reduction during the two regimes, respectively. For this configuration, the elutriation rate is equal to the loss rate because, as opposite to the CFB configuration, no cyclone is present. On the basis of the study carried out on the FB, under the conditions tested, the following conclusions can be made.

Action (i) Either decreasing the attrition propensity of the single particle or increasing the superficial velocity (by increasing the jet velocity)

Consequence:

a) the transition from the regime where the loss is dictated by the elutriation of pre-existing fines to where the loss is dictated by the attrition rate is delayed.

Action (ii) Increasing the single particle attrition propensity

Consequences:

a) The attrition rates increase
b) The Sauter mean diameter of the bed solids decreases

c) The Sauter mean diameter of the elutriated material would reflect the size of debris particles produced by attrition
d) The mass loss increases

Action (iii) Increasing the jet velocity (giving the superficial velocity)

Consequences:

a) The minimum mother particle size decreases
b) The attrition rates increase
c) The elutriation rate increases
d) Both coarsening and reduction of the average bed particle size is enhanced, during the two regimes, respectively.
e) The Sauter mean diameter tends to the debris particle size during the attrition dominated regime.
f) The mass loss increases.

6.4.2 Circulating Fluidised Bed Configuration

With the CFB configuration the loss rate is controlled by the presence of the cyclone, and therefore is not equal to the elutriation rate. In terms of attrition rate, the jet is always the main source of attrition. At high jet velocities, it is followed by the cyclone and bubbling bed, and vice versa at low velocities. The two regimes where the loss rate is dictated in order by the elutriation of the pre-existing fines and debris particles produced by attrition is still present. The transition between the two occurs earlier than the FB case because the loss rate is now controlled by the cyclone. On the basis of the study carried out on the CFB, under the conditions tested, the following conclusions are made.

Action (i) Decreasing the attrition propensity of the single particle

Consequences:

a) The transition from the regime where the loss rate is dictated by the elutriation of the pre-existing fines and debris particles produced by attrition is delayed.
b) The attrition rate decreases
c) During the 10 days tested, given the low attrition rate, the solids circulation is mainly composed by the accumulating larger fractions of the pre-existing fines

d) As a result of the previous point, the gas/solids separation efficiency is high and rapidly increases with time
e) The mass loss decreases

Action (ii) Increasing the attrition propensity of the single particle

Consequences:

a) The transition from the two regimes occurs earlier
b) The elutriated material is mainly composed by the debris particles produced by attrition
c) Due to the finer elutriated material, the gas/solids separation efficiency is low but would slowly increase with time due to the increasing of the solids loading
d) The mass loss increases

Action (iii) Increasing the jet velocity (giving the superficial velocity)

Consequences:

a) The minimum mother particle sizes decrease
b) The attrition rate increases
c) The solids circulation rate increases as well as the particle sizes eligible to elutriation.
d) The equilibrium solids circulation rate dictated by the rate of production of debris particles and recycle of relatively large fines occurs earlier
e) As a result of the previous point the Sauter mean diameter of the elutriated material does not change significantly with time
f) Due to the high gas velocity, the gas/solids separation efficiency is high and once the equilibrium solids circulation is achieved it does not change significantly with time.
g) The mass loss increases
h) The requirement of a make-up stream increases

Action (iv) Decreasing the jet velocity (giving the superficial velocity)

Consequences:

a) The minimum mother particle sizes increase

b) The attrition rate decrease
c) The solids circulation rate decreases as well as the particle sizes eligible to elutriation.
d) The equilibrium solids circulation rate is reached late, allowing the accumulation in the system of the larger fractions collected by the cyclone and causing the increase of the solids loading
e) Before the equilibrium solids circulation rate is reached, the Sauter mean diameter of the elutriated material increases
f) Due to the low gas velocity, the gas/solids separation efficiency is low but increases with time as a result of the increasing solids loading
g) The mass loss reduces
h) The requirement for make-up reduces

7. CONCLUSION AND FUTURE WORK

CHAPTER 7

7.1 Conclusions

Particle attrition in fluidised and circulating fluidised bed is a major issue. Particles are continuously subjected to mechanical, thermal and chemical stresses, thus tend to degrade with time. Attrition is responsible for the formation of small fines that are elutriated and mostly lost, as well as shrinking and/or severe breakage of particles. It is important to understand how the attrition propensity of a solids material can influence the performance of the process. For this purpose, a methodology has been developed to deduce particle attrition in complex systems such as cyclone and fluidised beds from the single particle breakability.

In this research project, the single particle breakability of a fresh (F-CLC) and equilibrium (E-CLC) manganese oxide particles, candidate oxygen carrier for the Chemical Looping Combustion process, has been characterised. An empirical model is then proposed for use in developing attrition correlations for the jet region and cyclone of fluidised beds. This is done through a combination of experimental and simulation work. They are then used as kernels in a population balance model of attrition for a fluidised and circulating fluidised bed.

A comprehensive literature review on particle attrition, from the single particle to the process level has been undertaken to understand the mechanisms and magnitude by which particle attrition occurs in these processes. Potential windows of improvements have been identified. The link between single particle breakability and the attrition observed in the cyclone, jet region and the overall fluidised bed has been established, as an outcome of the work.

7.1.1 Single Particle Attrition

The work at single particle level has been carried out at the University of Leeds. The materials are initially characterised in terms of size, porosity, morphology, and mechanical properties. The particle size distribution of the fresh material is found to be much coarser than the equilibrium. Both fresh and equilibrium particles have random and irregular shape, their internal structure is characterised by some meso and macro pores. In particular, the equilibrium material presents a much greater degree of porosity, or rather cavities, which can be explained by considering the important thermal and chemical stresses they have been through. Moreover, mechanical tests carried out using the nano-indentation technique have revealed their semi-brittle behaviour. Stiffness and hardness of the E-CLC is found to be different form F-CLC, suggesting the importance of considering the effect of temperature and chemical reaction on the particle mechanical properties.

Their single particle breakability is evaluated using the single particle impact test and the Scirocco impact test of the Malvern Mastersizer 2000®. The two impact tests give consistent results. The extent of breakage upon impact is such that chipping is the dominant mechanism and follows the model of chipping of semi-brittle material of Ghadiri and Zhang, (2002), which suggests that the breakage is a function of the breakability index ($\alpha H/K_c^2$), the particle size, density and the square of impact velocity. The equilibrium material is found to have a larger breakability index than the fresh one. Moreover, by comparing the results of non-washed and washed material, the fine dust adhering to the particles surfaces is found to overestimate the extent of breakage during the first three/four repeated impacts. Further experimental work has revealed that the extent of attrition varies with the impact angle, θ, with respect to the plane of impact, and is found to be proportional to $\sin\theta$. The validity of this dependency has been tested on breakage results from works reported in literature with quite good agreement. However, its physical nature remains unknown.

7.1.2 Cyclone Attrition

The work on the cyclone has been carried out at the University of Leeds. Cyclone attrition is evaluated experimentally for the fresh material as a function of the particle size (from 180 to 400 μm), the solids loading (from 0.1 to 1) and the gas inlet velocity (from 12 to

24 m s^{-1}) through 20 passes. The results show that the extent of attrition tends to reduce with the number of passes, more significantly at higher gas inlet velocities and solids loadings. Extending the test to 40 passes, after the cyclone is cleaned of the fines deposited on its wall, the extent of attrition seems to replicate the results obtained in the first 20 passes. It can be concluded that the layer of fines built on the cyclone wall plays an important role either by mitigating attrition or, probably, by affecting the collection of debris. Some future work will help understand this.

The most severe conditions of attrition are found at high gas inlet velocity, low solids loading, and small particle sizes. The Schumann's plot of the most severe cases reveal that the breakage pattern is determined by surface damage, i.e. chipping and surface abrasion. However, the PSD of the debris at all conditions show the presence of some large fragments.

A CFD-DEM analysis is carried out to check the effect of the pipe length and solids loading on the particle velocity at the entrance of the cyclone for different particle sizes. It is found that the reason why small particles experience higher attrition lies on the entrance effect, i.e. small particles would enter at higher velocity than large ones, and therefore have a greater impact energy. Even by using a mixture of different particle sizes, at very high solids loading (such as 10), and pipe length being three times as that used for the experiments, different particle sizes would still have different entrance velocities. This analysis is only valid for the particle size and density range used here.

In order to understand the particle dynamics leading to cyclone attrition, CFD-DEM simulations are performed, replicating the experimental set-up and operating conditions. The aim being the estimation, for different regions of the cyclone, of the frequency of particle-wall (P-W) and particle-particle (P-P) collisions, collision relative velocity and angle, sliding distance against the walls and normal load acting on the particles. In the regions immediately opposite to the entrance of the cyclone, P-W collisions are highly energetic and efficient in terms of breakage, and the frequency of collisions slightly increases with the solids loading. P-P collisions are also highly energetic and efficient, but the frequency of collisions become significant only at high solids loading. With reference to the entrance effect, in these regions, small particle sizes have a greater impact energy. Following the pre-dominant collisional behaviour in the entrance regions, further

downstream particles tend to aggregate in form of strands and descend towards the bottom outlet experiencing surface abrasion against the wall. In these regions, the normal load acting on the particles increases towards the conical part with the particle size. The solids flow pattern inside the cyclone is strongly affected by solids loading, which has a strong dampening effect on the fluid velocity, thus particles are found to travel longer paths at low solids loadings and at increasing gas inlet velocities.

The particle dynamics, as described above, are used to calculate attrition in each region of the cyclone, using the single particle breakage model upon impact for F-CLC, for collisional dominated regions, and the model of surface abrasion of Archard and Charj, (1953) for the sliding dominated regions. Under the conditions tested, the results show that collisional attrition is about one order of magnitude higher than that given by surface abrasion. The latter is more significant in the conical part of the cyclone. A fair agreement with the experimental results in terms of overall extent of attrition is obtained, confirming the dependency found with the gas inlet velocity, solids loading, and particle size, having a power index of 3, -0.2 and -1, respectively.

7.1.3 Jet Attrition in Fluidised Beds

The work on jet attrition in a fluidised bed has been carried out in IFP energies Nouvelles (Solaize, France). A semi-pilot scale fluidised bed apparatus is used to evaluate particle attrition induced by the jet of both F-CLC and E-CLC, as a function of jet velocity (from 30 to 55 m s^{-1}) and orifice size (3, 4 and 5 mm), in terms of steady state loss rate. The gas jet is formed from a single orifice mounted at the centre of a porous distributor. The latter provides the necessary background fluidisation needed to keep the superficial velocity constant for all the jet velocities. Both materials require about 10-15 days of fluidisation without the jet to reach a steady loss rate. This is due to the presence of pre-existing elutriable fines and the higher initial attrition caused by the surface asperities and weak spots. The steady state loss rate in absence of the jet is found to be slightly higher for E-CLC than F-CLC, consistent with the tendency observed at single particle level. This value is then subtracted from the overall attrition obtained in the presence of the jet to calculate jet-induced attrition. Once the gas jet is introduced it takes about 2 to 4 days to reach a new steady loss rate. E-CLC has shown to undergo jet attrition much more extensively than F-CLC. The power indices of the jet velocity and orifice size for F-CLC

are found to be 2 and 1.7, respectively. They differ from those obtained for E-CLC, 6 and 3.6, respectively. One reason could be that the fluidisation of E-CLC might have been carried out at the limit of the TDH or even below it. In fact, the data collected for E-CLC are somewhat scattered, as compared with those of F-CLC, and the SEM images of the fines collected on the filter show the presence of rather large particles of size comparable to the feed material. The fines collected on the filter are mainly composed of small particles of about 1 μm, organised in clusters. The particles after several weeks of fluidisation present still a rather irregular shape and are difficult to be distinguished from the non-processed material suggesting their tendency to lose surface chips.

7.1.4 Population Balance Model

The population balance model has been developed at IFP energies Nouvelles. The correlations for jet and cyclone attrition are eventually implemented in a population balance model for particle attrition in a fluidised and circulating fluidised bed, developed in-house, using Matlab®. Bubbling bed attrition is also included, using correlation from literature, and assumed to occur in the region of the bed above the jet height. The part of the population undergoing attrition is determined by the minimum mother particle size. This is evaluated for the jet/bubbling bed region and the cyclone, using the single particle breakage model upon impact, assuming the most dramatic conditions in the respective region, i.e. a normal impact at the maximum particle velocity achievable. The formation of debris is accounted for by assigning a PSD ranging from 0 to the maximum debris size. The latter is set based on the experimental results carried out on jet attrition. As the dominant pattern of breakage is found to be surface damage, the model only allows particle shrinking.

Particle attrition in the jet/bubbling bed region, entrainment of solids, particle attrition and gas/solids separation in cyclone and recycling are evaluated in series within the integration time step. The only variables are time and particle size; the latter dictates the transfer of particles to different size classes after attrition. These are predefined based on the PSD of the input material. By using different integration time steps of 0.1, 0.5 and 1 s, the loss rate and cumulative mass loss are not found to vary at all. On the other hand, the integration time step has little effect on the bed inventory average particle size because

of the different patterns of particles transfer between size classes, established for small and large integration time steps.

By reproducing the experimental history of the jet attrition tests, carried out on the pilot scale fluidised bed at IFP Energies Nouvelles on F-CLC, the model has proved to be fairly predictive for describing the PSD of the bed inventory measured experimentally at the end of the tests.

The PBM model is then used to simulate the behaviour of a pilot scale fluidised and circulating fluidised bed with make-up, for a period of 10 days as a function of different single particle breakability indices, such as 0.01, 0.1, 1, 10 and 100 times that of F-CLC, and jet velocities of 55, 75, 95 and 115 m s^{-1}. The latter also dictate the superficial velocities equal to 0.139, 0.190, 0.240, 0.291 m s^{-1}, respectively.

In the case of the fluidised bed, two regimes prevail where the loss is dominated in order by the elutriation of pre-existing fines and debris particles produced by attrition. The bed average particle size becomes large and smaller during the two regimes, respectively. For the fluidised bed configuration, elutriation is equal to the loss rate because no cyclone is present, and the jet attrition is always greater than the bubbling bed attrition. By either increasing the single particle breakability index or the superficial velocity (by increasing the jet velocity), the transition between the two regimes is anticipated and delayed, respectively. As attrition, elutriation and loss rate increase, the bed inventory average particle size decreases during the attrition dominated regime.

In the case of the circulating fluidised bed with make-up, the transition between the two regimes occurs earlier than the fluidised bed case because the loss rate is limited by the presence of the cyclone. By either increasing the single particle breakability index or the superficial velocity (by increasing the jet velocity), the attrition rate increases so the transition between the two regimes is anticipated, the solids circulation and loss rate increase and the bed inventory average particle size tend to decrease. The jet region is always the main source of attrition, followed by the cyclone and bubbling bed. The gas/solids collection efficiency tends to vary with time until the particle size distribution and the rate of the circulated solids reach an equilibrium that is dictated by the attrition rate, operating conditions, and cyclone efficiency.

The results of the PBM show that particle attrition profoundly affects the process performance, especially by accounting for the formation of fines which are not always simply lost. Their presence in the system is regulated by the operating conditions, attrition rates and collection by the cyclone. The complex mechanisms revealed here by PBM shows the significant influence of particle attrition on the bed inventory size distribution, solids circulation rate and gas/solids separation efficiency.

7.2 Future work

Keeping the focus on particle attrition, this research project is composed of four well distinct subjects such as the single particle, cyclone, fluidised bed and the population balance. The latter uses the inputs of the formers, therefore in order to vertically develop this research project some compromises had to be adopted and some topics could not be fully investigated. As a result, this thesis can inspire some interesting future investigations and improvements.

7.2.1 Single Particle Attrition

At the single particle level, the analysis of the mechanical properties can be completed, for both F-CLC and E-CLC, by evaluating the fracture toughness, using higher indentation loads than those used here in order to evaluate the quasi-static breakability index H/K_c^2 and check consistency with the relative breakage tendency found upon impact tests.

The coherence established between the results of the single particle impact test and the Scirocco impact test should be supported by using different materials. If this is confirmed, the Scirocco of the Malvern Mastersizer 2000 (commercially available), could potentially substitute the single particle impact test which is an in-house test equipment and not commercially available. The breakage analysis could be improved by assessing the full PSD after breakage rather than only using a cut-off sieve size for mother-particle/debris-particle separation. The effect of fatigue is checked by carrying out six repeated impacts at a fixed particle size and impact velocity, whilst almost no variation is observed for F-CLC throughout the six impacts, the extent of breakage of E-CLC decreases at high particle impact velocities. More than six impacts are needed to reveal the actual behaviour of the particles after repeated impacts and discover whether a constant breakage is

eventually achieved. The dependency of the extent of attrition found with the sinθ for inclined impacts is purely empirical. This implicitly assumes that the normal component of velocity is only responsible for a portion of the overall extent of breakage. Fundamental study is needed here to investigate the underlying mechanism of breakage under inclined impacts.

7.2.2 Cyclone attrition

The cyclone experimental work has been carried out with one material, i.e. only for F-CLC and not with E-CLC due to lack of time. The particle sizes used for the tests are quite large, the analysis could be extended to smaller particles. All the tests have been carried out with a fixed narrow particle size obtained by sieving. Thus, there is a need to test a wider PSD to check whether the single contribution of each particle size can be extrapolated to describe the overall attrition. It would be very interesting to verify that each particle size behaves in a mixture as it does alone proportionally to its mass fraction. Moreover, longer inlet pipes should be used in order to have constant particle entrance velocities. Different cyclone geometries and dimensions can be used to verify the applicability of the correlation.

The unexpected behaviour obtained from the 20^{th} to the 40^{th} pass after that the cyclone was cleaned of the fine deposits on the wall needs to be further investigated. First, a new test can be performed where at the end of each pass the cyclone is cleaned of the fines deposited to check whether the same trend is observed. If not, it might mean that the layer of fines built on the cyclone wall serves as an attrition mitigator by cushioning particle collisions and sliding.

The solids flow pattern given by the CFD-DEM simulations strongly depends on the contact parameters. They could be improved by evaluating the actual coefficient of restitution, sliding friction and rolling friction of the material that are here taken from literature. Further investigation is also needed to verify the discrepancy between the pressure drop obtained from the simulation and the experiments. The contribution of the particle surface abrasion by sliding against the wall is evaluated with the model of Archard and Charj, (1953) while this has not been experimentally proved on the material used. Moreover, its wear coefficient is obtained by extrapolation from an experimental point of cyclone attrition, while it could be assessed independently. Further analysis could

also be carried out by applying the model of surface abrasion of Ning and Ghadiri, (2006) instead, which is a function of hardness and fracture toughness. As proposed for the experimental work, a mixture of particle sizes can also be simulated, and attrition assessed using the same methodology.

7.2.3 Jet Attrition in Fluidised Beds

Jet attrition has been evaluated experimentally in a semi-pilot scale fluidised bed. In this work, jet attrition could not be related to the particle size because the full PSD was used for the tests. Thus, its effect remains unknown and requires future work. The difficulty lies on the effort and time required to sieve and collect enough material to run the semi-pilot scale fluidised bed with one size cut. Therefore, for the effect of particle size analysis it is suggested to use a smaller scale fluidised bed. After assessing the effect of a narrow size distribution, the complexity of the system could be extended to a mixture. A smaller scale is also more approachable by CFD-DEM. In fact, the methodology applied on the cyclone (CFD-DEM simulation coupled with the single particle breakage model) was not feasible to be used here due to the scale of the system. These simulations can help to have a better fundamental understanding of the mechanism of jet attrition, such as the particle entrainment within the jet core, the relative impact velocity and frequency of collisions. Alternatively, such a large system could have been simulated by CFD-DEM by considering only a slice of the column using periodic boundary conditions, once verified that the slice can be representative of the whole bed. Another approach could be the use of the coarse graining method to reduce the number of particles in the simulation. The applicability of the experimental correlation developed for F-CLC could be verified by using larger columns as well as multiple orifices.

The experimental jet attrition tests carried out on the E-CLC suggest a great discrepancy with the results obtained for F-CLC, which are in line with literature. As mentioned, under the conditions at which the tests for E-CLC are carried out, the bed freeboard height might have been shorter than the TDH compromising in this way the results by elutriating large particles as well. It is therefore important to repeat the test using a taller column.

Further investigation could be carried out on the PSD of the fines collected on the filter at different conditions of jet velocities, in order to verify the hypothesis that the very small

fines mainly derive from surface abrasion (in absence of a gas jet) and that the larger fines mainly originate from chipping in the jet.

7.2.4 Population Balance Model

The PBM has a lot of room for improvement. All the assumptions made to develop the model can be addressed and improved. The most important analysis to be carried out before further complicating the PBM is the sensitivity analysis on the number of classes. The minimum mother particle size for the jet could be more accurately estimated by the help of numerical analysis. The debris PSD could be correlated to the single mother particle as a function of its size, mechanism of breakage and magnitude of stress undergone. In here, only particle attrition by surface damage is considered, thus a better description could be achieved by including particle fragmentation. The estimation of the average particle residence time in the freeboard, cyclone and recycle line is quite rough and could be improved. The attrition correlations are at steady state and therefore ignore the initial high breakage of fresh material. Jet attrition is considered here to apply to all the bed solids included below the jet height while more precisely it is a stream of solids being entrained in the jet core that undergoes jet attrition. As mentioned before, this could be evaluated by numerical analysis. The fluidised bed is assumed to be always in the bubbling fluidisation regime while the shift to different regimes could be implemented. No effect of temperature or the chemical reaction are considered here while they are known to have a major role in attrition. The PBM developed here only allows to simulate either a fluidised bed or a circulating fluidised bed, the latter being composed of a fluidised bed, a cyclone and a recycle. The program could be made more flexible so that any type of configuration could be implemented such as a circulating fluidised bed with regenerator and more than one cyclone. The developed PBM code could be made more efficient or even parallelised and structured in a more user-friendly way. The whole analysis on the FB and CFB is performed for a duration of 10 days. Some trends have been identified but should be confirmed by further studies carried out on longer periods of time. Moreover, the robustness of the PBM can be verified by reproducing an industrial scale FCC process for which attrition features are well known in literature, such as single particle breakability index, jet, bubbling bed and cyclone attrition. This could help validate the methodology proposed in this work that aims at linking the single particle breakage propensity to particle attrition in the industrial process.

APPENDIX

A.1 Cyclone Attrition Appendix

The numbers of nodes and cells used for the mesh independency analysis for the fluid dynamic resolution in the cyclone are given in Table A-1.

Table A-1. Computational cells distribution in the fluid domain

	Basic mesh		**1st refinement**		**2nd refinement**	
Sub-domain reference number	Nodes	Hexahedra	Nodes	Hexahedra	Nodes	Hexahedra
1	12384	10752	22440	20000	39936	36288
2	8987	8064	14331	13000	26176	24192
3	5504	4032	10200	8000	18432	15120
4	3168	2560	6160	5200	8736	7488
5	3159	2432	5566	4500	9802	8208
6	6240	4864	9200	7200	16704	13680
7	4992	3648	9200	7200	16704	13680
8	11232	9728	20240	18000	36192	32832
9	6048	5120	11000	9600	18096	16128
10	37926	30000	52675	43200	69832	58800
11	1638	1200	2625	2016	3944	3136
12	25289	23040	42431	39000	61759	57600
13	8194	7392	14801	13600	25755	24000
Global	**134761**	**112832**	**220869**	**190516**	**352068**	**311152**

The gas tangential velocity and static pressure contours at 16 and 20 m s^{-1} at different solids loading of particles of 377.5 μm are reported in Figure A-1 and Figure A-2, respectively. The radial and axial velocity contours at 16, 20 and 24 m s^{-1} at different solids loading of particles of 377.5 μm are reported in Figure A-3 and Figure A-4, respectively. The solids flow pattern at 16 and 24 m s^{-1} are reported in Figure A-5. By CFD-DEM analysis, the average particle velocities in the inlet pipe of the cyclone, for a length twice as that used for the experimental work (equal to 0.33 m), for a mixture of different particle sizes at 0.1 of solids loading are reported in Figure A-6. Under the same conditions, the average particle velocities by using a solids loading equal to 10 are reported in Figure A-7 showing that there is always a difference in particle entrance velocity for different solids loading.

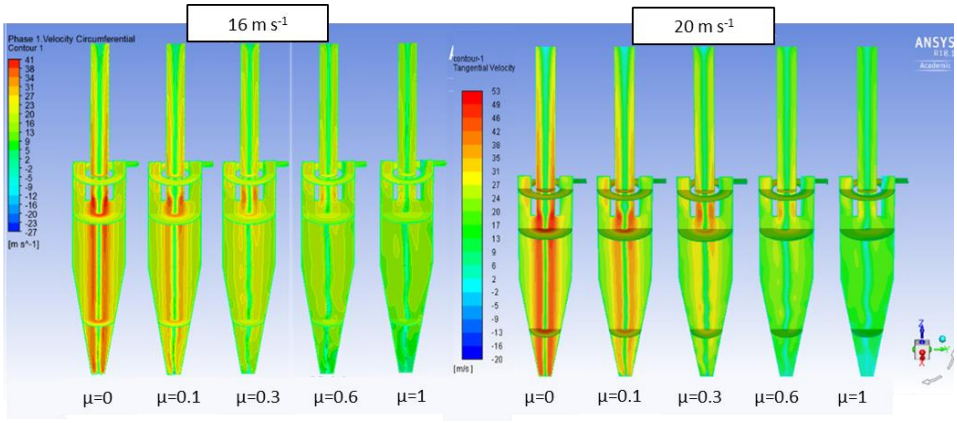

Figure A-1. Tangential velocity contours, at steady state, at 16 and 20 m s^{-1} inlet gas velocity and different solids loadings for a particle size of 377.5 μm

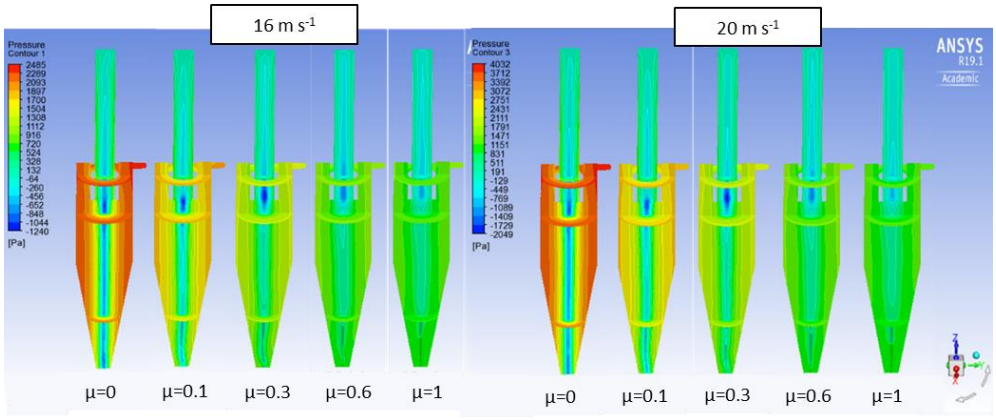

Figure A-2. Pressure contours, at steady state, at 16 and 20 m s^{-1} inlet gas velocity and different solids loadings

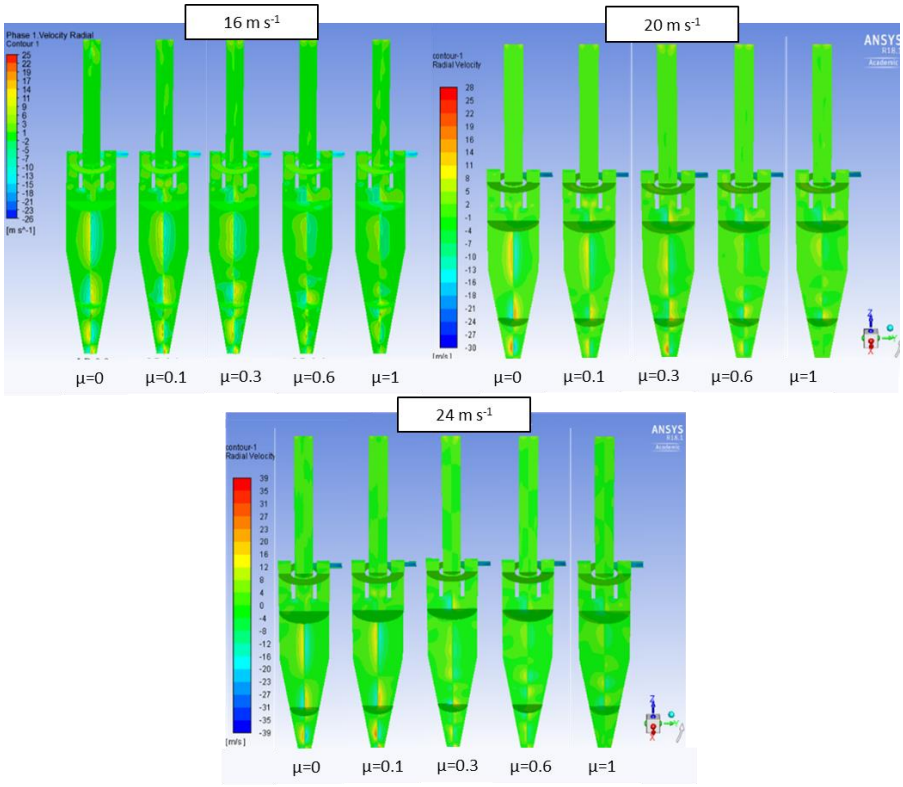

Figure A-3. Radial velocity contours, at steady state, at 16, 20, 24 m s^{-1} inlet gas velocity and different solids loadings

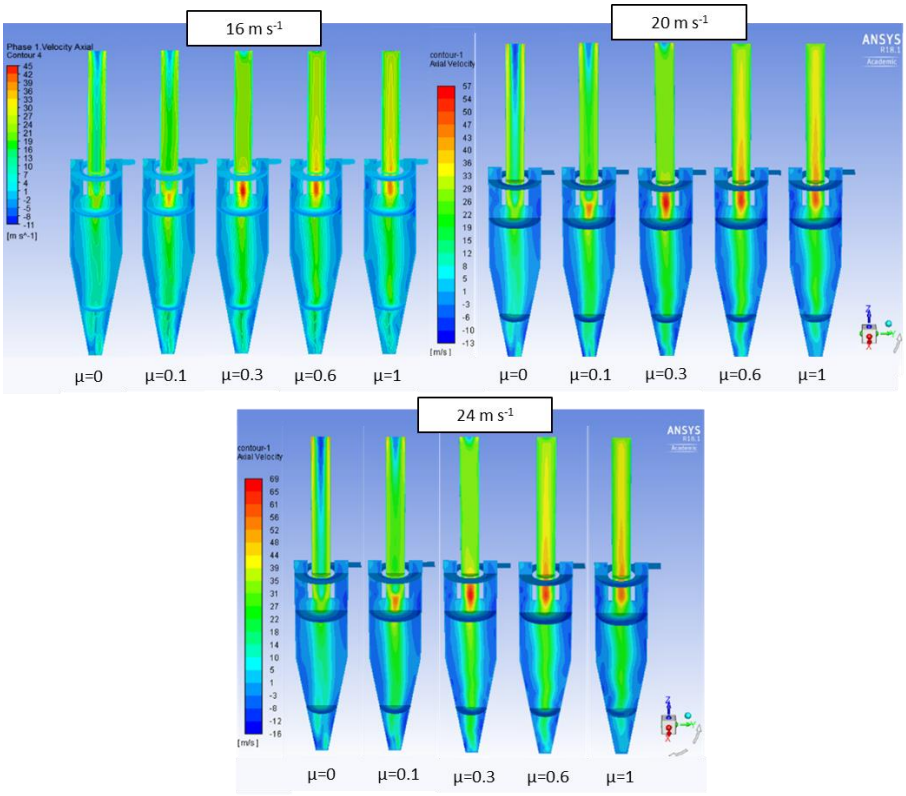

Figure A-4. Axial velocity contours, at steady state, at 16, 20, 24 m s^{-1} inlet gas velocity and different solids loadings

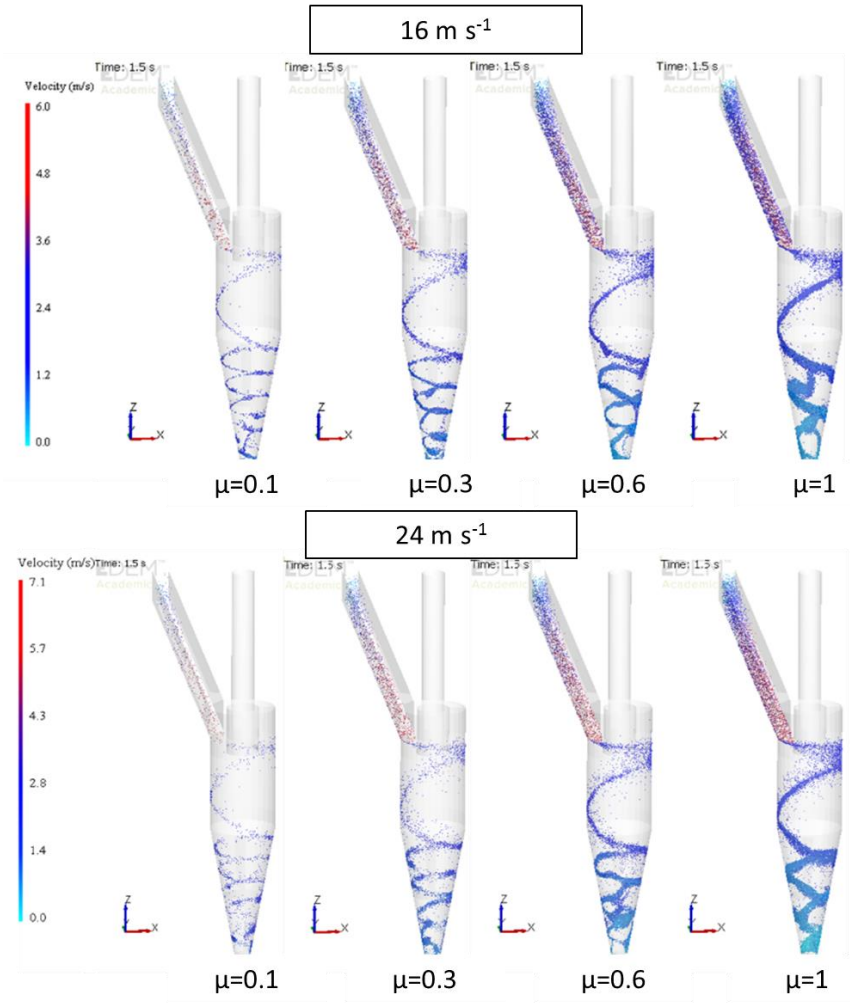

Figure A-5. Solid flow pattern at 16 and 20 m s^{-1} at different solids loadings

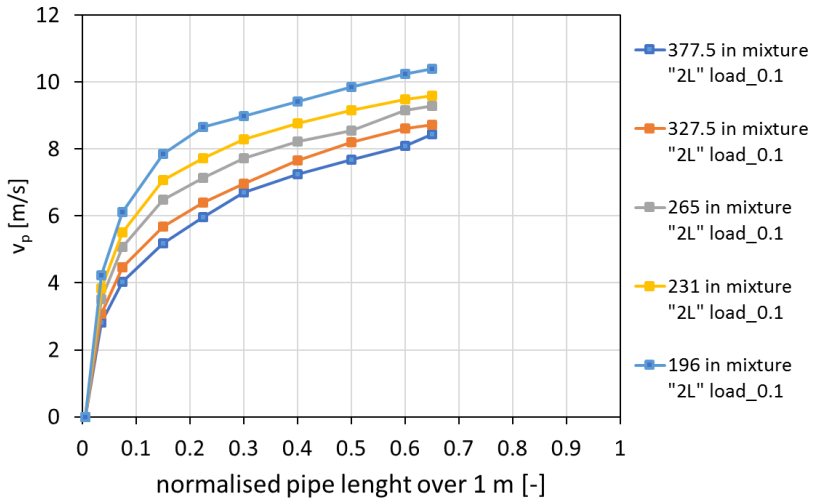

Figure A-6. Average particle velocity in the inlet pipe of the cyclone for different particle sizes and at low solids loading (0.1)

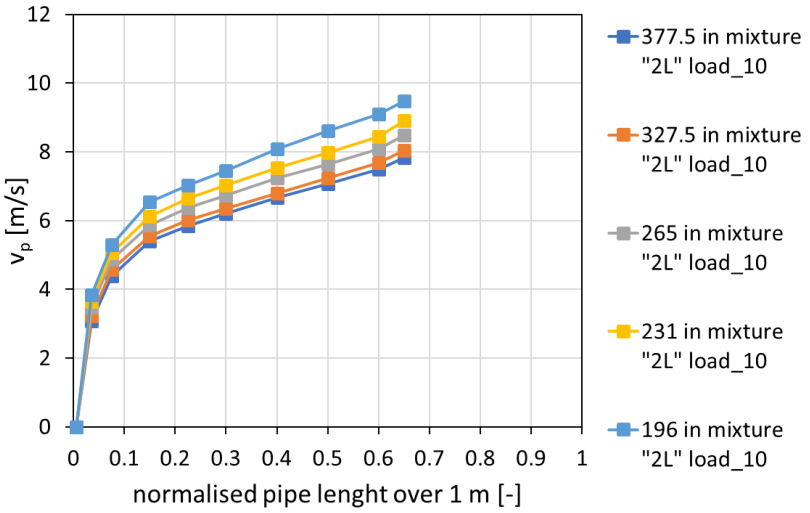

Figure A-7. Average particle velocity in the inlet pipe of the cyclone for a mixture of different particle sizes at high solids loading (equal to 10)

A.2 Jet Attrition Appendix

A.2.1 High Temperature Test "EXP 3"

The high temperature test, "EXP 3" is carried out on F-CLC to look at the effect of temperature by fluidising only with the porous base. The test conditions are reported in the table below and Figure A-8.

Table A-2. Experimental conditions for F-CLC to look at the effect temperature on the bubbling bed attrition

EXP 3 (*Batch 3* full PSD **F-CLC)**				
T [°C]	***room***	***200***	***400***	***600***
u_{jet} [m s^{-1}]	-			
d_{or} [m]	-			
h_{jet_theor} [m]	-	-	-	-
Q_{jet} [m^3 s^{-1}]	-	-	-	-
Q_{pb} [m^3 s^{-1}]	0.00189	0.00144	0.00116	0.00101
Q_{tot} [m^3 s^{-1}]	0.00189	0.00144	0.00116	0.00101
$d_{p,\infty}$ [µm]	53			

u_{sup} [m s^{-1}]	0.243	0.185	0.149	0.130
u_{mf_theor} [m s^{-1}]	0.069	0.053	0.042	0.037
u_{sup}/u_{mf_theor}	3.5	3.5	3.5	3.5
$m_{bed,0}$ [kg]	3.2			
TDH_{theor} [m]	0.260	0.191	0.162	0.124
$h_{bed,exp}$ [m]	Not measured			
h_{tot}-h_{bed} [m]	-			

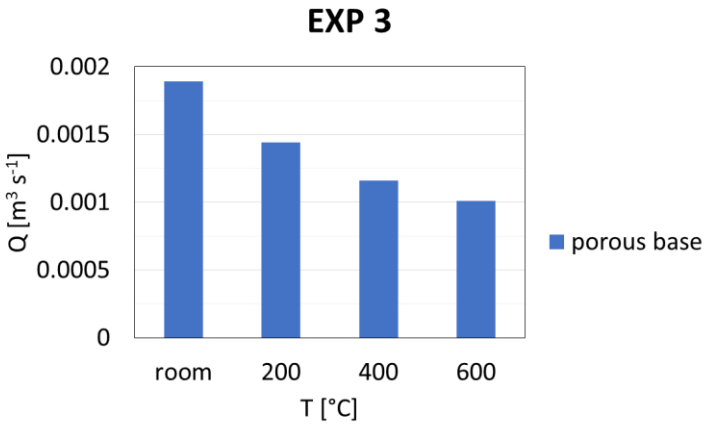

Figure A-8. Gas flow rates for the porous base for the evaluation of F-CLC bubbling bed attrition at different temperature (in order to have the same terminal velocity of $d_{p,\infty}$)

As shown in Figure A-9, attrition seems to decrease with temperature to a point where it becomes barely measurable. By returning at room temperature, after having increased the temperature from 200 to 600°C, attrition is nearly 8 times greater, meaning that some drastic changes have occurred to the material. Structural changes are very likely to happen as well as thermal decomposition at very high temperature. About the latter point, Teryama and Masao, (1983) demonstrated that MnO_2 decomposes at 586° into Mn_2O_3 and O_2. This is though not further investigated in this research project. Some insights can be given by looking at the particles by SEM, Figure A-10. The particles seem to be more rounded and surfaces more homogeneous. To unravel the transformation they have undergone, the Mercury porosimetry technique is used to evaluate any shift in particle density and internal porosity. The test revealed that structural changes have occurred. The internal porosity has increased from 17% to 27% as well the skeletal density from 4000 kg m^{-3} to 4360 kg m^{-3} which leads to an envelope density of 3180 kg m^{-3} as compared to

3300 kg m^{-3} of before the test. Structural as well as chemical changes are very likely to have occurred, but this has not furtherly been investigated.

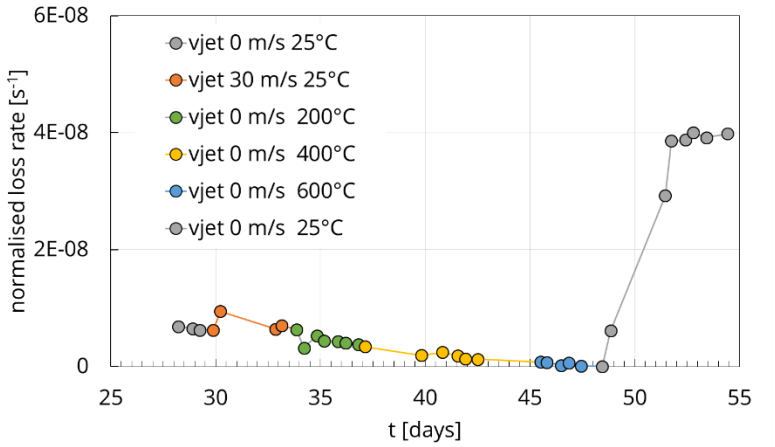

Figure A-9. Effect of temperature on attrition for F-CLC

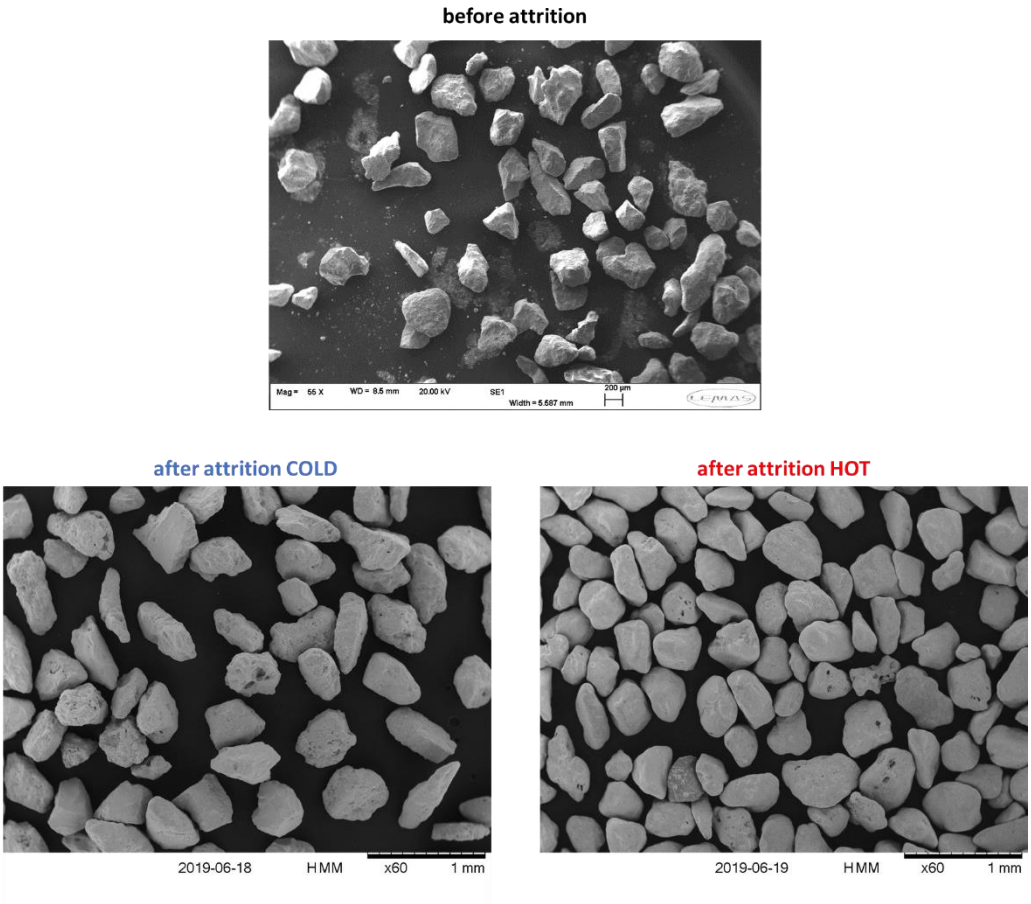

Figure A-10. F-CLC particles before attrition and after jet attrition at room and hot temperature

A.2.2 CFD-DEM Study of Jet Attrition in a Simple System"

A CFD-DEM study on the jet-induced attrition has been carried out for a very small and simple system, far from the actual semi-pilot scale used, to elucidate the dynamic of particles in the jet region and their likelihood to be entrained within jet and experience collisional attrition. The frequency of collision as well as the net flow of entrained particles within the jet is evaluated post processing and used to evaluate the overall attrition in combination with the single particle breakage model of chipping of (Ghadiri and Zhang, 2002).

The bed is cuboid of 100 mm×10 mm×600 mm. The jet is a 5 mm×10 mm rectangular slot and placed at centre bottom of the bed; air, at standard condition, is issued from it at 40 m s^{-1}. The particles are spheres, having a diameter of 925 µm and density of 3300 kg m^{-3}. The other DEM parameters such as coefficient of restitution, sliding friction and rolling friction, shear modulus and Poisson's ratio were specified as, 0.5, 0.5, 0.01, 0.1 G Pa and 0.25, respectively, as given by default by the software EDEM®. The total number of particles is set to 20000 for a total bed mass of 31.97 g. The system is simulated for 3.4 s. A time sequence of the simulation is reported below in Figure A-11.

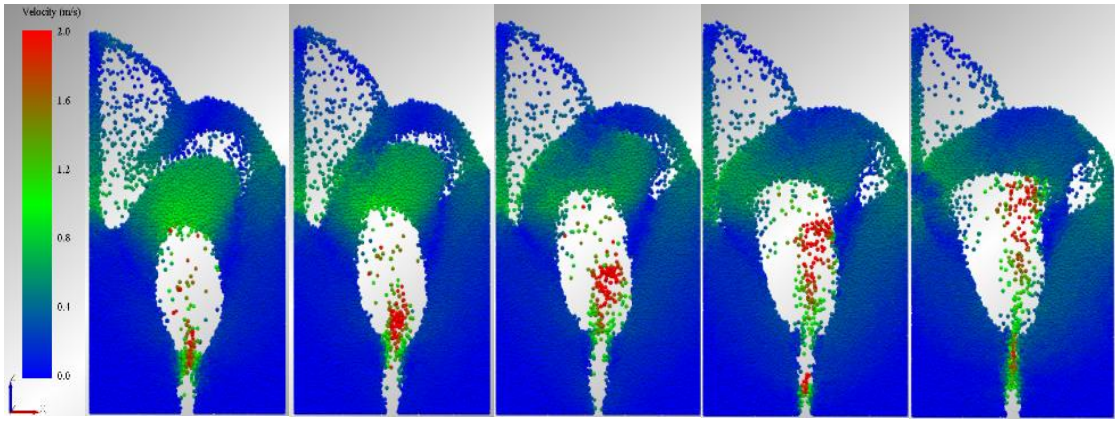

Figure A-11. Time sequence of particles behaviour in the core of the jet

The jet core region has been identified by as the internal regional with highest void fraction wherein the dynamics of particle motion is analysed in terms of particle velocity, number of collisions per particle and number flux of particles into the acceleration zone.

The acceleration channel, of about 20 mm, can be seen from Figure A-12. After that, the particle velocity in the jet core would remain quite constant. This is the velocity value at which the particles will collide with the slow-moving part of the bed.

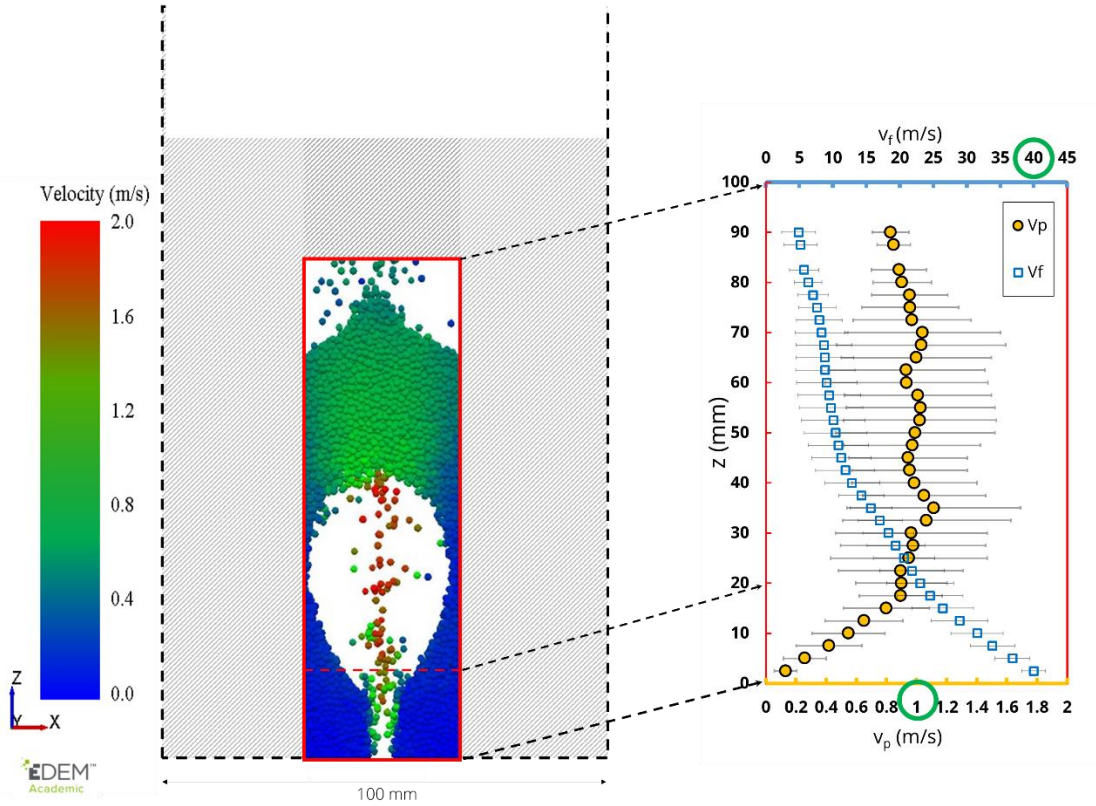

Figure A-12. Fluid and particle velocity analysis in the jet core

Considering the single particle breakage model of chipping of (Zhang and Ghadiri, 2002) defined in Chapter 3 in Equation. 3-5, defined as R_{chip}, the jet attrition can be expressed as:

$$R_{jet} = R_{chip} \dot{N}_{p,jet} N_{c/p} \eta_{col} \quad \text{(A-1)}$$

where $\dot{N}_{p,jet}$ is the net number flux of particles entrained in the jet core, $N_{c/p}$ the number of collisions per particle and η_{col} the efficiency of collisions, given the constraint of the transition velocity.

A.3 Population Balance Appendix

A.3.1 Start up

Given the averaging within the saving time step, the behaviour of the system at the start-up cannot be captured with accuracy. On this regard, a simulation of case "2" of 0.2 days at saving time step equal to the integration time step is carried out at the default conditions, jet velocity of 55 m s^{-1} and $X_{breakability}$ equal to 1. At the start-up, the solids front requires a time equal to τ_{FB} to reach the cyclone inlet, a time equal to (τ_{FB}+ τ_{cyc}) to leave the cyclone and a time equal to (τ_{FB}+ τ_{cyc}+ τ_{rec}) to return to the fluidised bed. As shown below in Figure A-13, the attrition rate is constant throughout, while the loss rate, which is null before (τ_{FB}+ τ_{cyc}), undergoes a sudden change in slope when the first loop is completed.

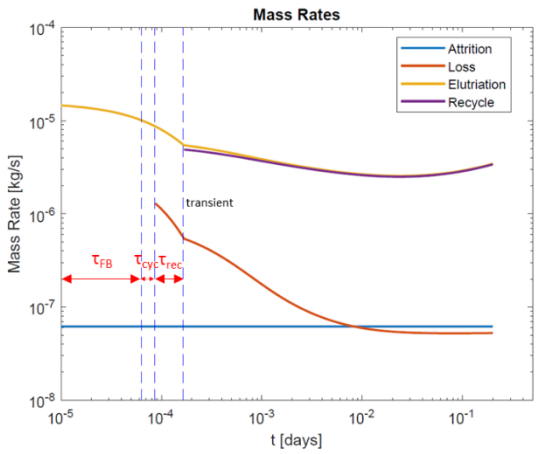

Figure A-13. Mass rates at start-up for the CFB

Under the conditions tested, it has been previously established that at the very beginning the loss rate is dominated by the elutriation of the pre-existing fines. Here it is even clearer how the sudden increase of the bed Sauter mean diameter occurs mainly before the solids circulation has completed the first loop because of the removal of the pre-existing fines, Figure A-14.

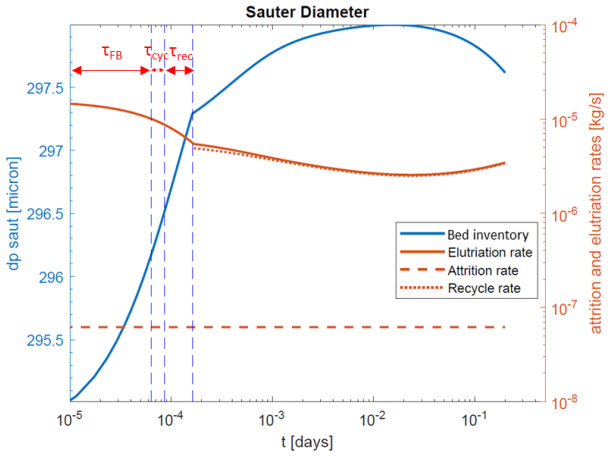

Figure A-14. Bed Sauter mean diameter at start-up for CFB

REFERENCES

©2016 Reade International Corp n.d. Manganese Oxide / Manganese Dioxide Powder (MnO2). Available from: http://www.reade.com/products/manganese-oxide-manganese-dioxide-powder-mno2.

Adánez, J., Gayán, P., García-Labiano, F. and de Diego, L.F. 1994. Axial voidage profiles in fast fluidized beds. *Powder Technology*. **81**(3),pp.259–268.

Agu, C.E., Pfeifer, C. and Moldestad, B.M.E. 2019. Prediction of void fraction and minimum fluidization velocity of a binary mixture of particles: Bed material and fuel particles. *Powder Technology*. **349**,pp.99–107.

Ahmadian, H. and Ghadiri, M. 2007. Analysis of enzyme dust formation in detergent manufacturing plants. *Advanced Powder Technology*. **18**(1),pp.53–67.

Ali, M., Bonakdar, T., Ghadiri, M. and Tinke, A. 2015. Particle Breakage in a Scirocco Disperser. *Powder Technology*. **285**,pp.138–145.

Amblard, B., Bertholin, S., Bobin, C. and Gauthier, T. 2015. Development of an attrition evaluation method using a Jet Cup rig. *Powder Technology*. **274**,pp.455–465.

ANSYS Fluent Theory Guide 2014. ANSYS Fluent Theory Guide. *Computer Communications*. **15317**(November),pp.724–746.

ANSYS Inc. 2013. ANSYS Fluent Theory Guide

Antonyuk, S., Khanal, M., Tomas, J., Heinrich, S. and Morl, L. 2006. Impact breakage of spherical granules: Experimental study and DEM simulation. *Chemical Engineering and Processing: Process Intensification*. **45**(10),pp.838–856.

Archard, J.F. and Charj, J.F.A. 1953. Contact and Rubbing of Flat Surfaces. *Journal of Applied Physics*. **24**(8),pp.981–987.

Arena, U., D'Amore, M. and Massimilla, L. 1983. Carbon attrition during the fluidized combustion of a coal. *AIChE Journal*. **29**(1),pp.40–49.

Asiedu-Boateng, P., Legros, R. and Patience, G.S. 2016. Attrition resistance of calcium oxide-copper oxide-cement sorbents for post-combustion carbon dioxide capture.

Advanced Powder Technology. **27**(2),pp.786–795.

ASTM 2013. Standard Test Method for Determination of Attrition and Abrasion of Powdered Catalysts by Air Jets. *ASTM international*. **D 5757-00**,pp.1–4.

Baeyens, J. and Geldart, D. 1986. *Gas Fluidization Technology* (Wiley, ed.). New York.

Balestrin, E., Decker, R.K., Noriler, D., Bastos, J.C.S.C. and Meier, H.F. 2017. An alternative for the collection of small particles in cyclones: Experimental analysis and CFD modeling. *Separation and Purification Technology*. **184**,pp.54–65.

Bayham, S.C., Breault, R. and Monazam, E. 2017. Applications of tribology to determine attrition by wear of particulate solids in CFB systems. *Powder Technology*. **316**,pp.59–68.

Bemrose, C.R. and Bridgwater, J. 1987. A review of attrition and attrition test methods. *Powder Technology*. **49**(2),pp.97–126.

Bentham, A.C., Kwan, C.C., Boerefijn, R. and Ghadiri, M. 2004. Fluidised-bed jet milling of pharmaceutical powders. *Powder Technology*. **141**(3),pp.233–238.

Bernardo, S., Mori, M., Peres, A.P. and Dionísio, R.P. 2006. 3-D computational fluid dynamics for gas and gas-particle flows in a cyclone with different inlet section angles. *Powder Technology*. **162**(3),pp.190–200.

Bertin, D., Cotabarren, I., Piña, J. and Bucalá, V. 2016. Population balance discretization for growth, attrition, aggregation, breakage and nucleation. *Computers and Chemical Engineering*. **84**,pp.132–150.

Blinichev, V. and Streltsov, V. 1968. An investigation of the size reduction of granular materials during their processing in fluidized beds. *Int. Chem. Eng.* **8**(4),pp.615–618.

Blinichev, V.N., Streltsov, V.V. and Lebedeva, E.S. 1968. International Journal of Chemical Engineering— An Open Access Journal. *International Journal of Chemical Engineering*. **8**,p.615.

Boerefijn, R. and Ghadiri, M. 1998. High speed video image analysis of flow of fine particles in fluidized bed jets. *Advanced Powder Technology*. **9**(3),pp.229–243.

Boerefijn, R., Ghadiri, M. and Salatino, P. 2007. *Attrition in Fluidised Beds*.

Boerefijn, R., Gudde, N.J. and Ghadiri, M. 2000. A review of attrition of fluid cracking catalyst particles. *Advanced Powder Technology*. **11**(2),pp.145–174.

Burns, S.J. and Hanley, K.J. 2017. Establishing stable time-steps for DEM simulations of non-collinear planar collisions with linear contact laws. *International Journal for Numerical Methods in Engineering*. **110**(2),pp.186–200.

Cabello, A., Gayán, P., García-Labiano, F., de Diego, L.F., Abad, A. and Adánez, J. 2016. On the attrition evaluation of oxygen carriers in Chemical Looping Combustion. *Fuel Processing Technology*. **148**,pp.188–197.

Cahyadi, A., Neumayer, A.H., Hrenya, C.M., Cocco, R.A. and Chew, J.W. 2015. Comparative study of Transport Disengaging Height (TDH) correlations in gas–solid fluidization. *Powder Technology*. **275**,pp.220–238.

Chen, T.P., Sishtla, C.I., Punwani, D. V. and Arastoopour, H. 1980. A Model for Attrition in Fluidized Beds *In*: *Fluidization*. Boston, MA: Springer US, pp. 445–452.

Chirone, R., Massimilla, L. and Salatino, P. 1991. Comminution of carbons in fluidized bed combustion. *Progress in Energy and Combustion Science*. **17**(4),pp.297–326.

Choi, J.H., Chang, I.Y., Shun, D.W., Yi, C.K., Son, J.E. and Kim, S.D. 1999. Correlation on the particle entrainment rate in gas fluidized beds. *Industrial and Engineering Chemistry Research*. **38**(6),pp.2491–2496.

Chu, K.W., Wang, B., Xu, D.L., Chen, Y.X. and Yu, A.B. 2011. CFD-DEM simulation of the gas-solid flow in a cyclone separator. *Chemical Engineering Science*. **66**,pp.834–847.

Chu, K.W., Wang, B., Yu, A.B. and Vince, A. 2009. CFD-DEM modelling of multiphase flow in dense medium cyclones. *Powder Technology*. **193**(3),pp.235–247.

Cleaver, J.A.S., Ghadiri, M. and Rolfe, N. 1993. Impact attrition of sodium carbonate monohydrate crystals. *Powder Technology*. **76**(1),pp.15–22.

Cocco, R., Arrington, Y., Hays, R., Findlay, J., Karri, S.B.R. and Knowlton, T.M. 2010. Jet cup attrition testing. *Powder Technology*. **200**(3),pp.224–233.

Cocco, Ray, Reddy Karri Yeook Arrington Roy Hays, S., Findlay Ted Knowlton, J., Reddy Karri, S., Arrington, Y., Hays, R., Findlay, J. and Knowlton, T. 2010. Particle attrition measurements using a jet cup *In*: *The 13th International Conference on Fluidization - New Paradigm in Fluidization Engineering*., pp. 1–8.

Couroyer, C. 2000. Attrition of Alumina Catalyst Carrier Beads.

Cundall, P.. and Strack, D.L. 1979. A discrete numerical model for granular assmeblies. *Geotechnique*. **29**(1),pp.47–65.

Derksen, J.J. 2003. Separation performance predictions of a stairmand high-efficiency cyclone. *AIChE Journal*. **49**(6),pp.1359–1371.

Derksen, J.J., Van Den Akker, H.E.A. and Sundaresan, S. 2008. Two-way coupled large-eddy simulations of the gas-solid flow in cyclone separators. *AIChE Journal*. **54**(4),pp.872–885.

Dessalces, G., Kolenda, F. and Reymond, J. 1994. Attrition evaluation for catalysts used in fluidized or circulating fluidized bed reactors *In*: *Preprints of the First International Particle Technology Forum, Part II*. Denver, pp. 190–196.

Dintwa, E., Tijskens, E. and Ramon, H. 2008. On the accuracy of the Hertz model to describe the normal contact of soft elastic spheres. *Granular Matter*. **10**(3),pp.209–221.

Donsi, G., Massimilla, L. and Colantuoni, L. 1980. *Fluidization* Matsen. (Plenum, ed.). New York.

Donsi, G., Massimilla, L. and Miccio, M. 1981. Carbon fines production and elutriation from the bed of a fluidized coal combustor. *Combustion and Flame*. **41**(C),pp.57–69.

Dowd, J.E. and Riggs, D.S. 1965. a Comparison of Estimates of Michaelis-Menten Kinetic Constants From. *The Journal of biological chemistry*. **240**(2),pp.863–869.

EDEM 2014. *EDEM 2.6 Theory Reference Guide* [Online]. Available from: www.dem-solutions.com.

Elsayed, K. 2015. Optimization of the cyclone separator geometry for minimum pressure

drop using Co-Kriging. *Powder Technology*. **269**(22),pp.409–424.

Elsayed, K. and Lacor, C. 2016. Analysis and optimisation of cyclone separators geometry using RANS and LES methodologies *In*: *Notes on Numerical Fluid Mechanics and Multidisciplinary Design*. Springer Verlag, pp. 65–74.

Elsayed, K. and Lacor, C. 2010. Optimization of the cyclone separator geometry for minimum pressure drop using mathematical models and CFD simulations. *Chemical Engineering Science*. **65**(22),pp.6048–6058.

Ergun, S. 1952. Fluid flow through packed columns. *Chem. Eng. Prog.* **48**,pp.89–94.

Ergun, S. and Orning, A. 1949. Fluid Flow through Randomly Packed Columns and Fluidized Beds. *Industrial and Engineering Chemiistry*. **41**(6),pp.1179–1184.

Evans, A.G. and Wilshaw, T.R. 1976. Quasi-static solid particle damage in brittle solids-I. Observations analysis and implications. *Acta Metallurgica*. **24**(10),pp.939–956.

Falola, A., Borissova, A. and Wang, X.Z. 2013. Extended method of moment for general population balance models including size dependent growth rate, aggregation and breakage kernels. *Computers & Chemical Engineering*. **56**,pp.1–11.

Forsythe, W.L. and Hertwig, W.R. 1949. Attrition Characteristics of Fluid Cracking Catalysts. *Industrial and Engineering Chemistry*. **41**(6),pp.1200–1206.

Forsythe WL, H.W. 1949. Attrition characteristics of fluid cracking catalysts. *Ind Eng. Chem* . **41**,pp.1200–1206.

Fraser, S.M., Abdel Razck, A.M. and Abdullah, M.Z. 1997. Computational and experimental investigations in a cyclone dust separator. *Proceedings of the Institution of Mechanical Engineers, Part E: Journal of Process Mechanical Engineering*. **211**(4),pp.247–257.

Fries, L., Antonyuk, S., Heinrich, S., Dopfer, D. and Palzer, S. 2013. Collision dynamics in fluidised bed granulators: A DEM-CFD study. *Chemical Engineering Science*. **86**,pp.108–123.

Fulchini, F., Nan, W., Ghadiri, M., Yazdan Panah, M., Bertholin, S., Amblard, B., Cloupet, A. and Gauthier, T. 2017. CFD-DEM Analysis of Particle Attrition in a Jet

in a Fluidised Bed *In*: *EPJ Web of Conferences*.

Gao, Z., Wang, Juan, Wang, Jiangyun, Mao, Y. and Wei, Y. 2019. Analysis of the effect of vortex on the flow field of a cylindrical cyclone separator. *Separation and Purification Technology*. **211**,pp.438–447.

Gauthier, T.A., Huard, M., Briens, C. and Berruti, F. 2010. A Review of Rapid Gas-Solid Separation Techniques *In*: *International Journal of Chemical Reaction Engineering*., p. 2.

Germaine, J.T. and Germaine, A. V. n.d. Grain Size Analysis *In*: *Geotechnical Laboratory Measurements for Engineers*. Hoboken, NJ, USA: John Wiley & Sons, Inc., pp. 84–116.

Ghadiri M, Cleaver JAS, T.V. 1995. Influence of distributor orifice size on attrition in the jetting region of fluidized beds *In*: *Preprints Fluidization VIII*. Tours, pp. 799–806.

Ghadiri, M. 2006. Hardness, Stiffness and Toughness of Particles *In*: *Powder Technology Handbook*., pp. 53–65.

Ghadiri, M. and Boerefijn, R. 1996. A Model of Attrition In the Jetting Region of Fluidised Beds. *KONA Powder and Particle Journal*. **14**,pp.5–15.

Ghadiri, M., Cleaver, J. and Yuregir, K. 1992. Attrition of sodium chloride crystals in a fluidized bed *In*: Engineering Foundation, ed. *Fluidization VII*. New York: Potter OE, pp. 604–610.

Ghadiri, M., Cleaver, J.A.S., Tuponogov, V.G. and Werther, J. 1994. Attrition of FCC powder in the jetting region of a fluidized bed. *Powder Technology*. **80**(2),pp.175–178.

Ghadiri, M. and Zhang, Z. 2002. Impact attrition of particulate solids. Part 1: A theoretical model of chipping. *Chemical Engineering Science*. **57**(17),pp.3659–3669.

Goldstein, J. 2003. *Scanning electron microscopy and x-ray microanalysis*. Kluwer Academic/Plenum Publishers.

Gwyn, J.E. 1969. On the Particle Size Distribution Function and the Attrition of Cracking Catalysts. *AIChE Journal*. **15**(1),pp.197–206.

Hadavi, V., Moreno, C.E. and Papini, M. 2016. Numerical and experimental analysis of particle fracture during solid particle erosion, part I: Modeling and experimental verification. *Wear*. **356**–**357**,pp.135–145.

Hærvig, J., Kleinhans, U., Wieland, C., Spliethoff, H., Jensen, A.L., Sørensen, K. and Condra, T.J. 2017. On the adhesive JKR contact and rolling models for reduced particle stiffness discrete element simulations. *Powder Technology*. **319**,pp.472–482.

Haig, C.W., Hursthouse, A., Mcilwain, S. and Sykes, D. 2014. The effect of particle agglomeration and attrition on the separation efficiency of a Stairmand cyclone. *Powder Technology*. **258**,pp.110–124.

Hansen, S. and Ottino, J.M. 1997. Fragmentation with abrasion and cleavage: analytical results. *Powder Technology*. **93**,pp.177–184.

Hartge, E.-U., Klett, C. and Werther, J. 2007. Dynamic simulation of the particle size distribution in a circulating fluidized bed combustor. *Chemical Engineering Science*. **62**(1–2),pp.281–293.

Haus, J., Hartge, E.-U., Heinrich, S. and Werther, J. 2018. Dynamic flowsheet simulation for chemical looping combustion of methane. *International Journal of Greenhouse Gas Control*. **72**,pp.26–37.

Haus, J., Hartge, E.-U., Heinrich, S. and Werther, J. 2017. Dynamic flowsheet simulation of gas and solids flows in a system of coupled fluidized bed reactors for chemical looping combustion. *Powder Technology*. **316**,pp.628–640.

Heinrich, S., Peglow, M., Ihlow, M. and Mörl, L. 2003. Particle population modeling in fluidized bed-spray granulation—analysis of the steady state and unsteady behavior. *Powder Technology*. **130**(1–3),pp.154–161.

Hertz, H. 1881. Uber die beruhrung fester elastischer Korper: J. für die Reine und Angewandte Mathematik. *Math.* **92**,pp.156–171.

Hoekstra, A.J., Derksen, J.J. and Van Den Akker, H.E.A. 1999. An experimental and numerical study of turbulent swirling flow in gas cyclones. *Chemical Engineering Science*. **54**(13–14),pp.2055–2065.

Hossain, M.M. and de Lasa, H.I. 2008. Chemical-looping combustion (CLC) for inherent CO2 separations-a review. *Chemical Engineering Science*. **63**(18),pp.4433–4451.

Hutchings, I.M. 1993. Mechanisms of wear in powder technology: A review. *Powder Technology*.

Jones, T.J., Russell, J.K., Lim, C.J., Ellis, N. and Grace, J.R. 2017. Pumice attrition in an air-jet. *Powder Technology*. **308**,pp.298–305.

Karri, R.S.B. and Werther, J. 2003. Gas Distributor and Plenum Design in Fluidized Beds *In*: *Handbook of fluidization and fluid-particle systems*.

Klett, C., Hartge, E.-U. and Werther, J. 2007. Time-dependent behavior of a catalyst in a fluidized bed/cyclone circulation system. *AIChE Journal*. **53**(4),pp.769–779.

Kobayashi, T., Tanaka, T., Shimada, N. and Kawaguchi, T. 2013. DEM-CFD analysis of fluidization behavior of Geldart Group A particles using a dynamic adhesion force model. *Powder Technology*. **248**,pp.143–152.

Kotsis, I., Enisz, M., Korim, T., Lenkei, M., Lendvay, L. and Zimny, P. 1998. Characterization of plasma sprayed coatings. *Hungarian Journal of Industrial Chemistry*. **26**(1),pp.1–7.

Kozołub, P., Klimanek, A., Białecki, R.A. and Adamczyk, W.P. 2017. Numerical simulation of a dense solid particle flow inside a cyclone separator using the hybrid Euler–Lagrange approach. *Particuology*. **31**,pp.170–180.

Kramp, M., Thon, A., Hartge, E.U., Heinrich, S. and Werther, J. 2011. The Role of Attrition and Solids Recovery in a Chemical Looping Combustion Process. *Oil and Gas Science and Technology*. **66**(2),pp.277–290.

Kumar, J., Peglow, M., Warnecke, G., Heinrich, S. and Mörl, L. 2006. Improved accuracy and convergence of discretized population balance for aggregation: The cell average technique. *Chemical Engineering Science*. **61**(10),pp.3327–3342.

Kunii, D. and Levenspiel, O. 1991. CHAPTER 8 – High-Velocity Fluidization *In*: *Fluidization Engineering*., pp. 193–210.

Kunii, D. and Levenspiel, O. 1990. Entrainment of Solids from Fluidized Beds I. Hold-

Up of Solids in the Freeboard II. Operation of Fast Fluidized Beds. *Powder Technology*. **61**,pp.193–206.

Kwan, C.C., Chen, Y.Q., Ding, Y.L., Papadopoulos, D.G., Bentham, A.C. and Ghadiri, M. 2004. Development of a novel approach towards predicting the milling behaviour of pharmaceutical powders. *European Journal of Pharmaceutical Sciences*. **23**(4–5),pp.327–336.

Lawn, B. 1993. *Fracture of Brittle Solids - second edition*.

Lawn, B.R. and Evans, A.G. 1977. A model for crack initiation in elastic / plastic indentation fields. *Journal of Material Science*. **12**,pp.2195–2199.

Lawn, B.R. and Evans, A.G. 1980. Elastic / Plastic Indentation Damage in Ceramics : The MediadRadial Crack System I '. *Journal of the American Ceramic Society*. **63**(9–10),pp.574–581.

Lawn, R.B. and Marshall, D.B. 1979. Hardness, Toughness, and Brittleness: An Indentation Analysis. *Journal of the American Ceramic Society*. **62**(7–8),pp.347–350.

Levenspiel, O., Kunii, D. and Fitzgerald, T. 1968. The Processing of Solids of Changing Size in Bubbling Fluidized Beds. *Powder Technology*. **2**,pp.87–96.

Li, T., Zhang, J. and Ge, W. 2004. Simple measurement of restitution coefficient of irregular particles. *China Particuology*. **2**(6),pp.274–275.

Linderholm, C., Lyngfelt, A., Béal, C., Trikkel, A., Kuusik, R., Jerndal, E. and Mattisson, T. 2009. Carbon Dioxide Capture for Storage in Deep Geologic Formations – Results from the CO2 Capture Project *In*: L. I. E. Stian, ed. *Advances in CO2 Capture and Storage Technology Results (2004-2009)*. Rykkinn, pp. 67–74.

Liu, D.H.F. and Liptak, B.G. 2013. *Environmental Engineer's Handbook*. Lewis Publishers, A CRC Press Company.

Lowrison, G.C. 1974. *Crushing and grinding : the size reduction of solid materials* (CRC Press, ed.). Cleveland, OH: Butterworths.

Lu, L. 2015. *Iron ore: Mineralogy, processing and environmental sustainability*. Elsevier.

Martignoni, W.P., Bernardo, S. and Quintani, C.L. 2007. Evaluation of cyclone geometry and its influence on performance parameters by computational fluid dynamics (CFD). *Brazilian Journal of Chemical Engineering*. **24**(1),pp.83–94.

Mashadi, A.B. and Newton, J.M. 1987. The characterization of the mechanical properties of microcrystalline cellulose: a fracture mechanics approach. *Journal of Pharmacy and Pharmacology*. **39**(12),pp.961–965.

Materic, V., Holt, R., Hyland, M. and Jones, M.I. 2014. An internally circulating fluid bed for attrition testing of Ca looping sorbents. *Fuel*. **127**,pp.116–123.

Merrick, D. and Highley, J. 1974a. Particle size reduction and elutriation in a fluidized bed process. *AIChE Symposium Series 70*. (137),pp.367–378.

Merrick, D. and Highley, J. 1974b. Particle size reduction and elutriation in a fluidized bed process *In*: *AIChE symposium series 137*., pp. 367–378.

Merry, J.M.D. 1975. Penetration of vertical jets into fluidized beds. *AIChE Journal*. **21**(3),pp.507–510.

Mindlin, R.D. 1949. Compliance of Elastic Bodies in Contact. *J. Appl. Mech., ASME*. **16**,pp.259–268.

Molerus, O. 1992. Heat transfer in gas fluidized beds part 2. Dependence of heat transfer on gas velocity. *Powder Technology*. **70**(1),pp.15–20.

Montagnaro, F., Salatino, P., Scala, F. and Urciuolo, M. 2011. A population balance model on sorbent in CFB combustors: The influence of particle attrition. *Industrial and Engineering Chemistry Research*. **50**(16),pp.9704–9711.

Mousavian, S.M., Ahmadvand, M. and Najafi, A.F. 2009. One-way and two-way coupling analyses on three phase flows in hydrocyclone separator. *Journal of Applied Mechanics, Transactions ASME*. **76**(6),pp.1–10.

Müller, C.R., Scott, S.A., Holland, D.J., Clarke, B.C., Sederman, A.J., Dennis, J.S. and Gladden, L.F. 2009. Validation of a discrete element model using magnetic resonance measurements. *Particuology*. **7**(4),pp.297–306.

Muschelknautz, U. 1997. *VDI Heat Atlas* 2nd ed. Dusseldorf.

Nilfisk 1854. *GM80* [Online]. Available from: https://www.nilfiskcfm.com/download/gm-80-product-sheet/?wpdmdl=1438&refresh=5d91f3226a2d91569846050.

Ning, Z. and Ghadiri, M. 2006. Distinct element analysis of attrition of granular solids under shear deformation. *Chemical Engineering Science*. **61**(18),pp.5991–6001.

Norouzi, H.R., Zarghami, R., Sotudeh-Gharebagh, R. and Mostoufi, N. 2016. *Coupled CFD-DEM Modeling: Formulation, Implementation and Application to Multiphase Flows* (I. DCW Industries, ed.). Wiley.

Papadopoulos, D.G. 1998. Impact Breakage of Particulate Solids.

Park, K., Hong, C., Han, J., Kim, B., Park, C. and Kwon, O.K. 2012. The Effect of Cyclone Shape and Dust Collector on Gas-Solid Flow and Performance. *World Academy of Science, Engineering and Technology*. **61**(1),pp.252–257.

Pell, M. 1990. Chapter 12 – Attrition in Fluidized Beds *In*: *Handbook of Powder Technology*., pp. 97–107.

Pis, J.J., Fuertes, A.B., Artos, V., Suarez, A. and Rubiera, F. 1991. Attrition of coal ash particles in a fluidized bed. *Powder Technology*. **66**(1),pp.41–46.

Pitchumani, R., Gupta, N., Meesters, G.M.H. and Scarlett, B. 2003. Analysis of single particle attrition during impact experiments. *Particle and Particle Systems Characterization*. **20**(5),pp.323–326.

Pougatch, K., Salcudean, M. and McMillan, J. 2010. Simulation of particle attrition by supersonic gas jets in fluidized beds. *Chemical Engineering Science*. **65**(16),pp.4829–4843.

Rajniak, P., Dhanasekharan, K., Sinka, C., MacPhail, N. and Chern, R. 2008. Modeling and measurement of granule attrition during pneumatic conveying in a laboratory scale system. *Powder Technology*. **185**(3),pp.202–210.

Rangelova, B.J., Mörl, L., Heinrich, S. and Dalichau, J. 2002. Decay Behavior of Particles in a Fluidized Bed ± Application of a Mass-Related Attrition Coefficient. . **25**,pp.639–646.

Raoufi, A., Shams, M., Farzaneh, M. and Ebrahimi, R. 2008. Numerical simulation and optimization of fluid flow in cyclone vortex finder. *Chemical Engineering and Processing: Process Intensification*. **47**(1),pp.128–137.

Raoufi, A., Shams, M. and Kanani, H. 2009. CFD analysis of flow field in square cyclones. *Powder Technology*. **191**(3),pp.349–357.

Ray, Y. and Jiang, T. 1987. Particle Attrition Phenomena in a Fluidized Bed. *Powder Technology*. **49**,pp.193–206.

Ray, Y.C., Jiang, T.S. and Jiang, T.L. 1987. Particle Population Model for a Fluidized Bed with Attrition. *Powder Technology*. **52**,pp.35–48.

Redemann, K., Hartge, E.U. and Werther, J. 2009. A particle population balancing model for a circulating fluidized bed combustion system. *Powder Technology*. **191**(1–2),pp.78–90.

Reppenhagen, J. and Werther, J. 2000. Catalyst attrition in cyclones. *Powder Technology*. **113**(1–2),pp.55–69.

Reynolds, G.K., Fu, J.S., Cheong, Y.S., Hounslow, M.J. and Salman, A.D. 2005. Breakage in granulation: A review. *Chemical Engineering Science*. **60**,pp.3969–3992.

Roberts, R.J., Rowe, R.C. and York, P. 1993. The measurement of the critical stress intensity factor (KIC) of pharmaceutical powders using three point single edge notched beam (SENB) testing. *International Journal of Pharmaceutics*. **91**(2–3),pp.173–182.

Rydén, M., Moldenhauer, P., Lindqvist, S., Mattisson, T. and Lyngfelt, A. 2014. Measuring attrition resistance of oxygen carrier particles for chemical looping combustion with a customized jet cup. *Powder Technology*. **256**,pp.75–86.

Safikhani, H., Akhavan-Behabadi, M.A., Shams, M. and Rahimyan, M.H. 2010. Numerical simulation of flow field in three types of standard cyclone separators. *Advanced Powder Technology*. **21**(4),pp.435–442.

Salman, A.D., Gorham, D.A. and Verba, A. 1995. A study of solid particle failure under

normal and oblique impact. *Wear*. **186**–**187**,pp.92–98.

Salman, A.D., Reynolds, G.K., Fu, J.S., Cheong, Y.S., Biggs, C.A., Adams, M.J., Gorham, D.A., Lukenics, J. and Hounslow, M.J. 2004. Descriptive classification of the impact failure modes of spherical particles. *Powder Technology*. **143**–**144**,pp.19–30.

Samimi, A. 2003. Characterisation of deformation and breakage of agglomerates.

Scala, F. and Salatino, P. 2010. Dolomite attrition during fluidized bed calcination and sulfation. *Combustion Science and Technology*. **175**,pp.2201–2216.

Schumann, R. 1940. *Principles of Comminution*. AIME Tech. (TP 1189).

Sciazko, M., Bandrowski, J. and Raczek, J. 1991. On the entrainment of solid particles from a fluidized bed. *Powder Technology*. **66**,pp.33–39.

Shepherd, C.B. and Lapple, C.E. 1939. Flow Pattern and Pressure Drop. *Industrial and Engineering Chemistry*. **31**(8),pp.972–984.

Slack, M. 2012. Best Practice Advice for Ac3-03 Cyclone Separator. *The QNET-CFD Network*. (D34_TA3_P32_AC3-03),pp.1–5.

Slack, M.D., Prasad, R.O., Bakker, A. and Boysan, F. 2000. Advances in cyclone modelling using unstructured grids. *Chemical Engineering Research and Design*. **78**,pp.1098–1104.

Sommerfeld, M. and Ho, C.A. 2003. Numerical calculation of particle transport in turbulent wall bounded flows. *Powder Technology*. **131**(1),pp.1–6.

Song, C., Pei, B., Jiang, M., Wang, B., Xu, D. and Chen, Y. 2016. Numerical analysis of forces exerted on particles in cyclone separators. *Powder Technology*. **294**,pp.437–448.

Taylor, L.., Papadopoulos, D.., Dunn, P.., Bentham, A.., Mitchell, J.. and Snowden, M.. 2004. Mechanical characterisation of powders using nanoindentation. *Powder Technology*. **143**–**144**,pp.179–185.

Teryama, K. and Masao, I. 1983. Study on Thermal Decomposition of MnO2 and Mn2O3

by Thermal Analysis. *Transactions of the Japan Institute of Metals*. **24**(11),pp.754–758.

Thornton, C. and Ning, Z. 1998. A theoretical model for the stick/bounce behaviour of adhesive, elastic- plastic spheres. *Powder Technology*. **99**(2),pp.154–162.

Tilton, J.N. 2008. *Perry's Chemical Engineers' Handbook, Section 6: Fluid and Particle Dynamics*.

Tsuji, Y., Tanaka, T. and Ishida, T. 1992. Lagrangian numerical simulation of plug flow of cohesionless particles in a horizontal pipe. *Powder Technology*. **71**(3),pp.239–250.

Unland, G. 2007. Chapter 4 The Principles of Single-Particle Crushing. *Handbook of Powder Technology*. **12**(07),pp.117–225.

Vaux, W.G. and Keairns, D.L. 1980. Particle Attrition in Fluid-Bed Processes *In*: *Fluidization*. Boston, MA: Springer US, pp. 437–444.

Verral, R.A., Fields, R.J. and Ashby, M.F. 1977. Deformation-Mechanism Maps for LiF and NaCl. *Journal of the American Ceramic Society*. **60**(5–6),pp.211–216.

Vervoorn, P.M.M. 1986. *Particle Attrition*. Delft.

Vogel, L. and Peukert, W. 2003. Breakage behaviour of different materials—construction of a mastercurve for the breakage probability. *Powder Technology*. **129**(1–3),pp.101–110.

Wang, L.G., Morrissey, J.P. and Ooi, J.Y. 2019. Development of a single particle breakage model incorporating oblique impact *In*: *Book of Extended Abstracts ESCC 2019*. Leeds, pp. 130–131.

Wang, Q., Luo, Z., Ni, M. and Cen, K. 2003. Particle population balance model for a circulating fluidized bed boiler. *Chemical Engineering Journal*. **93**(2),pp.121–133.

Wei, J., Zhang, H., Wang, Y., Wen, Z., Yao, B. and Dong, J. 2017. The gas-solid flow characteristics of cyclones. *Powder Technology*. **308**,pp.178–192.

Welt, J., Lee, W. and Krambeck, F.J. 1977. Catalyst attrition and deactivation in fluid

catalytic cracking system. *Chemical Engineering Science*. **32**(10),pp.1211–1218.

Wen, C.Y. and Yu, Y.H. 1966. Mechanics of fluidization. *Chemical Engineering Progress, Symposium Series*. **62**(1),pp.100–111.

Werther, J. 1992. Scale-up modeling for fluidized bed reactors. *Chemical Engineering Science*. **47**(9–11),pp.2457–2462.

Werther, J. and Hartge, E.U. 2004. A population balance model of the particle inventory in a fluidized-bed reactor/regenerator system. *Powder Technology*. **148**(2-3 SPEC. ISS.),pp.113–122.

Werther, J. and Reppenhagen, J. 2003. Attrition *In*: W. C. Yang, ed. *Handbook of Fluidization and Fluid-Particle Systems*. CRC Press.

Werther, J. and Reppenhagen, J. 1999. Catalyst Attrition in Fluidized-Bed Systems. *Reactors, Kinetics, and Catalysis*. **45**(9),pp.2001–2010.

Werther, J. and Reppenhagen, J. 2001. Catalyst Attrition in Fluidized-Bed Systems. *AIChE Journal*. **45**(9),pp.2001–2010.

Werther, J. and Xi, W. 1993. Jet attrition of catalyst particles in gas fluidized beds. *Powder Technology*. **76**.

Wilcox, D.C. 1993. *Turbulence modeling for CFD*. DCW Industries, Inc.

Xi, W. 1993. Katalysatorabrieb in Wirbelschichtreaktoren.

Xu, B.H. and Yu, A.B. 1997. Numerical simulation of the gas-solid flow in a fluidized bed by combining discrete particle method with computational fluid dynamics. *Chemical Engineering Science*. **52**(16),pp.2785–2809.

Xu, W., DeCroix, D.S. and Sun, X. 2014. Mechanistic based DEM simulation of particle attrition in a jet cup. *Powder Technology*. **253**,pp.385–392.

Yang, W.-C. 2003. *Handbook of Fluidization and Fluid-Particle Systems*.

Yates, J.G., Bejek, V. and Cheesman, D.J. 1986. Fluidization V *In*: K. Ostergaard and A. Sorensen, eds. *Engineering Foundation*. New York: Elsevier, p. 79.

Yuregir, K.R., Ghadiri, M. and Clift, R. 1986. Observations on impact attrition of granular

solids. *Powder Technology*. **49**(1),pp.53–57.

Zenz, F. and Kelleher, G. 1980. Studies of attrition rates in fluid– particle systems via free fall, grid jets, and cyclone impact *In*: *Powder Bulk Technology*., pp. 13–20.

Zhang, H., Degrève, J., Baeyens, J. and Wu, S. 2016. Powder attrition in gas fluidized beds. *Powder Technology*. **287**,pp.1–11.

Zhang, K., Brandani, S., Bi, J. and Jiang, J. 2008. CFD simulation of fluidization quality in the three-dimensional fluidized bed. *Progress in Natural Science*. **18**(6),pp.729–733.

Zhang, S.-H., Boerefijn, R. and Ghadiri, M. 1998. The effect of orifice size on the breakage of fluid cracking catalyst particles in fluidised bed jets *In*: *Proc.World Congr. on Particle Technology 3*. Brighton.

Zhang, Z. and Ghadiri, M. 2002. Impact attrition of particulate solids. Part 2: Experimental work. *Chemical Engineering Science*. **57**(17),pp.3671–3686.